Synthesis and Ultrafast Spectroscopy of Porphyrin Molecular Wires



William Kendrick

New College

University of Oxford

A thesis submitted for the degree of

Doctor of Philosophy

Michaelmas 2019

Acknowledgements

I would like to sincerely thank Professor Harry Anderson for his continued support and excellent supervision. Harry goes above and beyond what is expected of a supervisor and I am very grateful for all his encouragement and generosity with his time. Much of these acknowledgements will be directed towards other members of the group, which is in no small part due to the work atmosphere Harry fosters with his enthusiasm for science, patience with his students and general positive attitude.

This DPhil would not have been possible without the patience (/endurance?) of our collaborators at the Central Laser Facility. Dr Greg Greetham, Dr Igor Sazanovich, Dr Paul Donaldson and Dr Mike Towrie are thanked for sticking with me through all of the stupid questions, repeated experiments and many manuscript drafts. Professor Tony Parker is sincerely thanked for being the glue that held the project together; his motivation in what were long and sometimes demoralising access times kept me going and his commitment to science is energising.

My formative months in the group were helped massively by some kind and patient mentors; Dr Jonathan Cremers is thanked for sticking with me through the first few failed reactions and for being so generous with his time. I am also grateful to Dr Martin Peeks for getting me up to speed with everything photophysical. Przemek and Takayuki are thanked for being friendly fonts of general chemistry knowledge. Thanks also to Bart for being a human StackExchange for all my Python questions. Special thanks also to Michael for being a general sounding board and for keeping me sane during those long weeks in windowless laser labs.

I would also like to thank Dr James Thomas, Pernille Bols and Dr Steffen Woltering for taking the time to proof-read this thesis and for doing such a thorough and helpful job.

The group has been an amazing place to work and learn. Thank you to all members of the lab past and present: Jonathan, James, Michael, Anjul, Yaoyao, Przemek, Martin, Takayuki, Isa, Dan, Sabine, Michel, Bart, Andreas, Huawei, Pernille, Wenjun, Lorel, Lara, Kenny, Steffen, Virginia, Andrew, Keith, Henrik, Joe, Boom, Sebastian, Kate, Tom and Isaac for all playing a part in making the past 3 years so fun.

The most sincerest of thanks to all my friends, without which my life would be so much more boring; thank you to my Oxford friends, who have become my closest in such a short period of time; to the Leicester lads aka Coalville crew for staying as close as we've always been; and to my friends in London for offering an escape from the bubble and for the innumerable weekend memories. My final and most grateful thanks are to my family: Mum, Dad, Lucy and George (the dog). I wouldn't have achieved anything if not for your faultless support, encouragement and faith you've shown in me since forever.

Abstract

Porphyrins, found in nature in cyclic light harvesting arrays, are a fascinating class of compounds. Their synthesis and assembly into advanced light harvesting architectures have challenged chemists for decades, and their resulting photophysical properties such as energy transfer and charge localisation continue to teach us about fundamental physical effects. This thesis explores both of these aspects, starting first with the synthesis of a porphyrin nanoball before exploring the ultrafast spectroscopy of porphyrin molecular wires.

Chapter 1 introduces the chemistry of porphyrins. The syntheses of porphyrin monomers are discussed, highlighting the key route to functionalised porphyrins. A range of cyclic porphyrin arrays are presented, and the syntheses compared and contrasted. Finally, 3D porphyrin nanostructures are discussed, comparing and contrasting their formation via self-assembly and template-directed syntheses.

Chapter 2 presents a novel 3D pyridyl template for the formation of a 10-porphyrin nanoball. Several ball precursors are identified and synthesised, before ball formation proved unsuccessful. The factors affecting the unsuccessful ball formation are discussed in detail with the help of ^{1}H NMR and UV-vis-NIR titrations. The lessons learnt are applied to the design of a new template, for which a synthesis is suggested.

In Chapter 3 π-conjugated compounds are summarised. Two ultrafast spectroscopy techniques are introduced, 2D-infrared and time-resolved infrared, and their spectra derived from model examples to aid the reader in interpretation. The literature regarding ultrafast spectroscopy applied to π-conjugated polymers is summarised, before an area of underexplored research is identified.

Chapter 4 presents an in-depth ultrafast spectroscopic study of the radical cations of porphyrin oligomeric molecular wires. Using spectroelectrochemistry to generate the radical cations, 2D-IR and TRIR were undertaken to elucidate the mechanism of infrared band activation. The data show that the intensification of infrared bands upon oxidation is a result of strong coupling between vibrational motion and charge.

Supplement to Statement of Authorship

Chapter 2 - The original synthesis of ***b*-P10** was achieved by Dr Jonathan Cremers, who also performed the initial binding titrations presented on p. 31. The route to **T10** was devised and trialled by Dr Ludovic Favereau, and later repeated and optimised by me.

Chapter 4 - All Ultrafast Spectroscopy experiments were performed jointly with Michael Jirasek at the Central Laser Facility, Science and Technology Facilities Council. Experiments were designed and implemented jointly with instrument scientists Dr Gregory M. Greetham, Dr Igor V. Sazanovich, Dr Paul M. Donaldson, Dr Michael Towrie and Prof. Anthony W. Parker at the Central Laser Facility. The analysis of polarisation sensitive time-resolved infrared data (and associated figures) and density functional theory calculations were performed by Michael Jirasek. Samples of ***l*-P2** and ***c*-P6·T6** were provided from Michael Jirasek, Dr Martin Peeks and Dr Jonathan Cremers.

Contents

List of Publications and Awards xi
Abbreviations xii
1 Introduction 1
1.1 Outline 2
1.2 Porphyrins 2
1.2.1 Synthesis 2
1.3 '2D' porphyrin nanostructures 5
1.4 '3D' porphyrin nanostructures 11
1.4.1 Self-assembled 3D porphyrin architectures 11
1.4.2 Covalent 3D porphyrin architectures 16
1.5 Prospectus 20
2 Towards 3D Template Directed Synthesis of a 10-Porphyrin Nanoball 22
2.1 Abstract 23
2.2 Introduction 23
2.2.1 Prospective 25
2.2.2 Synthetic plan 27
2.3 The Template 30
2.3.1 T10 Synthesis 30
2.3.2 Preliminary investigations 31
2.4 Precursor synthesis 32
2.4.1 *X*-P5 32
2.4.2 *I*-P5 34
2.4.3 preball-P10 36
2.5 Ball formation tests 37
2.5.1 *x*-P5 and *I*-P5 38
2.5.2 Preball-P10 46
2.6 Conclusion 53
2.7 Future work 54
2.8 Experimental appendices 57
2.8.1 General experimental procedures 57
2.8.2 Synthetic procedures 58

2.8.3 Fluorescence measurements....94

3 Ultrafast Spectroscopies and Their Application to π-Conjugated Systems – A Chemist's Introduction....96

3.1 Outline....97

3.2 Introduction....97

3.3 Ultrafast infrared spectroscopy – A chemist's introduction....98

3.3.1 Time-resolved infrared (TRIR)....98

3.3.2 Applications of TRIR....100

3.3.3 Two-dimensional infrared spectroscopy (2D-IR)....101

3.3.4 Applications of 2D-IR....103

3.3.5 TRIR vs 2D-IR....105

3.4 Ultrafast IR spectroscopy applied to π-conjugated materials....107

3.5 Prospectus....109

4 Ultrafast Spectroscopies as Tools for Exploring Infrared-Active Vibrations (IRAVs) in Porphyrin Molecular Wires....110

4.1 Abstract....111

4.2 Introduction....111

4.2.1 Charge transport,polarons and IRAVs....111

4.2.2 Porphyrin radical cations....113

4.2.3 Spectroscopic approach....115

4.3 Results....116

4.3.1 Single shot 2D-IR – ULTRA....116

4.3.2 LIFEtime TR-2D-IR....118

4.3.3 Fitting of spectrokinetic data....122

4.3.4 TRIR spectroscopy....125

4.3.5 DFT calculations....127

4.4 Discussion....128

4.5 Experimental Appendices....132

4.5.1 Synthesis....132

4.5.2 Photophysical investigations....132

4.5.3 2D-IR kinetic fitting....136

1.1.1 Grow-in fitting....141

4.5.4 LIFEtime time domain traces....146

4.5.5 Polarisation sensitive TRIR 150

5 References 152

List of Publications and Awards

Publications

1. W. J. Kendrick, M. Jirásek, M. D. Peeks, G. M. Greetham, I. V. Sazanovich, P. M. Donaldson, M. Towrie, A. W. Parker and H. L. Anderson, 'Mechanisms of IR Amplification', *Chem. Sci.*, ASAP, nan: 10.1039/c9sc05717j.

Awards

1. *Thieme Poster Prize*, International Symposium on Functional π-Electron Systems (Fπ14), Berlin (De), June 2019

2. *Poster Prize*, Lasers for Science Facility / Artemis User Meeting, Oxford (UK), April 2019

3. *Eli Lilly Prize for Excellence in Organic Chemistry*, University of Oxford (UK), November 2017

Abbreviations

2D-ES	Two-dimensional electronic spectroscopy
2D-IR	Two-dimensional infrared spectroscopy
Ar	Aryl
CLF	Central Laser Facility
COSY	Correlated Spectroscopy
CPDMS	3-cyanopropyldimethylsilyl
d	doublet (in NMR)
DABCO	1,4-diazobicyclo[2.2.2]octane
dba	Dibenzylideneacetone
DDQ	2,3-Dichloro-5,6-dicyano-1,4-benzoquinone
DFT	Density functional theory
DNAQ	1,5-Dinitroantraquinone
dppf	1,1'-bis(diphenylphosphino)ferrocene
FWHM	Full-width at half-maximum
GPC	Gel permeation chromatography
HOMO	Highest occupied molecular orbital
IR	Infrared
IRF	Instrument response function
IVR	Intramolecular vibrational relaxation
JDMN	Juilolidinemalononitrile (9-(2,2-dicyanovinyl)julolidine)
LUMO	Lowest unoccupied molecular orbital
m	multiplet (in NMR)
MEH-PPV	Poly{[2-methoxy-5-(2-ethylhexyloxy)-1,4-phenylene]vinylene}
NBS	*N*-Bromosuccinimide
NICS	Nucleus-independent chemical shift
NMR	Nuclear magnetic resonance
NOESY	Nuclear Overhauser effect spectroscopy
OPV	Organic photovoltaics
OTTLE	Optically transparent thin layer electrochemical (cell)
PCBM	phenyl-C61-butyric acid methyl ester
s	singlet (in NMR)
SEC	Size-exclusion chromatography
SMC	Suzuki-Miyaura cross coupling
SOMO	Singly occupied molecular orbital
SWV	Square wave voltammetry
t	triplet (in NMR)
TBAF	Tetra-*n*-butylammonium fluoride
TBAP	Tetra-*n*-butylammonium hexafluorophosphate

TFA	Trifluoroacetic acid
THF	Tetrahydrofuran
THS	Trihexylsilyl
TICT	Twisted intramolecular charge transfer
TIPS	Triisopropylsilyl
TLC	Thin layer chromatography
TR-2D-IR	Time-resolved two-dimensional infrared spectroscopy
TREN	Tris(2-aminoethyl)amine
TRIR	Time-resolved infrared spectroscopy
UV-vis-NIR	Ultra-violet, visible and near infrared

1

Introduction

1.1 Outline 2
1.2 Porphyrins 2
1.2.1 Synthesis 2
1.3 '2D' porphyrin nanostructures 5
1.4 '3D' porphyrin nanostructures 11
1.4.1 Self-assembled 3D porphyrin architectures 11
1.4.2 Covalent 3D porphyrin architectures 16
1.5 Prospectus 20

1.1 Outline

This thesis is split broadly into two related themes: 3D template-directed synthesis as a route to a porphyrin nanoball and ultrafast spectroscopies for exploring the photophysical properties of porphyrin molecular wires. This chapter will introduce porphyrin synthesis and literature examples of 2D and 3D porphyrin architectures. The introduction to ultrafast spectroscopies of π-conjugated polymers and molecular wires will be covered in Chapter 3.

1.2 Porphyrins

Porphyrins (Figure 1.1) are an amazingly diverse class of compounds. Found extensively in nature, for example in light harvesting complexes in photosynthesis,[1–3] the utility of porphyrins is often derived from their photophysical properties. Comprising four pyrrole units connected by methine bridges, porphyrins are conjugated around the entire macrocycle and are consequently aromatic, satisfying Hückel's rule of [4*N*+2] π-electrons. Their utility can further be extended by the insertion of a metal centre, where the porphyrin macrocycle now acts as a tetradentate ligand. The resulting metal-centred porphyrins (metalloporphyrins, Figure 1.1b) can show markedly different behaviour to free-base porphyrins, such as in their photophysical behaviour or coordination chemistry via axial ligation.

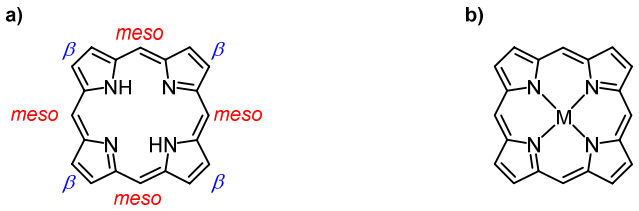
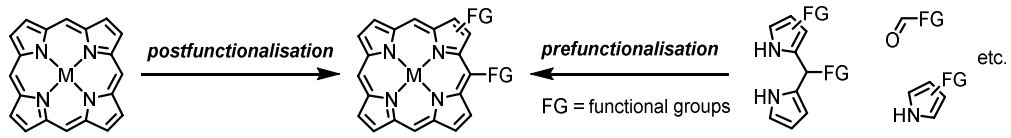


Figure 1.1. (a) The meso and β positions on a porphyrin macrocycle. (b) The general structure of a metalloporphyrin.

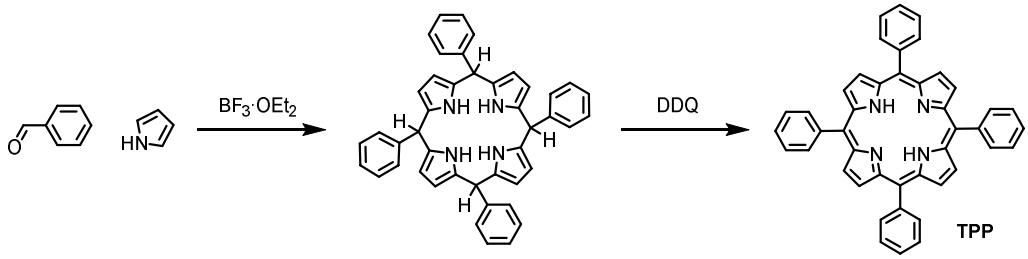
1.2.1 Synthesis

The synthesis and functionalisation of porphyrins can be approached via two different strategies: prefunctionalisation or postfunctionalisation (Scheme 1.1).[4,5] In prefunctionalisation, porphyrins are synthesised via ring closing reactions with precursors containing the desired functional groups. In postfunctionalisation, functional groups are attached to porphyrins after the formation of the macrocycle. Of course, in more complex synthetic targets both of these approaches can be used on the same molecule in a well-designed synthesis.



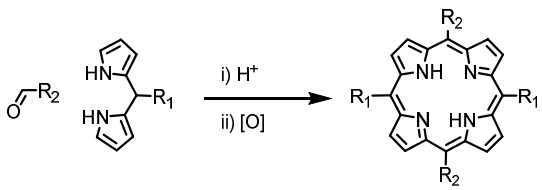
Scheme 1.1. Synthesis of functionalised porphyrins via post- and prefunctionalisation.

If four-fold symmetric porphyrins are required, the most sensible and high-yielding synthesis is that reported by Lindsey and co-workers.[6] A high-dilution synthesis between a functionalised pyrrole[7,8] and a functionalised aldehyde in the presence of a Lewis acid such as $BF_3{\cdot}OEt_2$, followed by aromatisation of the resulting porphyrinogen with an oxidant such as 2,3-dichloro-5,6-dicyanobenzoquinone (DDQ) forms the symmetric porphyrin in reasonable yields (35-50% in the case of tetraphenyl-porphyrin, **TPP**, Scheme 1.2).[6]



Scheme 1.2. Synthesis of tetraphenylporphyrin (**TPP**) via the high-dilution route optimised by Lindsey *et al.*[6]

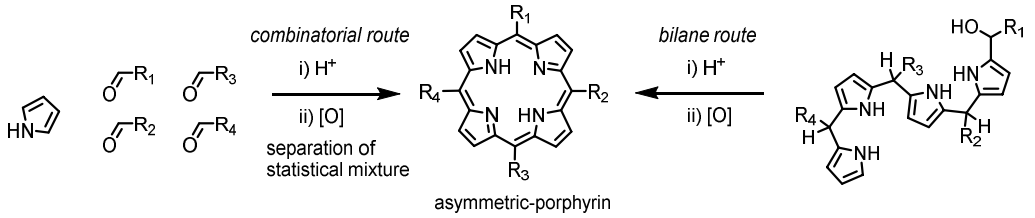
For less symmetric porphyrins, such as two-fold symmetric porphyrins, functionalised dipyrromethanes[9] can be condensed in a similar high-dilution procedure (Scheme 1.3) with functionalised aldehydes in a 2 + 2 acid-catalysed condensation followed by aromatisation with an oxidant such as DDQ in good yields (generally 50 – 100%).[10–12]



Scheme 1.3. 2 + 2 approach to the synthesis of two-fold symmetric substituted porphyrins.

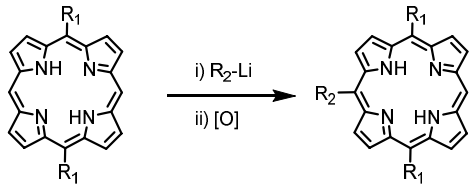
More asymmetric porphyrins become difficult to achieve. Perhaps the most straightforward, but lowest yielding, is to produce a statistical mixture of products from functionalised pyrroles and aldehydes, followed by careful separation of the desired compound (combinatorial approach, Scheme 1.4).[13–15] Another route is to perform a bilane cyclisation, where the functionalised units are assembled in a linear tetramer followed by acid-catalysed cyclisation and rearomatisation by an oxidant (bilane approach, Scheme 1.4).[14,16] Although this route forms the desired asymmetric porphyrin

as the major product, synthesis of the substituted bilanes is non-trivial and the product mixture remains complicated due to the scrambling of pyrrole units during ring formation.



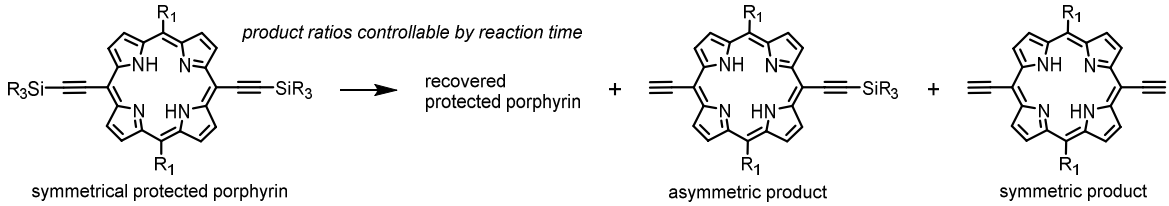
Scheme 1.4. Routes to asymmetric meso-substituted porphyrins. The combinatorial route can be accessed via simple precursors, but requires the difficult separation of statistical product mixtures. The bilane route is selective for the assymetric porphyrin, but requires non-trivial synthesis of bilanes.

Some asymmetry can be afforded by postfunctionalisation.[5,15] For example, reacting porphyrins with one equivalent of an organolithium reagent results in a nucleophilic addition reaction at the porphyrin meso-position, allowing asymmetric products of the type shown in Scheme 1.5 to be produced after rearomatisation.[13,15,17,18]



Scheme 1.5. Asymmetric porphyrin synthesis with organolithiums.

In general, introducing asymmetry into porphyrins requires non-trivial syntheses or low yielding one-pot procedures. For this reason, statistical reactions are often used where perhaps they would be avoided in other syntheses. For example, porphyrins with protected meso-alkynes have been routinely statistically deprotected to achieve asymmetric monomers, a technique commonly used in the Anderson group (Scheme 1.6).[19,20] The benefit of this route is the cost for asymmetry is paid for in the statistical mixture of products. If the reaction is stopped before significant production of fully deprotected porphyrin monomer, and the protecting groups are chosen such that resulting chromatography of the mixture is simple, the starting material can be fully recovered and resubmitted to reaction conditions increasing total yields above the statistical maximum.



Scheme 1.6. The statistical deprotection of meso-alkyne porphyrins commonly employed by the Anderson group.

The deprotected alkynes can be coupled together in an oxidative homo-coupling reaction to form butadiyne-linked oligomers. Unlike other porphyrin oligomers such as direct meso-meso-linked[21,22] and ethyne-linked,[23,24] butadiyne-linked confer conjugation and electronic communication across the porphyrin units due to the relatively low barrier of porphyrin rotation (Figure 1.2).[25]

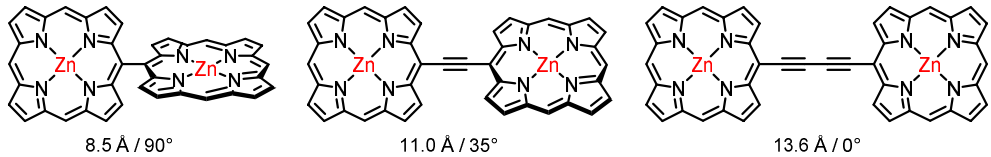


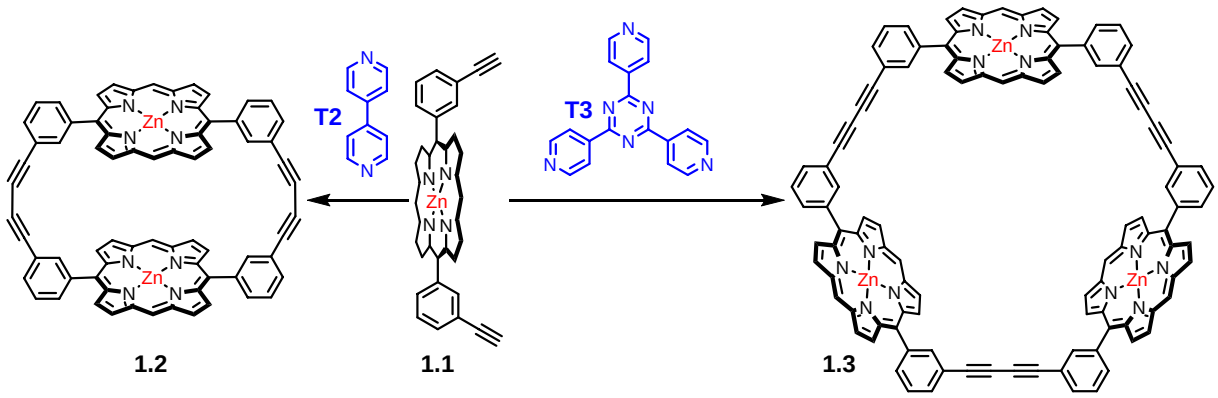
Figure 1.2. Types of porphyrin-porphyrin meso linkages and their associated minimum-energy dihedral angles showing the enhanced conjugation of ethyne and butadiyne-linked porphyrins.[21–25]

These oligomers are referred to as 'molecular wires' (the importance of molecular wires and π-conjugated materials in general will be discussed in Chapter 3). This thesis will explore the synthesis of butadiyne-linked porphyrin structures, before discussing the photophysics of molecular wires (Chapter 4). First, examples of the successful synthesis of porphyrin cyclic arrays and 3D nanostructures will be presented, comparing and contrasting their synthesis and properties against conjugated porphyrin oligomers synthesised by the Anderson group.

1.3 '2D' porphyrin nanostructures

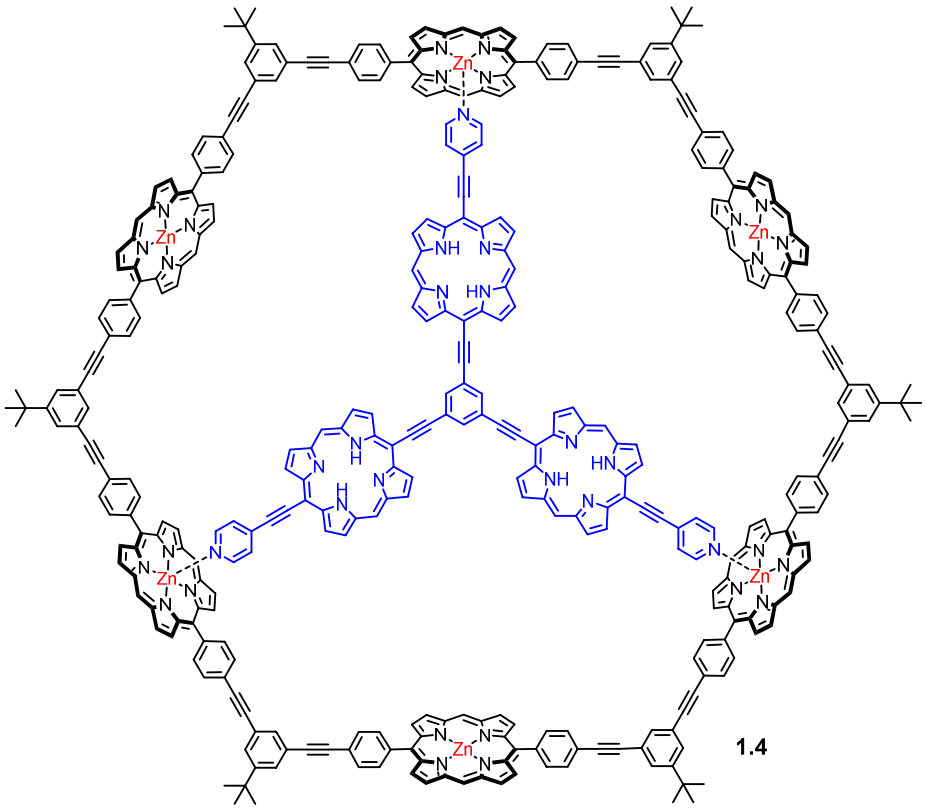
Metalloporphyrins can form axial non-covalent bonds via coordinating ligands such as pyridine. This behaviour has been exploited in the template-directed synthesis of '2D' porphyrin oligomeric nanostructures (where 2D refers to the number of dimensions the repeating units extend into, where 1D would be a linear oligomer, 2D would be rings, 3D would be spheres). Early examples demonstrated the utility of template-directed synthesis via the formation of differently sized cyclic porphyrin arrays depending on the template used during the formation (Scheme 1.7). Subjecting porphyrin monomer **1.1** to Glaser alkyne homo-coupling conditions in the presence of **T2** resulted in a 72% yield of

dimer **1.2**, whereas the same reaction repeated with the use of tridentate template **T3** instead resulted in trimer **1.3** being the major product in 52% yield, highlighting the importance of the template in the formation of porphyrin cyclic arrays.[26–29]



Scheme 1.7. Dimerisation and trimerisation of porphyrin **1.1** directed by pyridyl templates **T2** and **T3** respectively.[27,28] Solubilising aryl groups hidden for clarity.

Driven by the similarity of cyclic porphyrin arrays to nature's light harvesting complex, a whole range of cyclic porphyrin oligomers were prepared using template-directed syntheses.[26] An impressive example is the work of Gossauer and co-workers who synthesised hexaporphyrin **1.4** using a tridentate template (Scheme 1.8).[30]



Scheme 1.8. The structure of the cyclic porphyrin array **1.4** synthesised via a template driven synthesis by Gossauer and co-workers.[30] Solubilising aryl groups hidden for clarity.

Another example is that of the porphyrin nanobarrels by Osuka and co-workers.[31] Coupling together two β-functionalised porphyrins in a Suzuki cross coupling reaction afforded the porphyrin barrel in 10% yield (Figure 1.3). This is a tight cyclic porphyrin array which was found to bind C_{60} due to the favourable interactions with the large π faces of the porphyrins.

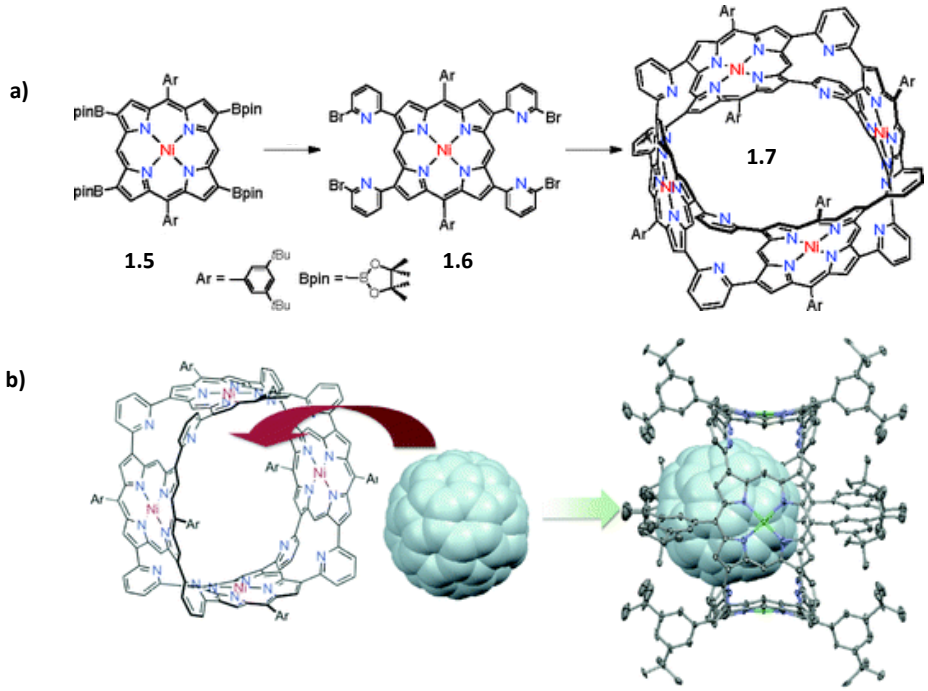
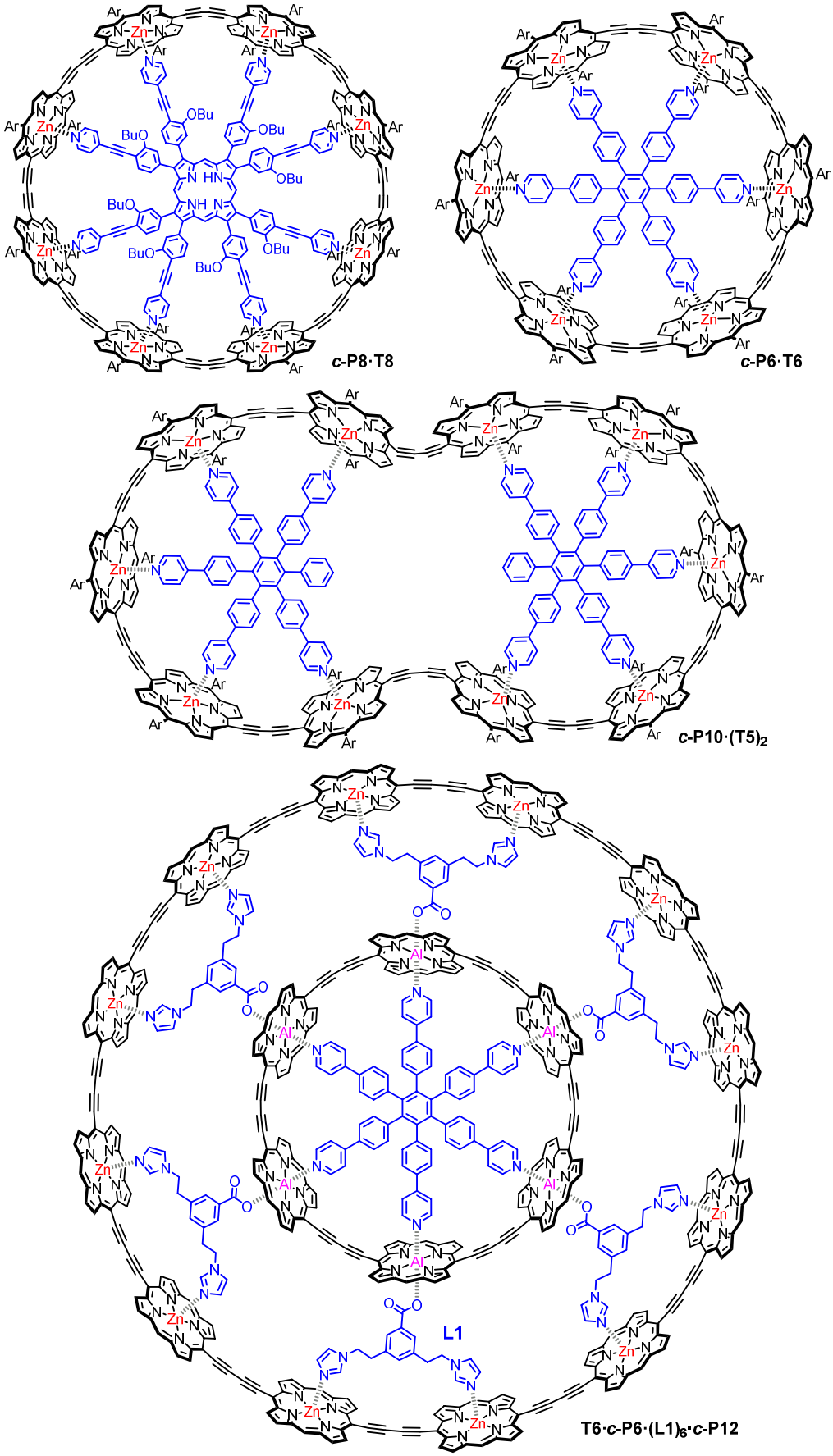


Figure 1.3. (a) Synthesis of porphyrin nanobarrel by Osuka and co-workers.[31] (b) Binding of C_{60} by the porphyrin nanobarrel. Adapted with permission from J. Song, N. Aratani, H. Shinokubo and A. Osuka, *J. Am. Chem. Soc.*, 2010, **132**, 16356–16357. Copyright (2010) American Chemical Society.

Although these arrays are cyclic, there is little electronic communication between the porphyrin units due to the twist between the porphyrin and linking aryls. Anderson and co-workers reported the synthesis of a range of fully conjugated cyclic porphyrin nanorings.[32,33,42–46,34–41] Initially beginning with the cyclisation of a linear octamer around an octadentate template to form ***c*-P8·T8**,[41] before also reporting a host of different ring sizes achieved through different template-directed approaches such as those presented in Scheme 1.9.[35]

The conjugated nature of the porphyrin nanorings imbues them with fascinating photophysical properties. For example, ultrafast fluorescence anisotropy measurements of a range of these nanorings have provided insight into the electronic delocalisation afforded by the global conjugation, finding that the excited states of such systems are delocalised over the whole π-system.[39,42,44,46–50]



Scheme 1.9. Examples of rings synthesised by Anderson and co-workers using pyridyl-based template-directed syntheses.[35] Solubilising aryl groups on **T6·*c*-P6·(L1)$_6$·*c*-P12** are hidden for clarity.

Another fascinating property of these systems is that of quantum interference. Quantum interference can be understood with analogy to a Mach-Zehnder interferometer, where a beam of light is split into two, directed down paths of differing lengths, and finally recombined. If the difference in path lengths is a multiple of the wavelength λ, then the signal undergoes constructive interference (Figure 1.4d). If the difference in path lengths is a multiple of λ/2 then the signal undergoes destructive interference and is not observed. Quantum interference is understood as the same effect but with the wavefunction of an electron, rather than an electromagnetic wave.

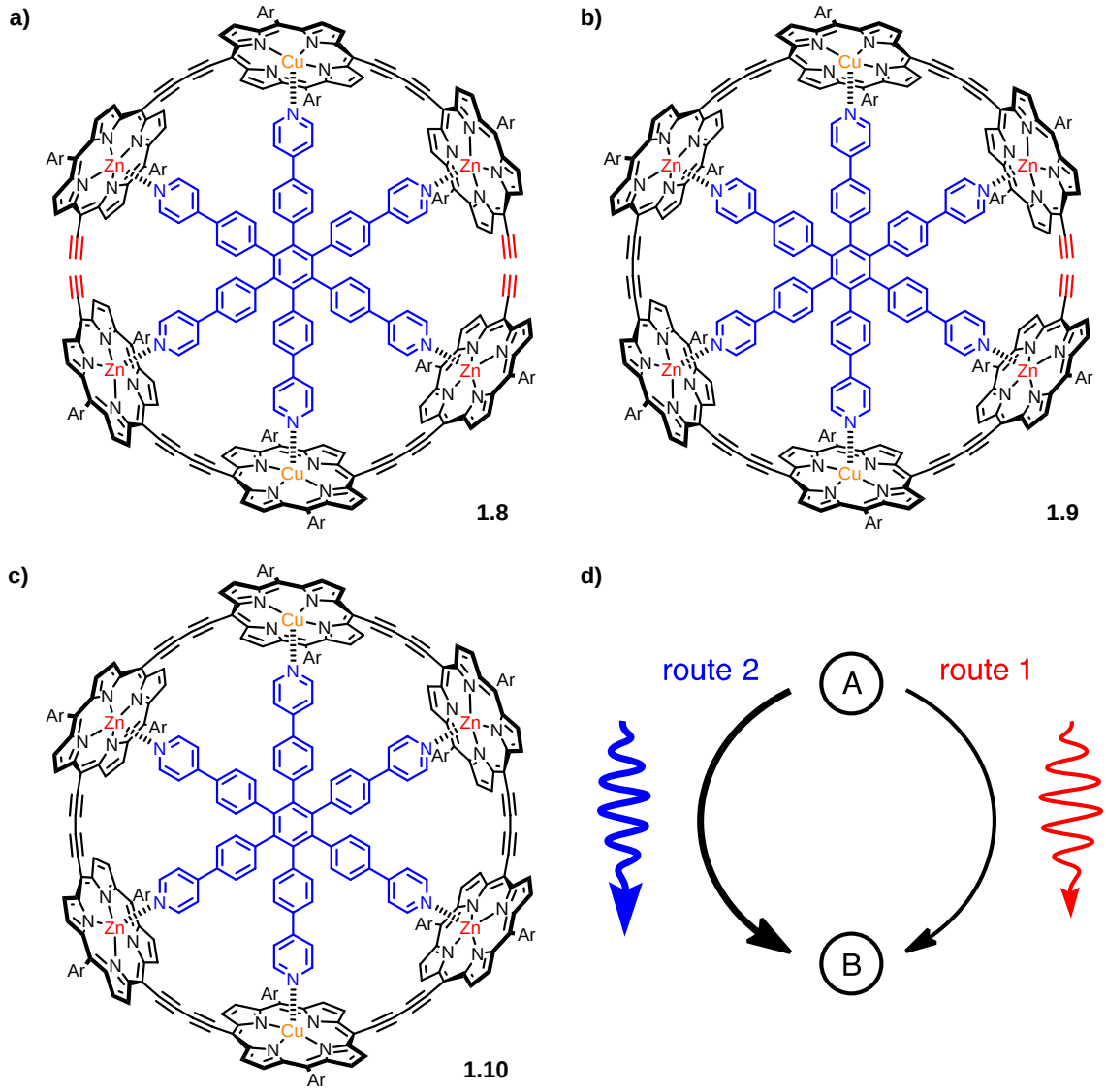
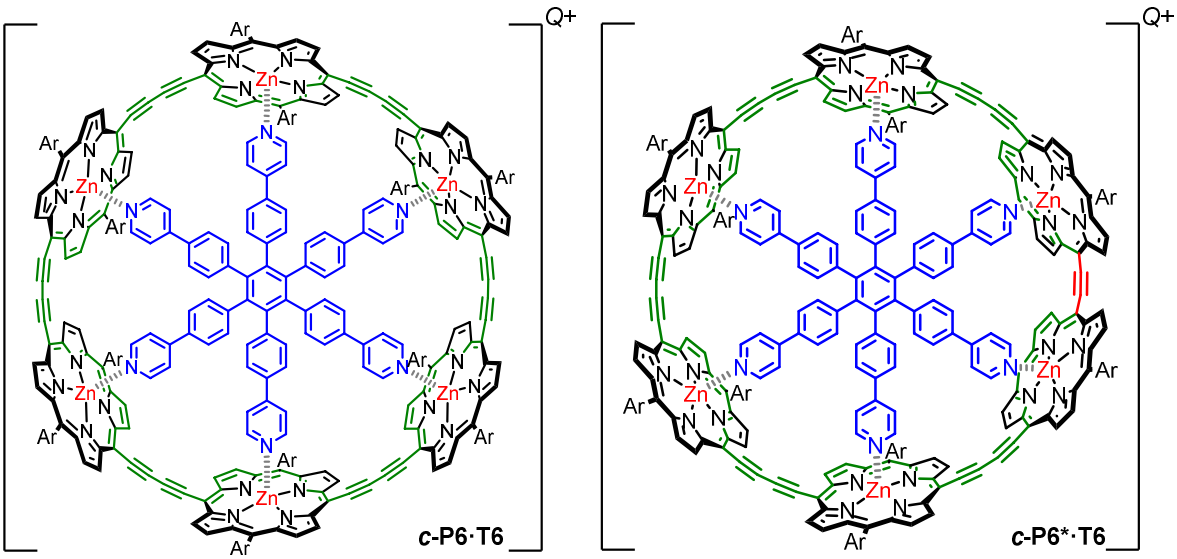


Figure 1.4. (a) Control complex with broken conjugation between copper centres. (b) Control complex with one conjugated pathway and one broken conjugation pathway between the metal centres. (c) Heterometallated nanoring with two conjugated pathways between copper centres. (d) Pictorial representation of quantum interference of two parallel and in-phase waves.[51]

Electron paramagnetic resonance (EPR) measured the through-bond exchange coupling, *J*, between two paramagnetic copper(II) centres in a series of porphyrin arrays

(Figure 1.4a-c).[51] By comparing and contrasting three compounds with differing conjugation, it was found that the exchange coupling between metal centres in **1.10** was four times larger than **1.9**, rather than only by a factor of two which would be expected by a classical description given by Kirchoff's circuit law.[52] This observed phenomenon was attributed to quantum interference; due to the delocalisation afforded by the conjugation, the wavefunction of electrons can interfere constructively with themselves (due to the two identical paths between metal centres), resulting in the observed exchange couplings compared to one conjugated pathway (**1.9**) or none (**1.8**).[51]

These conjugated nanorings have also pushed the boundaries of aromaticity. Hückel's rule predicts that molecules with delocalised circuits of [4*N*+2] (aromatic) or [4*N*] (antiaromatic) exhibit ring currents around their perimeters.[53] The direction of this ring current in aromatic molecules is such to generate an opposing magnetic field to the external field inside the ring, whereas for antiaromatic molecules the ring current flows in the opposite direction, in such a way as to increase the magnetic field on the inside of the ring.[54]



Scheme 1.10. ***c*-P6·T6**$^{Q+}$ and ***c*-P6*·T6**$^{Q+}$ and their global conjugation pathways. Increasing the oxidation number switched aromaticity from global aromaticity to antiaromaticity in line with Hückel's rule.[55,56]

In a neutral porphyrin nanoring, ***c*-P6·T6**, one can count a circumferential circuit of 84 π electrons (4N, Scheme 1.10). However, rather than showing global antiaromaticity, these systems display local aromaticity of the individual porphyrin units. Upon oxidation, this

ring begins to display global antiaromaticity (4+, 80 π electrons) and global aromaticity (6+, 78 π electrons) around a circumference of 7.5 nm, surpassing the previous record of 50 π electrons.[55,57]

In an elegant control study, porphyrin nanoring ***c*-P6*·T6** was prepared which is analogous to ***c*-P6·T6** with the exception of the replacement of one of the butadiyne linkages with a single acetylene.[50] This reduces the electron count of the circumferential circuit by 2, and as such consists of a circuit of 82 π electrons. When the nanoring is oxidised, the opposite behaviour to that of ***c*-P6·T6^{N+}** is observed, consistent with Hückel's rule.[56] These studies have been extended even further across a range of different ring sizes, alkyne connectivities and topologies,[56] as well as observation of the same phenomena in anions.[58]

1.4 '3D' porphyrin nanostructures

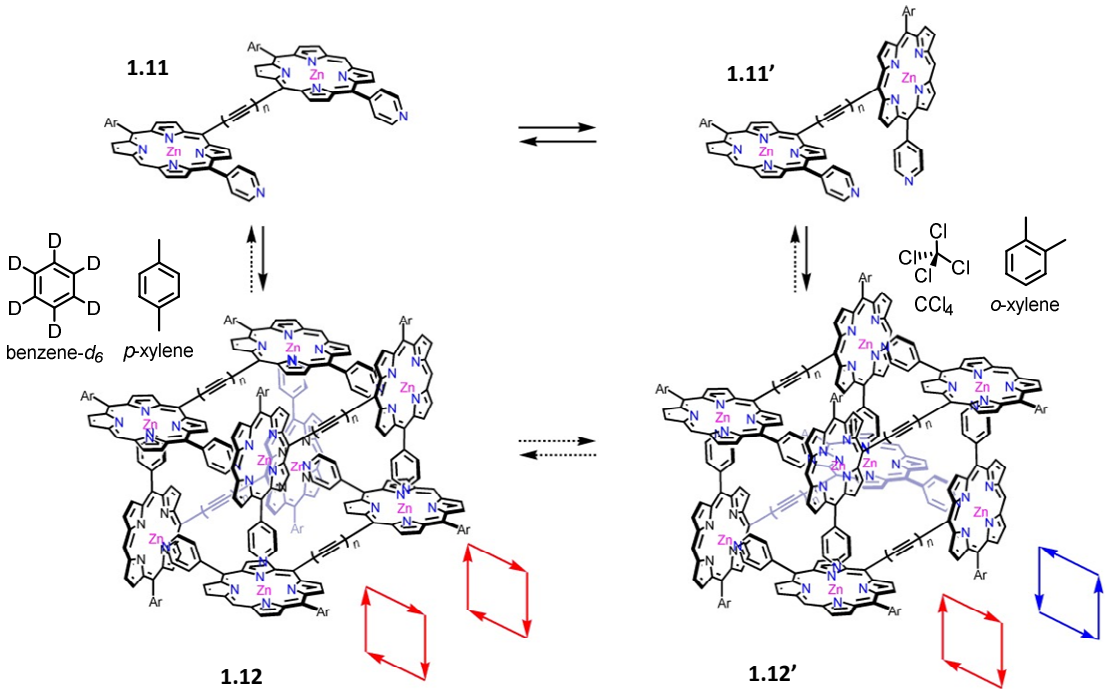
Moving away from disc or cycle shapes, there are many examples of three-dimensional porphyrin nanostructures. The examples are broadly split into two different types; self-assembled complexes and nanostructures synthesised by template-directed syntheses (effectively forming covalent links between different units on a self-assembled complex).[26,59–61]

1.4.1 Self-assembled 3D porphyrin architectures

One early example of self-assembled 3D nanostructures is the work of Aida and co-workers, who used pyridyl-functionalised porphyrins to self-assemble a porphyrin 'box'.[62–66] By taking advantage of the strong co-ordination between the pyridyl ligands and porphyrin metal-centres, self-assembled box complexes of two isomers were isolated and characterised (Scheme 1.11, **1.12** and **1.12'**).

Interestingly, the conformational isomers were sensitive to solvent. By exploring the solvatochromism of a range of solvents, it was found that the UV-vis spectrum of the boxes in CCl_4 was different than in benzene-d_6, even though the dielectric constants of the two solvents are almost identical (2.23 and 2.27 respectively). By changing the solvent, the isomers could be switched from one box to another with an associated change in the UV-vis spectrum as a result of increased conjugation in box **1.12** due to the coplanar orientation of the porphyrins in **1.11**. The switching was determined to be as a

result of the shape of the solvent, and the authors described a new type of 'conformational' solvatochromism (compared to solvatochromism as a result of solvent polarity). The authors were then able to determine regioisomers of xylene that differ mainly in the branching of the alkyne chain via the observed spectrum changes.



Scheme 1.11. Porphyrin dimer **1.11** and conformer **1.11'** (*n* = 2) can self-assemble into two box conformations **1.12** or **1.12'**. The conformation can be chosen by the solvent – planar molecules benzene-d_6 and *p*-xylene prefer the planar porphyrin dimer, whereas CCl_4 and *o*-xylene prefer the perpendicular dimer. Reproduced with permission from J. Aimi, Y. Nagamine, A. Tsuda, A. Muranaka, M. Uchiyama and T. Aida, *Angew. Chem., Int. Ed.*, 2008, **47**, 5153–5156. Copyright (2008) Wiley-VCH.

Hupp and co-workers have also reported self-assembled porphyrin boxes (Figure 1.5).[67–70] These porphyrin boxes act as hosts to a manganese dimer, resulting in a catalytic cavity. The size of the cavity provided size-selective catalysis between cis-stilbene vs cis-3,3',5,5'-tetra(tert-butyl)stilbene, with the smaller cis-stillbene being preferentially epoxidated (Figure 1.5b). Impressively, changing the porphyrin box building units to tin porphyrins with axially coordinated chiral phenylalanines made the box chiral and allowed for asymmetric catalysis in the sulfoxidation of p-tolyl sulfide, with the sulfoxide produced in 12% ee. Reversing the chirality of the axial ligand reversed the entioselectivity of the reaction, providing evidence of induced enantioselectivity by a chiral cavity.

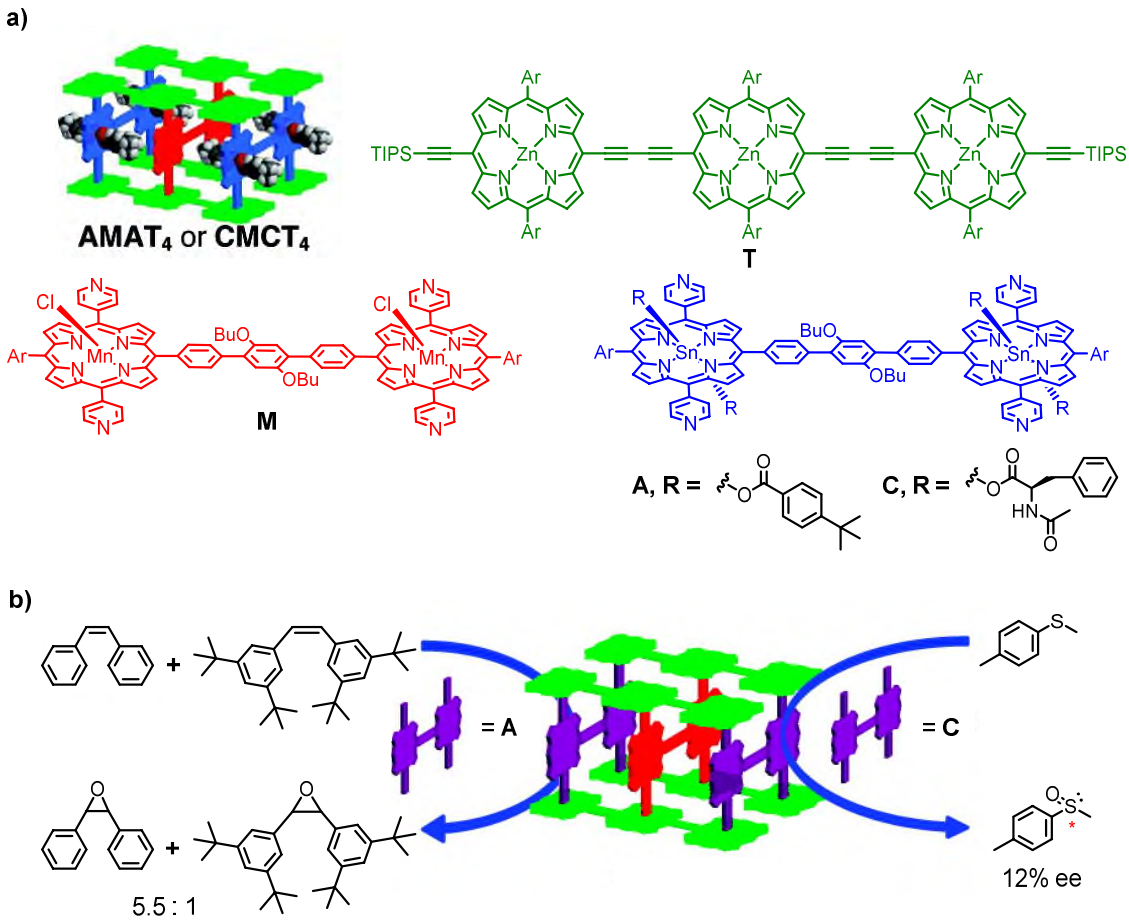
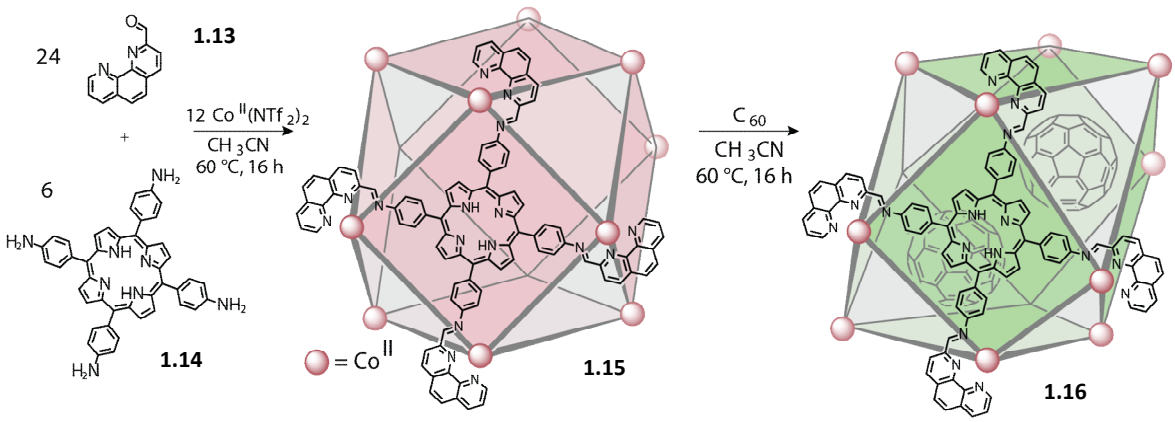


Figure 1.5. (a) Structure of porphyrin box **AMAT$_4$** or **CMCT$_4$** and the chemical structures of **T**, **M** and **A**/**C**. (b) Size selective catalysis of stilbene epoxidation with **AMAT$_4$** and enantioselective sulfoxidation afforded by the chiral cavity of **CMCT$_4$**. Adapted with permission from S. J. Lee, S.-H. Cho, K. L. Mulfort, D. M. Tiede, J. T. Hupp and S. T. Nguyen, *J. Am. Chem. Soc.*, 2008, **130**, 16828–16829. Copyright (2008) American Chemical Society.

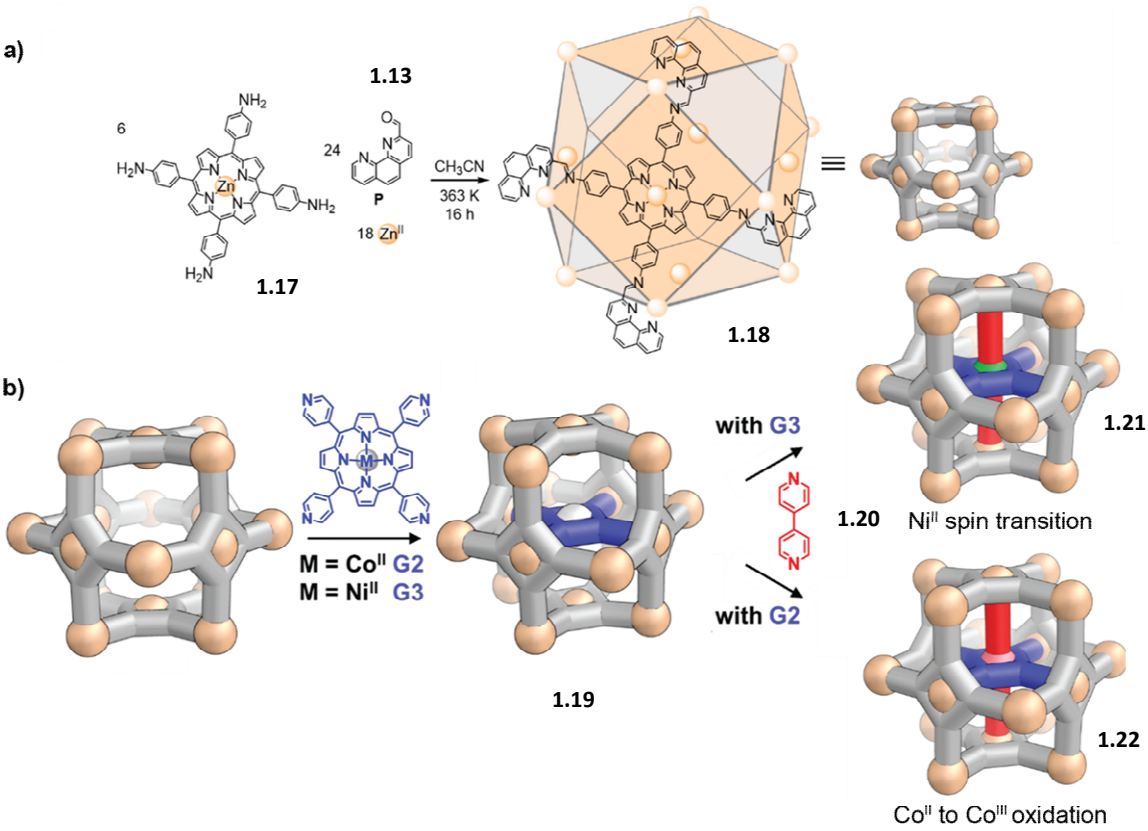
Another area of 3D porphyrin architectures are those of the self-assembled porphyrin metal-organic cages reported by Nitschke and co-workers such as **1.15** and **1.16** in Scheme 1.12.[71–75]



Scheme 1.12. Synthesis of a porphyrin based self-assembled cage by Nitschke and co-workers.[73] Adapted by permission from Springer Nature, F. J. Rizzuto and J. R. Nitschke, *Nat. Chem.*, 2017, **9**, 903–908. Copyright (2017).

Here, tetrakis(p-aminophenyl)porphyrins are condensed with an aldehyde bearing ligand such as 2-formyl-phenanthraline in the presence of a metal centre of the desired co-ordination number, for example cobalt(II). The ligands self-assemble to form the lowest energy structures, which with well-designed systems are often molecular cages such as **1.15** (Scheme 1.12). These cages display a wealth of chemistry, usually revolving around their ability to encapsulate hosts such as aromatic organic molecules,[71] boron clusters,[73] fullerenes[72,75] or even biomolecules such as polypeptides.[74]

A more recent example has used a cage to alter the chemistry of a guest molecule (Scheme 1.13).[76] By taking advantage of the porphyrin metal centres ability to coordinate an axial ligand, a tetradentate porphyrin guest (**G2**/**3**) was able to coordinate to the inside of the cage. Interestingly, the subsequent coordination of a pyridyl based ligand **1.20** altered the chemistry of the guest substantially (Scheme 1.13b).



Scheme 1.13. (a) Synthesis of metal-centred porphyrin cuboctahedral cage **1.18** by Nitschke and co-workers.[76] (b) Formation of host-guest complex **1.19** with metal centred porphyrin **G2**/**3** in the cavity. Addition of ligand **1.20** changes the chemistry of the respective metal centres. Adapted with permission from F. J. Rizzuto, W. J. Ramsay and J. R. Nitschke, *J. Am. Chem. Soc.*, 2018, **140**, 11502–11509. Copyright (2018) American Chemical Society.

In the case of a nickel guest porphyrin, coordination caused a spin transition of the metal in **1.21**. In the case of a cobalt guest porphyrin, coordination lowers the oxidation potential of the metal centre, resulting in oxidation of Co(II) to Co(III) in air in **1.22**. Neither

of these effects were observed in control experiments in solution, suggesting the cavities of 3D porphyrin architectures are capable of enabling novel reactivity of the guest species.

Another interesting example is the recently reported Ni^{II}-dimesitylnorcorrole (a porphyrinoid) molecular cage (Figure 1.6). This was self-assembled with the usual ligand and metal coordination employed in Nitschke's work. The resulting complex contains an entirely antiaromatic cavity due to the antiaromaticity of the porphyrinoids 16 π electron circuit. Introduction of guests to the cavity shifts their ^1H NMR values by 15 ppm compared to that of free guests due to the induced magnetic field from the antiaromatic ring currents.

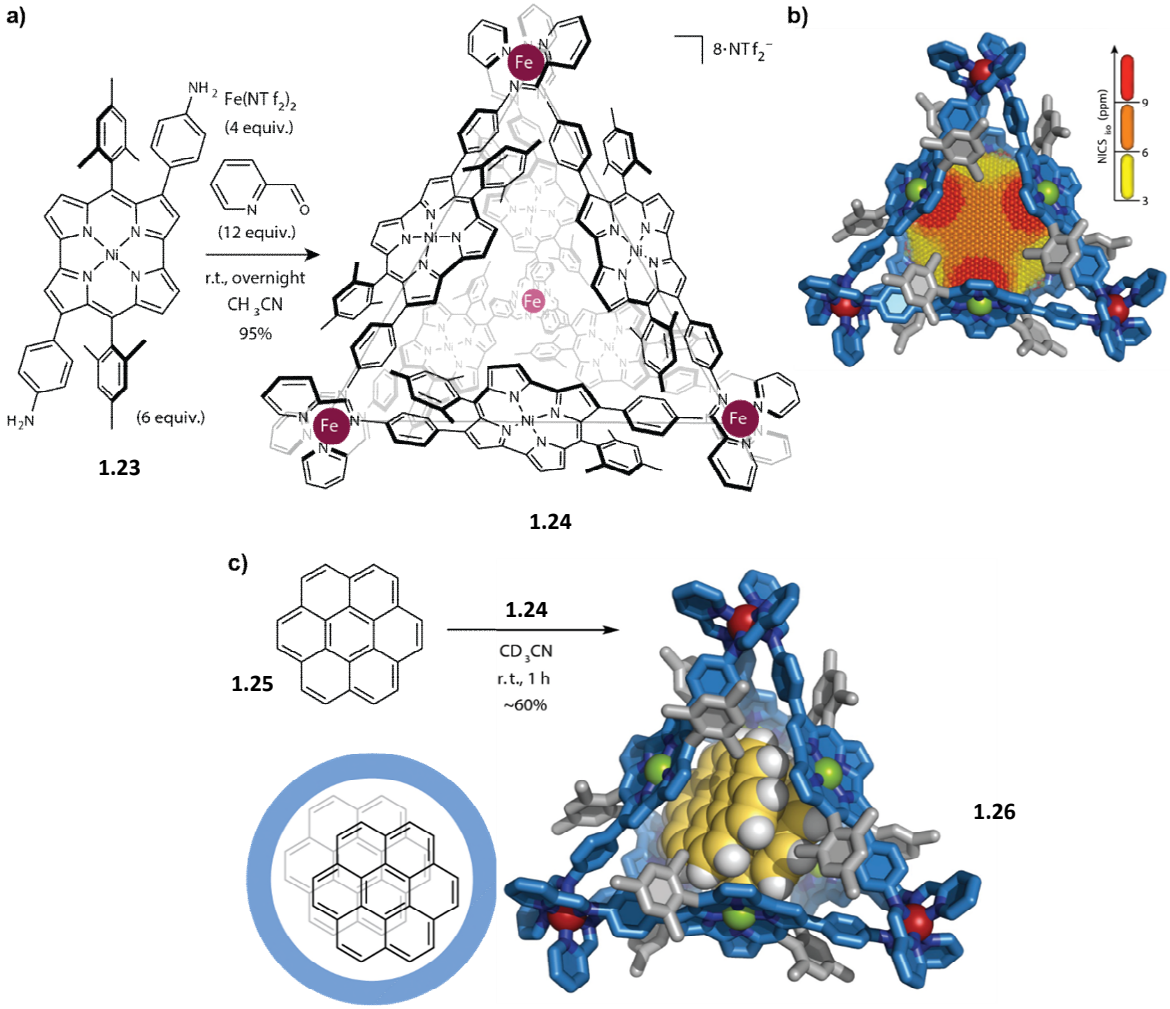
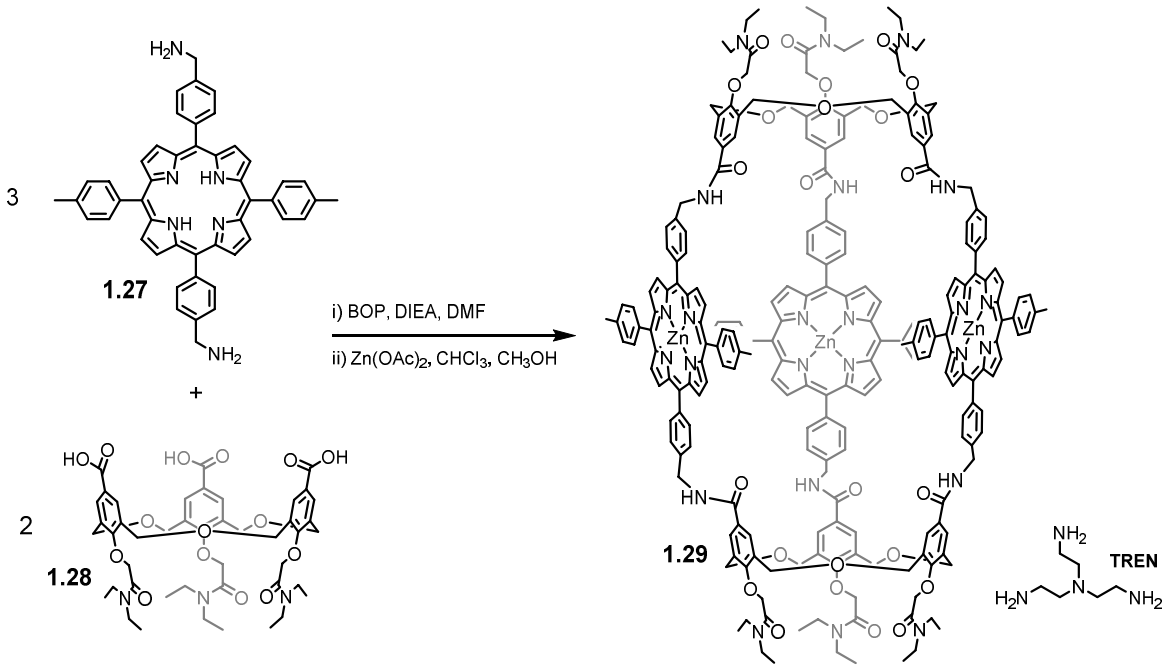


Figure 1.6. (a) Synthesis of porphyrin cage **1.24**, exhibiting an antiaromatic cavity. (b) Nucleus-independent chemical shift (NICS) DFT calculations showing the antiaromatic nature of the cavity. (c) Encapsulation of coronene in the porphyrin cage. The encapsulated annulene ^1H NMR spectra show a shift of +15 ppm compared to free annulene, consistent with deshielding afforded by antiaromatic cavity. Adapted by permission from Springer Nature, M. Yamashina, Y. Tanaka, R. Lavendomme, T. K. Ronson, M. Pittelkow and J. R. Nitschke, *Nature*, 2019, **574**, 511–515. Copyright (2017).

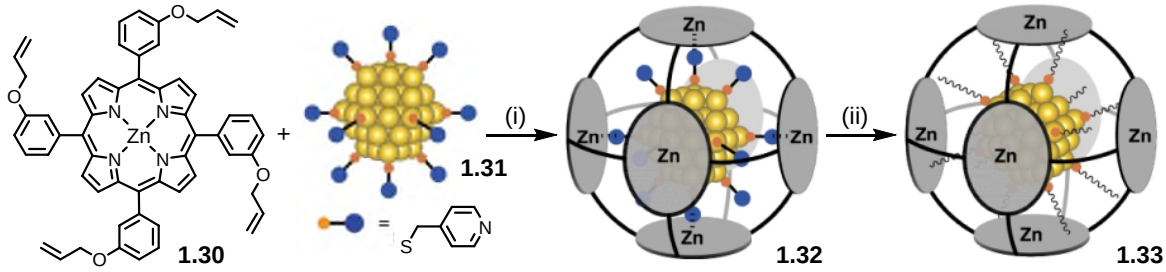
1.4.2 Covalent 3D porphyrin architectures

Covalently linked 3D porphyrin nanostructures are less common. Some important examples have been porphyrin 'boxes' or cages usually afforded by dynamic covalent chemistry such as alkyne metathesis or imine formation.[59,61,77] Early work by Shinkai and co-workers used homooxacalix[3]arenes to synthesise a molecular capsule, **1.29**, by an amide coupling (Scheme 1.14).[78] The three porphyrin sides of the capsule could facilitate the binding of tris(2-aminoethyl)amine (TREN). Interestingly, adding Na^+ caused a change in the conformation due to binding of calixaranes to the metal salt. This change in conformation increased the strength of binding of TREN by three orders of magnitude.



Scheme 1.14. Synthesis of porphyrin walled capsule **1.29**.[78]

Konishi utilised a template-directed approach, where gold nanoclusters functionalised with pyridyl ligands were used as a spherical template (Scheme 1.15). By using a porphyrin monomer **1.30** functionalised with alkenes in the meso-aryl groups, reversible olefin metathesis was able to form the final hexa-porphyrin nanocage in surprisingly high yields (50%). Cleaving the pyridyl ligands from the gold nanocluster failed to remove the cluster from the cavity, highlighting the small cavity formed by the hexaporphyrin cage (**1.33**).



Scheme 1.15. Synthesis of a hexaporphyrin nanocage using a pyridyl functionalised gold nanocluster as a template. Adapted from T. Inomata and K. Konishi, *Chem. Comm.*, 2003, **3**, 1282 with permission from The Royal Society of Chemistry.

Although 3D covalent porphyrin nanostructures are achievable, there are few examples where conjugation is effective over all three dimensions. One example from the Anderson group is that of a porphyrin nanotube, ***t*-P12·(T6)$_2$**.[79,80] The nanotube was prepared by template-directed synthesis using two hexapyridyl templates and a deprotected dimer **1.34** (Figure 1.7). The porphyrin nanotube shows red-shifted absorption band compared to the individual ***c*-P6·T6** (reflecting greater conjugation in the system) and fluorescence anisotropy measurements show there is ultrafast energy migration from excited states associated with the sides of the barrel and the six-porphyrin ring regions.

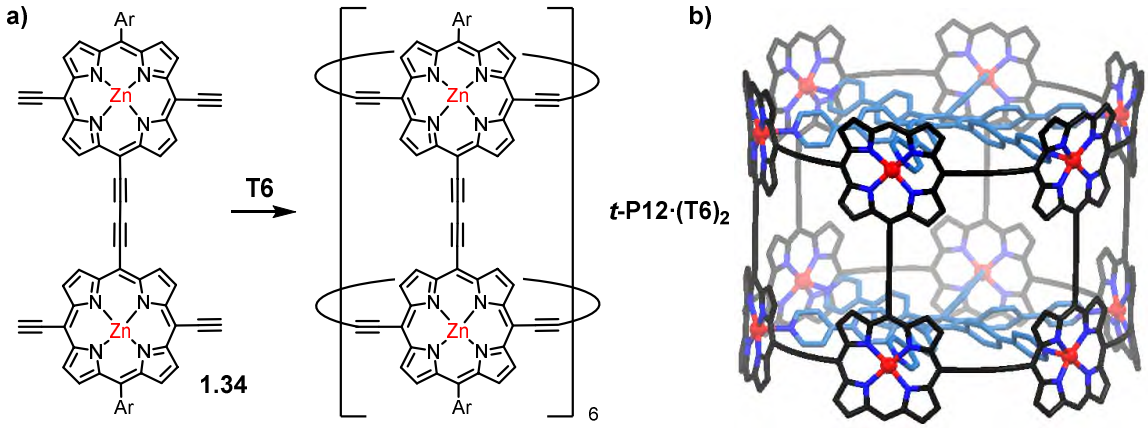


Figure 1.7. Synthesis of 12 porphyrin nanotube ***t*-P12·(T6)$_2$** using a template directed synthesis. (b) Calculated structure of porphyrin nanotube ***t*-P12·(T6)$_2$** (MM2 forcefield, aryl groups and hydrogens omitted).[81]

A more recent example is the synthesis of a conjugated zinc porphyrin nanoball.[82] This complex synthetic target was achieved using the same template-directed chemistry as discussed previously. A ***c*-P6·T6** analogue with meso alkyne groups on either end was synthesised (***c*-P6(H)$_4$·T6**, Figure 1.8). By coupling to mono-deprotected dimer, the ball precursor ***c*-P6(P2)$_4$·T6** could be synthesised. Template **T4** was the correct geometry to close the dangling ends of the porphyrin nanoball, and so Glaser coupling of the ball precursor followed by removal of the templates gave ***b*-P14**.

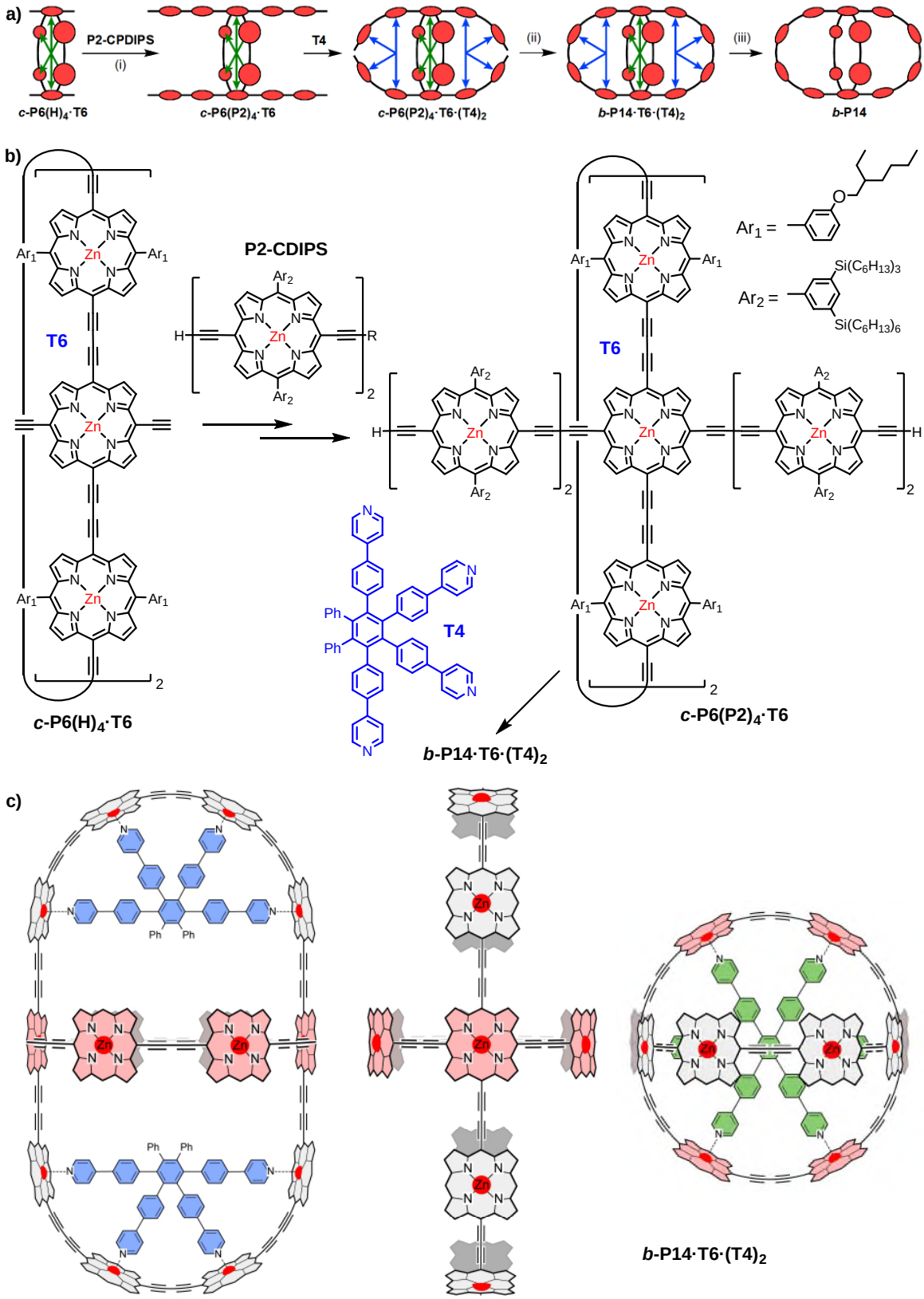
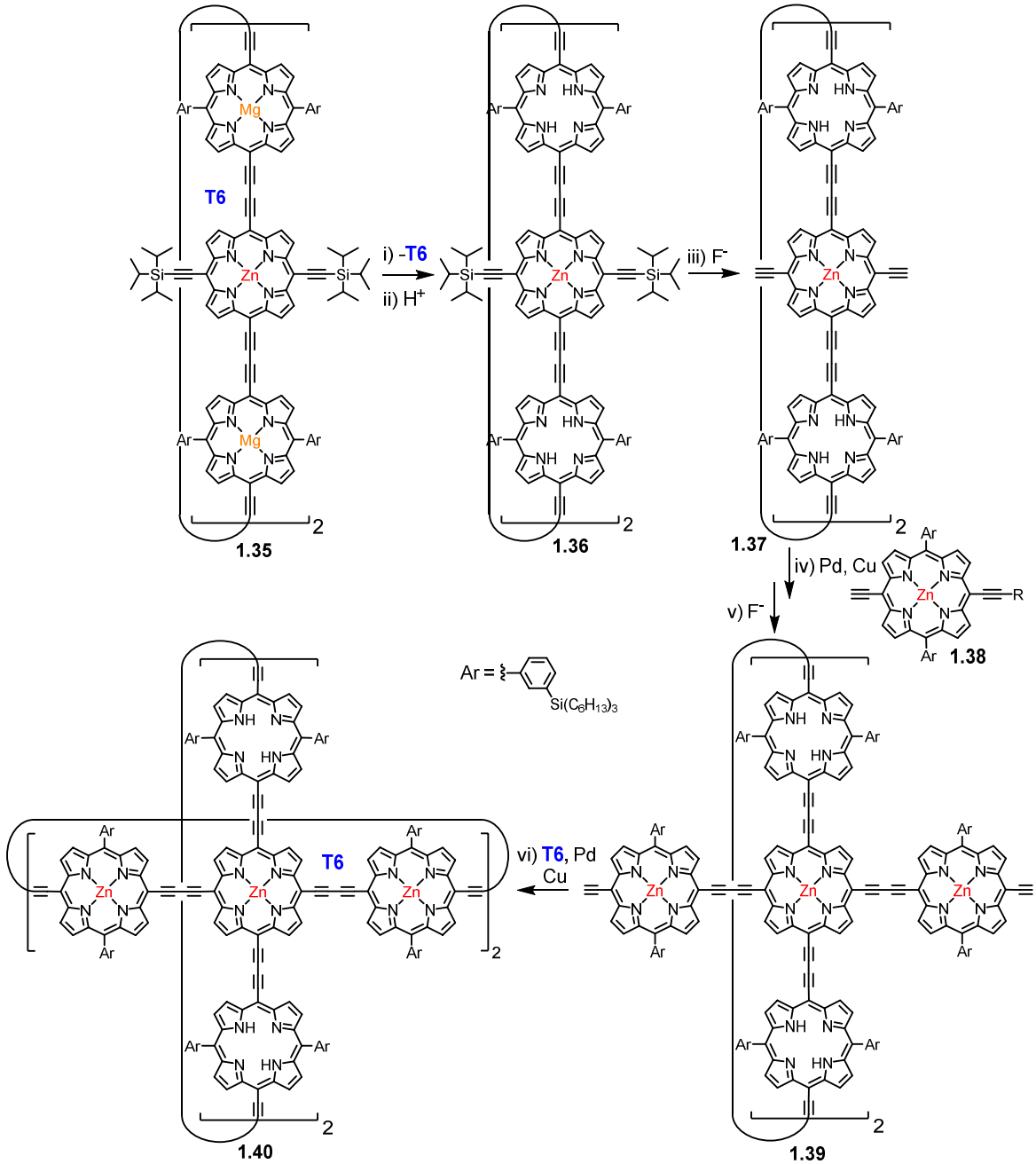


Figure 1.8. (a) Schematic representation of the synthetic strategy to ***b*-P14** using **T4** to close the 'dangling ends' of the porphyrin ball. (b) Simplified scheme of the formation of the preball complex ***c*-P6(P2)$_4$·T6**. (c) Pictorial representation of ***b*-P14·T6·(T4)$_2$** showing all three perspectives. Adapted with permission from J. Cremers, R. Haver, M. Rickhaus, J. Q. Gong, L. Favereau, M. D. Peeks, T. D. W. Claridge, L. M. Herz and H. L. Anderson, *J. Am. Chem. Soc.*, 2018, 140, 5352–5355. Copyright (2018) American Chemical Society.

DFT calculations suggest the electron density of the HOMO is distributed entirely over the π-system, albeit with a higher density on the six-porphyrin ring and tetraalkynyl (vertex) porphyrins. Fluorescence upconversion anisotropy experiments show that the excited state is delocalised across all three dimensions.



Scheme 1.16. Synthesis of partially metallated ***b*-P10** (**1.40**).[83]

Another porphyrin nanoball, ***b*-P10**, has also been prepared.[83] The synthesis of this nanoball required a different strategy to that of ***b*-P14**. It was unlikely that the same 'dangling arm' approach used in the synthesis of the larger ball would be successful again, as the binding to a bidentate template would most likely not be strong enough to

selectively close the arms (cf. to tetradentate template for ***b*-P14**). Instead, a heterometallation strategy was used. First, nanoring derivative **1.35** was synthesised from porphyrins bearing asymmetric solubilising aryl groups (Ar) in order to minimise steric interactions in the centre of the eventual ball product.

This ring contained zinc porphyrins on the alkyne functionalised porphyrins, and magnesium in all of the rest. By using a weak acid, magnesium porphyrins can be selectively demetallated in the presence of zinc metal centres. The magnesiums were removed and zinc monomers coupled on to create the dangling arms, resulting in ball precursor **1.39**. This nanoring derivative is effectively two metallated trimers held in the correct conformation for ring closure. By coordinating with **T6** and submitting to Glaser coupling conditions, the partially metallated nanoball **1.40** could be synthesised.

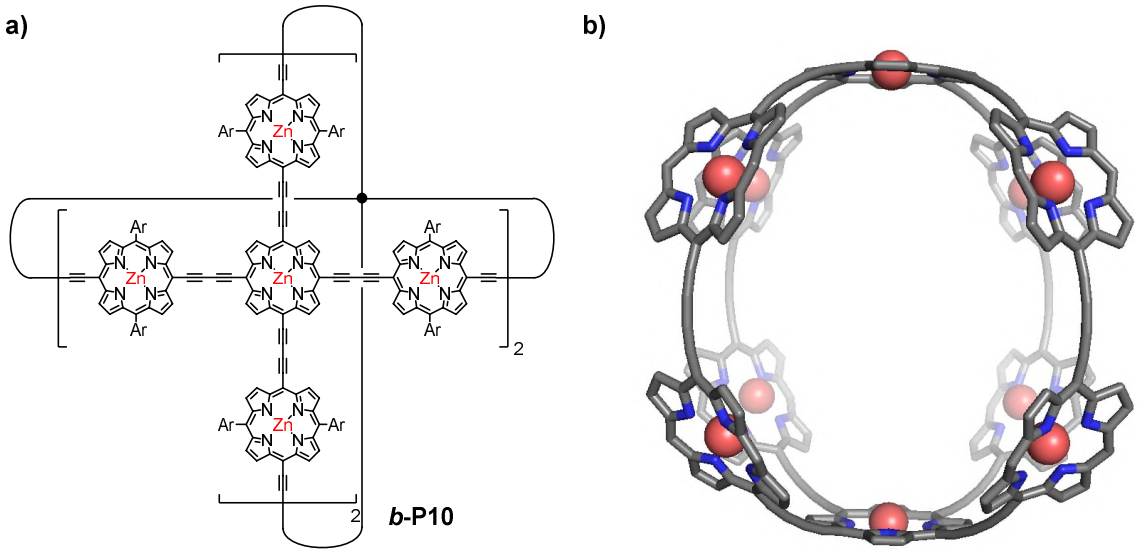


Figure 1.9. (a) Structure ***b*-P10**. (b) Calculated structure of ***b*-P10** (MM+ forcefield).

By removing the template with competing ligand and metallating the free-base porphyrins with zinc, ***b*-P10** was synthesised which consists of two orthogonal metallated 6-porphyrin nanorings. DFT studies of the nanoball suggested the electron density of the HOMO and degenerate LUMOs are delocalised across all three dimensions. However, further studies were not undertaken.

1.5 Prospectus

Porphyrins are versatile and functionalisable building blocks with which to make complex 2D and 3D architectures. Inspired by the cyclic porphyrin arrays found in biology, chemists have already reported many fascinating structures. One efficient strategy has been to take advantage of the coordination between metalloporphyrins and pyridyl based ligands

in template-directed syntheses. Conjugated porphyrin arrays are of particular interest due to the unique photophysical properties imbued by the global conjugation pathways such as global (anti)aromaticity and quantum interference. So far, '2D' and 3D conjugated porphyrin architectures have been synthesised using 2D templates such as **T6**, requiring complex syntheses in the case of ***b*-P10**. The first part of this thesis instead looks to use a 3D template to synthesise 3D porphyrin architectures from simpler readily accessible porphyrin building blocks.

2

Towards 3D Template Directed Synthesis of a 10-Porphyrin Nanoball

2.1 Abstract 23

2.2 Introduction 23

2.2.1 Prospective 25

2.2.2 Synthetic plan 27

2.3 The Template 30

2.3.1 T10 Synthesis 30

2.3.2 Preliminary investigations 31

2.4 Precursor synthesis 32

2.4.1 *X*-P5 32

2.4.2 *I*-P5 34

2.4.3 preball-P10 36

2.5 Ball formation tests 37

2.5.1 *x*-P5 and *I*-P5 38

2.5.2 Preball-P10 46

2.6 Conclusion 53

2.7 Future work 54

2.8 Experimental appendices 57

2.8.1 General experimental procedures 57

2.8.2 Synthetic procedures 58

2.8.3 Fluorescence measurements 94

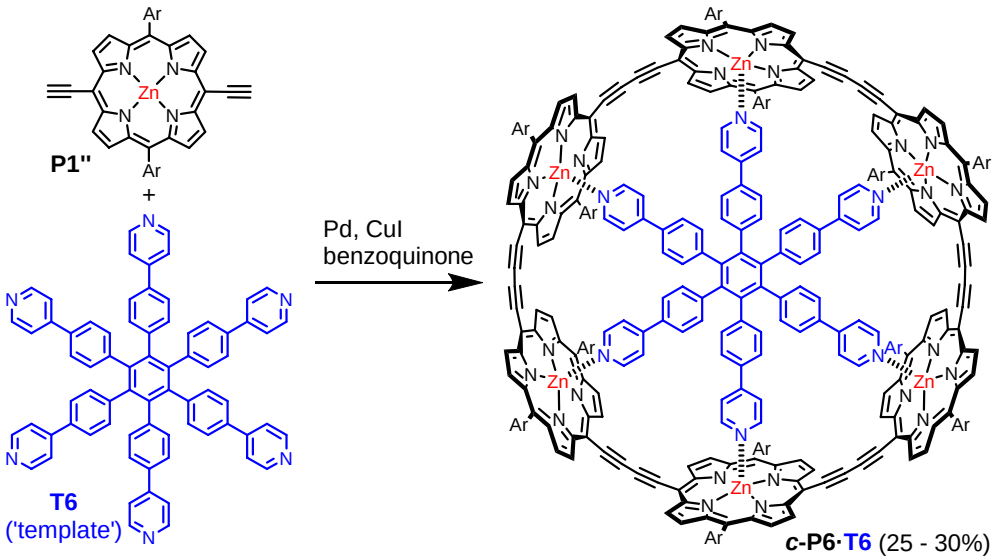
2.1 Abstract

A 10-porphyrin nanoball, ***b*-P10**, consisting of two orthogonally intersecting porphyrin nanorings is an attractive synthetic target because of the potential physical properties it exhibits. A 3D template, **T10**, and a range of porphyrin oligomeric precursors ***x*-P5**, ***l*-P5** and ***preball*-P10**, were synthesised to test formation of ***b*-P10**. The coordination of **T10** to the synthesised precursors occurred as expected, but ball formation was unsuccessful. Potential reasons for the lack of ball formation are discussed, and future work designed to overcome the observed problems is suggested.

2.2 Introduction

The synthesis and understanding of conjugated molecular materials is a fast moving and exciting field. The detailed understanding of structure-property relationships in conjugated molecular systems has led to rapid advances in organic material technologies, as evidenced in the widespread use of organic light-emitting diodes (OLEDs)[84–87] and organic photovoltaics (OPVs)[88–91] and the emergent use of organic field-effect transistors (OFETs) in organic electronics.[92–95] There are two research motivations of vital importance to organic materials development: the understanding of fundamental physical phenomena in π-conjugated materials and the precise control of synthetic architectures with which to explore said phenomena.

Conjugated porphyrin oligomers have demonstrated immense utility in both of these areas. Linear oligomers have provided insights into, amongst other things: the importance of π-overlap in the observed electronic behaviour[19,96,97], charge transport and delocalisation in molecular wires[98–100], single-molecule electronics[101–103] and near infrared OLED emitters.[104]



Scheme 2.1. Synthesis of porphyrin nanoring ***c*-P6·T6** using a template-directed synthesis.[46]

Alongside their unique electronic behaviour, these porphyrin oligomers offer a toolbox with which to construct a variety of fascinating architectures by using a template-directed synthesis approach so successfully employed by the Anderson group, with an illustrative example demonstrated in Scheme 2.1.[27,35] Examples include the synthesis of belt-shaped porphyrin nanorings,[32,36,106,107,37,38,40,41,43,45,50,105] figure-of-eight nanorings[106] and nested supramolecular nanoring complexes.[44] These '2D' structures (with regards to their conjugation being localised over a roughly 2D disc) show fascinating properties such as quantum interference[51] and global (anti)aromaticity[55,56,58,108] and have been used to further understand light harvesting and exciton delocalisation.[39,47,109]

It follows that extending these architectures into three dimensions opens up further possibilities of exciting discoveries. Examples of 3D conjugated porphyrin architectures include porphyrin nanotubes,[79,80] spiro nanorings[110] and most recently porphyrin nanoballs of 14[82] and 10 porphyrin units.[83] Of particular interest is the porphyrin nanoball ***b*-P10** (Figure 2.1). This ball consists of two identical and intersecting orthogonal porphyrin 6-nanorings, with shared vertices at either end of the ball.

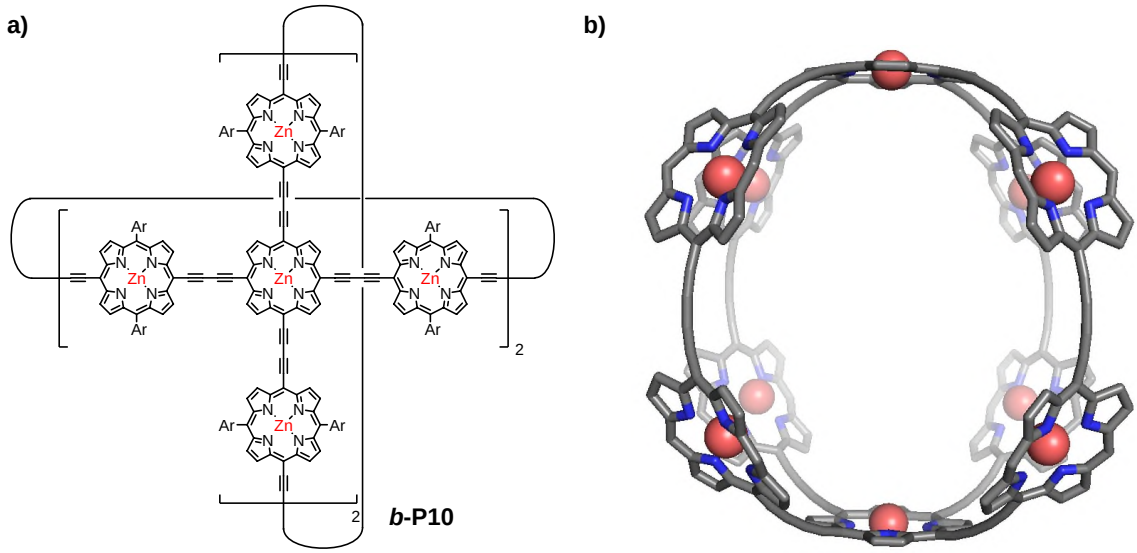
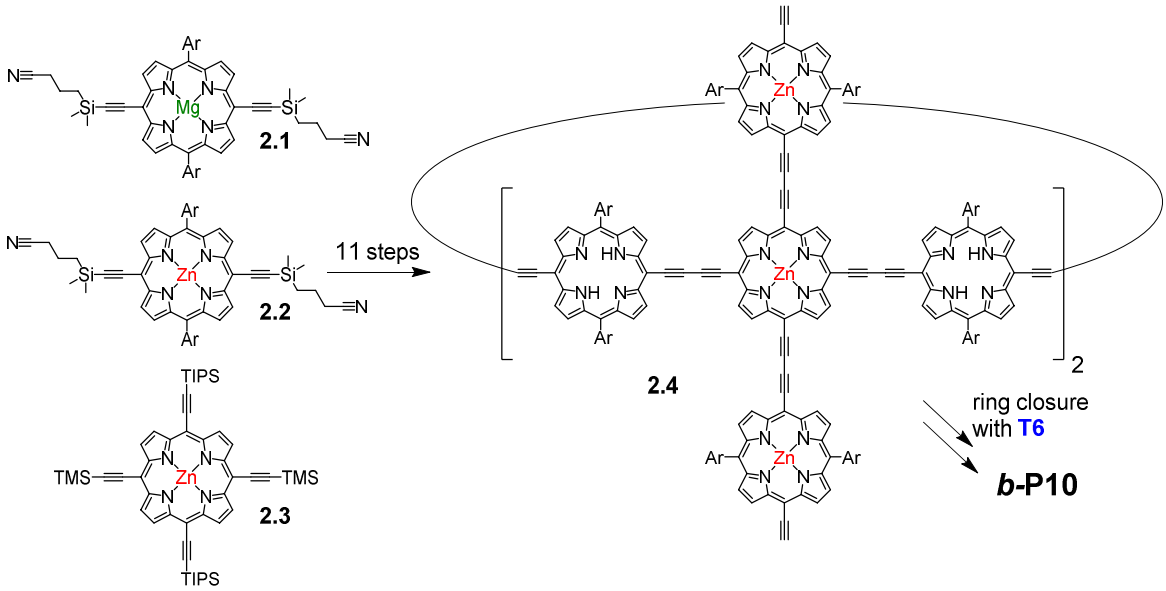


Figure 2.1. (a) Chemical structure of ***b*-P10** and (b) simplified model of ***b*-P10** (HyperChem, MM+). Ar represent solubilising aryl groups.

The orthogonality and identicalness of the two porphyrin nanorings will allow us to explore multiple phenomenological questions: will global (anti)aromaticity be present over the whole ball like discussed in Scheme 1.10 with ***c*-P6·T6**, or will it be localised on the single rings? Will there be quantum interference between ends of the ball vertices (like in heterometallated nanorings, Figure 1.4[51]), and if so, will it be larger than in the analogous nanorings due to the two extra pathways? ***b*-P10** also offers a scaffold of metal-centred porphyrins which can be used as coordination sites for the self-assembly of supramolecular complexes as seen in the cuboctahedral cage recently reported by Nitschke and co-workers.[76]

2.2.1 Prospective

***b*-P10** has been synthesised previously by using a series of heterometallated nanorings and cyclic template **T6**, summarised in Scheme 1.16 and Scheme 2.2.[83] This impressive and synthetically demanding route requires multiple statistical steps and the synthesis of three porphyrin stock monomers **2.(1-3)**.



Scheme 2.2. Synthesis of ***b*-P10** using **T6** and hetero-demetallation strategy demonstrated by Dr Jonathan Cremers.[83]

Rather than using **T6** in two separate steps, it was proposed that a 3D template could access the ***b*-P10** product starting from simpler porphyrin starting materials, whilst simultaneously removing the requirement to synthesise heterometallated oligomers, thus removing the need to synthesise one of the starting monomers. The following template **T10** was designed with pyridyl functionalities in the right geometry for effective binding to ***b*-P10**. Molecular modelling using an MM+ forcefield shows the template has the right conformation for binding inside ***b*-P10** (Figure 2.2c).

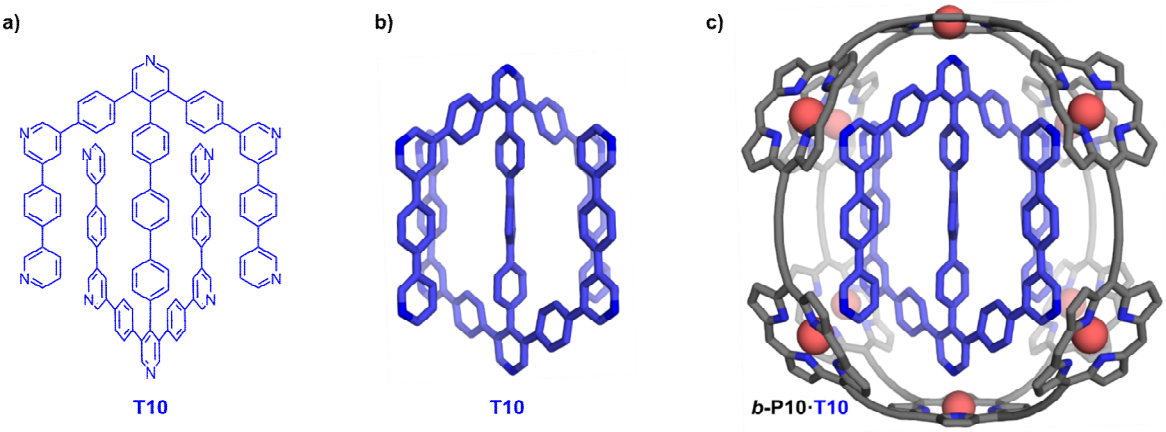
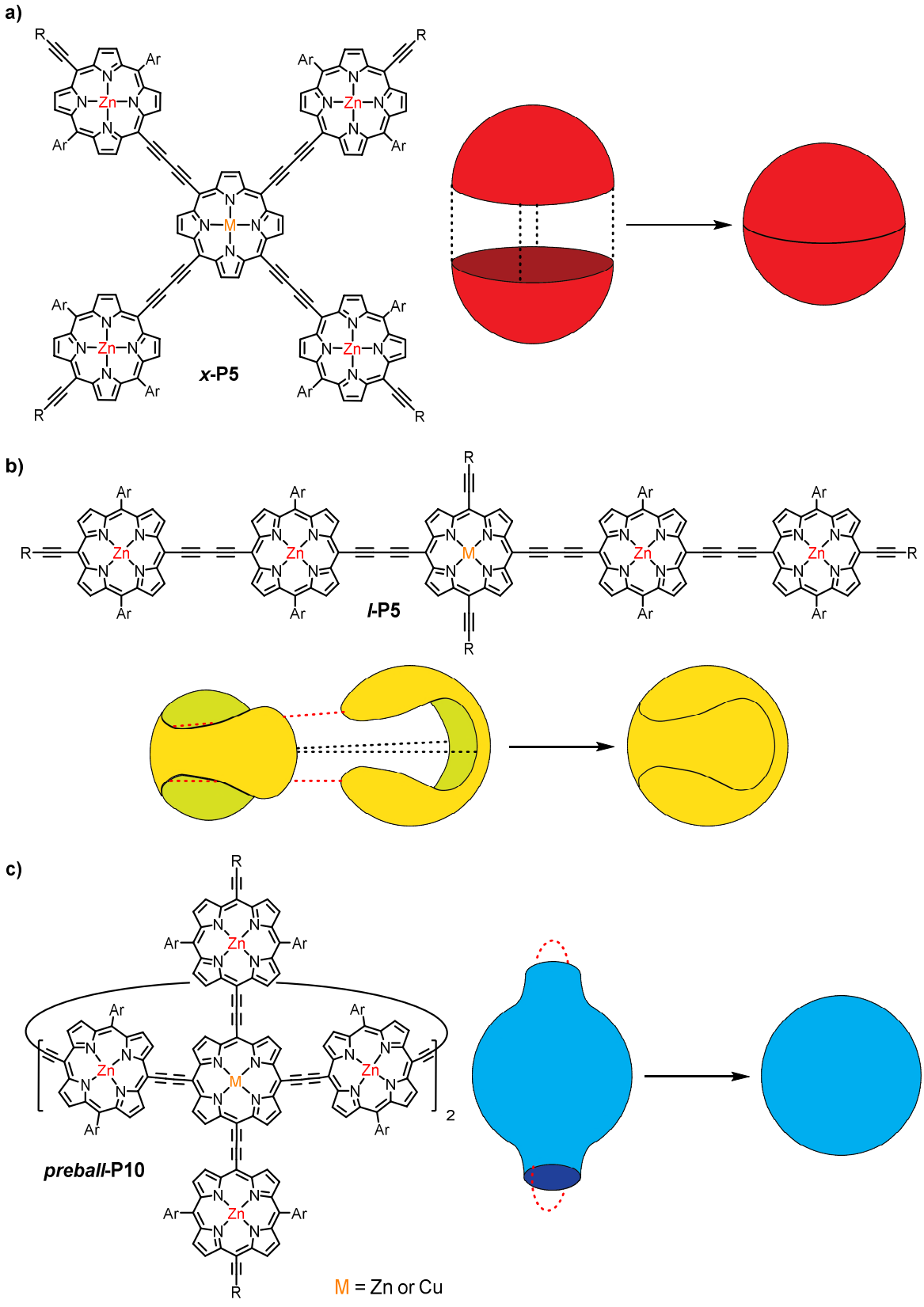


Figure 2.2. (a) Molecular structure of **T10**. (b) 3D visualisation of **T10**. (c) 3D visualisation of **T10** in the cavity of ***b*-P10**. (c) was calculated in HyperChem using MM+ forcefield.

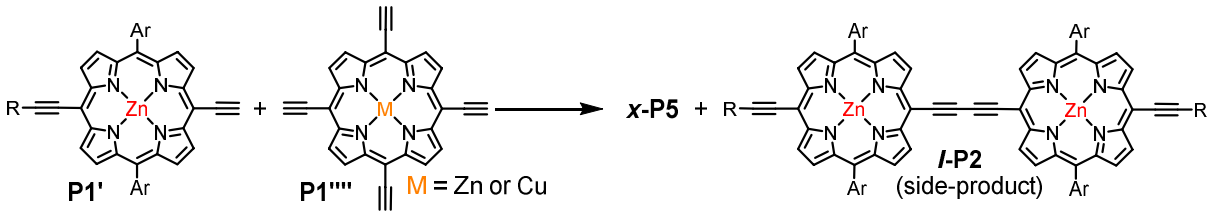
2.2.2 Synthetic plan



Scheme 2.3. Proposed ball precursors ***x*-P5**, ***l*-P5** and ***preball*-P10** with **T10** as the template. All precursors have the capability to be heterometallated at the central porphyrin position.

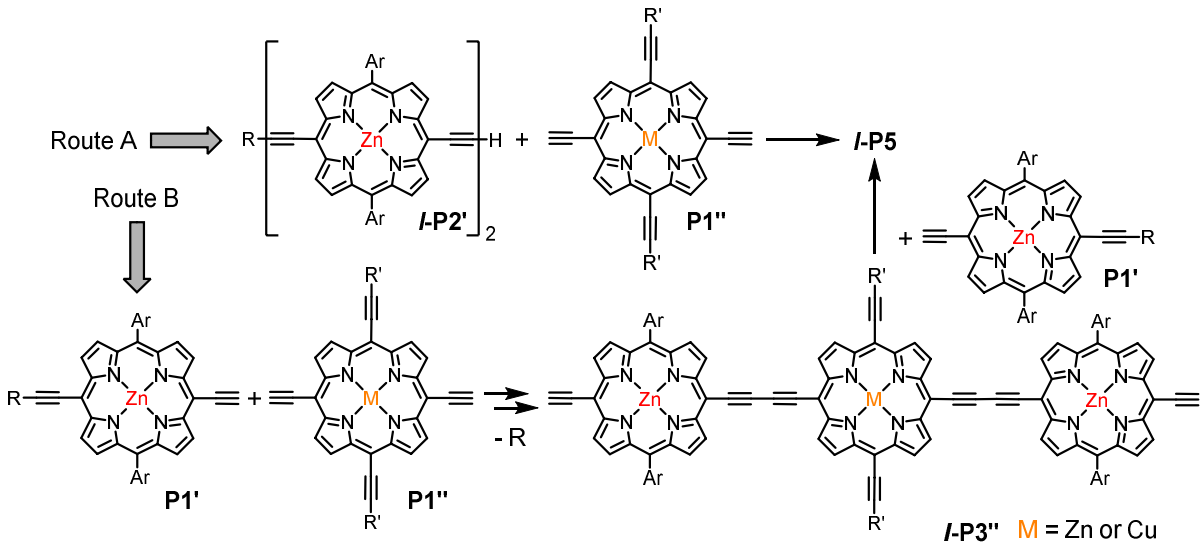
With ***b*-P10** as the template, precursors ***x*-P5**, ***l*-P5** and ***preball*-P10** were designed (Scheme 2.3). ***x*-P5** can be thought of as bringing together two halves of a ball around a central core (Scheme 2.3a). ***l*-P5** can be imagined as two halves of a tennis ball, where the ends of one pentamer must couple to the middle of another (Scheme 2.3b). Finally, ***preball*-P10** can be envisaged as an open ended tube, the ends of which can be closed by the template (Scheme 2.3c).

All three precursors were designed to be able to contain a copper centre in the central porphyrin to allow synthesis of ***b*-P10$_{Cu2}$**, a fascinating target for quantum interference investigations. Proposed synthetic routes are given below with generalised porphyrin (**P**) structures, where ***l*-** and ***c*-** prefixes refer to linear and cyclic oligomers respectively. The number of primes refers to the number of unprotected alkynes. ***x*-P5** ('cross pentamer') consists of a central tetraalkynyl porphyrin core with each alkynyl functionalised with another porphyrin monomer. This is the simplest of the compounds as ***x*-P5** can be achieved in one step from porphyrin monomers.



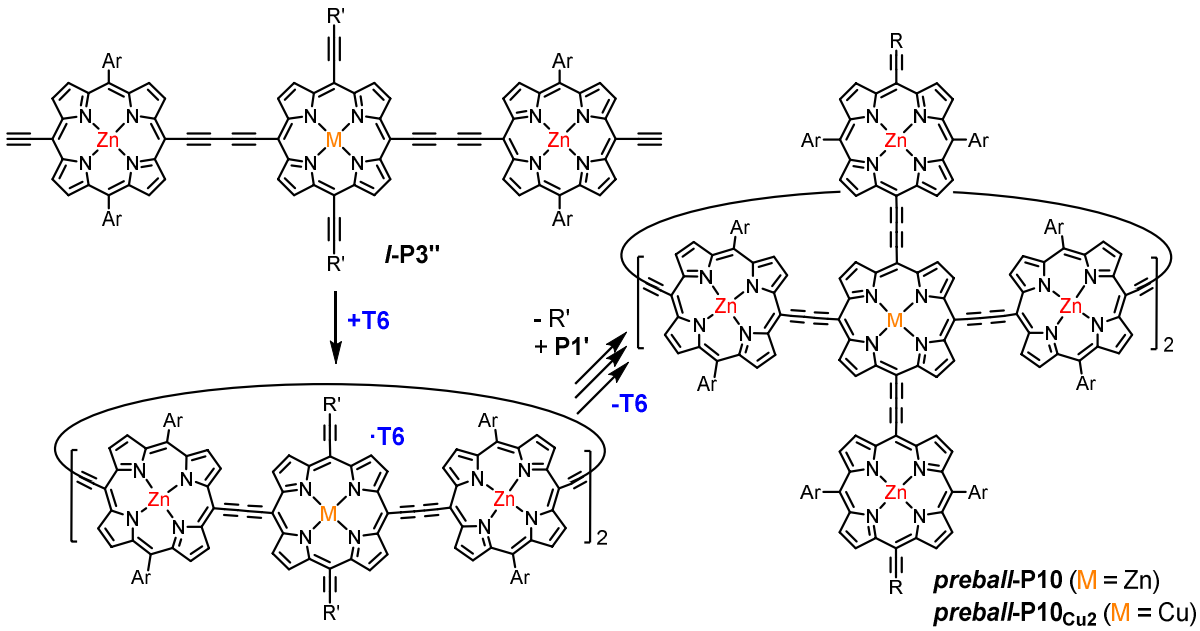
Scheme 2.4. Proposed synthesis of ***x*-P5** from porphyrin monomers.

The synthesis of the linear pentamer ***l*-P5** can be achieved in two ways, either through the coupling of a mono-deprotected dimer to a central orthogonally protected tetraalkynyl porphyrin (route A) or via successive elongation using mono-deprotected porphyrin monomers (route B). Route A was initially chosen due to the expected side product of ***x*-P5** formation being the fully protected dimer, ***l*-P2**.



Scheme 2.5. Proposed synthesis of ***l*-P5** either via ***l*-P2'** (route A) or consecutive monomer addition (route B).

The proposed route to ***preball*-P10** is less straightforward, requiring the cyclisation of trimer ***l*-P3''** with template **T6**. The resulting ring can be functionalised with pendant porphyrin monomers which could be ring-closed with **T10**. This route is less elegant than via the simpler precursors ***l*-P5** and ***x*-P5**, but does offer the benefit of avoiding the demetallation steps required in the original synthesis of ***b*-P10**.

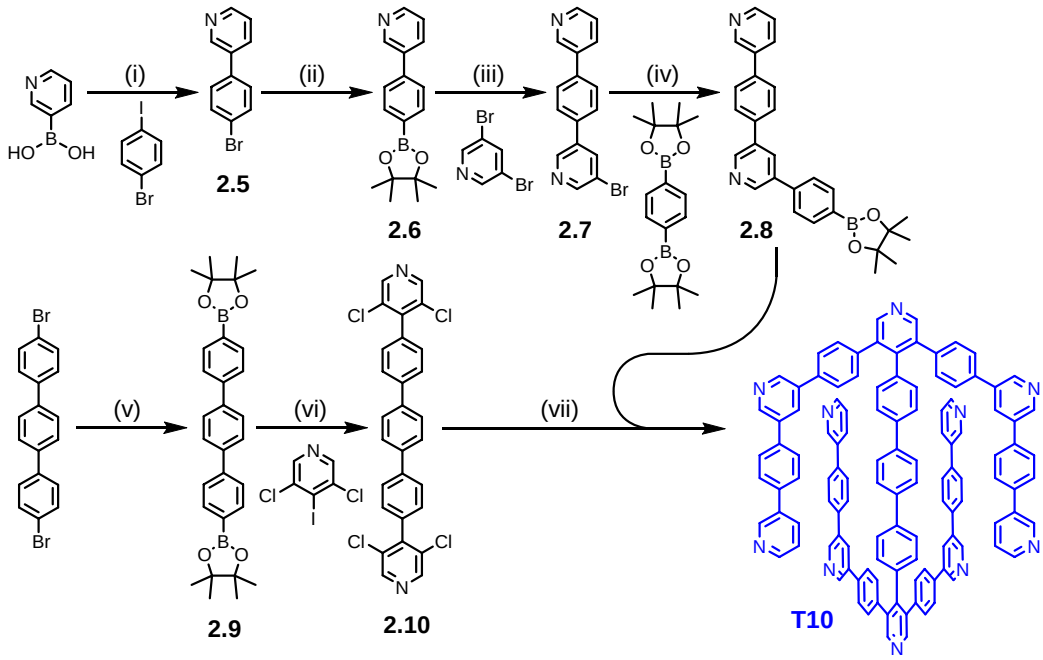


Scheme 2.6. Proposed synthesis of ***preball*-P10**.

2.3 The Template

2.3.1 T10 Synthesis

A convergent synthesis was used to make **T10** by separating the template into the central core, **2.10**, and the arm, **2.8**.



Scheme 2.7. Synthesis of **T10**. (i) $Pd(PPh_3)_2Cl_2$, Na_2CO_3, THF/EtOH/H_2O, 62%; (ii) $Pd(dppf)Cl_2$, B_2pin_2, AcOK, DMF, 75%; (iii) $Pd(PPh_3)_2Cl_2$, Na_2CO_3, THF/EtOH/H_2O, 61%; (iv) $Pd(PPh_3)_2Cl_2$, Na_2CO_3, THF/EtOH/H_2O, 35%; (v) $Pd(dppf)Cl_2$, B_2pin_2, AcOK, dioxane, 51%; (vi) $Pd(PPh_3)_2Cl_2$, Cs_2CO_3, dioxane/H_2O, 40%; (vii) $Pd(OAc)_2$, SPhos, Cs_2CO_3, toluene/EtOH/H_2O, 25%.

The arm (**2.8**) was synthesised using a Suzuki-Miyaura based methodology. First, the synthesis of known compounds **2.5**[111] and **2.6**[112] was achieved through a Suzuki-Miyaura cross-coupling (SMC) of 3-pyridinylboronic acid with 1-bromo-4-iodobenzene followed by a Miyaura borylation.[113] **2.6** could be purified from residual bis(pinacolato)diboron by vacuum sublimation (100 °C, 5 x 10^{-1} mbar), which gave the product as rocky white crystals on the cold finger. Another SMC with 3,5-dibromopyridine gave **2.7**. An SMC with 1,4-benzenediboronic acid bis(pinacol)ester gave the final arm **2.8** in 35% yield. **2.8** was difficult to purify using flash chromatography due to streaking and the appearance of two spots as a result of boron ester over-adsorption.[114] Loading the mobile phase with > 2.5% pinacol w.r.t. mass of solvent was found to reduce over-adsorption greatly, to the extent the TLC analysis showed only a single sharp spot (compared to two broad streaky spots without pinacol).

The central core, **2.10**, was synthesised from the commercially available 4,4''-dibromo-p-terphenyl via a Miyaura borylation to form **2.9**,[113,115] followed by a SMC with

3,5-dichloro-4-pyridine. Using 3,5-dichloro-4-pyridine allows the more labile iodo-position to undergo the cross coupling first, leaving four chloro positions available for coupling to the template arms.[116]

2.3.2 Preliminary investigations

Dr Jonathan Cremers performed UV-vis-NIR titrations to assess whether the structure of **T10** is suitable to be a template, by first assessing whether it is a good host to ***b*-P10**, synthesised from the route shown in Scheme 2.2.

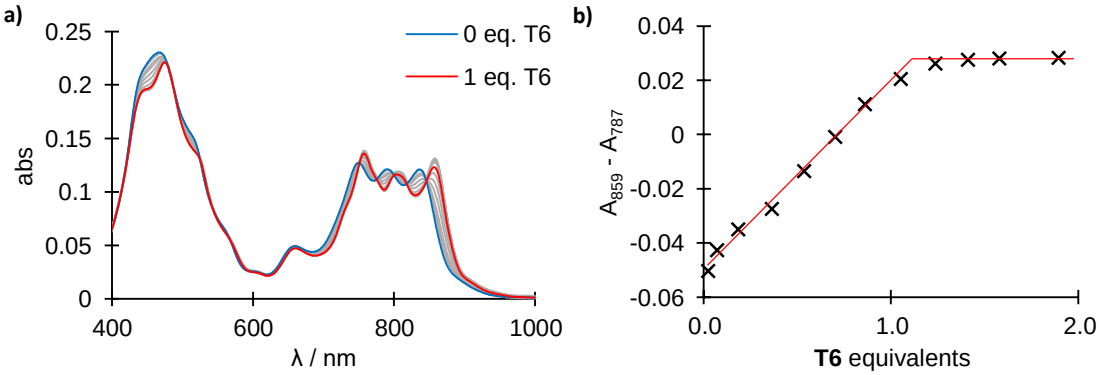


Figure 2.3. UV-vis-NIR titration of **T6** into ***b*-P10**, showing ***b*-P10** (blue line) and ***b*-P10·T6** (red line) in toluene at 298 K. The change in absorption as a function of the T6 concentration is shown, indicating the formation of a strong one-to-one complex with a red lines as guides for the eye plotted through the experimental data points. Figures adapted from Jonathan Cremers Thesis with permission.

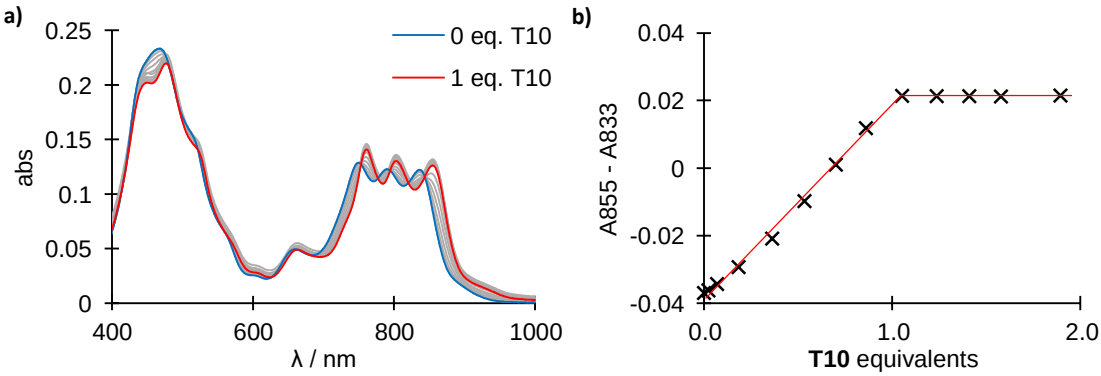


Figure 2.4. UV-vis-NIR titration of **T10** into ***b*-P10**, showing ***b*-P10** (blue line) and ***b*-P10·T10** (red line) in toluene at 298 K. The change in absorption as a function of the T6 concentration is shown, indicating the formation of a strong one-to-one complex with a red lines plotted as guides for the eye through the experimental data points. Figures adapted from Jonathan Cremers Thesis with permission.

Figure 2.3 and Figure 2.4 show that both **T6** and **T10** are good guests for ***b*-P10** as evidenced by the strong 1:1 binding and the characteristic sharpening of the Q-band (λ ~ 800 nm), presumably from the reduction in potential conformational environments available to the chromophores.[36,44] Another hallmark of template inclusion is the decrease in fluorescence quantum yield upon binding of a template due to the rigidification of the porphyrin nanorings.[46]

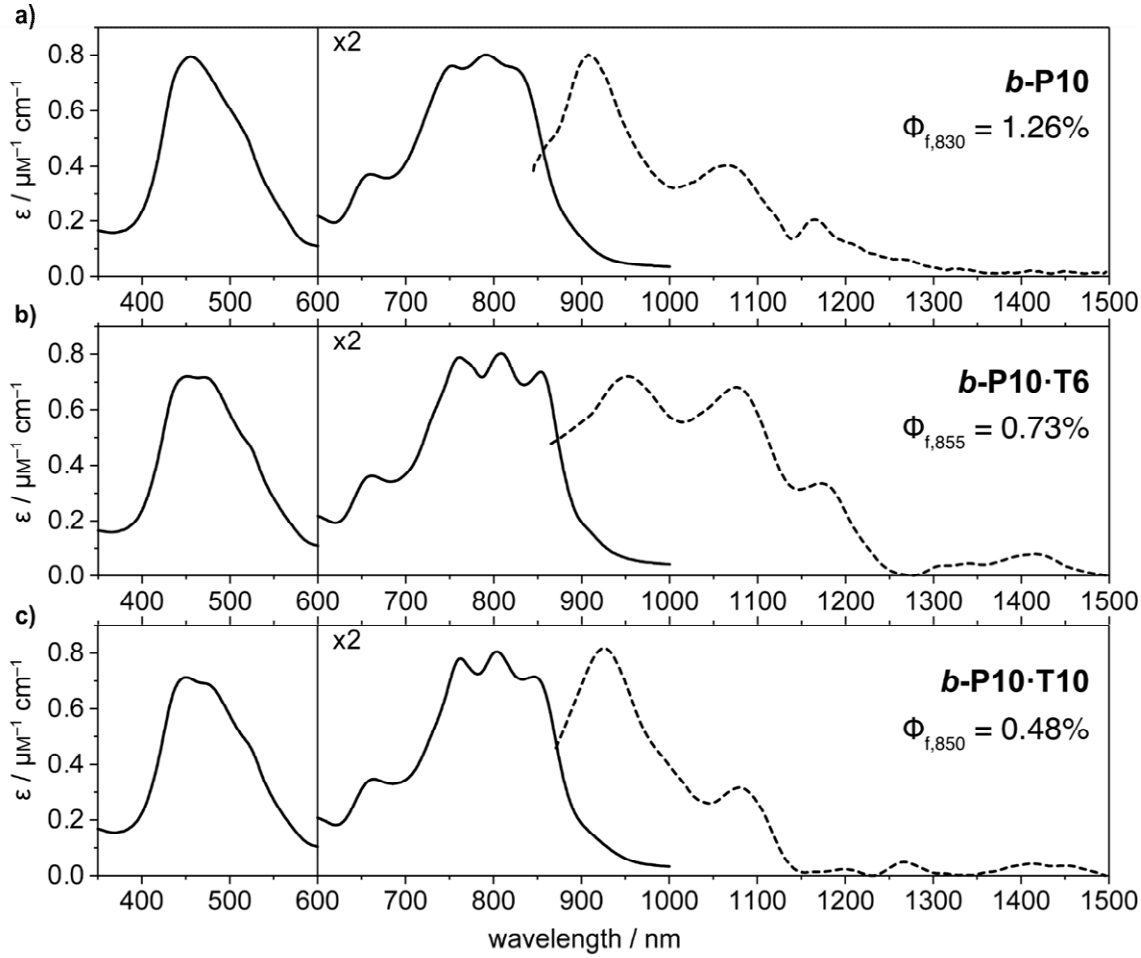


Figure 2.5. UV-vis-NIR absorption (solid black line) and fluorescence (dashed black line) for (a) ***b*-P10**, (b) ***b*-P10·T6** and (c) ***b*-P10·T10** and the calculated quantum yields for each compound in toluene/1% pyridine at 298 K. Dips at 1150 nm are as a result of absorbing solvent.

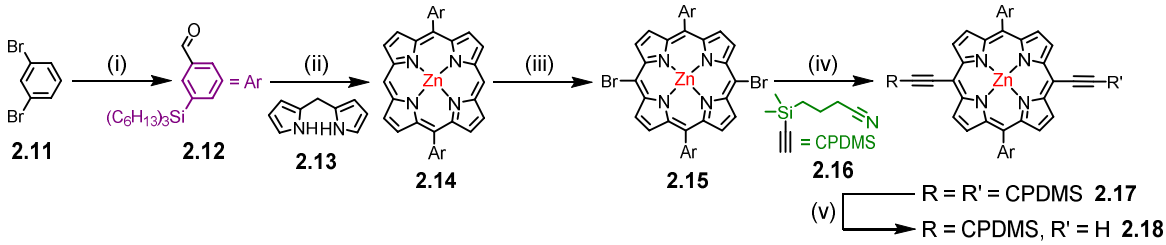
The fluorescence quantum yield of ***b*-P10** is low due to the disallowed $S_1 \rightarrow S_0$ transition, as reported previously with ***c*-P6**.[46] Adding **T6** rigidifies one of the orthogonal rings in ***b*-P10** and consequently halves the observed quantum yield. The complex ***b*-P10·T10** exhibits an ever lower quantum yield, providing evidence for the rigidification of both orthogonal rings by **T10**. The preliminary evidence presented in Figure 2.3 and Figure 2.5 suggested **T10** had a good chance of being an effective template for ball formation.

2.4 Precursor synthesis

2.4.1 *X*-P5

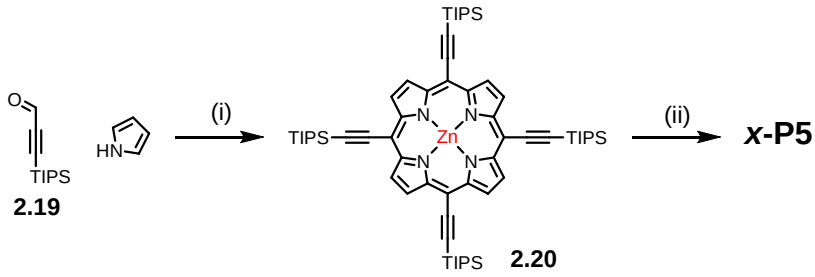
The ball precursors varied in complexity, with ***x*-P5** being the most simple due to its 4-fold symmetry and ***preball*-P10** being the most complex due to the porphyrin nanoring moiety. Common to all precursors is the porphyrin monomer **2.18**. This can be prepared in

reasonable yields from the acid-catalysed condensation of dipyrromethane (DPM. **2.13**) and solubilising aromatic group 3-(trihexylsilyl)benzaldehyde (**2.12**) followed by oxidation with 2,3-dichloro-5,6-dicyano-1,4-benzoquinone (DDQ) and insertion of a zinc metal centre with zinc acetate. Quantitative bromination of the *meso* porphyrin positions with *N*-bromosuccinimide (NBS) followed by Sonogashira cross-coupling reaction with 4-(ethynyldimethylsilyl)butanenitrile (CPDMS acetylene, **2.16**) afforded the porphyrin monomer **2.17**.



Scheme 2.8. Synthesis of mono-deprotectd porphyrin monomer **2.18** (**P'**). (i) *n*-BuLi, trihexylsilane, Et_2O then *n*-BuLi, DMF, Et_2O, 49%; (ii) TFA, CH_2Cl_2 then DDQ, CH_2Cl_2 then $Zn(OAc)_2{\cdot}2H_2O$, $CHCl_3$, 59%; (iii) NBS, $CHCl_3$/pyridine, 99%; (iv) Pd_2dba_3, CuI, PPh_3, toluene/DIPA, 100%; (v) TBAF, $CHCl_3$, 42%.

CPDMS protecting groups were chosen for two reasons. Firstly, they can be chemoselectively deprotected with a K_2CO_3/MeOH mixture in the presence of triisopropylsilyl (TIPS) acetylenes, which allowed for the orthogonal deprotection required in the synthesis of ***l*-P5** and ***preball*-P10**. Secondly, the synthesis of mono-deprotected monomer **2.18** was achieved by statistical deprotection of the acetylenes which produced a mixture of fully-protected, mono-deprotected and fully-deprotected monomers. The polar cyano moiety made separation of this mixture easier using silica chromatography.[117,118] Mono-deprotected monomer **2.18** was consequently achieved by adding sub-stoichiometric amounts tetra-*n*-butylammonium fluoride (TBAF) dropwise. Once a suitable product mixture of the bi-, mono- and non-deprotected porphyrin was reached, the compounds were separated using silica flash chromatography, yielding monomer **2.18** in 42% yield.

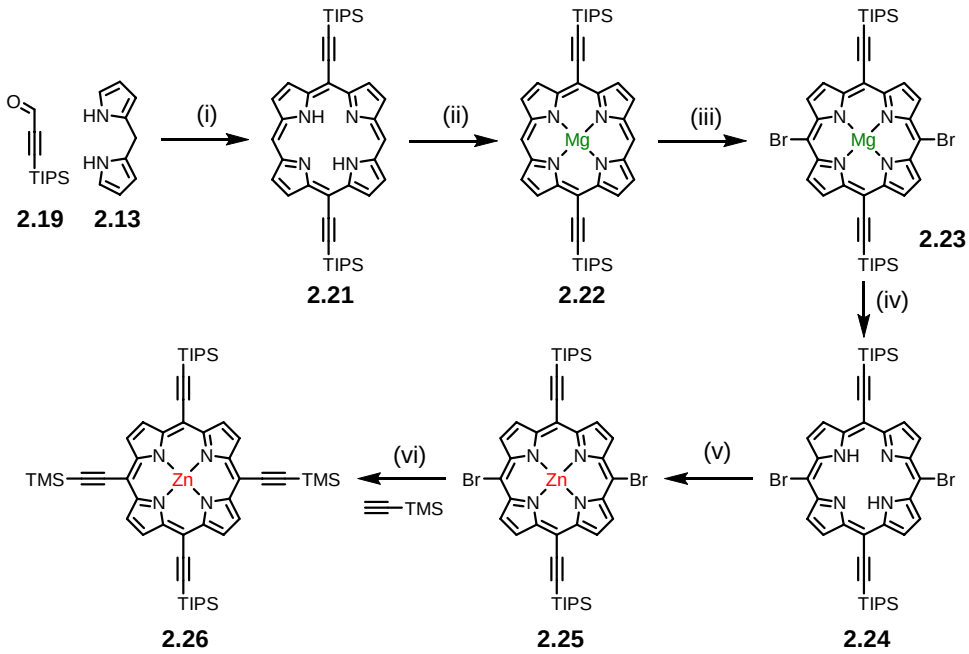


Scheme 2.9. Synthesis of ***x*-P5** via tetraalkynyl porphyrin **2.20**. (i) $BF_3{\cdot}OEt_2$ then DDQ, CH_2Cl_2, 40%; (ii) a) TBAF, CH_2Cl_2/THF then b) **2.18**, $Pd(PPh_3)_2Cl_2$, CuI, 1,4-benzoquinone, CH_2Cl_2, 10%.

The known middle unit **2.20** was synthesised through an adapted literature procedure consisting of an acid-catalysed condensation of TIPS acetylene aldehyde **2.19** and pyyrole, followed by oxidation with DDQ[119] and zinc metalation with zinc acetate, forming the product in 40% yield.[120] Deprotection of this central porphyrin with TBAF followed by a Pd/Cu co-catalysed alkyne Glaser-Hay-type homo-coupling[121] (referred to herein as Glaser coupling) with **2.18** gave a mixture of coupled oligomers. Separation of ***x*-P5** from other polymers and oligomers was achieved using recycling gel permeation chromatography (GPC), giving **x-P5** as a red solid in 10% yield (calculated from **2.20**).

2.4.2 *l*-P5

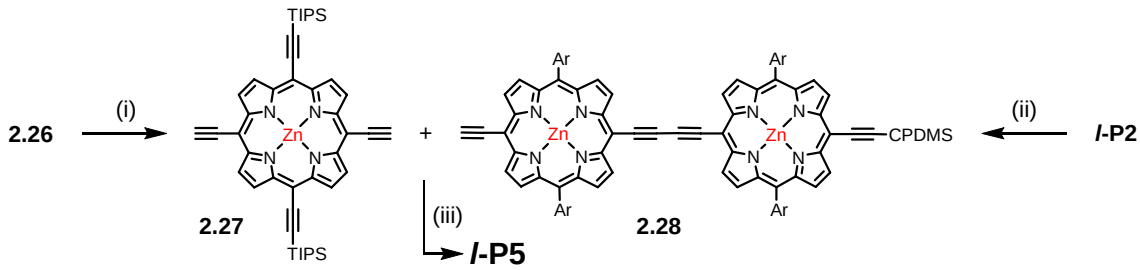
The next most complex precursor is ***l*-P5**. Dimer ***l*-P2** is a major side product of the formation of ***x*-P5**, and so initial attempts at synthesising ***l*-P5** consisted of coupling an orthogonally protected middle porphyrin with mono-deprotected dimer. The orthogonally protected porphyrin was synthesised as reported previously and summarised in Scheme 2.10.[122]



Scheme 2.10. Synthesis of orthoganally protected tetraalkynyl porphyrin **2.26**. (i) $BF_3{\cdot}OEt_2$ then DDQ, CH_2Cl_2, 25%; (ii) MgI_2, pyridine/Et_3N, 99%; (iii) NBS, $CHCl_3$/pyridine; (iv) dichloroacetic acid (DCA), $CHCl_3$, 67%; (v) $Zn(OAc)_2{\cdot}2H_2O$, $CHCl_3$, 100%; (vi) Pd_2dba_3, CuI, PPh_3, toluene/DIPA, 86%.

First, triisopropylsilylpropynal **2.19** and dipyrromethane **2.13** were condensed with boron trifluoride, followed by oxidation and re-aromatisation with DDQ. Due to the electron withdrawing alkyne groups in **2.21**, a more electropositive metal centre than zinc is required to afford clean bromination. Consequently, magnesium was inserted by refluxing

porphyrin **2.21** overnight with magnesium iodide.[123] Bromination is achieved in the *meso* positions with NBS. Removal of the magnesium with dichloroacetic acid (DCA) followed by insertion of zinc with zinc acetate afforded the zinc metallated porphyrin **2.25** in two steps. A Sonogashira cross coupling with ethynyltrimethylsilane (TMS acetylene) afforded the final product **2.26**. In this case, the only requirement for the protecting groups is orthogonal deprotection and so TMS (deprotected with basic methanol) and TIPS (stable to these conditions) alkynes were chosen in place of the more expensive polar cyano protecting groups.



Scheme 2.11. Synthesis of ***l*-P5** from mono-deprotected dimer **2.28**. (i) K_2CO_3, THF, 100%; (ii) TBAF, $CHCl_3$/EtOH, 16%; (iii) $Pd(PPh_3)_2Cl_2$, CuI, 1,4-benzoquinone, $CHCl_3$/DIPA, 10%.

Mono-deprotection of dimer ***l*-P2** was achieved with TBAF to afford **2.28** in 16% yield. Orthogonal deprotection of **2.26** with K_2CO_3/MeOH afforded **2.27** in quantitative yield. Coupling these two together with palladium and copper co-catalysed Glaser conditions afforded ***l*-P5** in 10% yield after isolation via recycling GPC.

Although this route was successful, separation of the statistical mixtures of dimer was difficult. Slow column chromatography failed to yield clean fractions, and often fast running bands contained mixtures of all products. An NMR of the fully deprotected dimer provides a potential reason for this awkward behaviour (Figure 2.6).

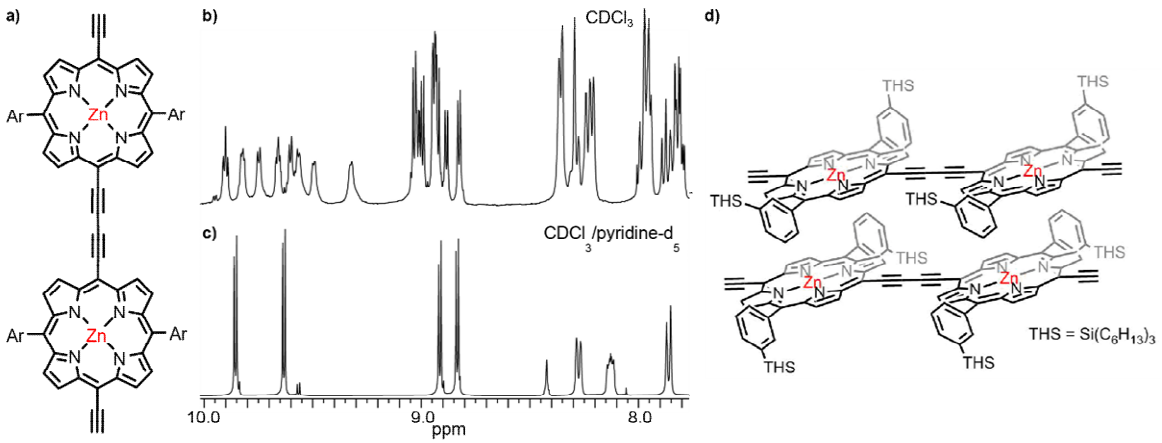


Figure 2.6. (a) Fully deprotected dimer, ***l*-P2''**. (b) ^{1}H NMR of ***l*-P2''** in $CDCl_3$ and (c) in $CDCl_3$/pyridine-d_5 (400 MHz, 298 K). (d) Proposed stacking behaviour of ***l*-P2** derivatives, encouraged because of the asymmetric aryl solubilising groups exposing large porphyrin faces that favour π-π stacking.

It seems that the dimers stack very strongly in the absence of pyridine (Figure 2.6b) as evidenced by the more than four β proton environments observed. Adding pyridine-d_5 (Figure 2.6c) simplifies the observed spectra to the expected symmetry of four β protons, due to the coordination of pyridine disfavouring molecular aggregates. Although silica chromatography was usually run with 1-5% pyridine, it could be that the aggregation of these dimer units is stronger than previously expected due to the meta-trihexylsilyl solubilising groups leaving a large aromatic face exposed for π- π- stacking. The removal of the alkyne protecting groups further reduces steric bulk and could encourage aggregation, which may explain why the statistical mixtures behaved so inconsistently on silica compared to the fully protected equivalents. The asymmetry of the solubilising groups may allow discrete dimer formation such as the one proposed in Figure 2.6d, which would explain the relative sharpness (compared to random aggregates) of the NMR presented in Figure 2.6b.

Another route was designed to avoid the dimer aggregation. In this route, a trimer can be accessed by using mono-deprotected monomer **2.18** and middle porphyrin **2.27** in a Glaser coupling. This trimer can then be orthogonally deprotected and Glaser coupled with more of mono-deprotected monomer **2.18**. This has the benefit of avoiding the dimer but at the expense of three extra steps, two of which are only moderately yielding Glaser couplings. The product mixture is also more easily separable by recycling GPC due to the major constituents being pentamer and dimer, rather than pentamer and tetramer in the old route.

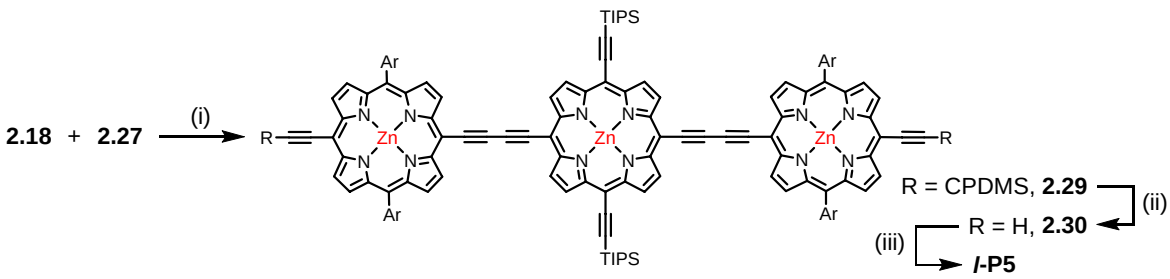


Figure 2.7. Synthesis of ***I*-P5** via trimer intermediate **2.29**. (i) $Pd(PPh_3)_2Cl_2$, CuI, 1,4-benzoquinone, $CHCl_3$/DIPA, 23%; (ii) K_2CO_3, THF/MeOH, 100%; (iii) **2.18**, $Pd(PPh_3)_2Cl_2$, CuI, 1,4-benzoquinone, $CHCl_3$/DIPA, 28%.

2.4.3 preball-P10

The final precursor to be synthesised was the nanoring-based ***preball*-P10**. This was realised from the same trimer used for the synthesis of ***I*-P5**, **2.30**. Glaser coupling in the presence of **T6** afforded the porphyrin nanoring **2.31** in 50% yield, following purification

by GPC.[49] The four protected TIPS alkynes can be deprotected quantitatively with TBAF to yield **2.32**. Glaser coupling the deprotected ring to an excess of mono-protected porphyrin **2.18** afforded the functionalised porphyrin nanoring **2.33**, after removal of dimer and polymer side-products via recycling GPC. Removal of the template using an excess of competing ligand 1,4-diazabicyclo[2.2.2]octane (DABCO) finally provided the ***preball*-P10** complex.[49]

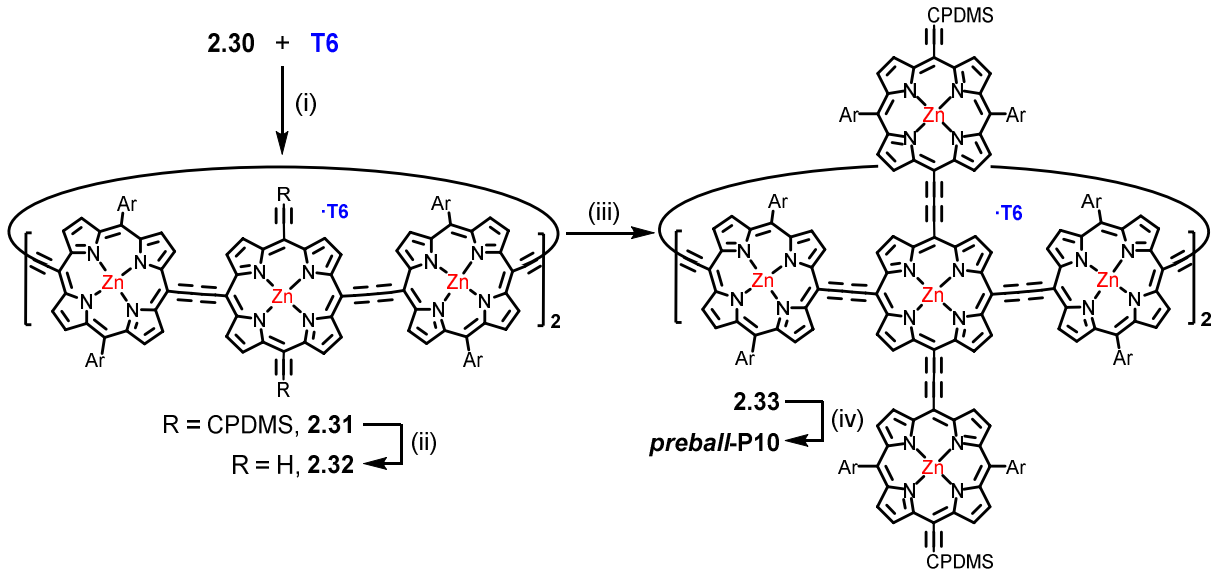


Figure 2.8. Synthesis of ***preball*-P10** via nanoring intermediate **2.31**. (i) $Pd(PPh_3)_2Cl_2$, CuI, 1,4-benzoquinone, $CHCl_3$/DIPA, 50%; (ii) TBAF, CH_2Cl_2, not purified; (iii) **2.18**, $Pd(PPh_3)_2Cl_2$, CuI, 1,4-benzoquinone, $CHCl_3$/DIPA, 25%; (iv) DABCO/pyridine, 77%.

2.5 Ball formation tests

With the ball precursors in hand, initial titrations were undertaken to ensure the expected coordination complexes are present in solution. UV-vis-NIR titrations of **T10** (which shows no absorption in the UV-vis-NIR range) and the ball precursors show that the expected stoichiometric complexes are formed.

In all of the titrations, there is a clear red shift upon addition of **T10**. This is consistent with the template coordinating to the precursors and coplanarising the porphyrins, causing an increase in conjugation; an effect observed in many porphyrin compounds of this type.[46,49,96,123] ***x*-P5** (Figure 2.9a) and ***preball*-P10** (Figure 2.9c) appear to form stable complexes at 0.5 equivalents (2:1 precursor to template binding) and 1 equivalent (1:1) with **T10** respectively.

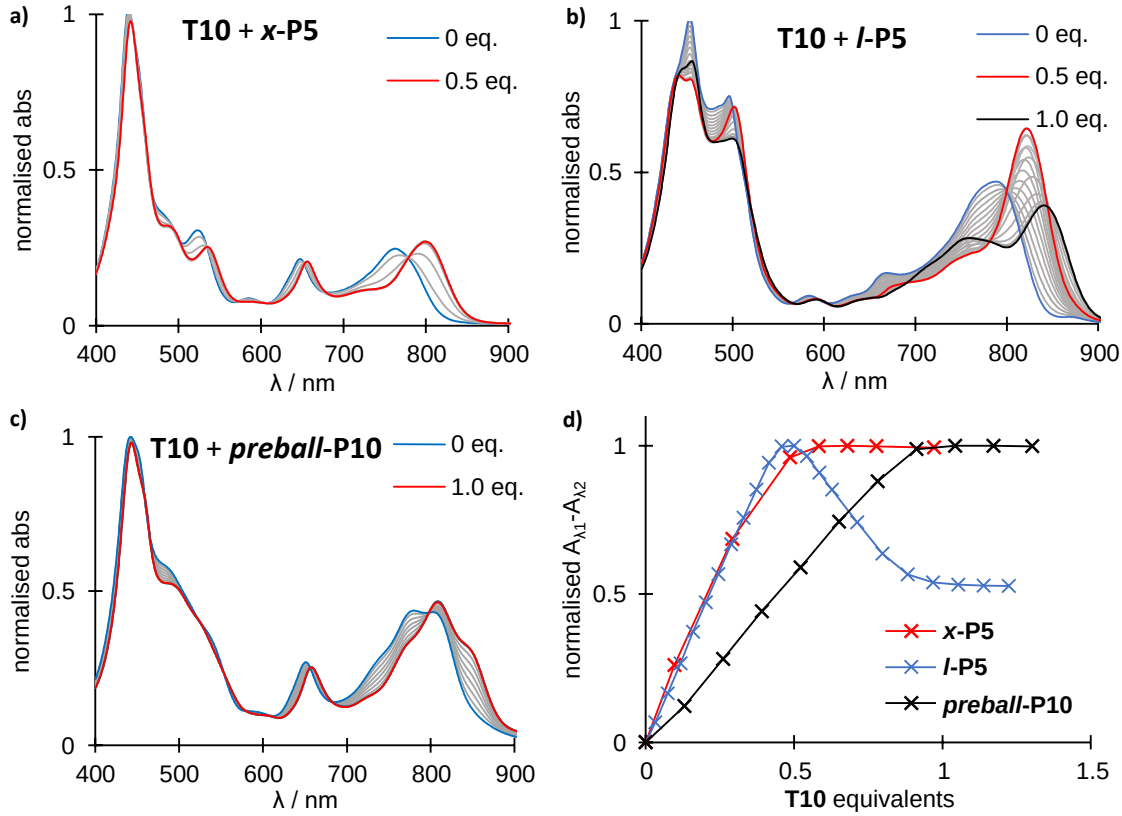


Figure 2.9. UV-vis-NIR titrations of **T10** into (a) ***x*-P5**, (b) ***l*-P5** and (c) ***preball*-P10**. (d) Plotted UV-vis-NIR titrations showing the observed stoichiometry for the three precursors complex with **T10**. Plotted is the difference in absorbance between a feature relating to initial species, λ_1, and a feature relating to a complex, λ_2, for a given concentration of **T10**. Precursor (λ_1, λ_2): ***l*-P5** (785 nm, 823 nm); ***x*-P5** (763 nm, 801 nm); ***preball*-P10** (779 nm, 850 nm). Plots (a)-(c) are normalised to the initial (0 eq.) max absorbance to allow for comparison in plot (d).

***l*-P5** shows two apparent species upon titration with **T10**. There is a first species with a red shifted and sharpened absorption band that occurs at 0.5 equivalents (2:1). This species seems to be unstable to increasing concentration of **T10**, and prefers to form a stable complex at 1 equivalent which does not change upon increasing **T10** concentration.

2.5.1 *x*-P5 and *l*-P5

The agreement between expected and observed binding behaviour looked promising for trials of ball formation with the simpler precursors ***x*-P5** and ***l*-P5**. Both precursors were deprotected fully to form ***x*-P5''''** and ***l*-P5''''** with excess TBAF.

2.5.1.1 *x*-P5

Ball formation using ***x*-P5** and **T10** was trialled on both a small (~ 1 mg) and larger (~ 10 mg) scale. In order to minimise the effect of **T10** insolubility, the 2:1 complex was formed first by titration of a known stock solution of **T10** into a solution of ***x*-P5**. Once the UV-vis of the mixture was consistent with the final spectrum in Figure 2.9a (red), the mixture

was submitted to Glaser-Hay type reaction conditions by adding a catalyst solution containing $Pd(PPh_3)_2Cl_2$, CuI and 1,4-benzoquinone in $CHCl_3$/DIPA. After leaving overnight, work-up was achieved by passing through a short silica plug (first trial) or passing directly over a size-exclusion column (SEC, Biobeads SX-1 in toluene/1% pyridine) in the second trial. The SEC was introduced to avoid the need to take the solution to dryness, after observing insoluble precipitates in the reaction flask and on top of the silica plug.

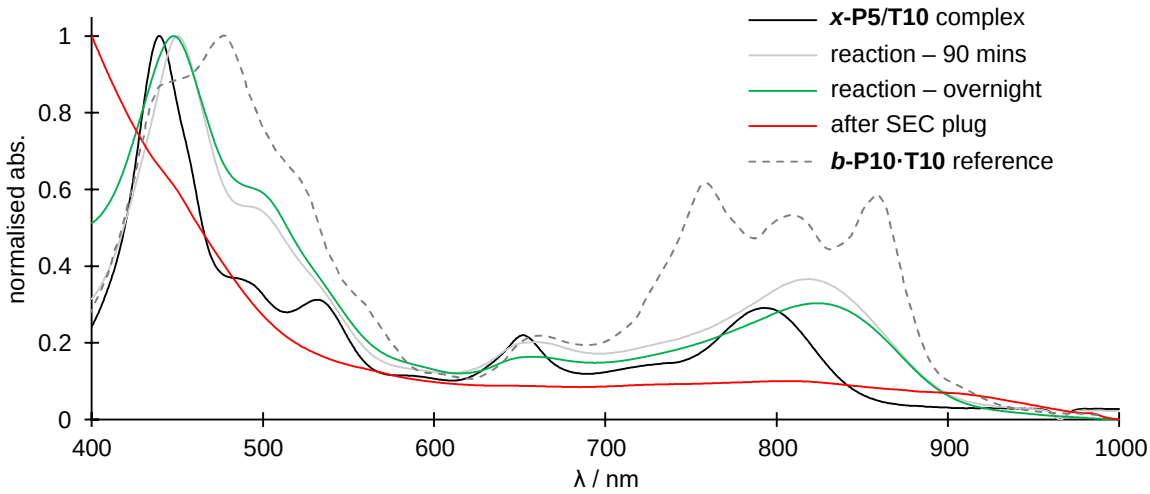


Figure 2.10. UV-vis-NIR reaction analysis of attempted ***b*-P10·T10** formation via an ***x*-P5/T10** complex ($CHCl_3$, 298 K).

The reactions yielded no product, with much of the reaction mixture remaining on the SEC as an insoluble precipitate. UV-vis-NIR and GPC monitoring of the reaction progress gives some insight into why. In the UV-vis, a red-shift of the absorption maxima is seen upon addition of catalyst, concurrent with an increase in conjugation. After leaving overnight (due to no observed pattern of ***b*-P10·T10** after 90 minutes) the height of the Q band (λ = 830 nm) decreased relative to the Soret band (λ = 450 nm). This change in Q band character could be attributed to two factors: either as a result of decomposition and consequent loss of conjugation, or via the formation of non-bound polymers which display broadened Q band absorptions as a result of the broader distribution of porphyrin-porphyrin torsional angles.[25,124]

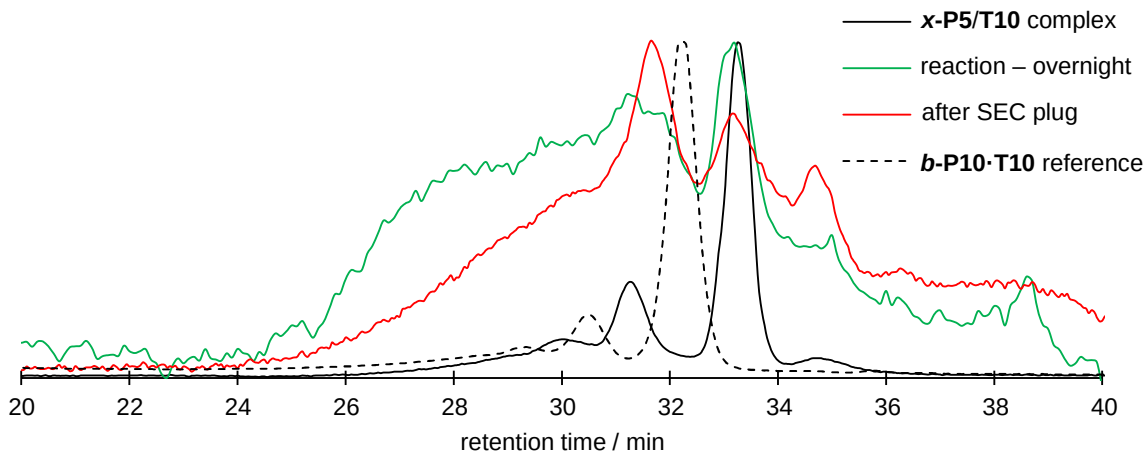


Figure 2.11. Analytical GPC (PLGel columns, THF/1% pyridine, detection at 750 nm) traces of selected reaction stages during attempts at ***b*-P10·T10** formation via an ***x*-P5/T10** complex.

The analytical GPC trace for the reaction mixture (Figure 2.11, green trace) seemed to contain no peaks similar to both the final product, ***b*-P10·T10** (Figure 2.11, dashed trace), or the starting ***x*-P5/T10** mixture (Figure 2.11, black trace). In general the traces are broadened, probably due to polymer formation. Upon passing through the SEC (Figure 2.11, red trace) still no peaks were found close to the expected ***b*-P10·T10** peak. Recycling GPC of the mixture post-SEC also failed to yield any product, instead showing a complex mixture of larger products (Figure 2.12).

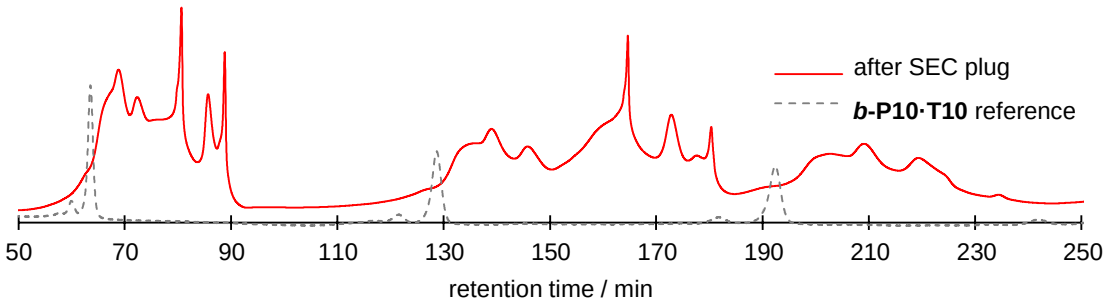


Figure 2.12. Recycling GPC (JAIGEL columns, toluene/1% pyridine, detection at 750 nm, 3 cycles shown) trace of the isolated reaction mixture after attempts at ***b*-P10·T10** formation from ***x*-P5/T10** complex.

2.5.1.2 *l*-P5

***l*-P5** was trialled twice on a small (~ 3 mg) scale, using the optimised conditions reported for Glaser-Hay type couplings used successfully for previous nanoring and nanoball syntheses.[82] The **T10** complex was formed in solution first via titration with known stock solutions and comparison to Figure 2.9b (red spectrum), before the catalyst mixture was added.

As with **x-P5**, the reaction was monitored with both UV-vis-NIR and analytical GPC. Addition of catalyst and stirring for 90 minutes showed a red shift consistent with increased conjugation compared to the ***l*-P5/T10** complex. Leaving the reaction stirring overnight with additional catalyst resulted in an increased Q-band intensity.

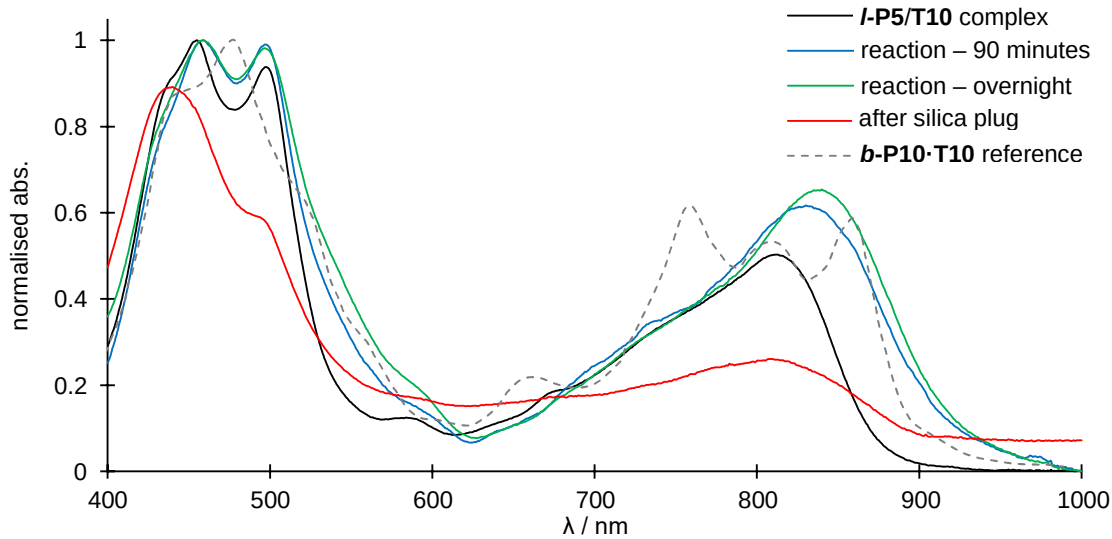


Figure 2.13. UV-vis-NIR reaction analysis of attempted ***b*-P10·T10** formation via an ***l*-P5/T10** complex ($CHCl_3$, 298 K).

The absorption spectrum of ***b*-P10·T10** is shown as a grey dotted line in Figure 2.13. It is clear that this is not the major product of the reaction, but it is possible that there is some desired product within the broad envelope of the Q-band absorption. Upon passing through a short silica plug ($CHCl_3$/pyridine), most of the reaction mixture precipitated and remained as an insoluble solid on top of the silica. The resulting material absorbs very little in the Q-band in comparison to the Soret band (Figure 2.13, red line). In general, the intensity of the Q-band in relation to the Soret band of porphyrins can be correlated with the amount of conjugation/electronic communication between the porphyrins (i.e. an increase is seen upon increasing oligomeric chain length or rigidifying of porphyrin oligomers). It seems likely therefore that higher order oligomeric species are present in solution in the reaction mixture, but precipitate upon work-up leaving only the smaller, more soluble porphyrins in the final product mixture.

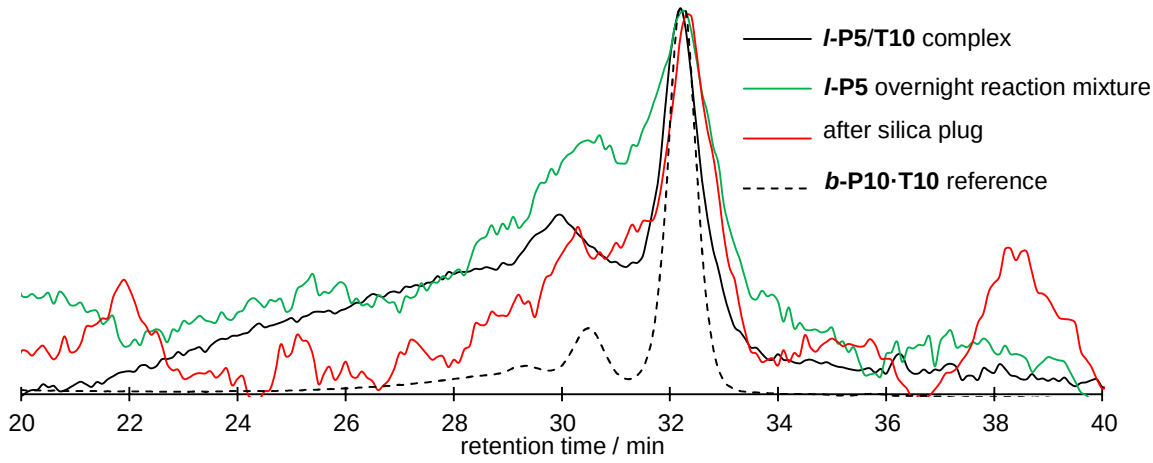


Figure 2.14. Analytical GPC (PLGel columns, THF/1% pyridine, detection at 750 nm) traces of selected reaction stages during attempts at ***b*-P10·T10** formation via an ***l*-P5/T10** complex. The trace for after silica plug has been baseline corrected.

Analytical GPC traces of the reaction mixture before (Figure 2.14, green trace) and after passing through the silica plug (Figure 2.14, red trace) show a broad envelope of products that looks similar to the initial complex (Figure 2.14, black trace) and ***b*-P10·T10** (Figure 2.14, dashed trace). However, these traces are noisy due to the small amount of product available for analysis as a result of the insolubility of the product mixture in THF.

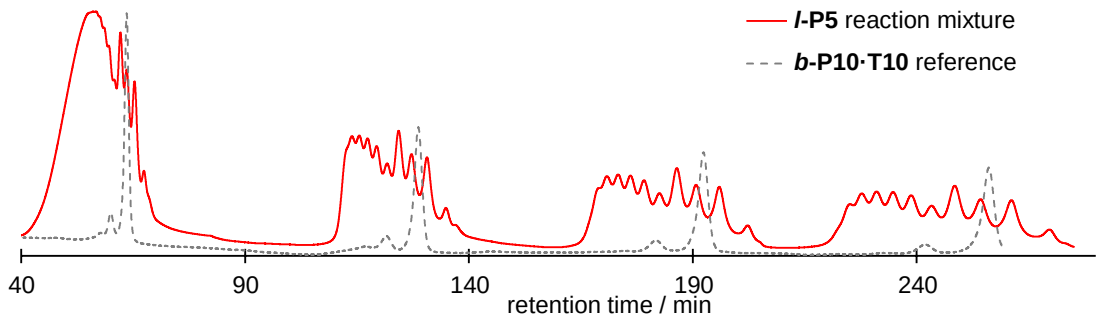


Figure 2.15. Recycling GPC (JAIGEL columns, toluene/1% pyridine, detection at 750 nm) trace of the isolated reaction mixture after attempts at ***b*-P10·T10** formation from ***l*-P5/T10** complex. Four cycles shown.

Analysis of the isolated product mixture on analytical recycling GPC showed a large envelope of polymeric and oligomeric products. The sharp peaks around the reference peak were initially promising, but after three cycles the retention times were no longer identical. No peaks yielded enough material for further evaluation. The difference in retention time could be because of the reference and the reaction traces were ran on different days. Even so, the low yield of soluble products and the consequent complexity

of the product mixture demonstrate the unsuitability for **T10** to act as a template for the formation of ***b*-P10** from ***l*-P5**.

2.5.1.3 Discussion

At first sight the unsuccessful attempts to synthesise ***b*-P10·T10** seemed at odds with the previously reported binding behaviour; the precursors appear to form the expected coordination compounds, and extensive experience forming nanorings and nanoballs tells us the alkyne coupling itself should be reliable. One key tenet of template-directed synthesis is the requirement of the template to have not only the correct fit for the final product, but also be rigid enough such that the reaction is directed to units on the same complex.[34,41,46] In the case of the template **T10**, although it fits well into ***b*-P10**, it is conformationally flexible with many degrees of rotation around the pyridyl axes (Figure 2.16b).

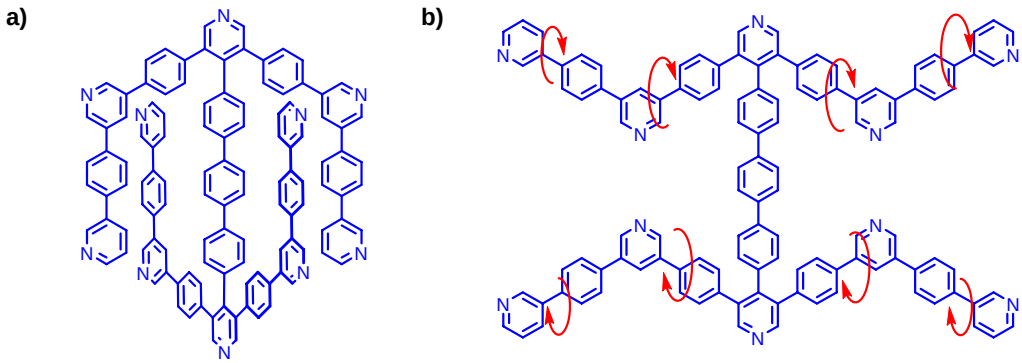


Figure 2.16. (a) **T10** as presented in this chapter in the optimal conformation for ball formation. (b) **T10** in a more likely conformation, with red arrows highlighting degrees of rotation detrimental for ball formation.

The results of this conformational flexibility is that there is a much greater entropic cost to pay for assembling the precursor-template complex into the right conformation. For ***x*-P5**, the formation of a 2:1 complex is not necessarily evidence for the formation of the required complex for ball formation.

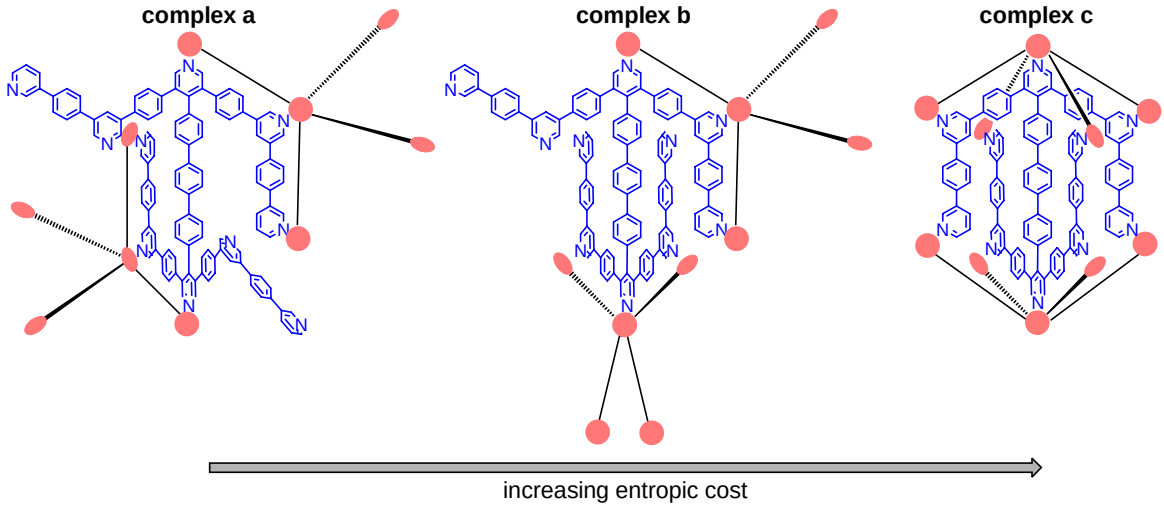


Figure 2.17. A selection of potential ***x*-P5/T10** complex complexes.

A complex like complex **a** or **b** (Figure 2.17) consist of two bound trimer motifs. The complex of a linear trimer bound to a template **T3** has the formation constant, K_f, of 9.4 x 10^9 M^{-1}, demonstrating formation of a strong complex.[125]

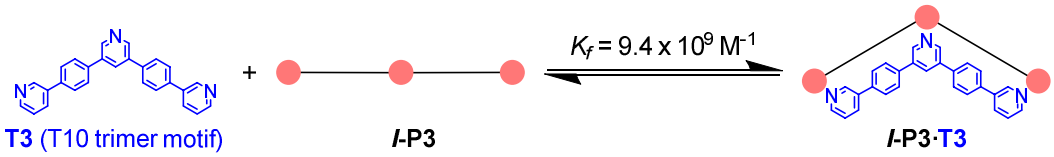


Figure 2.18. Binding of ***l*-P3** to **T3**, demonstrating the strong binding expected.

As the trimer binding is relatively strong, it may be that the extra binding of the porphyrin arms may not be strong enough to overcome the entropic cost of organising the template **T10**. In reality, it may be that a mixture of complexes is present in solution. For steric reasons, complex **a** and **b** would have the non-bound porphyrins facing outwards, which may favour polymer growth rather than intramolecular ring closure.

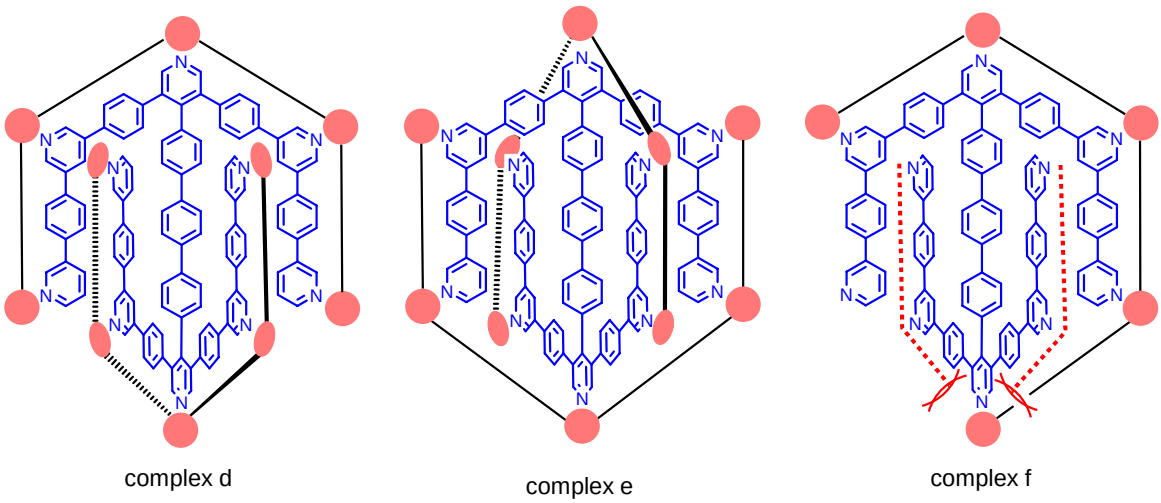


Figure 2.19. A selection of potential ***l*-P5/T10** complex conformations. Red lines in complex **f** demonstrate the blocking of a second coordinating ligand, meaning the 2:1 complex must be in complex **d** or **e**.

For ***l*-P5**, the story is similar. There are two complexes, **d** and **e** (Figure 2.19), which would be the likely occupied complexes upon formation of a 2:1 complex. This is because a linear hexamer is known to bind strongly to a similarly shaped motif, **T6**, and so it follows that the linear pentamer must also be bound strongly (Figure 2.20). If the observed complex is a 2:1 complex, then the only way which two pentamers could bind strongly would be via complex **d** or **e**, as any complex similar to complex **f** would block the binding of a second pentamer.

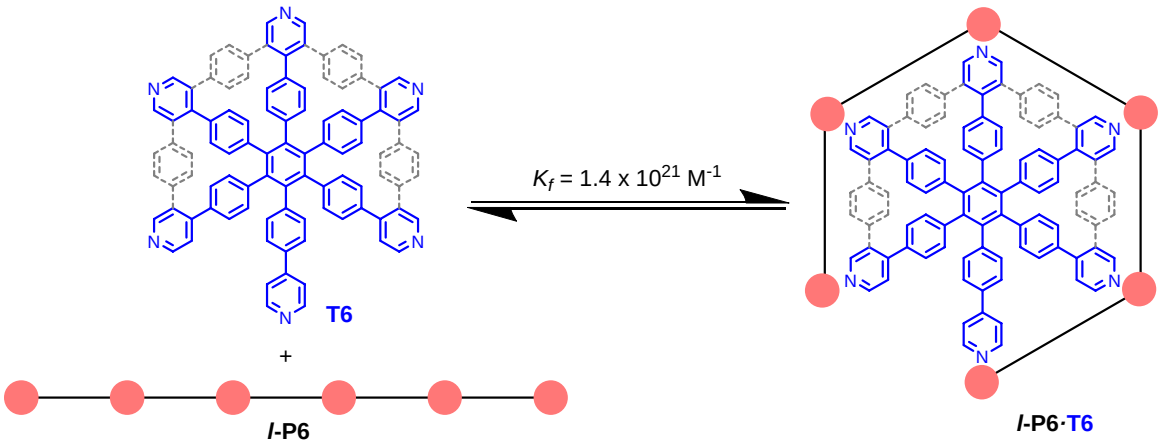


Figure 2.20. Binding of ***l*-P6** to **T6**, demonstrating the strong binding expected. Grey dashed lines relate to the equivalent **T10** moiety for comparison.[49]

Another major factor is the asymmetry of the precursor. In order to close properly to form the ball the alkyne at the end of one pentamer must selectively couple to the middle of the other (Figure 2.21, green arrows). If the end couples to another end (or middle to another middle) of either the other pentamer on the complex or another pentamer in solution from another complex, then the resulting oligomer cannot undergo ball

formation (Figure 2.21, blue arrows). On top of this, the favouring of a 1:1 complex with template:pentamer stoichometries > 0.5 (Figure 2.9b) makes this doubly disadvantageous; the newly formed oligomer will probably not be able to bind strongly to the template due to a mismatched shape, and thus will drive the average complex in solution to the 1:1 complex, further disfavouring ball formation.

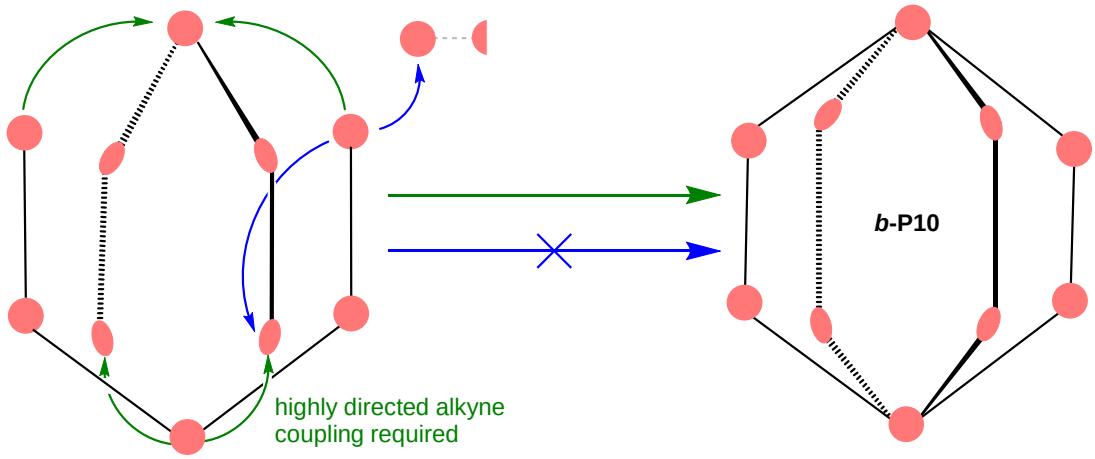


Figure 2.21. ***l*-P5/T10** complex with **T10** hidden, showing the required directionality of alkyne-coupling. Green indicates correct coupling required for ball formation, blue represent incorrect couplings and consequent polymer formation.

2.5.2 Preball-P10

Although ***x*-P5** and ***l*-P5** were not successfully converted to ***b*-P10**, ***preball*-P10** still offered a novel route to ***b*-P10**. In theory, the pre-organisation of **preball-P10** should favour ball formation. This is because the binding of nanorings to **T6** is amazingly strong (K_f = 6.6 x 10^{38} M^{-1} in toluene, Figure 2.22)[49] and consequently **T10** should also bind tightly to the ring. This is borne out in the observed strong 1:1 complex in Figure 2.9d.

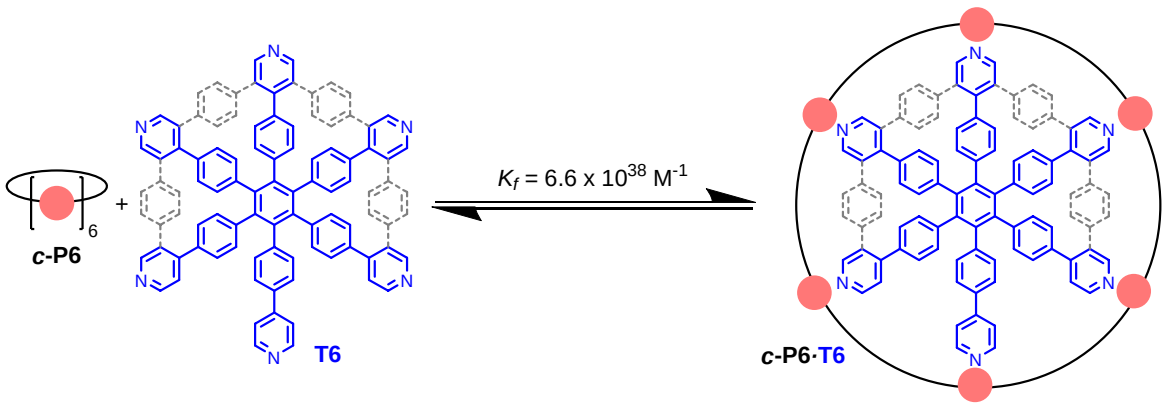


Figure 2.22. Strong binding of ***c*-P6** into **T6**.[49] Dashed grey areas represent **T10** moiety, demonstrating the expected strong binding of **T10** into ***preball*-P10**.

To our surprise, initial tests on ~ 3 mg of material failed to yield any observable ball products. It has been discovered in the group recently that templates can become

kinetically trapped in ***c*-P6** hosts – that is, they equilibrate slowly and thus stay in the conformation at which they initially bind on an a time scale of hours to weeks. This is as a direct result of the enormous formation constants. In the case of ***b*-P10**, this leaves two potential 1:1 complexes.

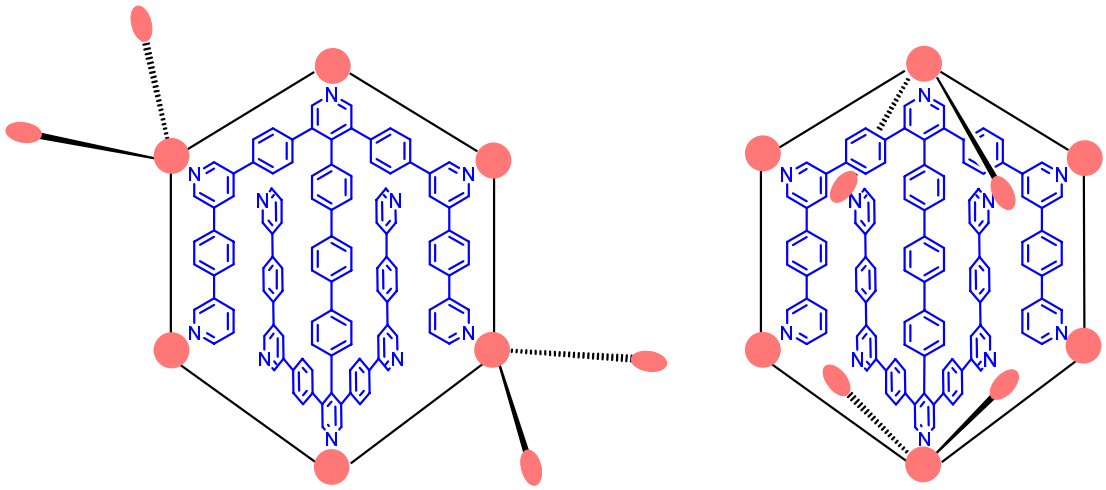


Figure 2.23. The two complex possible for ***preball*-P10·T10**. Complex **g** is statistically twice as likely than h.

If the templates are kinetically trapped, complex **g** and **f** (Figure 2.23) should be in a statistical ratio of 2:1. To test this, NMR experiments were undertaken with the formed ***preball*-P10·T10** complex. To make the complex, an excess of **T10** solution was titrated into ***b*-P10**. The solution was then passed over a short silica plug in CH_2Cl_2/pyridine. The ball, decorated with long alkyl solubilising groups, passes quickly over the plug, whereas the free excess template moves little due to the high polarity afforded by the 10 pyridyl moieties. Template inclusion was confirmed with UV-vis-NIR (comparing to the titration shown in Figure 2.9c).

The NMR of ***preball*-P10·T10** is messy and broad, consistent with the complex being in a range of complexes (Figure 2.24a). To prove that the sample was clean and the observed spectrum was not as a result of either impure material or contaminants, the sample was taken to dryness and re-dissolved in pyridine-d_5. This afforded a clean, sharp spectrum (Figure 2.24b) similar to ***preball*-P10** (Figure 2.24c) as a result of the template being knocked out. The similarity between this spectrum and the actual ***preball*-P10** NMR spectrum proves the observed spectrum is as a result of conformational disorder or formation of a mixture of complexes.

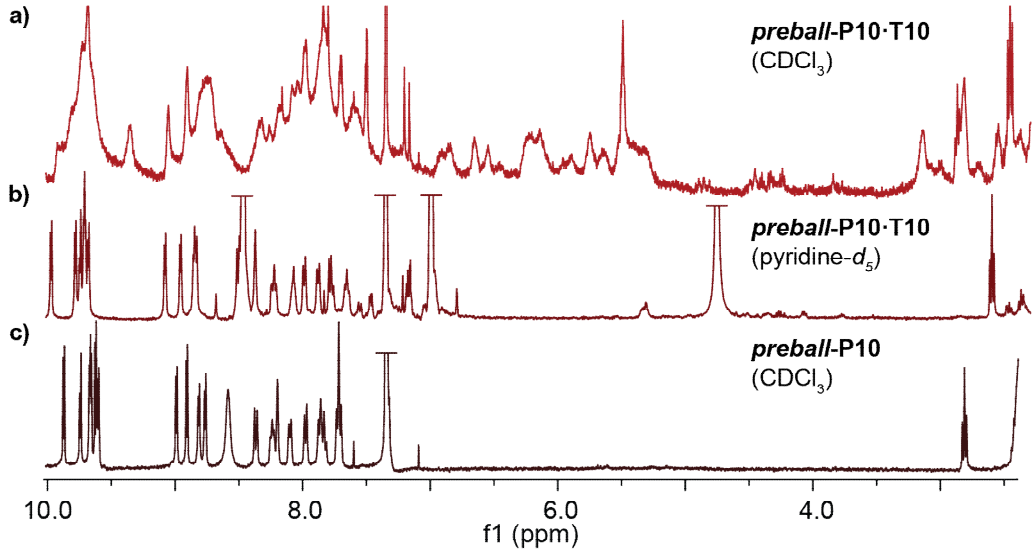
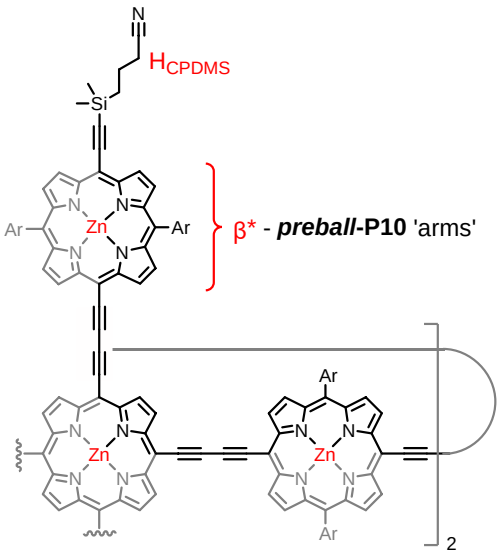


Figure 2.24. ^{1}H NMR spectra (400 MHz, 298 K) of (a) ***preball*-P10·T10** in $CDCl_3$, (b) ***preball*-P10·T10** in pyridine-d_5 and (c) ***preball*-P10** in $CDCl_3$ as a reference, showing the messy spectrum in (a) is as a result of conformational disorder.

One interesting feature to note in the NMR of ***preball*-P10·T10** is the characteristic CPDMS proton at 2.60 ppm. This is usually a sharp triplet, and is often unaffected by asymmetry due to the relative isolation of CPDMS protecting groups from the rest of the compound. In this case, however, the peaks are split into two in a ratio of 2:1 (Figure 2.25b). This is a clear indication of the kinetic trapping of templates into complexes **g** and **h**.

To prove this, pyridine-d_5 was titrated into the NMR solution of ***preball*-P10·T10** in $CDCl_3$. Upon addition of pyridine-d_5, two general features were observed. Firstly, various signals in the β region coalesced into four sharp doublets, with relative integrals of 1:1:1:1 (Figure 2.25a). Secondly, the CPDMS proton peaks sharpened and coalesced into one signal (Figure 2.25b). This behaviour can be explained by the coordinating pyridine knocking off the relatively labile porphyrin 'arms' (Scheme 2.12). The arms are then locally identical between the two complexes (complexes **i** and **j**, Figure 2.26), causing the NMR signals to sharpen.



Scheme 2.12. Location of H_{CPDMS} and the β* protons on the ***preball*-P10** 'arms'.

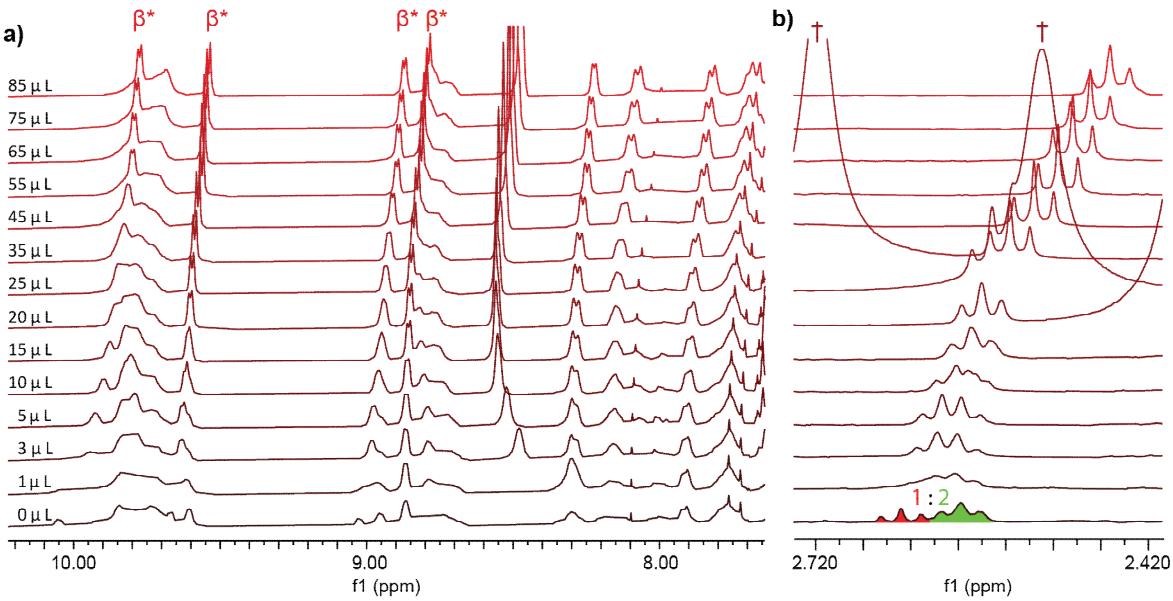


Figure 2.25. NMR (400 MHz, 298 K) of ***preball*-P10·T10** titration with pyridine-d_5 showing (a) the sharpening of four proton environments as a result of pyridine coordination to ***preball*-P10** 'arms' and (b) H_{CPDMS} protons in a 1:2 ratio coalescing upon increased pyridine concentration. † corresponds to a H_2O peak as a result of hygroscopic pyridine.

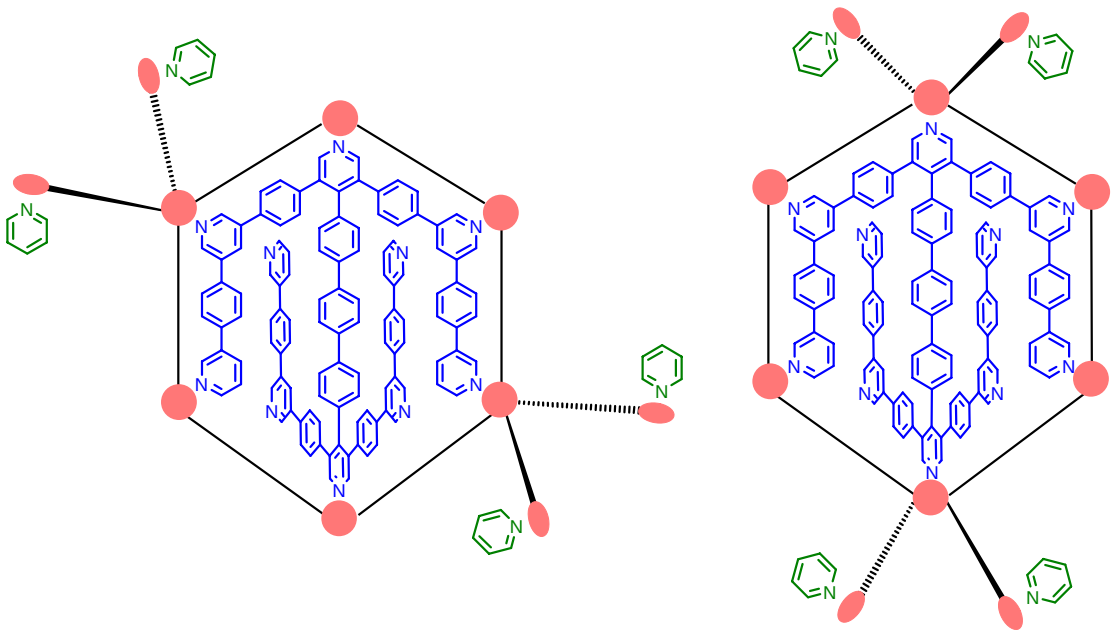


Figure 2.26. Complexes expected for ***preball*-P10·T10** after addition of excess pyridine-d_5 such as in the NMR titration presented in Figure 2.25.

From this evidence, it seems that the template is kinetically trapped in a statistical mixture of conformations, a common phenomenon with self-assembled complexes.[126] In hindsight this is no surprise – the enormous binding constant for **T6** into ***c*-P6** suggests some degree of irreversibility. It may be, however, that complex **h** (with 10 bound porphyrins) is the thermodynamic minimum due to the maximised favourable enthalpy of binding. To test if this was the case, I designed several strategies to overcome the barrier between conformations.

The first involved using pyridine as a competitive ligand, as a competitively coordinating solvent can act as a catalyst in the chemical exchange between complexes. As the pyridine concentration reaches a threshold level, the complex may become denatured (as evidenced by Figure 2.24b). At concentrations of pyridine immediately lower than this threshold point, the binding should be weakened such that there is some degree of equilibration between complexes. If the pyridine is removed slowly, for example by azeotropic evaporation with toluene, then perhaps the intermediate point can be reached where there is equilibration between the complexes. Another method is to heat the complex, supplying enough thermal energy to overcome any activation barrier between conformations. Both of these methods were trialled and the NMR spectra are presented in Figure 2.27.

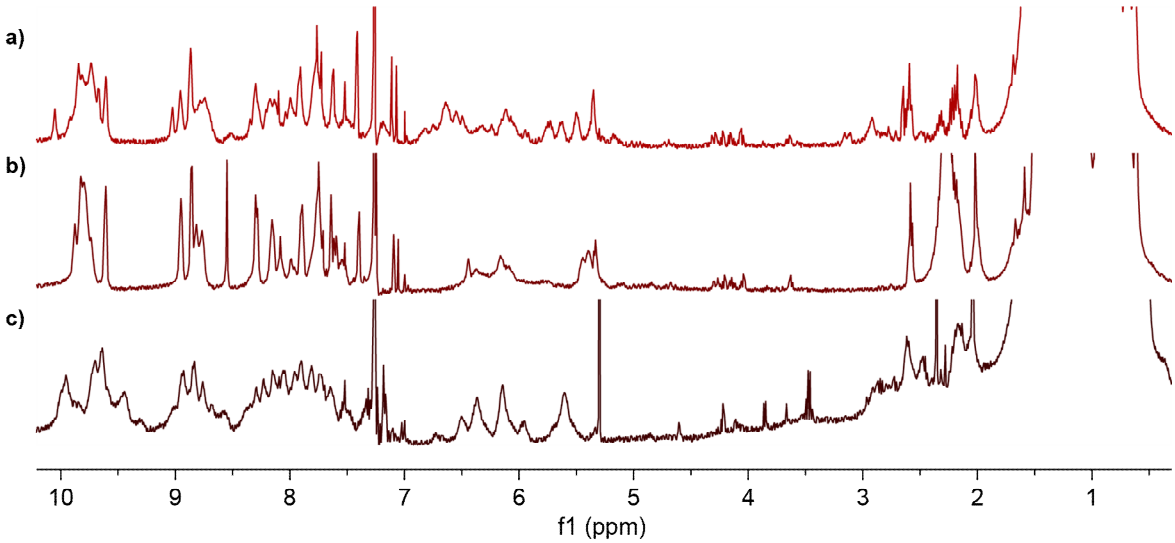


Figure 2.27. ^{1}H NMR spectra (400 MHz, 298 K) spectra of ***preball*-P10** in $CDCl_3$ after (a) initial formation, (b) equilibration in pyridine and (c) heating to 80°C in toluene for 2 hours.

Although in both cases the NMR observed after equilibration was slightly different, the similarity and messy nature of the spectra suggests a more favourable distribution of complexes was not reached. In the case of equilibration with pyridine, it is likely that the intermediate pyridine concentration at which the template is labile is much higher than that required to coordinate the ***preball*-P10** porphyrin legs, and as such the actual equilibration would be between complexes **i** and **j**. The observation that the legs can be coordinated while the template remains inside the ring (Figure 2.25) is evidence for this. As there is no enthalpic benefit to **j** over **i**, only a maximum ratio of 1:1 would be expected.

With this in mind, 10 mg of ***preball*-P10·T10** was pre-equilibrated by dissolving in neat pyridine. This was diluted with toluene, before the solvents were removed *in-vacuo*. More toluene was added and the solvent removed again. After this, the complex was deprotected with excess TBAF, passed through a silica plug and submitted to Glaser-Hay reaction conditions. As with ***l*-P5** and ***x*-P5**, the reaction was monitored with UV-vis-NIR and GPC. In this case, however, neither were as instructive due to the similarity between the starting material and product (the difference in molecular weight between ***preball*-P10·T10** and ***b*-P10·T10** is 4 Da, or 0.04% of the total mass, and their UV-vis-NIR spectra are similar). Only the UV-vis-NIR spectra are presented here for that reason (Figure 2.28).

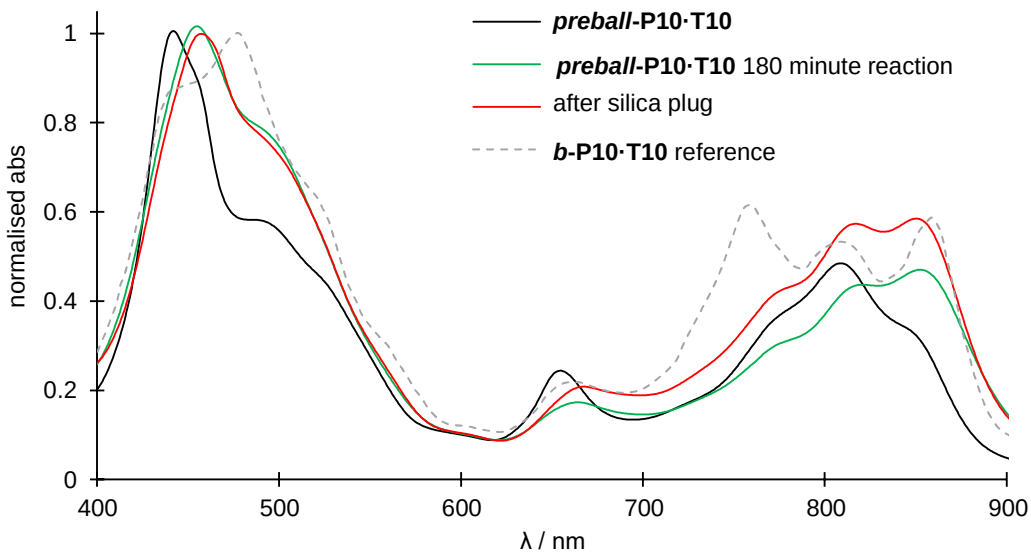


Figure 2.28. UV-vis-NIR of various stages of the attempted formation of ***b*-P10·T10** via ***preball*-P10·T10** ($CHCl_3$, 298 K).

Upon submitting to reaction conditions for 180 minutes, the UV-vis-NIR showed a broadening of the Q-band and slight structuring (Figure 2.28, green line), with a particular increase in the peak at 880 nm. It was inconclusive as to whether this corresponded to ***b*-P10·T10** (Figure 2.28, grey dashed line). Promisingly though, passing the reaction mixture through a silica plug produced little insoluble precipitate and the following UV-vis-NIR showed significant Q band character (Figure 2.28, red line), suggesting some conjugated oligomers had been produced in the reaction.

The product mixture was loaded onto the recycling GPC. Here, it became obvious there was significant polymer production, with broadened baseline spreading across the entire chromatogram shown in Figure 2.29. Initially, the peak at ~ 60 minutes looked to be well matched with a reference trace of ***b*-P10·T10**. At longer retention times, though, the peak broadened significantly and split into two.

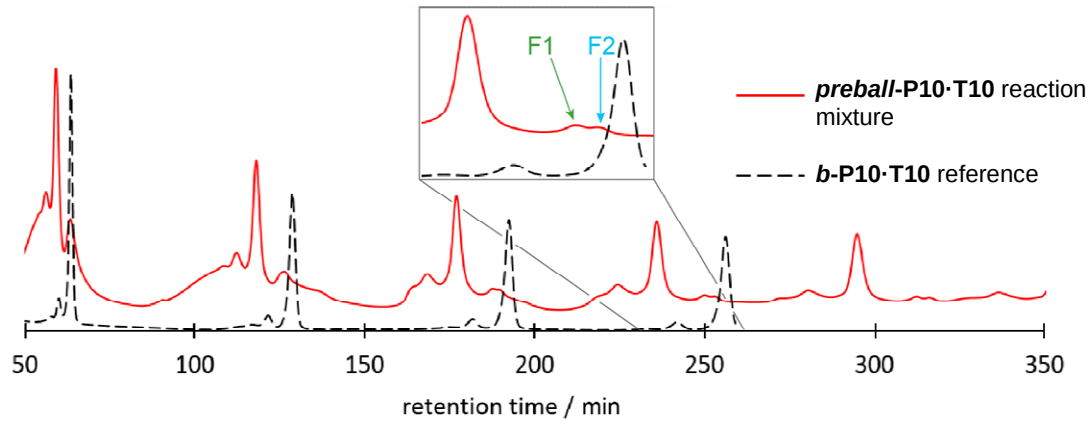


Figure 2.29. Recycling GPC (JAIGEL columns, toluene/1% pyridine, detection at 750 nm) of the isolated reaction mixture of ***preball*-P10·T10** and ***b*-P10·T10** reference. 5 cycles are presented. Inset shows most similar fractions to the reference which were isolated.

Isolation of these peaks resulted in enough material to take a UV-vis. Both of these showed structure similar to ***b*-P10·T10**, but neither were identical. From this result, then, it seems likely that the ***preball*-P10·T10** complex is not pre-organised enough to template the reaction efficiently (c.f. 14 mg of ball precursor via route shown in Scheme 2.2 afforded 1.5 mg of ball product[83]).

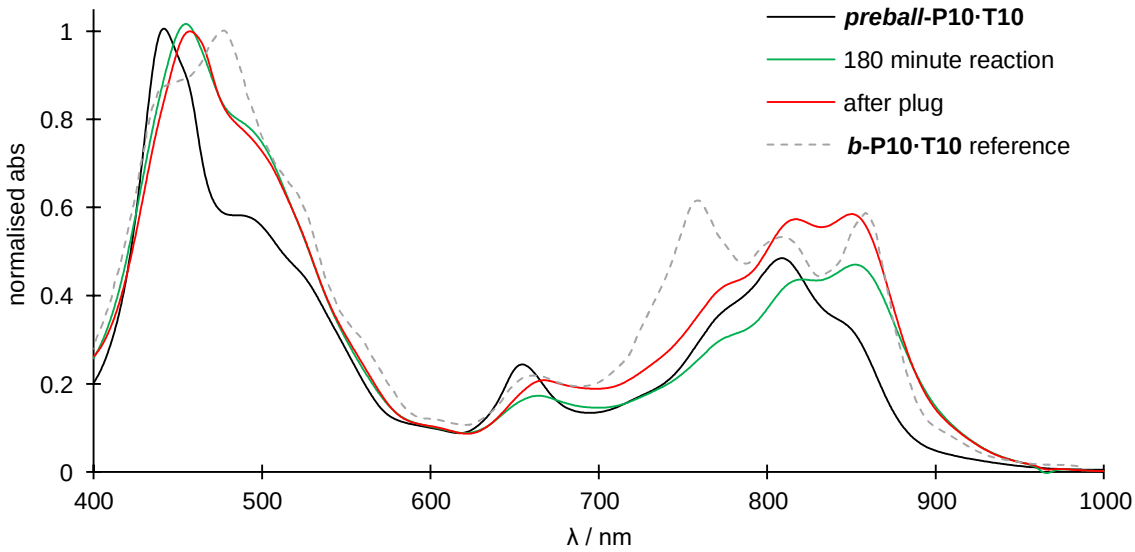


Figure 2.30. UV-vis-NIR analysis of the isolated fractions F1 and F2, compared to reference spectra of ***b*-P10·T10** and ***preball*-P10·T10** ($CHCl_3$, 298 K).

2.6 Conclusion

A 3D template, **T10**, was synthesised and characterised. Precursors ***x*-P5**, ***l*-P5** and ***preball*-P10** were synthesised and found to bind to the template with the expected stoichometries. Upon submitting to ball formation conditions, however, no ***b*-P10·T10** product was isolated. For ***l*-P5** and ***x*-P5**, significant insoluble material was afforded, most likely as a result of extensive polymer formation. In the case of ***x*-P5**, this could be

attributed to the formation of the incorrect coordination complexes required for ball formation as a result of the conformationally flexible template.

For ***l*-P5**, the orthogonality of the alkynes requires high directionality to avoid polymer formation. As the template is relatively flexible, it may be that the alkyne coupling is not particularly selective. The required 2:1 complex is also only stable at the correct ***l*-P5**:**T10** ratio of 2:1, with the complex preferring a 1:1 complex at higher concentrations of **T10**. As a result, any polymer formation will remove ***l*-P5** from the solution and drive the equilibrium conformation to an unfavourable one for ball formation, seeding more polymer and driving the equilibrium conformation further away again.

As expected, the binding of **T10** into ***preball*-P10** is strong. The nanoring moiety of ***preball*-P10** should overcome the conformational flexibility of **T10** by self-assembling the template in the cavity of the nanoring. Unfortunately, the template is kinetically trapped in two conformations as evidenced by NMR, with the unfavourable conformation for ball formation being statistically twice as likely to be formed. Attempts at equilibrating the two conformations were only moderately successful. Ball formation reactions did provide fractions with similar UV-vis-NIR spectra to ***b*-P10**, but only by trace amounts.

This work highlights an important aspect of porphyrin nanoring and nanoball chemistry: a good guest does not necessarily make a good template. We know **T10** binds strongly in the cavity of ***b*-P10**. In this case, however, the pre-organisation and entropic cost is paid during the synthesis of ***b*-P10** itself, and so the relatively flexible **T10** can reach thermodynamic minimum by binding inside the cavity of the nanoball. In the absence of reversible bond formation, such as those utilised in dynamic covalent chemistry,[127] the initial reactions will reflect the nature of the original **precursor:template** conformation, rather than the thermodynamic minimum of the product. As a result, conformational variability and flexibility in the template will only serve to reduce the efficacy of the reaction.

2.7 Future work

***b*-P10** remains an exciting synthetic target, and work is ongoing to repeat the synthesis of ***b*-P10** via the route outlined in Scheme 2.2. This synthesis will be repeated with 3,5-trihexysilyl solubilising groups (two meta THS groups compared to one) to avoid the

problem of product insolubility. We then hope to study the global (anti)aromaticity of the ball and explore the host-guest chemistry of the cavity. The ball derivative with a copper centre on the vertices of the ball is of particular interest. Unfortunately, it seem **T10** is unable to act as a template to form this from the ball precursors ***x*-P5**, ***l*-P5** or ***preball*-P10** which would be required to reach this synthetic target.

It seems likely that the reason **T10** did not work was due to its conformational flexibility, but the strong binding between the template and the nanoball is proof that **T10** could act as a template if the conformation was locked. With this in mind, one can design a new template, **T10***, that has the correct geometry for nanoball formation but with a locked conformation (with the exception of the minimal entropic contributions from rotation of the pyridyl 'arms', Figure 2.31 red arrows).

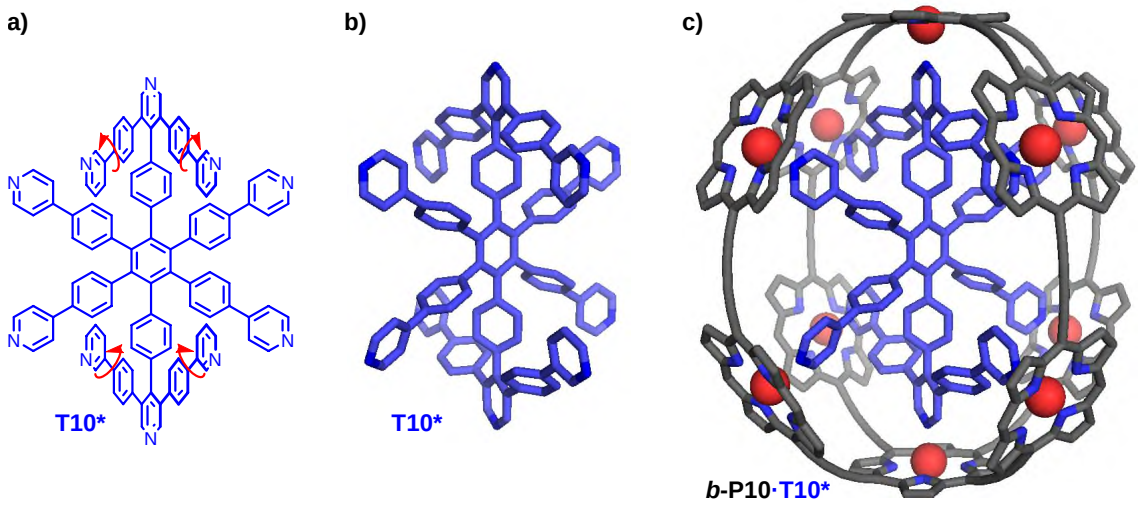
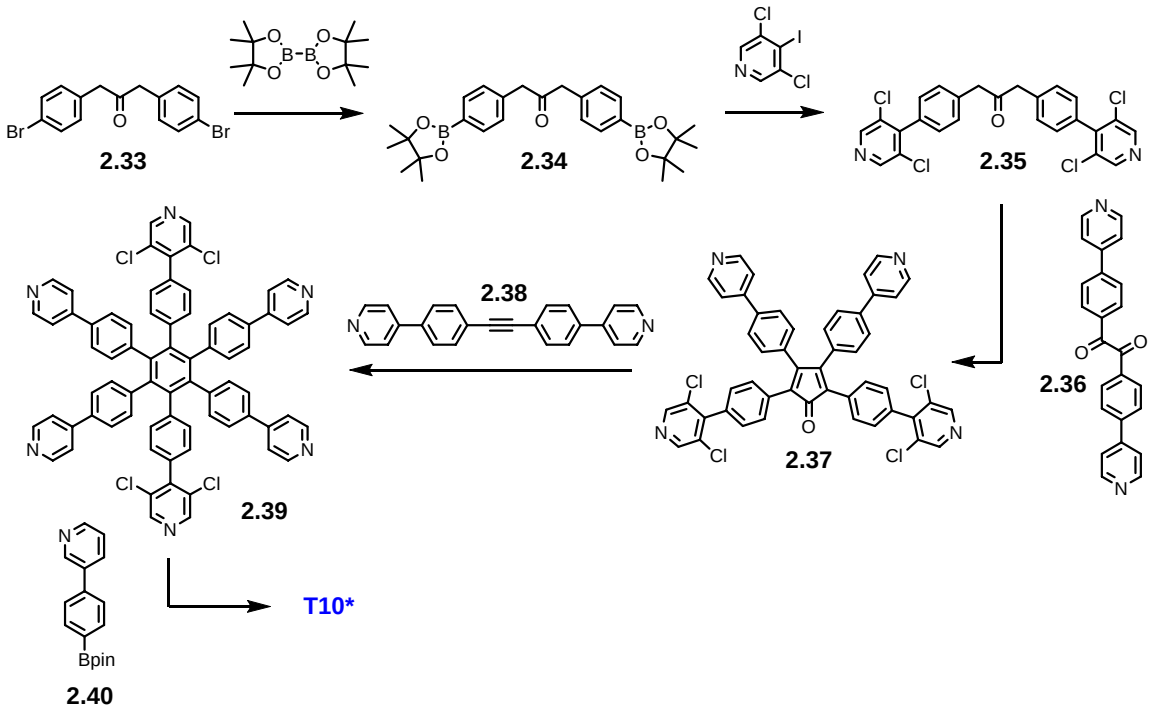


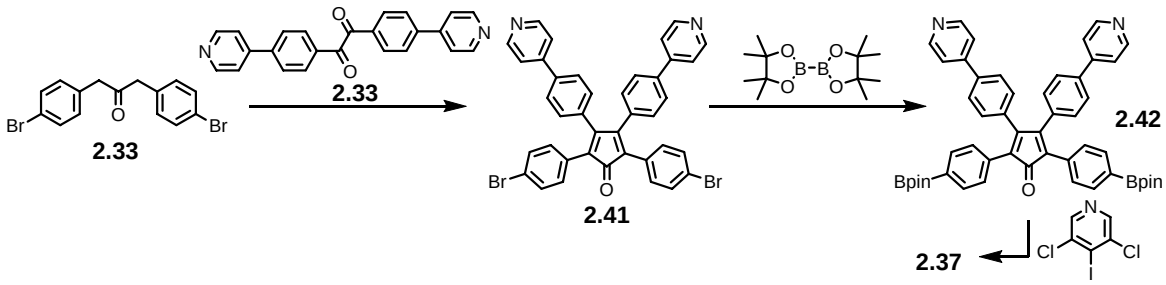
Figure 2.31. (a) Molecular structure of **T10*** showing degrees of rotation with red arrows. (b) 3D visualisation of **T10***. (c) Calculated structure (MOPAC, PM6) of ***b*-P10·T10***.

The proposed **T10*** could be synthesised using the following route shown in Scheme 2.13. Compounds **2.33**, **2.36**, **2.38**[128] and **2.40**[129] have all been reported previously. A Miyaura borylation of **2.33** would form ketone **2.34**. Coupling this with 3,5-dichloro-4-iodopyridine via a SMC would yield ketone **2.35**. An aldol condensation with benzil derivative **2.36** would form tetracyclone **2.37** which could then undergo a [4+2] Diels-Alder cyclisation to form **T6** derivative **2.39**. Finally, coupling **2.39** to **2.40** should afford **T10***.



Scheme 2.13. Proposed synthesis of **T10***.

One potential issue of the route proposed in Scheme 2.13 is the sensitivity of ketone **2.34** to the base required in the Miyaura borylation. A literature search suggested the tetracyclone is stable to Miyaura borylation conditions,[130] and as such the following route could be used instead to reach intermediate **2.37**.



Scheme 2.14. Alternative route to **2.37**.

T10* would not solve all of the problems identified in this chapter. For ***l*-P5** the asymmetry of the alkynes may still limit the yields of ball formation. For ***preball*-P10** the kinetic trapping of templates will still be expected to be a problem due to the **T6** moiety contained in **T10***.

x*-P5**, however, is more promising. If the problem with ***x*-P5** was that the conformational flexibility favoured complexes with bound trimer moieties (Figure 2.17, complexes **a** and **b**), then **T10 may favour ball formation as ***x*-P5** is more likely to bind

with all five porphyrin sites due to the restricted conformational flexibility and increased preorganisation of the template.

2.8 Experimental appendices

2.8.1 General experimental procedures

Dry toluene, $CHCl_3$, CH_2Cl_2, THF, NEt_3 and pyridine were obtained from the solvent drying system MBraun MBSPS-5-BenchTop under nitrogen atmosphere (H_2O content < 20 ppm as determined by Karl-Fischer titration). Diisopropylamine ($^iPr_2NH$/DIPA) was distilled freshly from CaH_2. Unless specified otherwise, all other solvents were used as commercially supplied. Flash chromatography was carried out on silica gel 60 under positive pressure. Analytical thin-layer chromatography was carried out on aluminium-backed silica gel 60 F254 plates. Visualization was achieved using UV light when necessary.

$^1H/^{13}C$ NMR spectra NMR data were recorded at 500/125 MHz using a Bruker AVII500 (with DUAL cryoprobe) or DRX500, or at 400/100 MHz using a Bruker AVII400 or AVIII400, or at 700 MHz using a Bruker AVIII700 (with TCI cryoprobe) at 298 K unless noted otherwise. Chemical shifts are quoted as parts per million (ppm) relative to residual $CHCl_3$ (δ_H 7.26 ppm for ^1H NMR and at δ_C 77.2 ppm for ^{13}C NMR) and coupling constants (J) are reported in Hertz. Multiplicity (s = singlet, d = doublet, t = triplet, q = quartet, and m = multiplet) and coupling constants were reported whenever possible. MALDI-ToF spectra were measured at the EPSRC UK National Mass Spectrometry Facility (NMSF, Swansea) using the Applied Biosystems Voyager DE-STR or at the University of Oxford using a Waters Micro MX spectrometer or Bruker Autoflex Speed utilizing dithranol or trans-2-[3-(4-tert-butylphenyl)-2-methyl-2-propenylidene]malononitrile (DCTB) as a matrix.

UV-vis-NIR absorbance measurements were recorded at 25 °C with a Perkin-Elmer Lambda 20 photospectrometer using quartz 1 cm cuvettes and temperature was controlled by a PTP-1 peltier unit from Perkin Elmer. Unless stated otherwise, measurements were carried out at 25 °C under ambient conditions. Fluorescence measurements were carried out using a calibrated Edinburgh Instruments FS5 spectrofluorometer equipped with double monochromators, with different wavelength-adapted gratings, and two detectors: a photomultiplier tube (PMT) R13456 from Hamamatsu for 250 – 950 nm, an analogue detector for 850 – 1700 nm. The exciting power of the xenon lamp after the monochromator was typically under 1 mW for the slits

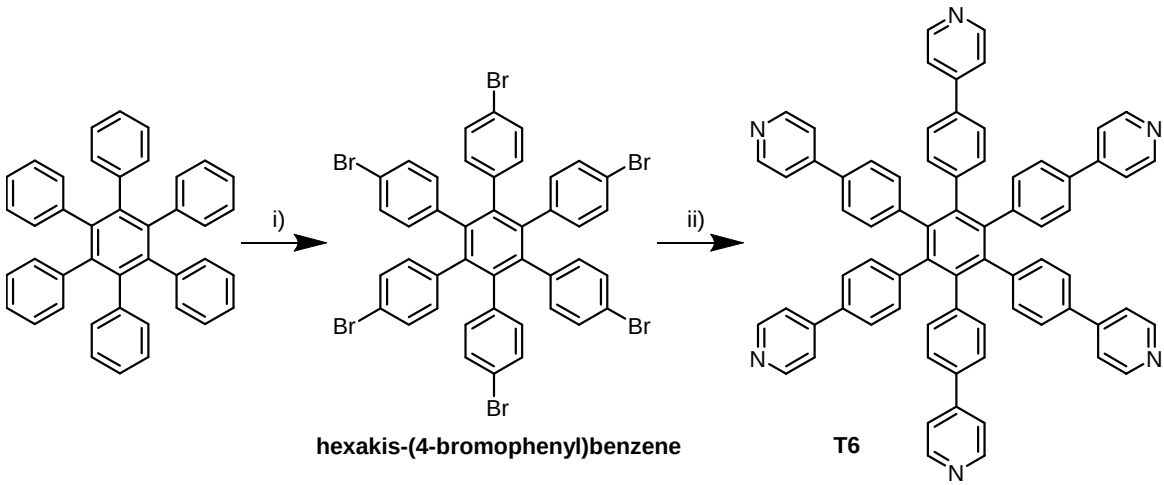
used. The calibration for wavelength accuracy, linearity of the detection system and determination of the spectral responsivity (spectral emission correction) was performed by Edinburgh Instruments.

Size exclusion chromatography (SEC) was carried out using Bio-Rad Bio-Beads S-X1 (40–80 µm bead size). Analytical GPC was performed using JAIGEL-3H-A (8φ×500) and JAIGEL-4H-A (8φ×500) columns in THF + 1% pyridine as eluent with a flow rate of 1.0 mL/min. Semi-preparative GPC was carried out on a Shimadzu Recycling GPC system equipped with a LC-20 AD pump, SPD-20A UV detector and a set of JAIGEL 3H (20 × 600 mm) and JAIGEL 4H (20 × 600 mm) columns in toluene + 1% pyridine as the eluent at a flow rate of 3.5 mL/min.

For reported procedures/syntheses, ^{1}H NMR was deemed sufficient evidence for the correct product and consequently more detailed characterisations were not undertaken.

2.8.2 Synthetic procedures

T6[49]



i)[49,131] Neat bromine (3 mL) was added dropwise, in 1 mL portions using a new 1 mL syringe each time, to finely ground hexaphenylbenzene (1.00 g, 1.87 mmol) in a 2-neck flask connected to a washing flask filled with dilute NaOH solution to trap the evolving HBr. The mixture was stirred for 45 min. EtOH (20 mL) was carefully added, while cooling the reaction flask in a dry-ice/acetone bath. The precipitate was collected by filtration, washed with ethanol, then washed with water. [The washings, i.e. the filtrate, not the product was quenched with $Na_2S_2O_3$ to destroy bromine.] The solid product was stirred

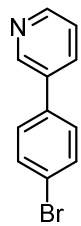
with CH_2Cl_2 (5–10 mL), then MeOH (5–10 mL), each time pipetting off and discarding the supernatant solution until this solution was colourless. The product was then dried under high vacuum to yield 1.28 g of white solid (67% yield).

^{1}H NMR (400 MHz, $CDCl_3$, 298 K): δ (ppm) 7.05 (pseudo d {AA'XX'}, J = 8.5 Hz, 12H), 6.61 (pseudo d {AA'XX'}, J = 8.3 Hz, 12H).

ii)[49] To a solution of hexakis-(4-bromophenyl)benzene (600 mg, 594 µmol) in diethylene glycol (18.0 mL) and THF (42 mL) was added $PdCl_2(PPh_3)_2$ (80 mg, 114 µmol). After addition of water (24 mL), $NaHCO_3$ (0.9 g, 10.72 mmol) and 4-pyridineboronic acid (1.76 g, 14.4 mmol), the mixture was deoxygenated and stirred at 70 °C for 5 days. Solvents were removed and the crude product was purified by column chromatography on flash silica gel (CH_2Cl_2 : MeOH : NEt_3; gradient 100:1:0.25 to 100:10:0.5) to give the template as a white solid. The solid product was washed with methanol and dried under high vacuum (188 mg, 31%).

^{1}H NMR (400 MHz, $CDCl_3$, 298 K): δ (ppm) 6.96 (pseudo d {AA'XX'}, *J* = 8.5 Hz, 12H), 7.18 (pseudo d {AA'XX'}, *J* = 8.5 Hz, 12H), 7.29 (pseudo d {AA'XX'}, *J* = 5.5 Hz, 12H), 8.36 (pseudo d {AA'XX'}, *J* = 5.5 Hz, 12H).

2.5[111]



3-Pyridine boronic acid (4.78 g; 38.9 mmol; 1.1 eq), 1-bromo-4-iodobenzene (10.0 g; 35.4 mmol; 1.0 eq), sodium carbonate (5.62 g; 53.0 mmol; 1.5 eq) and bis(triphenylphosphine)palladium(II) dichloride (1.23 g; 1.76 mmol; 0.05 eq) were charged in a 2-neck flask equipped with a reflux condenser and dissolved in a tetrahydrofuran/ethanol/water mixture (250 mL; 2/2/1 v/v/v). The solution was degassed by three freeze-pump-thaw, backfilled with argon and stirred at 60°C for 16 hours. The product was extracted with dichloromethane (3 x 100 mL), washed with brine and water, dried over magnesium sulphate, filtered and evaporated to dryness. The remaining catalyst impurities were removed by chromatography (SiO2; petroleum ether 3:1 ethyl acetate removes the catalyst, petroleum ether 1:1 ethyl acetate affords the

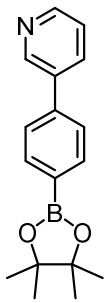
expected product) to yield 1 as a yellowish oil that slowly crystallises over weeks (5.2 g; 62%).

^{1}H NMR (400 MHz, $CDCl_3$, 298 K): δ (ppm) 8.79 (d, 1.8 Hz, 1H), 8.59 (dd, 4.8 & 1.8Hz, 1H), 7.79 (dt like ddd, 7.8 & 1.8 Hz, 1H), 7.56 (d, 8.4 Hz, 2H), 7.40 (d, 8.4 Hz, 2H), 7.32 (dd, 7.8 & 4.8 Hz, 1H).

^{13}C NMR (101 MHz, $CDCl_3$, 298 K): δ (ppm) 148.9, 148.1, 136.8, 135.5, 134.1, 132.3, 128.7, 123.6, 122.6.

MS (ESI): *m/z* = 236.0 ($C_{11}H_9BrN$, $[M+H]^+$ requires 235.98979).

2.6[112]



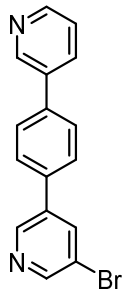
3-(4-Bromophenyl)pyridine **2.5** (1.5 g, 6.5 mmol), bis(pinacolateo)diboron (1.82 g, 7.2 mmol), KOAc (1.92 g, 19.6 mmol), [1,1'-bis(diphenylphosphino)ferrocene]dichloropalladium(II) (0.285 g, 0.35 mmol) were added to a flame-dried two necked flask equipped with reflux condenser. The flask was vacuumed for 30 minutes and then backfilled with argon. Dry DMF (25 mL) was added via syringe and the mixture was vigorously stirred at 80°C for 5 hours. The reaction mixture was filtered through a silica plug (washing with EtOAc) and concentrated under reduced pressure. Product was isolated by column chromatography (3:1 petroleum ether (40-60):EtOAc) giving a yellow oil with considerable contamination with bis(pinacolateo)diboron. The oil was further purified in a vacuum sublimation apparatus overnight (100 °C, 5 x 10^{-1} mbar) with **2.6** isolated as white crystals on the cold finger (1.34 g, 75% yield).

^{1}H NMR (400 MHz, $CDCl_3$, 298 K): δ (ppm) 8.87 (d, 1.92 Hz, 1H), 8.61 (dd, 4.86 & 1.62 Hz, 1H), 7.92 (d, 8.26 Hz, 2H), 7.90 (t, 1.92 Hz, 1H), 7.60 (d, 8.26 Hz, 2H), 7.38 (dd, 8.02 & 4.86 Hz, 1H), 1.37 (s, 12H) .

^{13}C NMR (100 MHz, $CDCl_3$, 298 K): δ (ppm) 148.7, 148.3, 140.4, 136.5, 135.5, 134.4, 126.4, 123.5, 83.9, 24.9.

MS (ESI): *m/z* = 282.2 ($C_{17}H_{21}BNO_2$, $[M+H]^+$ requires 282.16655).

2.7



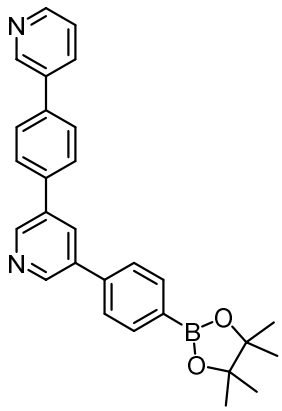
3,5-Dibromopyridine (4.52 g; 19 mmol), **2.6** (1.2 g; 4.23 mmol), sodium carbonate (0.76 g; 7.2 mmol) and bis(triphenylphosphine)palladium(II) dichloride (0.178 g; 0.25 mmol) were charged in a 2-neck flask equipped with a reflux condenser and dissolved in a tetrahydrofuran/ethanol/water mixture (60 mL; 2/2/1 v/v/v). The solution was degassed by 3 freeze-pump-thaw cycles, backfilled with argon and stirred at 60°C for 12 hours. The products were extracted with dichloromethane (3 x 100 mL), washed with water, brine and water again, dried over magnesium sulphate, filtered and evaporated to dryness. The mixture of catalyst, 3,5-dibromopyridine excess and **2.7** was separated by chromatography (SiO2; gradient of 200/1/0 to 200/1/4 dichloromethane/trimethylamine/methanol) to yield **2.7**, which was furthered purified by recrystallization from methanol to yield a white powder (0.80 g; 61%).

^{1}H NMR (400 MHz, $CDCl_3$, 298 K): δ (ppm) 8.90 (d, 2.0 Hz, 1H), 8.81 (d, 1.7Hz, 1H), 8.69 (d, 1.7 Hz, 1H), 8.64 (d, 4.6 Hz, 1H), 8.09 (t like dd, 1.7 Hz, 1H), 7.95 (d, 7.6 Hz, 1H), 7.73 (d, 8.4 Hz, 2H), 7.70 (d, 8.4 Hz, 2H), 7.43 (dd, 7.6, 4.6 Hz, 1H).

^{13}C NMR (101 MHz, $CDCl_3$, 298 K): δ (ppm) 149.8, 149.1, 148.4, 146.4, 138.4, 137.7, 136.9, 134.4, 128.1, 128.0, 127.9, 127.8, 123.8, 121.1.

HRMS (ESI): *m/z* = 311.01782 ($C_{16}H_{12}N_2Br$, $[M+H]^+$ requires 311.01784).

2.8



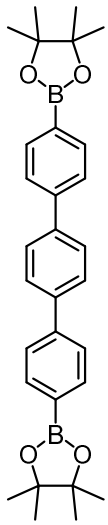
1,4-Bis(4,4,5,5-tetramethyl-1,3,2-dioxaborolan-2-yl)benzene (2.88 g, 8.72 mmol), **2.7** (0.68 g, 2.19 mmol), Na_2CO_3 (0.34 g, 3.21 mmol) and $Pd(PPh_3)_2Cl_2$ (0.08 g, 0.11 mmol) were charged in a 2-neck flask equipped with a reflux condenser and dissolved in a tetrahydrofuran/ethanol/water mixture (75 mL; 2:2:1 v:v:v). The solution was degassed by three freeze-pump-thaw cycles, backfilled with argon and stirred at 60°C for 30 minutes. The products were extracted with CH_2Cl_2 (3 x 100 mL), washed with water, brine and water again, dried over $MgSO_4$, filtered and evaporated to dryness. The mixture of catalyst, $PhBpin_2$ excess and product was separated by chromatography (CH_2Cl_2:MeOH:Pinacol 100:0:0.5 to 98:2:0.5 v:v:wt) to yield **2.8**, which was furthered purified by recrystallization from ethanol to yield a white powder (0.33 g, 35%).

^{1}H NMR (400 MHz, $CDCl_3$, 298 K): δ (ppm) 8.92 (m, 1H), 8.88 (m, 2H), 8.64 (dd, *J* = 4.8, 1.6 Hz, 1H), 8.11 (t, *J* = 2.2 Hz, 1H), 7.99 – 7.90 (m, 3H), 7.81 – 7.71 (m, 4H), 7.70 – 7.64 (m, 2H), 7.41 (dd, *J* = 7.9, 4.9, 1H), 1.38 (s, 12H).

^{13}C NMR (101 MHz, $CDCl_3$, 298 K): δ (ppm) 148.7, 148.2, 147.3, 147.1, 140.2, 137.7, 137.5, 136.6, 135.9, 135.6, 134.3, 132.8, 128.0, 127.9, 126.5, 123.7.

HRMS (ESI): *m/z* = 435.22407 ($C_{28}H_{28}O_2N_2B$, $[M+H]^+$ requires 435.22384).

2.9[115]



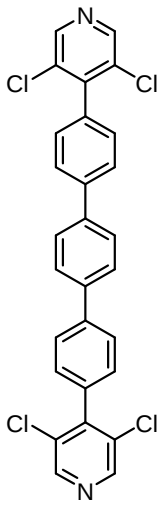
4,4''-Dibromo-p-terphenyl (410 mg, 1.08 mmol), bis(pinacolato)diboron (686 mg, 2.7 mmol), 1,1'-bis(diphenylphosphino)ferrocene]dichloropalladium(II) (176 mg, 0.216 mmol) and potassium acetate (636 mg, 6.48 mmol) were added to 1,4-dioxane (16.5 mL) in a dried Schlenk tube. The solution was degassed by 3 freeze-pump-thaw cycles, backfilled with argon and heated at 80 ˚C for 20 hours. The mixture was allowed to cool to room temperature, diluted with CH_2Cl_2, washed with water, dried with $MgSO_4$ and filtered. The resulting catalyst, starting material and product mixture was purified using chromatography (SiO_2, 8:2 CH_2Cl_2:Petrol ether). The collected product was recrystallized by layered addition of MeOH to CH_2Cl_2 to give **2.9** as a white fluffy solid (235 mg, 45%).

^{1}H NMR (400 MHz, $CDCl_3$, 298 K): δ (ppm) 7.93 (d, J = 8.1 Hz, 4H), 7.73 (s, 8H), 7.68 (d, J = 8.1 Hz, 4H), 1.39 (s, 24H).

^{13}C NMR (100 MHz, $CDCl_3$, 298 K): δ (ppm) 143.3, 140.2, 135.4, 127.6, 126.4, 83.9, 24.9.

MS (ESI): *m/z* = 506.6 ($C_{30}H_{36}B_2O_4Na$, $[M+Na]^+$ requires 505.27).

2.10



4,4''-Bis(4,4,5,5-tetramethyl-1,3,2-dioxaborolan-2-yl)-1,1':4',1''-terphenyl (**2.9**, 300 mg, 0.62 mmol), 3,5-dichloro-4-iodopyridine (682 mg, 2.49 mmol), dichlorobis(triphenylphosphine)palladium(II) (43.6 mg, 0.062 mmol) and cesium carbonate (811 mg, 2.49 mmol) were charged in a 2-neck flask attached to a reflux condenser and placed under an argon atmosphere. 1,4-dioxane (4.5 mL) and water (2.25 mL) were added and the mixture degassed by bubbling with N_2. The reaction was stirred overnight at 80 °C. The reaction mixture was diluted with water (50 mL) and extracted with CH_2Cl_2 (3 x 100 mL), before the organic layer was dried with

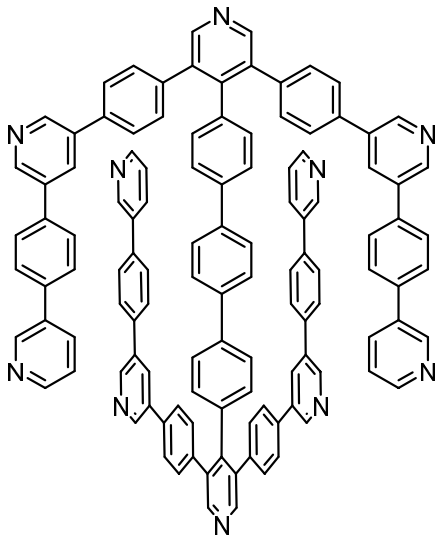
$MgSO_4$ and filtered. The mixture of catalyst, starting material and product was separated by chromatography (SiO_2, gradient of 1:1:0 to 100:0:1 CH_2Cl_2:petrol ether:MeOH) to give **2.10** (130 mg, 40%).

^{1}H NMR (400 MHz, $CDCl_3$, 298 K): δ (ppm) 8.63 (s, 4H), 7.81 (d, J = 8.4 Hz, 4H), 7.79 (s, 8H), 7.41 (d, J = 8.4 Hz, 4H).

^{13}C NMR (101 MHz, $CDCl_3$, 298 K): δ (ppm) 147.8, 146.3, 141.2, 139.6, 132.9, 132.0, 129.5, 127.7, 127.1.

HRMS (ESI): *m/z* = 523.01103 ($C_{28}H_{17}Cl_4N_2$, $[M+H]^+$ requires 523.01164).

T10



Caesium carbonate (250 mg; 768 µmol; 20 eq), **2.10** (20 mg; 38 µmol; 1 eq), **2.18** (167 mg; 384 µmol; 10 eq), palladium(II) acetate (1.7 mg; 7.7 µmol; 0.2 eq) and S-Phos (6.3 mg; 15.4 µmol; 0.4 eq) were charged in a 2-neck flask equipped with a reflux condenser and dissolved in a toluene/ethanol/water mixture (7 mL; 5/1/1 v/v/v). The solution was degassed by three freeze-pump-thaw cycles, backfilled with argon and stirred at 70°C for 3 hours. The products were extracted with CH_2Cl_2 (3 x 100 mL), washed with water, brine and water again, dried over magnesium sulphate, filtered and evaporated to dryness. The mixture of catalyst, deborylated excess of **2.8**, side-products and **T10** was separated by chromatography (SiO_2; CH_2Cl_2:MeOH 95:5 to 94:6). **T10** was furthered purified by other careful chromatography and recrystallization from a CH_2Cl_2/pentane mixture to yield a white powder (16 mg; 25%).

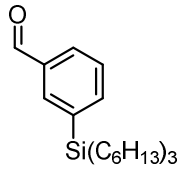
^{1}H NMR (400 MHz, CD_2Cl_2/5% CD_3OD, 298 K): δ (ppm) 8.77 (d, 2.1 Hz, 4H), 8.73 (d, 2.1 Hz, 4H), 8.70 (d, 2.1 Hz, 4H), 8.63 (s, 4H), 8.50 (dd, 4.8 & 2.1 Hz, 4H), 8.10 (t, 2.1 Hz, 4H), 7.95 (dt, 7.2 & 2.1 Hz, 4H), 7.71 (d, 8.2 Hz, 8H), 7.67 (d, 8.2 Hz, 8H), 7.54 (d, 8.2 Hz, 8H), 7.53

(s, 4H), 7.42 (dd, 7.2 & 4.8 Hz, 4H), 7.39 (d, 8.2 Hz, 4H), 7.28 (d, 8.2 Hz, 8H), 7.00 (d, 8.2 Hz, 4H).

^{13}C NMR (100 MHz, $CDCl_3$, 298 K): δ (ppm) 149.1, 147.7, 147.1, 146.3, 146.1, 146.0, 139.1, 138.9, 137.5, 137.2, 136.9, 136.2, 136.2, 136.1, 136.0, 135.9, 135.1, 134.8, 132.9, 130.9, 130.5, 127.7, 127.6, 126.9, 126.7, 126.1, 123.9.

HRMS (ESI): *m/z* = 1610.63868 ($C_{116}H_{77}N_{10}$, $[M+H]^+$ requires 1610.63607).

2.12



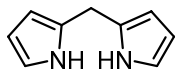
To a stirring solution of 1,3-dibromobenzene (9.00 g, 40.1 mmol) in Et_2O (318 mL) at -20 °C, was added *n*-butyl lithium (1.6 M in hexane, 26.3 mL, 42.1 mmol) dropwise, under argon atmosphere. The solution was stirred for 90 min before adding trihexylsilylchloride (17.1 mL, 44.1 mmol) dropwise via a syringe. The solution was allowed to warm to room temperature. After stirring for another 90 min, the reaction mixture was washed with water, dried over $MgSO_4$ and filtered. The solution was concentrated and passed through a silica plug with petrol ether. The volatiles were removed *in vacuo* affording a clear yellow oil that was redissolved in dry Et_2O (178 mL) to which *n*-butyl lithium (1.6 M in hexane, 35 mL, 56 mmol) was added dropwise under Ar at 0°C. The solution was stirred at this temperature for 30 min and then at room temperature for 90 min. *N,N*-Dimethylformamide (5.3 mL, 89.8 mmol) was added and the mixture was stirred for 1 hr. Aqueous saturated ammonium chloride solution (250 mL) was added and the organic layer was separated. The aqueous layer was extracted with Et_2O. The combined organic layer was washed with an aqueous solution of $NaHCO_3$ and with water, dried over $MgSO_4$ and filtered. The crude product was purified by column chromatography on silica gel eluting with a gradient of CH_2Cl_2 and petrol (starting from 0% to 10% CH_2Cl_2). The solvent was removed to give 3-(trihexylsilyl)benzaldehyde **2.12** (7.65 g, 49%) as a pale yellow oil.

^{1}H NMR (400 MHz, $CDCl_3$, 298 K): δ (ppm) 10.03 (s, 1H), 7.97 (d, *J* = 1.5 Hz, 1H), 7.84 (dt, *J* = 7.6, 1.6 Hz, 1H), 7.74 (dt, *J* = 7.2, 1.4 Hz, 1H), 7.51 (t, *J* = 7.5 Hz, 1H), 1.63-0.80 (39H, m, THS).

^{13}C NMR (101 MHz, $CDCl_3$, 298 K): δ (ppm) 193.0, 140.2, 139.8, 135.6, 135.5, 129.9, 128.3, 33.4, 31.5, 23.7, 22.6, 14.1, 12.3.

HRMS (ESI): *m/z* = 389.32350 ($C_{25}H_{45}OSi$, $[M+H]^+$ requires 389.32342).

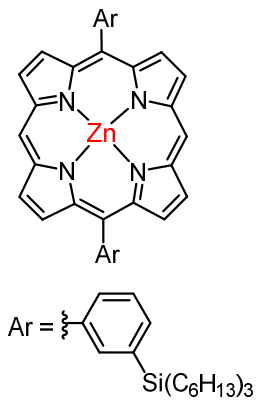
2.13[9]



Formaldehyde (33% w/w solution in water, 10.8 mL, 120 mmol) was added to pyrrole (200 mL, 2.88 mol) and the solution degassed by repeated evacuation and stirring under N_2. Trifluoroacetic acid (1.08 mL, 6.18 mmol) was added by syringe under vigorous stirring and in the N_2 atmosphere. The reaction was allowed to proceed for 5 minutes before CH_2Cl_2 (200 mL) was added, followed immediately by Na_2CO_3 (aq., sat., 200 mL). The organic layer was washed with Na_2CO_3 (aq) (sat., 2 × 200 mL) and water (200 mL), then dried over Na_2SO_4. The solvent and then excess pyrrole were removed on the rotovapor. Distillation of the oily residue in a Kugelrohr apparatus (220 °C, 10 mbar) yielded the product as a white crystalline solid (9.45 g, 52%).

^{1}H NMR (400 MHz, $CDCl_3$, 298 K): δ (ppm) 7.91 (br s, 2H), 6.67 (m, 2H), 6.17 (m, 2H), 6.04 (m, 2H), 3.96 (s, 2H).

2.14



3-(Trihexylsilyl)benzaldehyde **2.12** (5.28 g, 13.6 mmol) and dipyrromethane (1.98 g, 13.6 mmol) were dissolved in a fresh Winchester bottle of CH_2Cl_2 (2.5 L). The solution was degassed by bubbling the solution with N_2 for 20 minutes and stirring under nitrogen. Trifluoroacetic acid (1.8 mL, 27.2 mmol) was added and the reaction mixture stirred in the dark for 3 hours. DDQ (4.63 g, 20.4 mmol) was added and stirring continued for 20 minutes. After quenching of the acid by addition of triethylamine (14 mL) the mixture was concentrated to a volume of about 300 mL on the rotary evaporator and passed over a silica plug (CH_2Cl_2). The product was redissolved in $CHCl_3$ (300 mL). $Zn(OAc)_2{\cdot}2H_2O$ (4.04 g, 19.0 mmol) was dissolved in methanol (44 mL) and added to the reaction mixture. The reaction

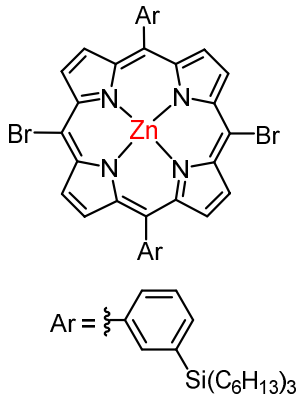
was stirred at 40 ˚C for 2 h. The mixture was passed through a short plug of silica gel using 1% pyridine in CH_2Cl_2 to give **2.15** as a pink oil (4.34 g, 59%).

^{1}H NMR (400 MHz, $CDCl_3$, 298 K): δ (ppm) 10.24 (2H, s, H_g), 9.39 (4H, d, *J* = 4.4 Hz, H_f), 9.09 (4H, d, *J* = 4.4 Hz, H_e), 8.39 (2H, m, H_c), 8.22 (2H, m, H_d), 7.90 (2H, m, H_a), 7.75 (2H, m, H_b), 1.63-0.80 (78H, m, THS).

MS (MALDI-ToF): *m/z* = 1088.803 ($C_{68}H_{96}N_4Si_2Zn$, $[M]^+$ requires 1088.64649).

2.15

To a solution of zinc porphyrin **2.14** (2.00 g, 1.83 mmol) in $CHCl_3$ (283 mL) and pyridine (28 mL) was added freshly recrystallized *N*-bromosuccinimide (0.653 g, 3.67 mmol). After stirring for 5 minutes acetone (44 mL) was added to quench the reaction. The mixture was passed through a short plug of silica gel using $CHCl_3$ to give **2.15** as a green oil (2.28 g, 99%).

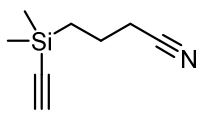


^{1}H NMR (400 MHz, $CDCl_3$ /~1% pyridine-d_5, 298 K): δ (ppm) 9.66 (d, *J* = 4.7 Hz, 4H), 8.87 (d, *J* = 4.7 Hz, 4H), 8.25 (m, 2H), 8.12 (m, 2H), 7.88 (m, 2H), 7.72 (m, 2H), 1.55-0.81 (m, 78H).

MS (MALDI-ToF): *m/z* = 1244.656 ($C_{68}H_{94}Br_2N_4Si_2Zn$, $[M]^+$ requires 1244.4675).

UV-vis ($CHCl_3$): λ_{max}/nm (log(ε)) 427 (5.39), 568 (4.02), 609 (3.78).

2.16[118]



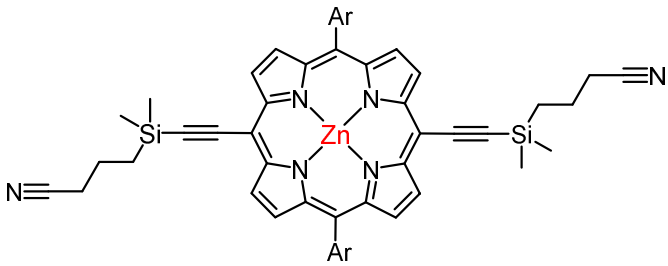
Chloro(3-cyanopropyl)dimethylsilane (3.64 g, 22.5 mmol) was added to ethynyl magnesium bromide (0.5 M in THF, 50 mL, 25 mmol) in THF under argon atmosphere. The mixture was heated to reflux and stirred for one hour. The reaction mixture was diluted with diethyl ether (50 mL), water (50 mL) and HCl (0.1 mL). The organic layer was separated and washed with H_2O (3 x 50 mL), dried with $MgSO_4$, filtered and passed through a silica plug (CH_2Cl_2). Volatiles were removed *in vacuo* yielding the product as an orange oil (3.07 g, 90%).

^{1}H NMR (400 MHz, $CDCl_3$, 298 K): δ (ppm) 2.41 (s, 1H), 2.40 (t, J = 7.1 Hz, 2H), 1.82- 1.70 (m, 2H), 0.81-0.75 (m, 2H), 0.19 (s, 6H).

^{13}C NMR (100 MHz, $CDCl_3$, 298 K): δ (ppm) 119.7, 94.7, 88.3, 20.6, 20.5, 15.5, -2.0.

MS (CI): *m/z* = 152.0894 ($C_8H_{14}NSi$, $[M]^+$ requires 152.0896).

2.17

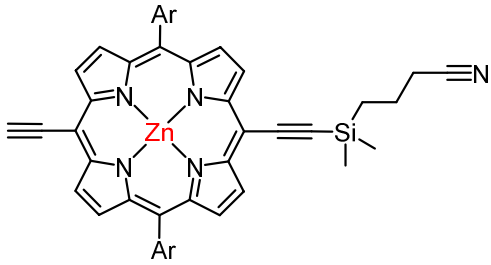


Pd_2dba_3 (294 mg, 0.32 mmol), CuI (184 mg, 0.96 mmol), PPh_3 (252 mg, 0.96 mmol) and **2.15** (4 g, 3.2 mmol) were placed under argon. Dry toluene (105 mL) and dry *i*-Pr_2NH (105 mL) were added and the reaction mixture deoxygenated by three vacuum freeze/pump/thaw cycles. Cyanopropyldimethylsilyl acetylene **2.16** (1.45 g, 9.60 mmol) was added by syringe. The reaction mixture was stirred at 50 °C for 3 h. The solvents were removed and the residue was passed through a short silica gel column (1% pyridine in $CHCl_3$) to give **2.17** as a green oil (4.45 g, 100%).

^{1}H NMR (400 MHz, $CDCl_3$/~1% pyridine-d_5, 298 K): δ (ppm) 9.62 (d, *J* = 4.6 Hz, 4H), 8.89 (d, *J* = 4.6 Hz, 4H), 8.31 – 8.22 (m, 2H), 8.13 (m, 2H), 7.89 (m, 2H), 7.73 (m, 2H), 2.57 (t, *J* = 6.9 Hz, 4H), 2.21 – 2.06 (m, 4H), 1.54-0.83 (M, 82H), 0.60 (s, 12H).

MS (MALDI-ToF): *m/z* = 1389 ($C_{84}H_{118}ZnN_6Si_4$, M+ requires 1389).

2.18

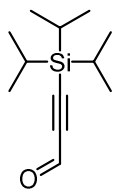


Bis-CPDMS-porphyrin **2.17** (1.87 g, 1.35 mmol) was dissolved in $CHCl_3$ (118 mL) and ethanol (1.18 mL). Tetra-*n*-butylammonium fluoride (1.35 mL, 1.0 M solution in THF, 1.35 mmol) was added dropwise to the stirred solution. The progress of the reaction was monitored by TLC until an optimal product mixture was reached. The mixture immediately was passed through a short plug of silica gel (1% pyridine in $CHCl_3$). Column chromatography (10:1:1 to 6:1:1 = petroleum ether:ethyl acetate:pyridine) gave **2.18** as a green oil (720 mg, 42%), fully deprotected porphyrin (310 mg, 20%) and starting material (260 mg, 14%).

^{1}H NMR (400 MHz, $CDCl_3$/~1% pyridine-d_5, 298 K): δ (ppm) 9.66 (d, *J* = 4.5 Hz, 2H), 9.60 (d, *J* = 4.5 Hz, 2H), 8.87 (d, *J* = 4.5 Hz, 4H), 8.27 (m, 2H), 8.16 – 8.09 (m, 2H), 7.88 (m, 2H), 7.72 (m, 2H), 4.15(s, 1H), 2.57 (t, *J* = 6.9 Hz, 2H), 2.22 – 2.07 (m, 2H), 1.56-0.82 (m, 80H), 0.61 (s, 6H).

MS (MALDI-ToF): *m/z* = 1265.814 ($C_{78}H_{107}N_5Si_3Zn$, $[M]^+$ requires 1264.379).

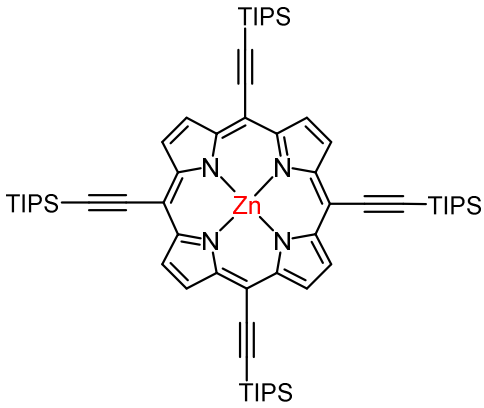
2.19[122,132]



n-Butyl lithium (44 mL, 2.5 M solution in hexane, 71 mmol) was added dropwise to a stirred solution of triisopropylsilylacetylene (15 mL, 67.5 mmol), in dry THF (150 mL). The mixture was for 20 minutes at 0 ˚C. The mixture was then cooled to -78 ˚C before dry DMF (4.9 mL, 71 mmol) was added by cannula transfer. The mixture was allowed to warm to 0 ˚C and stirred for 20 minutes, before stirring for an hour at room temperature. The reaction mixture was cooled to 0 ˚C and quenched with H_2SO_4 (5 % aq., 120 mL). Saturated $NaHCO_3$ solution was added to the reaction mixture until the pH of the reaction mixture was 5. The mixture was extracted with CH_2Cl_2 (4 x 50 mL) then washed with H_2O (100 mL). The solution was dried over $MgSO_4$ and concentrated before being passed over a short silica plug (10 % ethyl acetate in petroleum ether). Removal of the solvents yielded the product as a yellow oil (12.63 g, 89%).

^{1}H NMR (400 MHz, $CDCl_3$, 298 K): δ (ppm) 9.20 (s, 1H, -CHO), 1.27-1.00 (m, 21H).

14[119,120]

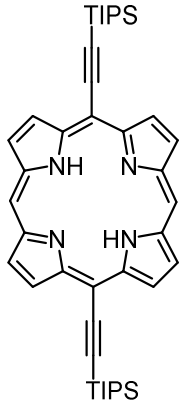


$BF_3{\cdot}OEt_2$ (0.11 mL) was added to a stirred solution of aldehyde **2.19** (1.2 g, 5.7 mmol) and pyrrole (0.38 g, 5.7 mmol) in CH_2Cl_2 (1 L) at −78 °C under an argon atmosphere. It was then allowed to warm slowly to room temperature. Stirring was continued for an additional 1 h and DDQ (0.95 g, 4.25 mmol) was added. After ten minutes, the solvent was removed under vacuum and the residue was purified by a silica plug (petroleum ether). The isolated free-base porphyrin (0.583 g, 0.57 mmol) was redissolved in $CHCl_3$ (56 mL). $Zn(OAc)_2{\cdot}2H_2O$ (0.55 g, 2.55 mmol) in MeOH (4 mL) was added and the mixture was refluxed overnight. The solution was evaporated and passed through a short silica plug, eluting with a mixture of $CHCl_3$/1% pyridine. The solvent was removed and the product recrystallized from DCM/MeOH to give pure zinc porphyrin (0.37 g, 24%) as pink crystals.

^{1}H NMR (400 MHz, $CDCl_3$/∼1% pyridine-d_5, 298 K): δ (ppm) 9.68 (s, 8H, β), 1.52 – 1.40 (m, 84H, TIPS-H).

MS (MALDI-ToF): *m/z* = 1092.744 ($C_{64}H_{92}N_4Si_4Zn$, $[M]^+$ requires 1092.569).

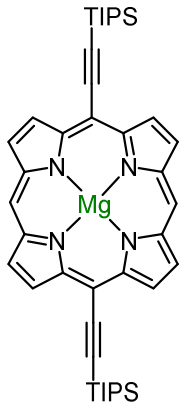
2.21[133]



Dipyrromethane **2.13** (1.47 g, 10.1 mmol) was dissolved in CH_2Cl_2 (600 mL). The solution was degassed and kept under N_2 atmosphere. To this solution triisopropylsilylpropynal **2.19** (2.26 mL, 10.1 mmol) was added followed by $BF_3{\cdot}Et_2O$ (0.40 mL, 3.2 mmol). The mixture was stirred for 45 min in the dark under N_2 atmosphere, over which time it turned dark blue. DDQ (3.44 g, 15.2 mmol) was then added and the mixture stirred for 10 min. The resulting brown solution was filtered through three consecutive plugs of silica gel with CH_2Cl_2 as the eluent, to remove DDQ residues and tar. After removal of the solvent *in vacuo*, recrystallization from CH_2Cl_2/MeOH yielded the product (0.74 g, 20%) as a purple solid.

^{1}H NMR (400 MHz, $CDCl_3$, 298 K): δ (ppm) 10.14 (2H, s, H1), 9.73 (4H, d, J = 4.6 Hz, H3), 9.32 (4H, d, J = 4.6 Hz, H2), 1.52-1.46 (42H, m, H4), -2.62 (2H, s, H5).

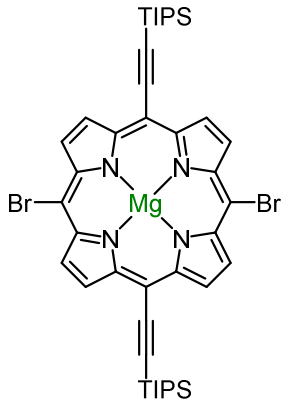
2.22[122]



A solution of the free-base porphyrin **2.21** (700 mg, 1.04 mmol) and MgI_2 (1.45 g, 5.2 mmol) in pyridine (84 mL) and Et_3N (4.2 mL) was refluxed overnight under nitrogen atmosphere, during which time the mixture became bright green. The solvent was removed *in vacuo* and the residue re-dissolved in CH_2Cl_2 and filtered over a silica plug (1% pyridine in CH_2Cl_2). Solvent evaporation afforded the product (800 mg, 99%) as a one-to-one complex with pyridine as a dark green/purple solid.

^{1}H NMR (400 MHz, $CDCl_3$/~1% pyridine-d_5, 298 K): δ (ppm) 10.13 (s, 2H), 9.81 (d, *J* = 4.3 Hz, 4H), 9.32 (d, *J* = 4.3 Hz, 4H), 1.54-1.47 (42H, m).

2.23[122]

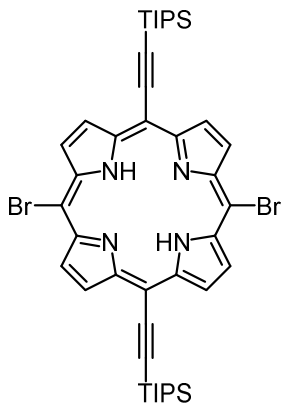


A solution of porphyrin **2.22** (500 mg, 0.65 mmol) in dry $CHCl_3$ (50 mL) and pyridine (0.5 mL) was bubbled with N_2 before *N*-bromosuccinimide (185 mg, 1.04 mmol) was added under magnetic stirring. Two consecutive 40 mg batches of *N*-bromosuccinimide were added at 2 hour intervals and the reaction monitored by MALDI mass spectrometry. Upon completion, the reaction was quenched with acetone (16 mL). The solvent was removed *in vacuo* and the residue was purified by column chromatography (4:1 PE 40-60:CH_2Cl_2, + 1% pyridine) affording the product (440 mg, 79%) as a blue solid.

^{1}H NMR (400 MHz, $CDCl_3$/~1% pyridine-d_5, 298 K): δ (ppm) 9.65 (d, *J* = 4.6 Hz, 4H), 9.61 (d, *J* = 4.6 Hz, 4H), 1.56 – 1.43 (42H, m).

MS (MALDI-ToF): *m/z* = 849.854 ($C_{42}H_{50}Br_2MgN_4Si_2$, $[M]^+$ requires 850.177).

2.24[122]



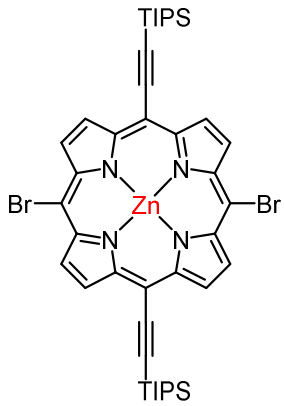
To a solution of porphyrin **2.23** (440 mg, 0.52 mmol) in $CHCl_3$ (20 mL) was added dichloroacetic acid (335 µL, 2.6 mmol) under magnetic stirring. The reaction was monitored by TLC (10:1:1 PE 40-60:EtOAc:pyridine). Upon completion (10 min), the solution was washed with water, concentrated and filtered through silica (2:1 PE 40-60:CH_2Cl_2 to pure CH_2Cl_2). The solvent was removed *in vacuo* to afford the free-base porphyrin (290 mg, 67%) as a green/purple solid.

^{1}H NMR (400 MHz, $CDCl_3$, 298 K): δ (ppm) 9.40 (d, *J* = 4.7 Hz, 4H), 9.32 (d, *J* = 4.8 Hz, 4H), 1.58-1.52 (m, 42H), -3.96 (s, 2H).

MS (MALDI-ToF): *m/z* = 829.548 ($C_{42}H_{52}Br_2N_4Si_2$, $[M]^+$ requires 828.208).

2.25[122]

To a solution porphyrin **2.24** (290 mg, 0.35 mmol) in $CHCl_3$ (43 mL) was added a solution of $Zn(OAc)_2{\cdot}2H_2O$ (384 mg, 1.75 mmol) in methanol (3 mL) and the reaction mixture was refluxed for 2 h. The solution was concentrated and the material filtered over a short silica plug ($CHCl_3$). The volatiles were removed *in vacuo* to afford the zinc porphyrin as a 1:1 complex with pyridine (330 mg, 100%) as a green/purple solid.

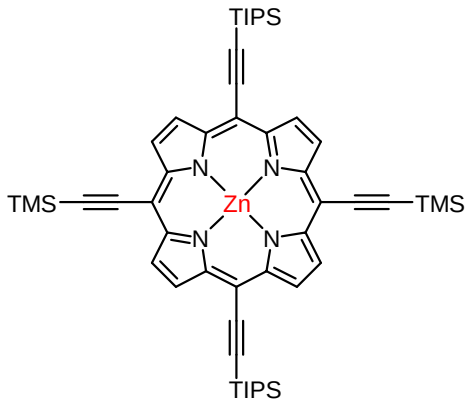


^{1}H NMR (400 MHz, $CDCl_3$/~1% pyridine-d_5, 298 K): δ (ppm) 9.54 (d, *J* = 4.7 Hz, 4H), 9.48 (d, *J* = 4.7 Hz, 4H), 1.52-1.45 (42H, m).

MS (MALDI-ToF): *m/z* = 892.6 ($C_{42}H_{50}Br_2ZnN_4Si_4$, $[M]^+$ requires 892.1).

2.26[122]

In a 100-mL two-necked flask were placed porphyrin **2.25** (320 mg, 0.36 mmol), Pd_2dba_3 (65.9 mg, 0.072 mmol), CuI (14 mg, 0.072 mmol) and PPh_3 (37.7 mg, 0.14 mmol). Toluene (21 mL) and *i*-Pr_2NH (10.5 mL) were added and the mixture was deoxygenated by three freeze-pump-thaw cycles. Trimethylsilylacetylene (0.154 mL, 1.08 mmol) was added and the reaction mixture was stirred at 50 °C for 2 h. after which TLC showed the reaction was completed. The solvent was removed *in vacuo* and the residue was purified by column chromatography (3:1 to 1:1 PE:CH_2Cl_2) affording the desired product (290 mg, 86%) as a green/purple solid.

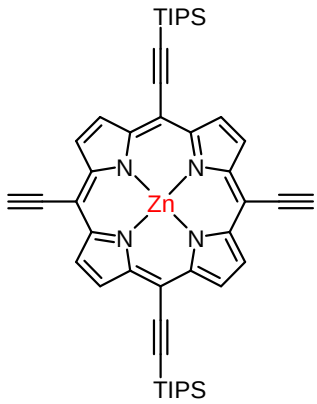


^{1}H NMR (400 MHz, $CDCl_3$/~1% pyridine-d_5, 298 K): δ (ppm) 9.66 (d, *J* = 4.3 Hz, 4H), 9.63 (d, *J* = 4.5 Hz, 4H), 1.48 – 1.45 (m, 42H), 0.62 (s, 18H).

MS (MALDI-ToF): *m/z* = 925.080 ($C_{42}H_{50}Br_2ZnN_4Si_4$, $[M]^+$ requires 926.381).

2.27

Porphyrin **2.26** (73 mg, 0.078 mmol) was dissolved in a mixture of THF (5 mL) and methanol (5 mL). K_2CO_3 (0.22 g, 1.57 mmol) was added and the mixture was stirred at room temperature for 30 min. The mixture was passed through a short plug of silica gel (1% pyridine in $CHCl_3$) to give a purple solid (60 mg, 100%).

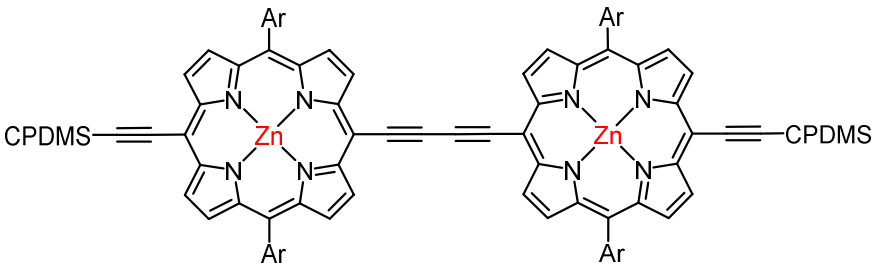


^{1}H NMR (400 MHz, $CDCl_3$/~1% pyridine-d_5, 298 K): δ (ppm) 9.66 (d, *J* = 4.5 Hz, 4H), 9.63 (d, *J* = 4.6 Hz, 4H), 4.15 (s, 2H), 1.48 – 1.41 (m, 42H).

MS (MALDI-ToF): *m/z* = 781.467($C_{46}H_{52}N_4Si_2Zn$, $[M]^+$ requires 780.302).

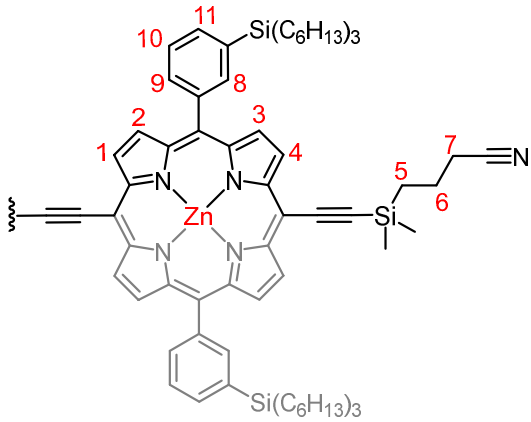
***l*-P2**

***l*-P2** was isolated as a side product from any Glaser coupling reaction with **2.18.** ***l*-P2** was also synthesised on purpose with the following procedure:



Porphyrin **2.18** (260 mg, 0.21 mmol) was dissolved in toluene (21 mL). A catalyst solution of $PdCl_2(PPh_3)_2$ (7.3 mg, 0.011 mmol), CuI 20.9 mg, 0.11 mmol) and 1,4-benzoquinone (45.4 mg, 0.42 mmol) in toluene (21 mL) and freshly distilled *i*-Pr_2NH (10.5 mL) was added and the mixture stirred at room temperature for 1 hour. The reaction mixture was passed through a short silica plug ($CHCl_3$/10% pyridine), followed by size exclusion chromatography on Biobeads SX-1 (toluene/1% pyridine) giving ***l*-P2** as a dark blue solid (196 mg, 74%).

^{1}H NMR (500 MHz, $CDCl_3$/~1% pyridine-d_5, 298 K): δ (ppm) 9.89 (d, J = 4.7 Hz, 4H, H1), 9.61 (d, J = 4.5 Hz, 4H, H4), 8.95 (d, J = 4.7 Hz, 4H, H2), 8.88 (d, J = 4.5 Hz, 4H, H3), 8.32 (d, J = 11.0 Hz, 4H, H8), 8.19 (m, 4H, H9), 7.91 (d, J = 7.4 Hz, 4H, H11), 7.76 (m, 4H, H10), 2.59 (t, J = 7.0 Hz, 4H, H7), 2.22 – 2.11 (m, 4H, H6), 1.55 – 0.55 (m, 172H, Si-CH + H5).

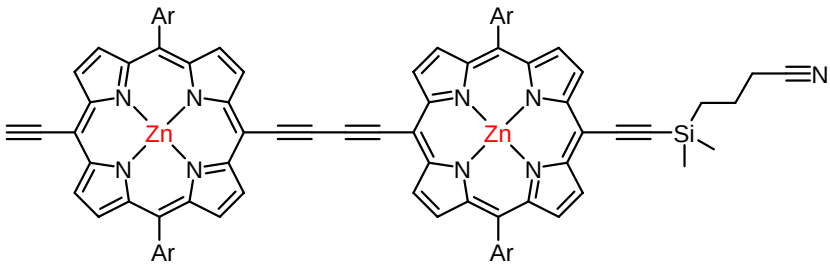


UV-vis-NIR ($CHCl_3$): λ_{max}/nm (ε/10^5 $M^{-1}cm^{-1}$) = 727 (0.76), 665 (0.55), 581 (0.24), 491 (1.6), 456 (2.9), 441 (2.4).

MS (MALDI-ToF): *m/z* = 2527.7 ($C_{156}H_{212}N_{10}Si_6Zn_2$, $[M]^+$ requires 2526.7).

2.28

Porphyrin dimer ***I*-P2** (203 mg, 0.080 mmol) was dissolved in $CHCl_3$ (7.3 mL) and ethanol (0.15 mL).



Tetra-*n*-butylammonium fluoride (0.08 mL, 1.0 M solution in THF, 0.080 mmol) was added dropwise to the stirred solution. The progress of the reaction was monitored by TLC until an optimal product mixture was reached. The mixture immediately was passed through a short plug of silica gel (1% pyridine in $CHCl_3$). Column chromatography (10:1:1 to 6:1:1 = petroleum ether:ethyl acetate:pyridine) gave **2.28** as a blue solid (30 mg, 16%).

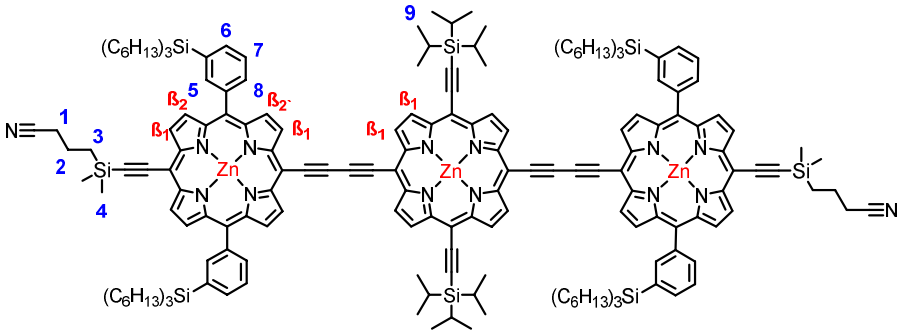
^{1}H NMR (400 MHz, $CDCl_3$/~1% pyridine-d_5, 298 K): δ (ppm) 9.85 – 9.75 (m, 4H, β_{Ac}), 9.58 (d, J = 4.6 Hz, 2H, β_{Ac}), 9.51 (d, J = 4.6 Hz, 2H, β_{Ac}), 8.86 (m, 4H, β_{Ar}), 8.81 – 8.72 (m, 4H,

β_{Ar}), 8.27 – 8.18 (m, 4H), 8.09 (m, 4H), 7.82 (m, 4H), 7.67 (m, 4H), 4.09 (s, 1H, Acetylene), 2.50 (t, J = 7.0 Hz, 2H, CPDMS-CH_2), 2.15 – 2.03 (m, 2H, CPDMS-CH_2), 1.55 – 0.27 (m, 164H, SiH, CPDMS-CH_2).

MS (MALDI-ToF): *m/z* = 2365.96 ($C_{150}H_{201}N_9Si_5Zn_2$, $[M]^+$ requires 2396.343).

2.29

Porphyrin **2.27** (60 mg, 0.083 mmol) and porphyrin **2.18** (525 mg, 0.42 mmol) were dissolved in $CHCl_3$ (52 mL). A catalyst solution was prepared by dissolving $PdCl_2(PPh_3)_2$ (42 mg, 0.06 mmol), CuI (44 mg, 0.23 mmol) and 1,4-benzoquinone (125 mg, 1.16 mmol) in $CHCl_3$ (28 mL) and *i*-Pr2NH (1.4 mL). The catalyst solution was added to the porphyrin solution and the reaction mixture was stirred at room temperature for 1 h. The crude reaction mixture was passed through a short plug of silica gel (1% pyridine in $CHCl_3$), passed over a size exclusion column on Biobeads SX-1 (1% pyridine in toluene), and finally the oligomers were separated by recycling GPC (1% pyridine in toluene) to give the porphyrin trimer **2.29** as a dark oily solid (62 mg, 23%).

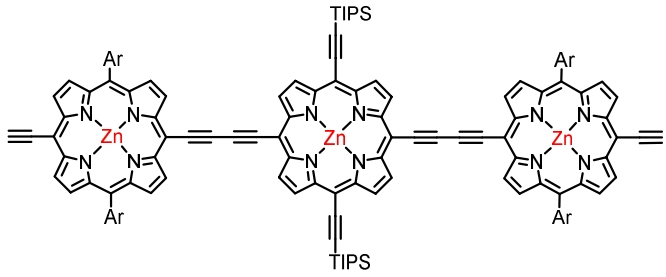


^{1}H NMR (400 MHz, $CDCl_3$/~1% pyridine-d_5, 298 K): δ (ppm) 9.91 (d, *J* = 4.5 Hz, 4H, β_1), 9.87 (d, *J* = 4.5 Hz, 4H, β_1), 9.74 (d, *J* = 4.5 Hz, 4H, β_1), 9.61 (d, *J* = 4.5 Hz, 4H, β_1), 8.98 (d, *J* = 4.6 Hz, 4H, β_2), 8.88 (d, *J* = 4.5 Hz, 4H, β_2), 8.33 (d, *J* = 9.5 Hz, 4H, H5), 8.19 (m, 4H, H8), 7.92 (m, 4H, H6), 7.77 (m, 4H, H7), 2.59 (t, *J* = 7.0 Hz, 4H, H1), 2.24 – 2.10 (m, 4H, H2), 1.59 – 0.85 (m, 202H, H3+H9+THS), 0.62 (s, 12H, H9).

UV-vis-NIR ($CHCl_3$) λ_{max}/nm (ε/10^5 $M^{-1}cm^{-1}$) = 755 (1.1), 639 (0.44), 588 (0.23), 508(1.8), 458 (2.1), 436 (2.4).

MALDI-TOF: *m/z* = 3305 ($C_{202}H_{262}Zn_3N_{14}Si_8$, $[M]^+$ requires 3307).

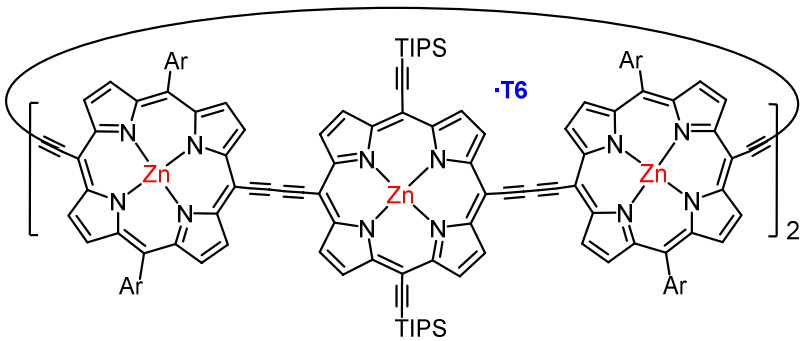
2.30



Porphyrin trimer **2.29** (60 mg, 18 µmol) was dissolved in THF (12 mL). K_2CO_3 (50 mg, 0.36 mmol) was dissolved in methanol (5.2 mL). The solutions were combined and the reaction mixture was stirred at room temperature for 1 h. The reaction mixture was passed through a short plug of silica gel (5% pyridine in CH_2Cl_2) giving **2.30** red solid (60 mg, 100%).

^{1}H NMR (400 MHz, $CDCl_3$/~1% pyridine-d_5, 298 K): δ (ppm) 9.91 (d, *J* = 4.6 Hz, 4H), 9.86 (d, *J* = 4.5 Hz, 4H), 9.74 (d, *J* = 4.5 Hz, 4H), 9.67 (d, *J* = 4.6 Hz, 4H), 8.99 (d, *J* = 4.5 Hz, 4H), 8.88 (d, *J* = 4.5 Hz, 4H), 8.33 (dt, *J* = 9.0, 1.4 Hz, 4H), 8.19 (m, 4H), 7.91 (dd, *J* = 7.4, 1.3 Hz, 4H), 7.77 (td, *J* = 7.5, 2.1 Hz, 4H), 4.18 (s, 2H), 1.61 – 0.86 (m, 198H).

2.31



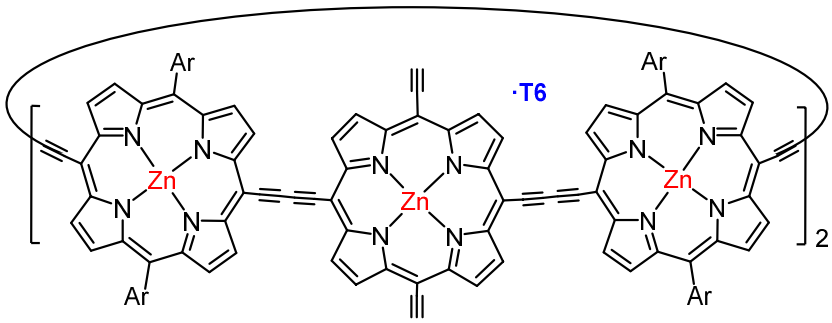
Fully deprotected trimer **2.30** (40 mg, 13.08 µmol) was dissolved in $CHCl_3$ (11 mL, filtered through alumina) and freshly distilled *i*-Pr_2NH (0.2 mL). Hexadentate template **T6** (6.7 mg, 6.7 µmol) was added and the resulting mixture was sonicated for 0.5 h. A catalyst solution was prepared by dissolving $Pd(PPh_3)_2Cl_2$ (2.9 mg, 4 µmol), CuI (7.7 mg, 41 µmol) and 1,4-benzoquinone (5.8 mg, 53.6 µmol) in $CHCl_3$ (8.8 mL) and freshly distilled *i*-Pr_2NH (0.2 mL). This solution was added to the reaction mixture, which was stirred vigorously at room temperature for 16 h. The crude reaction solution was purified by silica column chromatography (5% pyridine in CH_2Cl_2), size exclusion column on Biobeads SX-1 (1% pyridine in toluene), and finally by recycling GPC (1% pyridine in toluene) to give **2.31** as a red solid (23 mg, 50%).

^{1}H NMR (400 MHz, $CDCl_3$/~1% pyridine-d_5, 298 K): δ (ppm) 9.56 (m, 16H), 9.46 (m, 16H), 8.75 (m, 16H), 8.28 (m, 4H), 8.15 (m, 8H), 7.98 (m, 4H), 7.89 (m, 8H), 7.73 (m, 8H), 5.59 – 5.35 (m, 24H), 4.98 (m, 12H), 2.49 – 2.14 (m, 12H), 1.59 – 0.40 (m, 396H).

UV-Vis ($CHCl_3$) λ_{max}/nm (ε/10^5 $M^{-1}cm^{-1}$) = 842 (4.9), 801 (5.1), 764 (3.5), 722 (0.9), 545 (1.9), 491 (5.2), 437 (2.9).

MS (MALDI-ToF): *m/z* = 7106.9 ($C_{452}H_{524}Zn_6N_{30}Si_{12}$, $[M]^+$ requires 7106.5), 6110.0 ($C_{380}H_{476}Zn_6N_{24}Si_{12}$ –T6, $[M\text{-}T6]^+$ requires 6109).

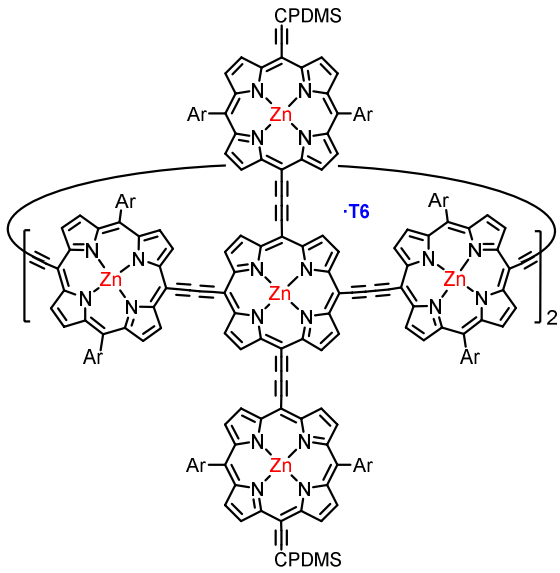
2.32



Ring **2.31** (10 mg, 1.54 μmol) was dissolved in CH_2Cl_2 (1.8 mL). Tetra-*n*-butylammonium fluoride (0.25 mL, 1.0 M solution in THF, 246.4 μmol) was added and the reaction was stirred for 15 min. The crude reaction mixture was purified by silica column chromatography (5% pyridine in $CHCl_3$) to give ring **2.32** as a red solid (10 mg, 100%). The product was taken to the next step without further purification.

^{1}H NMR (400 MHz, $CDCl_3$/~1% pyridine-d_5, 298 K): δ (ppm) 9.59 – 9.42 (m, 16H), 9.37 (d, *J* = 17.3 Hz, 16H), 8.67 (dt, *J* = 9.7, 4.7 Hz, 16H), 8.19 (d, *J* = 9.1 Hz, 4H), 8.07 (d, *J* = 7.9 Hz, 8H), 7.90 (t, *J* = 7.0 Hz, 4H), 7.81 (d, *J* = 7.4 Hz, 8H), 7.71 – 7.59 (m, 8H), 5.50 – 5.22 (m, 24H), 4.93 – 4.74 (m, 12H), 4.11 (s, 4H), 1.59 – 0.82 (m. 312H).

2.33



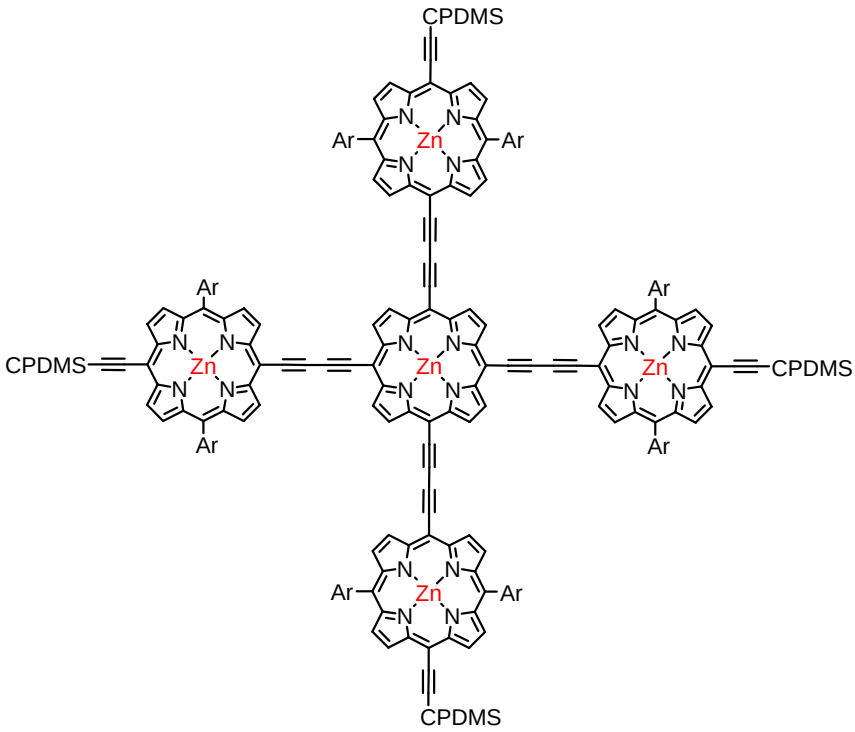
Porphyrin **2.32** (10 mg, 0.0015 mmol) and porphyrin **2.18** (78.4 mg, 0.062 mmol) were dissolved in $CHCl_3$ (12.6 mL). A catalyst solution of $Pd(PPh_3)_2Cl_2$ (4.3 mg, 0.0061 mmol), CuI (4.9 mg, 0.026 mmol) and 1,4-benzoquinone (14.9 mg, 0.138 mmol) in $CHCl_3$ (3.7 mL) and freshly distilled *i*-Pr_2NH (0.31 mL) was added and the mixture stirred at room temperature for 10 minutes. The reaction mixture was passed through a short silica plug ($CHCl_3$/10% pyridine), followed by size exclusion chromatography on Biobeads SX-1 (toluene/1% pyridine) and recycling GPC (toluene/1% pyridine) giving **2.33** as a brown/red solid (4.4 mg, 25%).

^{1}H NMR (400 MHz, $CDCl_3$/~1% pyridine-d_5): δ (ppm) 9.88 (m, 8H), 9.69 (m, 8H), 9.63 (m, 8H), 9.58 (m, 16H), 9.53 (m, 8H), 8.99 (m, 8H), 8.89 (m, 8H), 8.73 (m, 16H), 8.34 (dm, 8H), 8.22 – 8.15 (m, 16H), 8.08 (s, 4H), 7.94 (d, *J* = 7.3 Hz, 12H), 7.88 – 7.74 (m, 16H), 7.73 – 7.60 (m, 8H), 5.68 – 5.36 (m, 24H), 5.04 (d, *J* = 45.5 Hz, 12H), 2.60 (t, *J* = 7.0 Hz, 8H), 2.24 – 2.11 (m, 8H), 1.66-0.69 (m, 656H).

MALDI-TOF: *m/z* = 10528.31 ($C_{656}H_{816}N_{44}Si_{20}Zn_{10}$, [M-**T6**]$^+$ requires 10509.35).

UV-vis ($CHCl_3$) λ_{max}/nm (ε/10^5 $M^{-1}cm^{-1}$) = 850 (2.1), 810 (2.4), 776 (2.1), 658 (1.5), 522 (2.6), 491 (3.5), 446 (6.5).

***x*-P5**



To a solution of **2.20** (15 mg, 0.014 mmol) in a mixture of CH_2Cl_2 (9 mL) and THF (8 mL) was added TBAF (0.082 mL, 1.0 M in THF). After the mixture was stirred at room temperature for 1 hr. The solution was passed through a short silica plug (CH_2Cl_2/5% pyridine) and concentrated under reduced pressure. The blue solid (14 mg) was immediately used for further reactions due to its instability.

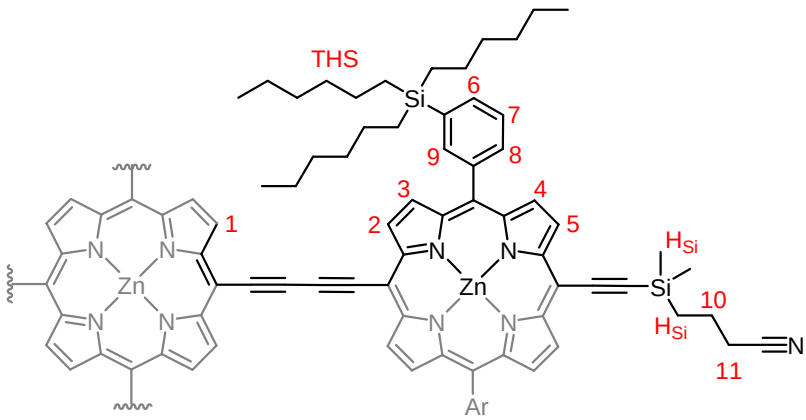
The isolated porphyrin (14 mg, 0.029 mmol) and porphyrin **2.18** (330 mg, 0.26 mmol) were dissolved in CH_2Cl_2 (20 mL) and freshly distilled *i*-Pr_2NH (4 mL). $Pd(PPh_3)_2Cl_2$ (6 mg, 0.0085 mmol), CuI (2.3 mg, 0.012 mmol) and 1,4-benzoquinone (5.4 mg, 0.050 mmol) were added and the mixture stirred at room temperature for 3 hours. The reaction mixture was passed through a short silica plug (CH_2Cl_2/5% pyridine). Dimer side product was removed using a size exclusion column with Biobeads SX-1 (toluene/1% pyridine). ***X*-P5** was isolated using recycling GPC (toluene/1% pyridine) as a brown/red solid (16 mg, 10%).

^{1}H NMR (500 MHz, $CDCl_3$/~1% pyridine-d_5, 298 K) δ 9.95 (s, 8H, H1), 9.93 (d, J = 4.5 Hz, 8H, H2), 9.60 (d, J = 4.6 Hz, 8H, H5), 8.97 (d, J = 4.6 Hz, 8H, H3), 8.86 (d, J = 4.5 Hz, 8H, H4), 8.31 (d, J = 10.9 Hz, 8H, H9), 8.17 (t, J = 7.3 Hz, 8H, H8), 7.89 (d, J = 7.4 Hz, 8H, H6), 7.75

(d, J = 7.8 Hz, 8H, H7), 2.57 (t, J = 6.9 Hz, 8H, H11), 2.16 – 2.12 (m, 8H, H10), 1.72 – 0.36 (m, 344H, H_{Si}/THS).

MS (MALDI-ToF): *m/z* = 5519.0 (C_{340} H_{432} $N_{24}Si_{12}Zn_5$, $[M]^+$ requires 5518.8).

UV-vis ($CHCl_3$): λ_{max}/nm ($\varepsilon/10^5$ $M^{-1}cm^{-1}$) = 764 (1.0), 649 (0.90), 587 (0.44), 524 (1.3), 487 (1.4), 441 (3.8).



The high symmetry of ***x*-P5** makes assignment straightforward. The large singlet at 9.95 ppm is a singlet corresponding to the β proton on the central porphyrin unit as evidenced by the integral and the (lack of) splitting pattern. The rest of the aromatic protons can be assigned following the assumptions that the signals above 9.50 ppm refer to β protons next to acetylenes and that the signal at 9.60 ppm corresponds to the β proton closest to the CPDMS protecting group.

This is a safe assumption – generally β positions next to acetylenes are more deshielded than those next to aryl solubilising groups. The peak at 9.60 ppm is the least deshielded $\beta_{acetylene}$ proton as it does not sit opposite another porphyrin unit. Based on this assumption the rest of the protons can be assigned using COSY and NOESY signals.

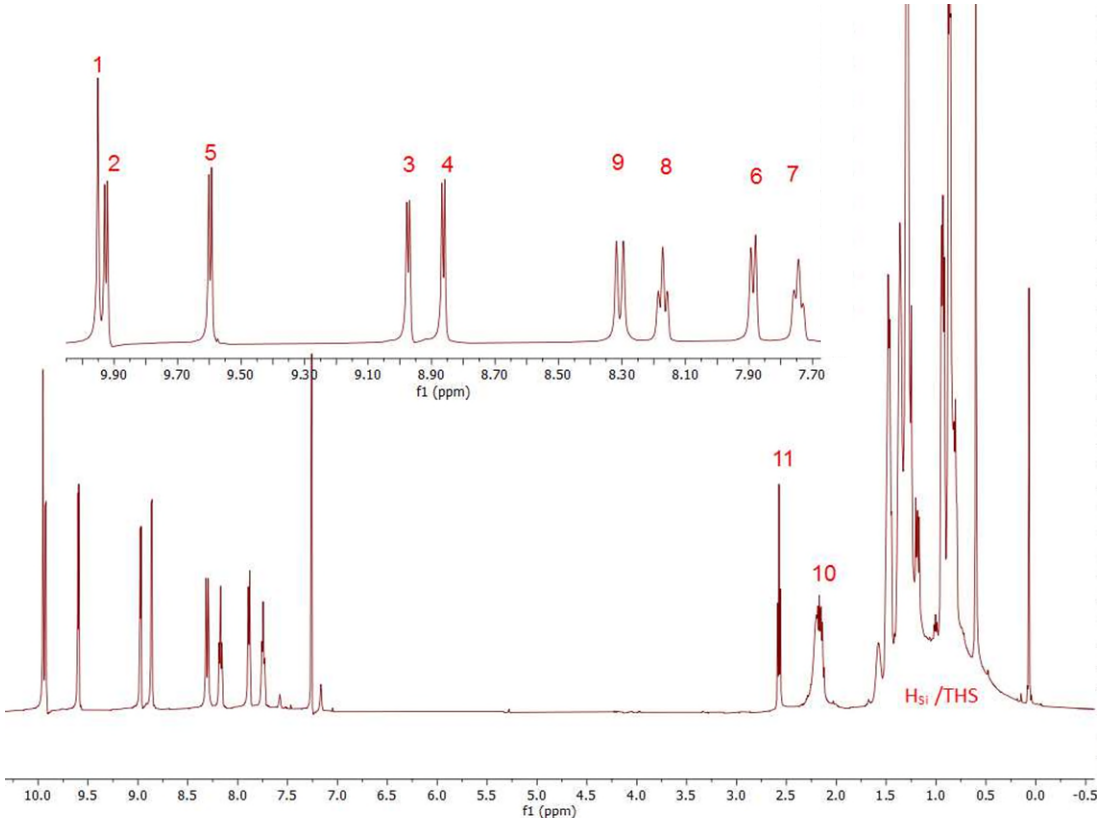


Figure 2.32. ^{1}H NMR spectrum of ***x*-P5** (500 MHz, $CDCl_3$/~1% pyridine-d_5, 298 K).

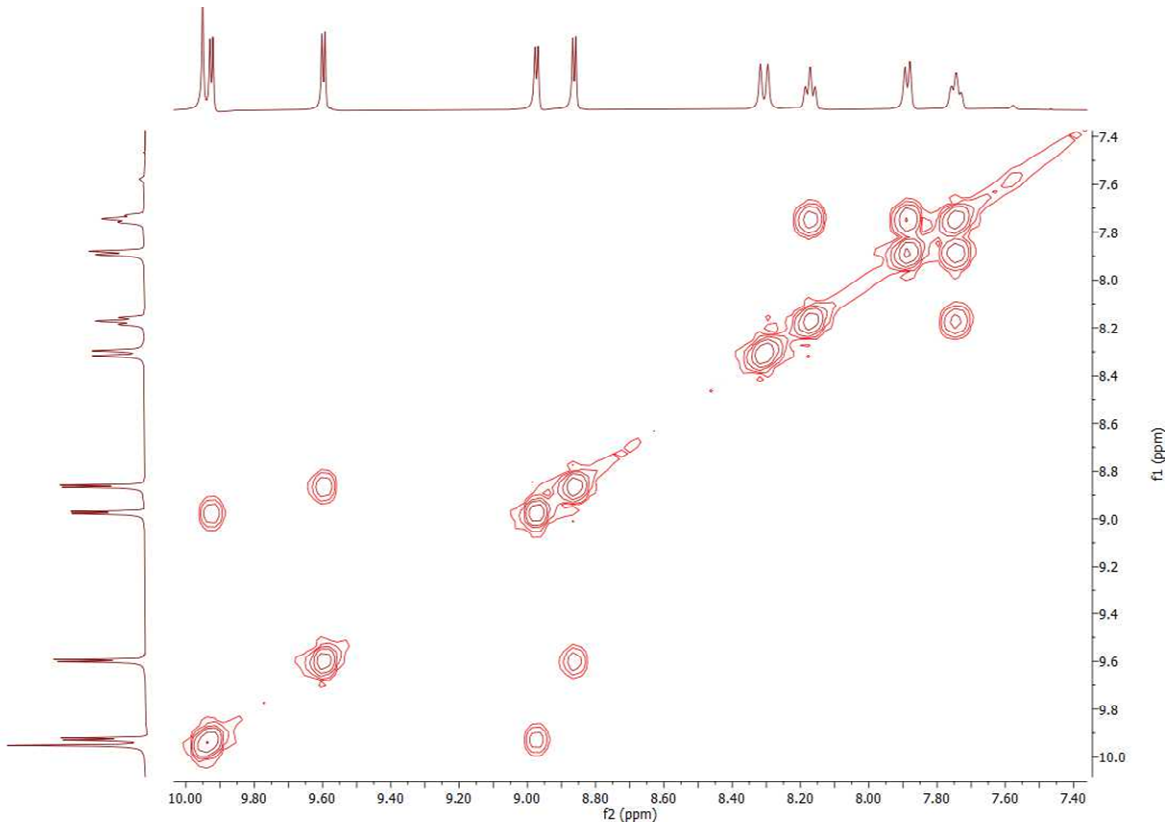


Figure 2.33. ^{1}H NMR 2D COSY spectrum of ***x*-P5** (500 MHz, $CDCl_3$/~1% pyridine-d_5, 298 K).

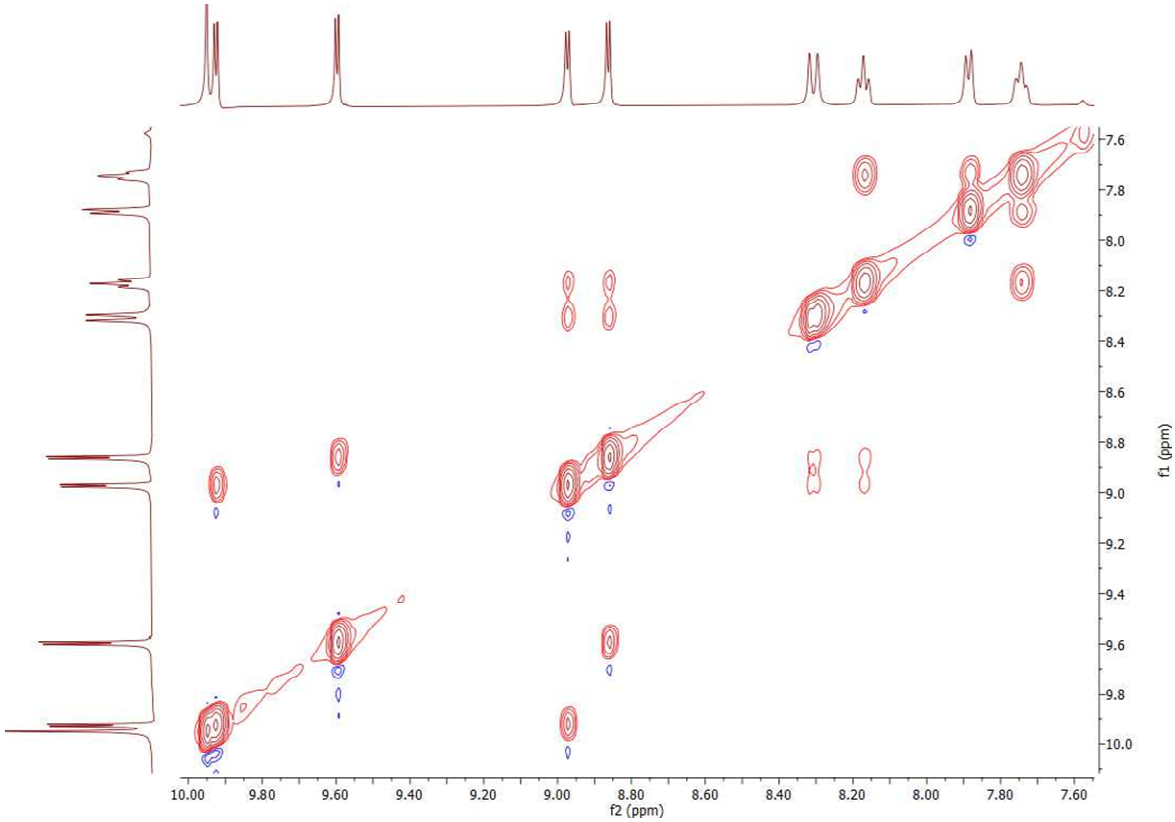


Figure 2.34. ^{1}H NMR 2D NOESY spectrum of ***x*-P5** (500 MHz, $CDCl_3$/~1% pyridine-d_5, 298 K).

***x*-P5''''**

Porphyrin pentamer ***x*-P5** (10 mg, 0.002 mmol) was dissolved in CH_2Cl_2 (4 mL) and pyridine (0.2 mL). Tetra-*n*-butylammonium fluoride (80 µL, 1.0 M solution in THF, 80 µmol) was added and the mixture stirred at room temperature. After 15 minutes TLC indicated the formation of the fully deprotected product. The reaction mixture was passed through a short silica plug ($CHCl_3$/10% pyridine) and passed over a SEC (Biobeads SX-1, Toluene/1% pyridine) and the solvent removed *in vacuo* to yield ***x*-P5''''** as a brown/orange solid (10 mg, ~100%). The product was taken immediately to the next step without further purification. NMR analysis showed appearance of a single singlet acetylene peak of integral 4, indicating full conversion.

^{1}H NMR (400 MHz, $CDCl_3$/~1% pyridine-d_5, 298 K): δ (ppm) 10.01 – 9.88 (m, 16H), 9.67 (d, *J* = 4.5 Hz, 8H), 8.98 (d, *J* = 4.5 Hz, 8H), 8.87 (d, *J* = 4.5 Hz, 8H), 8.31 (d, *J* = 8.3 Hz, 8H), 8.17 (d, *J* = 6.5 Hz, 8H), 7.89 (d, *J* = 7.4 Hz, 8H), 7.75 (d, *J* = 7.5 Hz, 8H), 4.17 (s, 4H, acetylene), 1.66 – 0.25 (m, 312H).

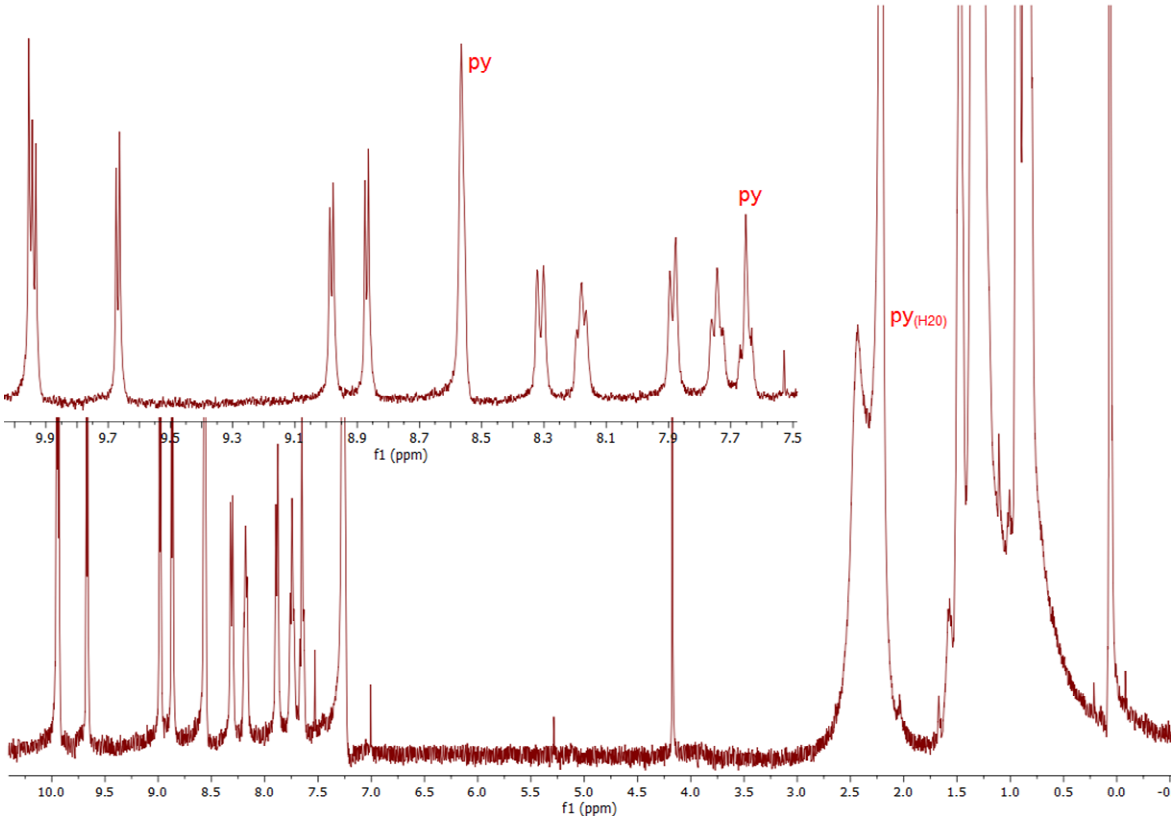
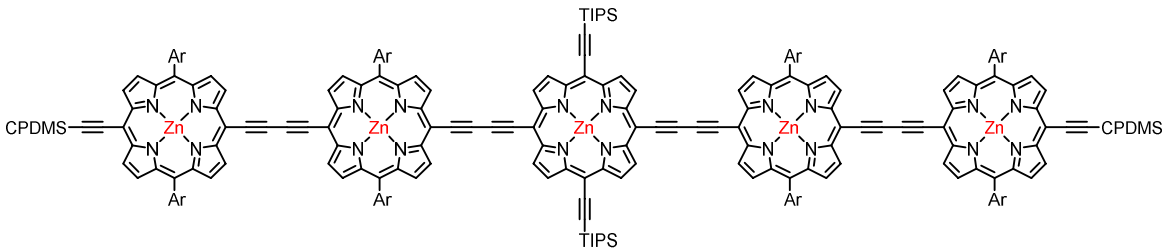


Figure 2.35. ^{1}H NMR of ***x*-P5''''** (400 MHz, $CDCl_3$/~1% pyridine-d_5, 298 K).

***l*-P5**



Porphyrin **2.27** (4.7 mg, 0.006 mmol) and porphyrin dimer **2.28** (30 mg, 0.013) was dissolved in $CHCl_3$ (1 mL). A catalyst solution of $Pd(PPh_3)_2Cl_2$ (0.63 mg, 0. 9 µmol), CuI (0.57 mg, 0.003 mmol) and 1,4-benzoquinone (1.84 mg, 0.017 mmol) in $CHCl_3$ (0.18 mL) and freshly distilled *i*-Pr_2NH (0.02 mL) was added and the mixture stirred at room temperature for 1 hour. The reaction mixture was passed through a short silica plug ($CHCl_3$/10% pyridine), followed by size exclusion chromatography on Biobeads SX-1 (toluene/1% pyridine) and recycling GPC (toluene/1% pyridine) to give ***l*-P5** (3.37 mg, 10%) as a brown solid.

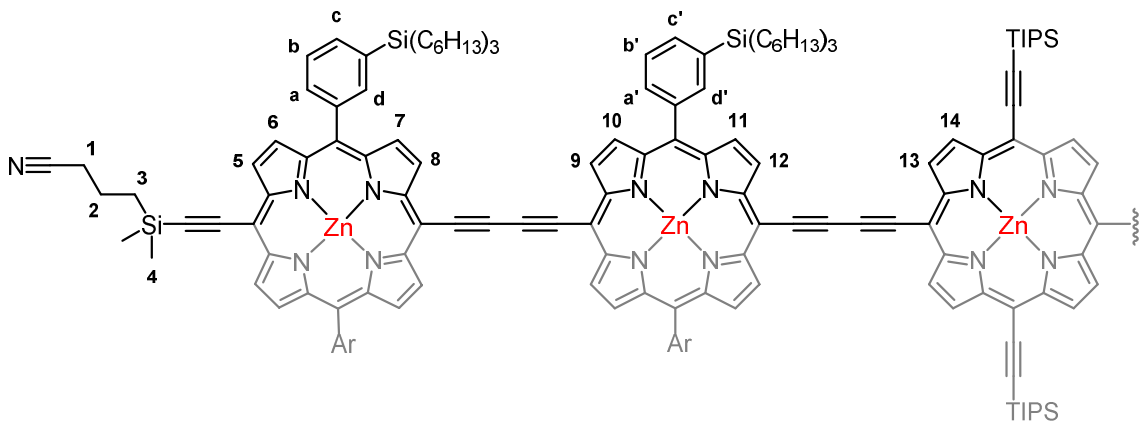
Or

2.30 trimer (10 mg, 0.0032 mmol) and 2.18 (40 mg, 0.031) was dissolved in $CHCl_3$ (4 mL). A catalyst solution of $Pd(PPh_3)_2Cl_2$ (2.5 mg, 0. 0036 mmol), CuI (2.6 mg, 0.014 mmol) and 1,4-benzoquinone (7.6 mg, 0.070 mmol) in $CHCl_3$ (2 mL) and freshly distilled *i*-Pr_2NH (0.1 mL) was added and the mixture stirred at room temperature for 1 hour. The reaction mixture was passed through a short silica plug ($CHCl_3$/10% pyridine), followed by size exclusion chromatography on Biobeads SX-1 (toluene/1% pyridine) and recycling GPC (toluene/1% pyridine) to give ***I*-P5** (5 mg, 28%) as a brown solid.

^{1}H NMR (400 MHz, $CDCl_3$/~1% pyridine-d_5, 298 K): δ (ppm) 9.95 – 9.90 (m, 12H, $H_{8/9/12}$), 9.89 (d, *J* = 4.5 Hz, 4H, H_{13}), 9.76 (d, *J* = 4.5 Hz, 4H, H_{14}), 9.65 (d, *J* = 4.6 Hz, 4H, H_5), 9.03 – 8.94 (m, 12H, $H_{7/10/11}$), 8.89 (d, *J* = 4.6 Hz, 4H, H_6), 8.38 (d, *J* = 8.7 Hz, 4H, $H_{a'}$), 8.32 (d, *J* = 7.9 Hz, 4H, H_a), 8.25 (t, *J* = 7.0 Hz, 4H, $H_{d'}$), 8.18 (ddd, *J* = 7.8, 6.2, 1.9 Hz, 4H, H_d), 7.97 – 7.93 (m, 4H, $H_{b'}$), 7.91 (dt, *J* = 7.6, 1.3 Hz, 4H, H_b), 7.81 (td, *J* = 7.6, 2.1 Hz, 4H, $H_{c'}$), 7.79 – 7.73 (m, 4H, H_c), 2.57 (q, *J* = 6.6, 6.1 Hz, 4H, H_1), 2.22 (td, *J* = 14.9, 14.0, 7.0 Hz, 4H, H_2), 1.60 – 0.74 (m, 370H, $H_{3/4/THS}$).

UV-vis ($CHCl_3$) λ_{max}/nm (ε/10^5 $M^{-1}cm^{-1}$) = 790 (1.6), 663 (0.68), 588 (0.34), 497 (2.9), 456 (3.5).

MS (MALDI-ToF): *m/z* = 5583.08 ($C_{346}H_{450}N_{22}Si_{12}Zn_5$, $[M]^+$ requires 5568.957738).



Some peaks remain unassignable due to overlapping multiplets. Most peaks can be assigned starting from the assumption that there are two well separated β-H envelopes.

The most deshielded signals are those next to the acetylene (5, 8, 9, 13, 13, 14), whilst more shielded ones are those next to the electronically non-communicating aryl groups (6, 7, 10, 11). The peaks at 9.65 and 8.89 are the β positions next to the alkyne and aryl solubilising groups on the end porphyrin, as both of these are the least deshielded in their respective proton environments due to them not experience the deshielding ring current of neighbouring porphyrin rings. It is possible that the peak at 9.65 could be the β proton next to the tips alkyne instead (H_{14}), however the peak at 9.76 shows a clear COSY correlation to the acetylene βs at ~9.85, and so these two signals must be the β protons on the central porphyrin core containing two acetylene environments.

The solubilising protons are split into two groups due to their two different environments. A 1D NOE ^{1}H NMR spectrum excited at 8.16 ppm showed correlations to porphyrin β H_6. COSYs can then resolve the rest of the solubilising group protons. The solubilising aryl on the end of the porphyrin is less-deshielded, most likely as a result of it being in the vicinity of a single porphyrin unit rather than in the middle of the chain.

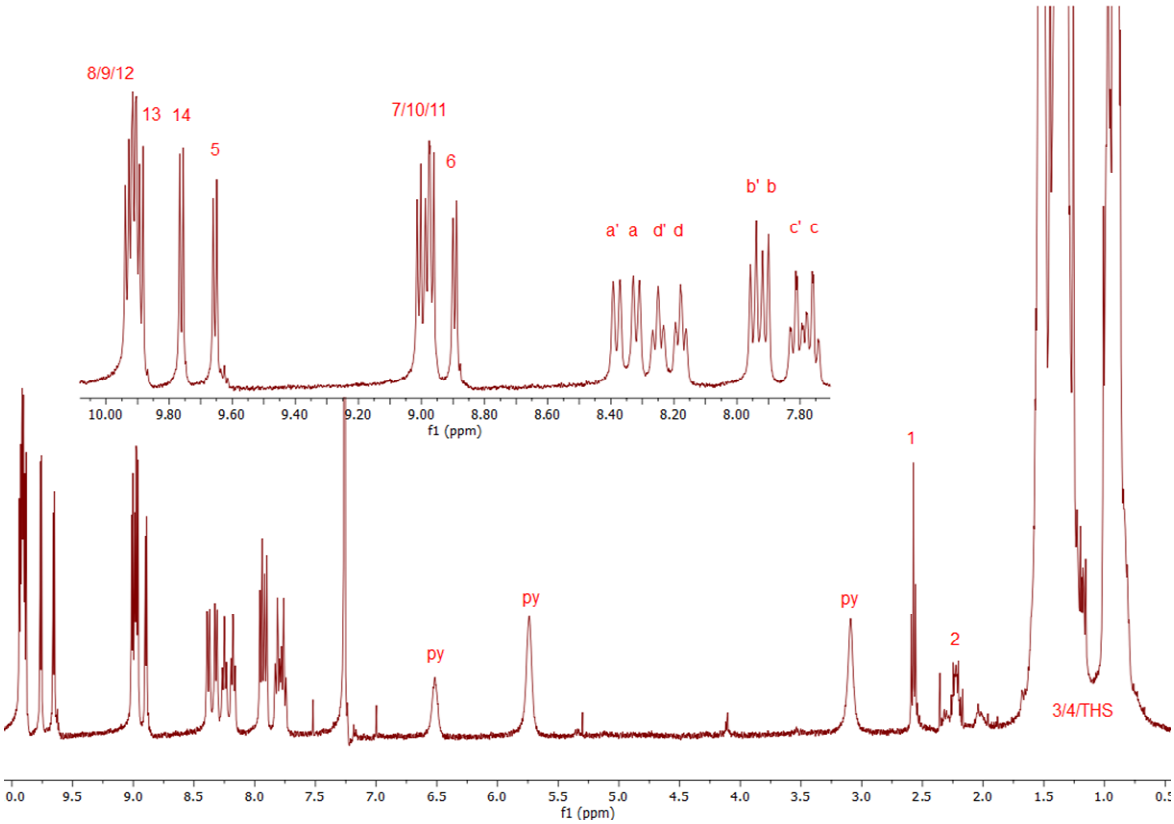


Figure 2.36. ^{1}H NMR spectrum of ***I*-P5** (500 MHz, $CDCl_3$/~1% pyridine-d_5, 298 K).

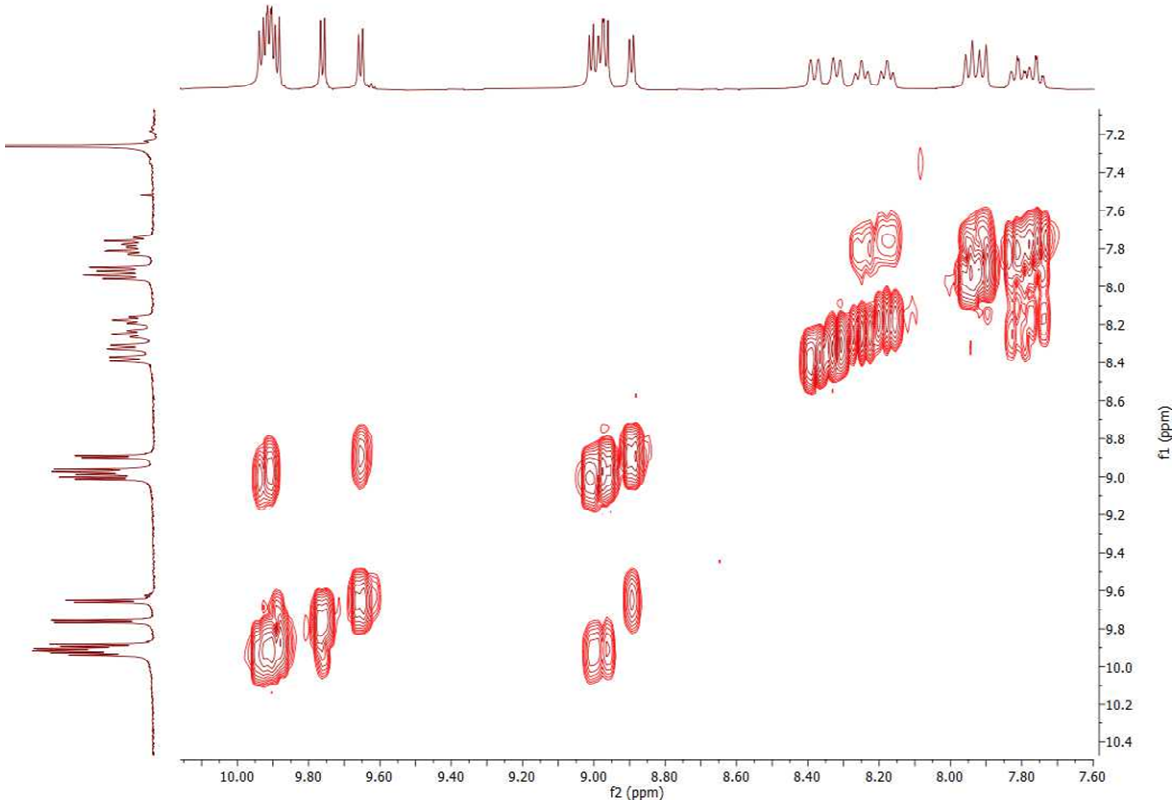


Figure 2.37. ^{1}H 2D NMR COSY spectrum of ***l*-P5** (500 MHz, $CDCl_3$/~1% pyridine-d_5, 298 K).

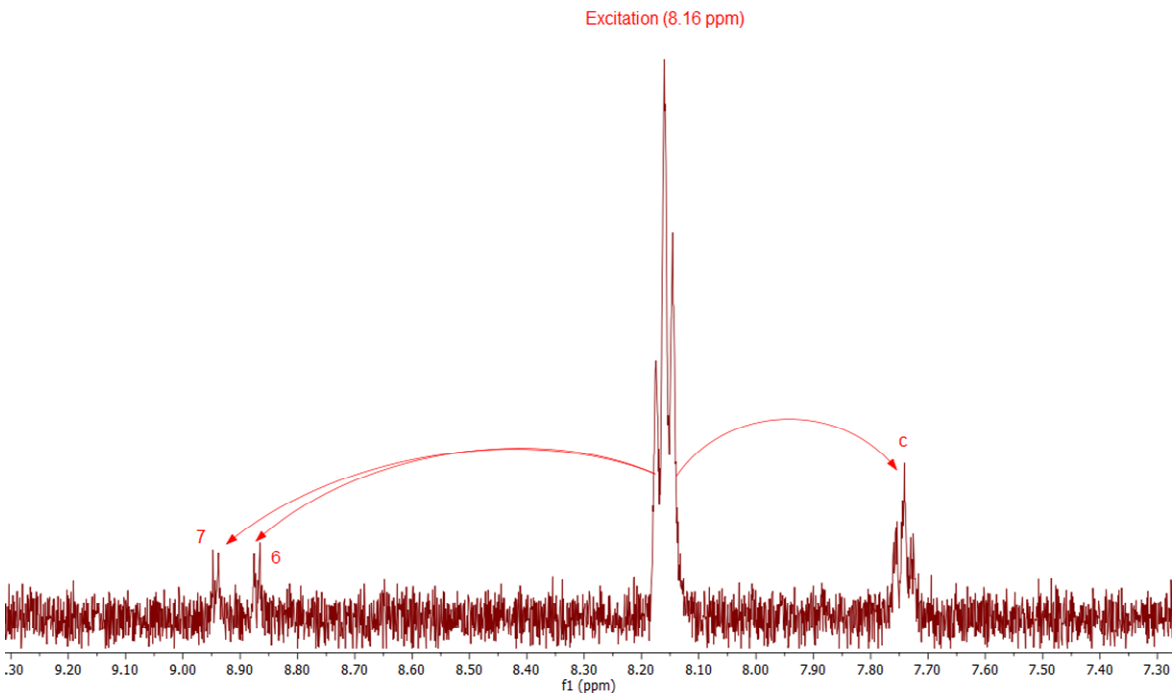
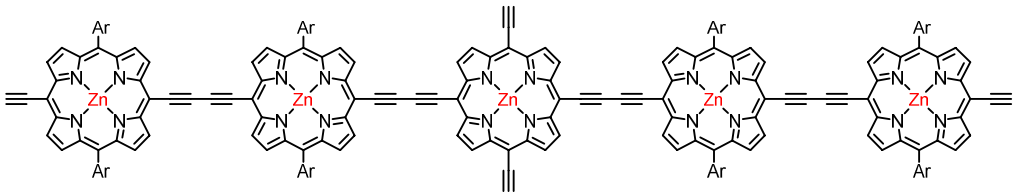


Figure 2.38. ^{1}H 1D NMR NOE spectrum of ***l*-P5**, excited at 8.16 ppm (500 MHz, $CDCl_3$/~1% pyridine-d_5, 298 K).

***l*-P5’’’’**



***l*-P5** (5 mg, 0.896 mmol) was dissolved in $CHCl_3$ (6.5 mL). Tetra-*n*-butylammonium fluoride (36 µL, 1.0 M solution in THF, 36 µmol) was added and the mixture stirred at room temperature. After 15 minutes TLC indicated the formation of the fully deprotected product. The reaction mixture was passed through a short silica plug ($CHCl_3$/10% pyridine) and passed over a SEC (Biobeads SX-1, Toluene/1% pyridine) and the solvent removed *in vacuo* to yield ***l*-P5’’’’** as a brown/orange solid (2 mg, 44%). The product was taken immediately to the next step without further purification. NMR analysis showed appearance of a two singlet acetylene peaks of integrals 2, indicating full conversion.

^{1}H NMR (400 MHz, $CDCl_3$/~1% pyridine-d_5, 298 K): δ (ppm) 9.86 – 9.81 (m, 16H), 9.68 (d, *J* = 4.5 Hz, 4H), 9.60 (d, *J* = 4.6 Hz, 4H), 8.92 (d, *J* = 4.5 Hz, 4H), 8.90 – 8.87 (m, 8H), 8.80 (d, *J* = 4.5 Hz, 4H), 8.30 (d, *J* = 8.3 Hz, 4H), 8.24 (d, *J* = 8.6 Hz, 4H), 8.15 (d, *J* = 7.0 Hz, 4H), 8.13 – 8.07 (m, 4H), 7.86 (d, *J* = 7.5 Hz, 4H), 7.83 (d, *J* = 7.6 Hz, 4H), 7.70 (dt, *J* = 15.1, 7.4 Hz, 8H), 4.18 (s, 2H, acetylene), 4.10 (s, 2H, acetylene), 1.71 – 0.41 (m, 312H).

MS (MALDI-ToF): *m/z* = 5015.8 ($C_{316}H_{388}N_{20}Si_8Zn_5$, $[M]^+$ requires 5018.3).

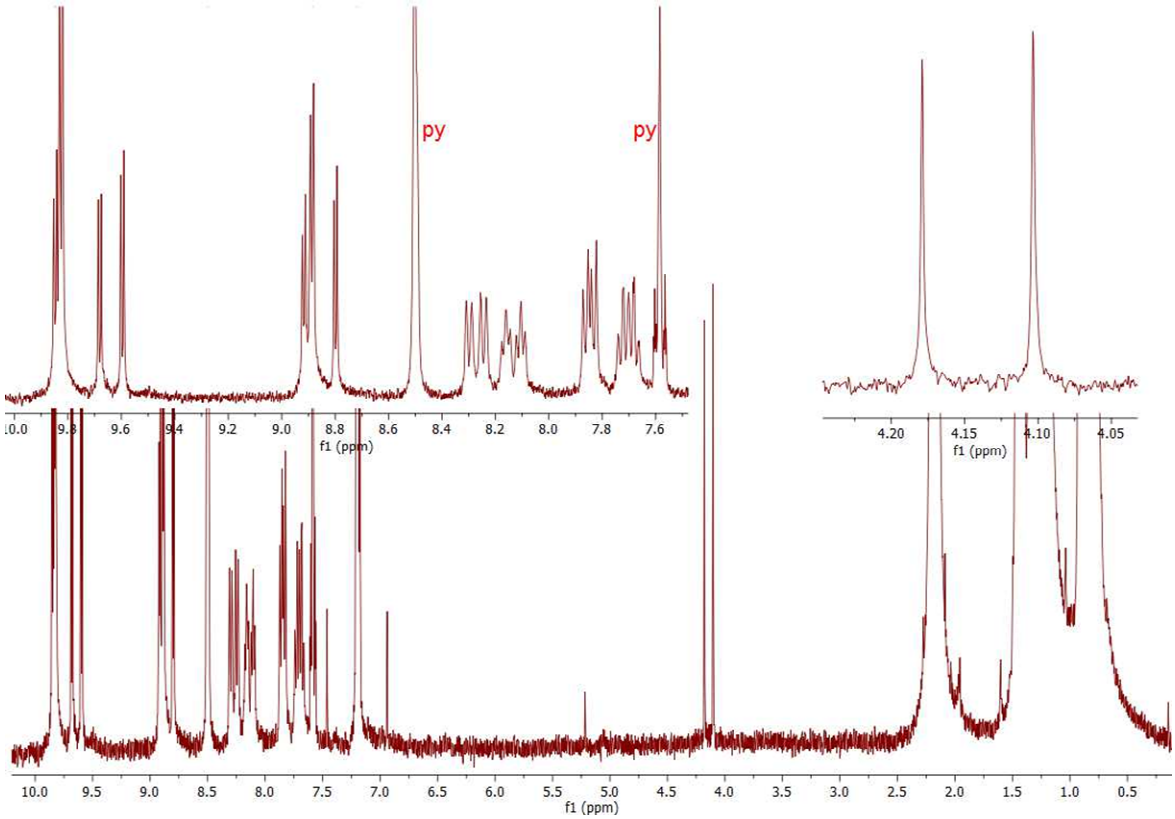
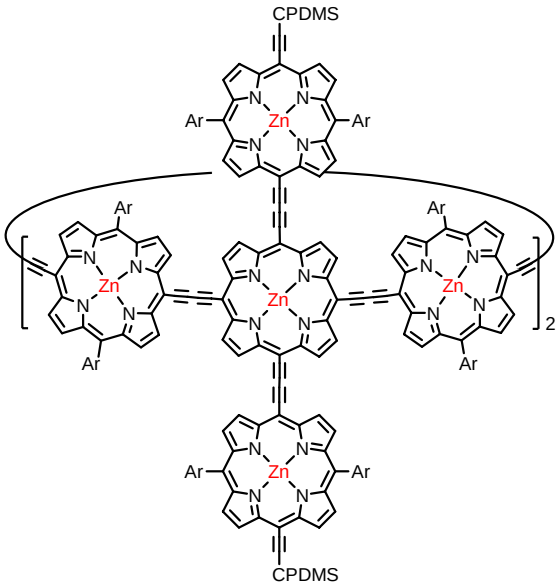


Figure 2.39. ^{1}H NMR of ***I*-P5''''** (400 MHz, $CDCl_3$/~1% pyridine-d_5, 298 K).

Preball-P10



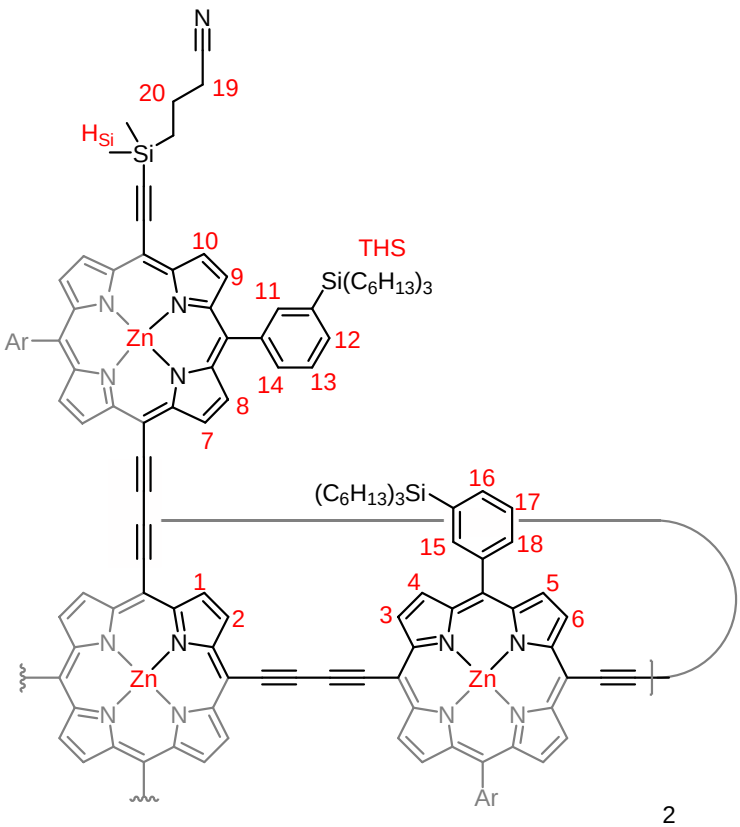
A size exclusion column (300 mm length, 20 mm diameter) with Biobeads SX-1 was prepared in pyridine. A saturated DABCO solution in pyridine was prepared which was used to saturate the top of the column with DABCO (ca. 30% of the column length). **2.33** (5.2 mg, 7.5 µmol) was dissolved in the minimal amount of pyridine and loaded on the

column. The product was eluted with the saturated pyridine/DABCO solution (ca. 10% of the column length) followed by eluting with pure pyridine, isolating ***preball*-P10** (3.12 mg, 77%).

^{1}H NMR (500 MHz, $CDCl_3$/~1% pyridine-d_5, 298 K): δ (ppm) 9.86 (d, J = 4.4 Hz, 8H, H3), 9.72 (d, J = 4.4 Hz, 8H, H2), 9.64 (m, 16H, H1 + H7), 9.60 (d, J = 4.4 Hz, 8H, H6), 9.58 (d, J = 4.6 Hz, 8H, H10), 8.95 (d, J = 4.4 Hz, 8H, H4), 8.87 (d, J = 4.4 Hz, 8H, H5), 8.77 (d, J = 4.4 Hz, 8H, H8), 8.72 (d, J = 4.4 Hz, 8H, H9), 8.30 (d, J = 10.1 Hz, 8H, H15), 8.17 (m, 8H, H18), 8.13 (s, 8H, H11), 8.03 (m, 8H, H14), 7.90 (m, 8H, H16), 7.81 – 7.74 (m, 16H, H12 + H17), 7.64 – 7.59 (m, 8H, H13), 2.58 (t, J = 7.0 Hz, 8H, H19), 2.15 – 2.12 (m, 8H, H20), 1.55 – 0.55 (m, 656H, H_{Si}/THS).

UV-vis ($CHCl_3$): λ_{max}/nm (ε/10^5 $M^{-1}cm^{-1}$) = 810 (3.5), 781(3.5), 737 (2.1), 655 (2.1), 540 (2.6), 489 (4.5), 445 (7.8).

MS (MALDI-ToF): *m/z* = 10533 ($C_{656}H_{816}N_{44}Si_{20}Zn_{10}$, $[M]^+$ requires 10533).



2

As with ***x*-P5** and ***l*-P5** the β envelopes can be split into those next to the acetylene and those next to the aryl solubilising groups. The least deshielded proton in the β_{aryl} region can be assigned as proton 10. Protons 1 and 2 COSY only to each other. COSYs between β protons and NOESYs between β and Ar (e.g. 9-11) can assign the rest of the protons.

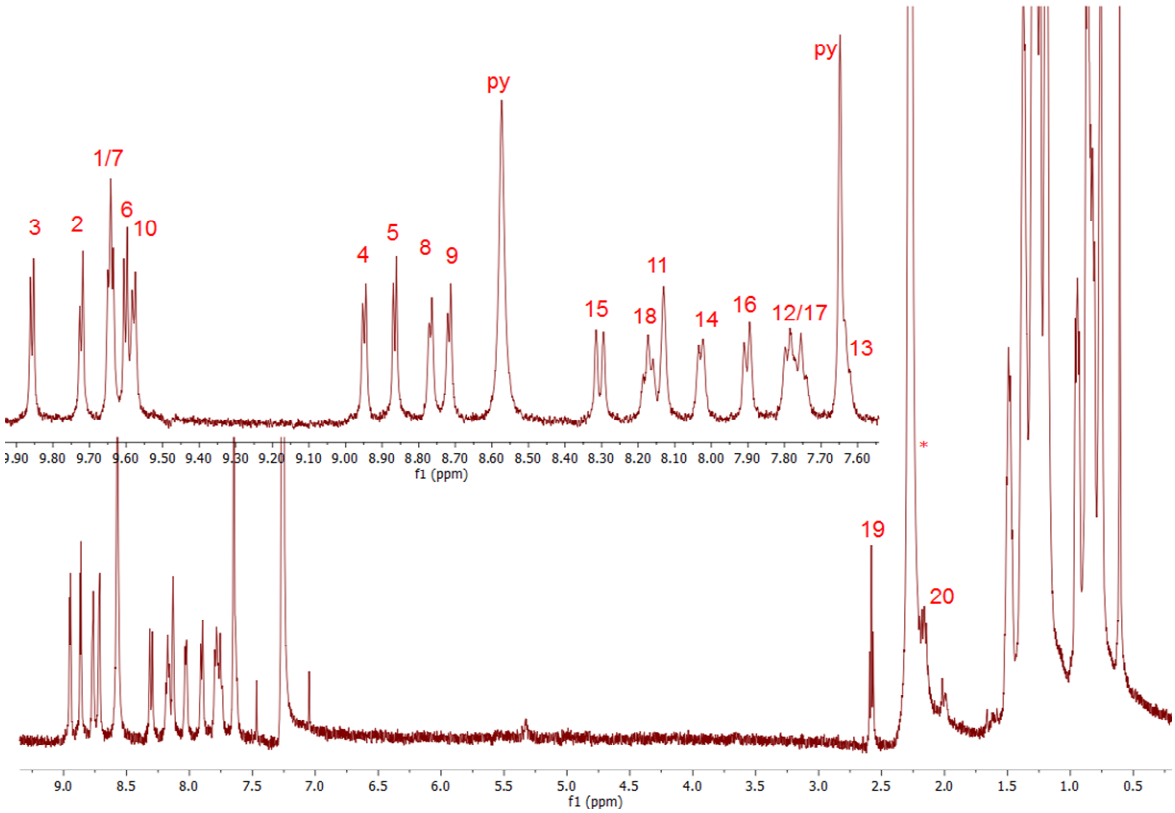


Figure 2.40. ^{1}H NMR of ***preball*-P10** (500 MHz, $CDCl_3$/~1% pyridine-d_5, 298 K).

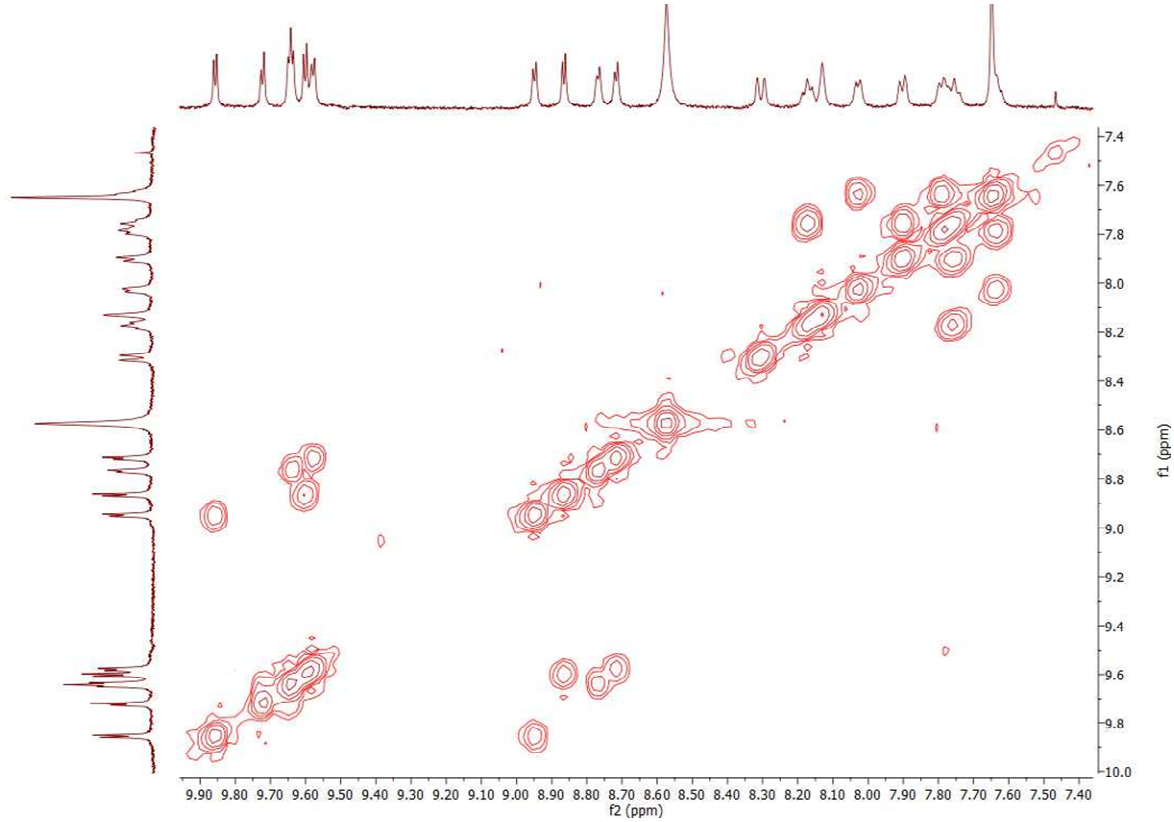


Figure 2.41. ^{1}H 2D NMR COSY of ***preball*-P10** (500 MHz, $CDCl_3$/~1% pyridine-d_5, 298 K).

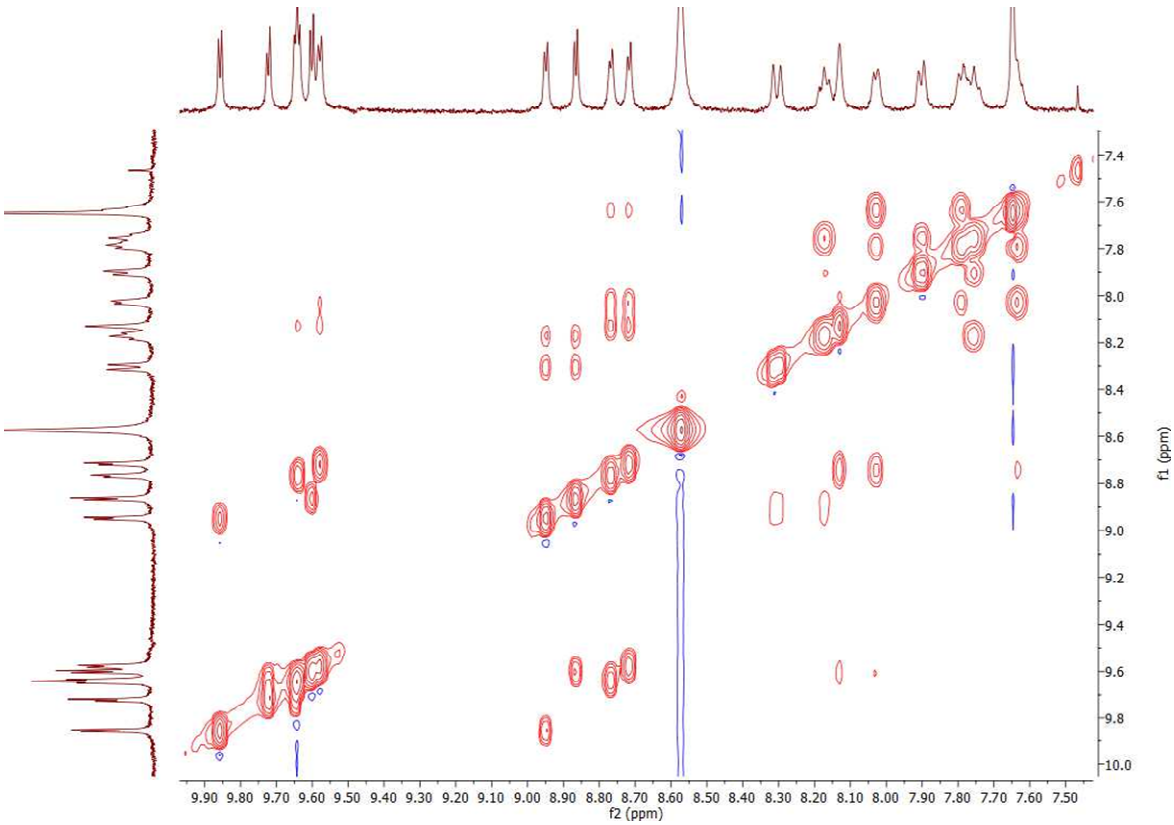
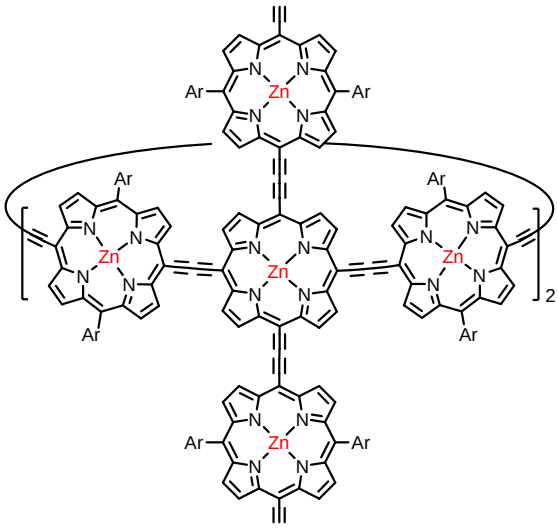


Figure 2.42. ^{1}H 2D NMR NOESY of ***preball*-P10** (500 MHz, $CDCl_3$/~1% pyridine-d_5, 298 K).

***Preball*-P10’’’’**



***preball*-P10** (10 mg, 0.9 µmol) was dissolved in CH_2Cl_2 (7 mL). Tetra-*n*-butylammonium fluoride (45 µL, 1.0 M solution in THF, 45 µmol) was added and the mixture stirred at room temperature. After 15 minutes MALDI-ToF indicated the formation of the fully deprotected product. TLC was unsuitable due to the starting material and product streaking on the plate. The reaction mixture was passed through a short silica plug ($CHCl_3$/10% pyridine) and passed over a SEC (Biobeads SX-1, Toluene/1% pyridine) and the solvent removed *in vacuo* to yield ***preball*-P10’’’’** as a brown/orange solid (10 mg, ~ 100%). The product was taken immediately to the next step without further purification. NMR analysis showed appearance of a singlet acetylene peak of integral 4, indicating full conversion. This NMR was ran in the absence of pyridine-d_5, and as such coordinated pyridine is observed upfield due to the local ring effect of the porphyrin units.

^{1}H NMR (400 MHz, $CDCl_3$, 298 K): δ (ppm) 9.82 (d, *J* = 4.4 Hz, 8H), 9.69 – 9.46 (m, 40H), 8.91 (m, 8H), 8.82 (m, 8H), 8.72 (d, *J* = 4.5 Hz, 8H), 8.67 (d, *J* = 4.6 Hz, 8H), 8.25 (s, 8H), 8.14 (s, 8H), 8.07 (s, 8H), 7.98 (d, *J* = 7.0 Hz, 8H), 7.85 (d, *J* = 7.5 Hz, 8H), 7.73 (d, *J* = 7.6 Hz, 16H), 7.58 (d, *J* = 7.4 Hz, 8H), 4.13 (s, 4H).

MS (MALDI-ToF): *m/z* = 10027.7 ($C_{632}H_{772}N_{40}Si_{16}Zn_{10}$, $[M]^+$ requires 10032.5).

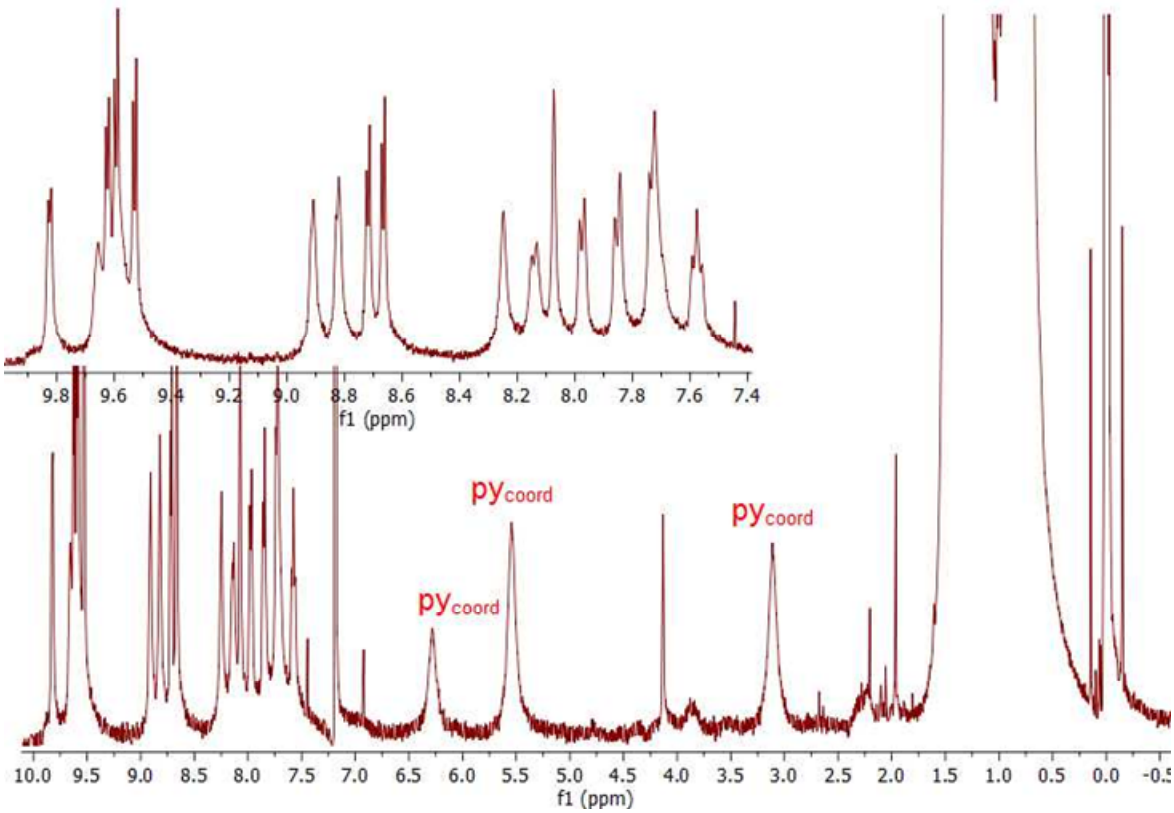


Figure 2.43. ^{1}H NMR of ***preball*-P10'''** (400 MHz, $CDCl_3$, 298 K).

2.8.3 Fluorescence measurements

Fluorescence quantum yields Φ_f were measured using linear butadiyne-linked porphyrin hexamer as a reference.[47] Its reported Φ_f of 28% (toluene, 1% pyridine) was further verified using an integrated sphere. The following formula was used for the calculation of the relative Φ_f:

$$\Phi_f(S) = \Phi_r(R) \cdot \frac{1 - 10^{-A_R}}{1 - 10^{-A_S}} \cdot \frac{n_S^2}{n_R^2} \cdot \frac{\int I_S(v)dv}{\int I_R(v)dv} \qquad (2.1)$$

where A is the optical density at the excitation wavelength, n the refractive index of the solvent, $\int I_i(v)dv$ the integrated spectral fluorescence photon flux which was approximated by the integrated blank and dark-count corrected signals of the emission (in wavenumbers).

The low quantum yield and red-shifted emission of most of the reported compounds prevented the measurement of absolute quantum yields using an integrating sphere. Several accumulated spectra were necessary to obtain emission profiles with acceptable S/N. All fluorescence samples were prepared with optical densities under 0.1 under ambient conditions to avoid reabsorption effects. Excitation spectra of all

compounds were acquired at several different emission wavelengths without evidence of fluorescent impurities.

3

Ultrafast Spectroscopies and Their Application to π-Conjugated Systems – A Chemist's Introduction

3.1 Outline 97

3.2 Introduction 97

3.3 Ultrafast infrared spectroscopy – A chemist's introduction 98

3.3.1 Time-resolved infrared (TRIR) 98

3.3.2 Applications of TRIR 100

3.3.3 Two-dimensional infrared spectroscopy (2D-IR) 101

3.3.4 Applications of 2D-IR 103

3.3.5 TRIR vs 2D-IR 105

3.4 Ultrafast IR spectroscopy applied to π-conjugated materials 107

3.5 Prospectus 109

3.1 Outline

This chapter will cover the basics of ultrafast IR spectroscopy and detail some applications to the field of π-conjugated materials. The techniques of time-resolved infrared (TRIR) and two-dimensional infrared (2D-IR) spectroscopies will be introduced and the interpretation of their spectra explained. Illustrative examples from the literature will serve to highlight the key applications of these spectroscopies before a summary of their application to π-conjugated materials. Finally, an area of underexplored research will be presented, which will be pursued in Chapter 4.

3.2 Introduction

π-Conjugation in organic molecules is a fundamental concept that is essential to the understanding of chemical reactivity, molecular structure and photophysical properties of compounds. Conjugation occurs as a result of an overlapping in-phase combination of p orbitals, from which form π bonds.[134] As conjugation is increased by lengthening the carbon chain, and therefore the number of contributing p orbitals, the HOMO-LUMO gap is decreased. If the conjugation is long enough (and the HOMO-LUMO gap small enough) the molecule begins to absorb light in the visible spectrum. This effect is responsible for much of the colour we see around us, such as the carotene pigments in carrots[135] and their derivatives found in bird plumage.[136] Perhaps the most ubiquitous example is that of chlorophyll, the porphyrin-based pigment found in plants that is responsible for the green colours of vegetation.[137]

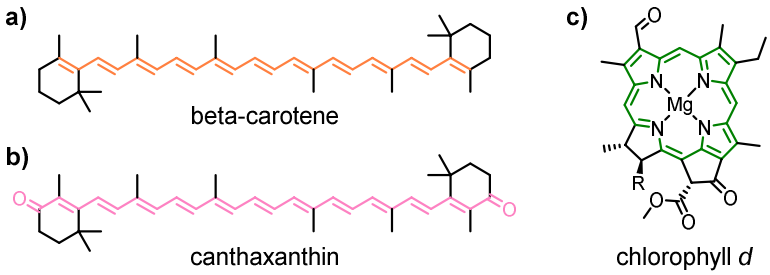
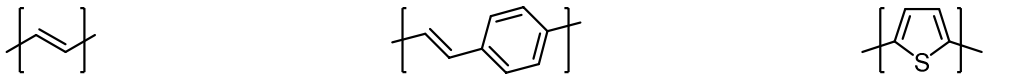


Figure 3.1. The colours of life. (a) beta-carotene is responsible for the orange colour in carrots.[135] (b) Carotene derivative canthaxanthin bio-accumulates in birds, adding pink colours to their plumage.[136] (c) Chlorophyll-*d* is a porphyrinoid responsible for the green colours of plants.[137] The conjugation is highlighted in each case (note: the highlighted colour corresponds to reflected /non-absorbed light).

By extending this concept even further, one can arrive at the field of π-conjugated oligomers and polymers. Here, conjugation is maintained over several repeating conjugated units. These compounds display a range of useful and interesting properties, mainly stemming from the semi-conductor properties conferred by the low HOMO-LUMO

gap (or band gap, in polymers) and the ability to accept or donate charges into the conjugation.[138] π-Conjugated polymers have found use in organic field-effect transistors (OFETs),[92,139] organic photovoltaic devices[89,91,140–142] and light-emitting devices such as organic LEDs (OLEDs).[143] Conjugated polymers are also finding applications in emergent technologies such as thermoelectric materials,[144,145] spintronics[146–148] and in energy storage.[149–151] The huge potential and utility of these compounds resulted in the Nobel Prize in Chemistry (2000) being rewarded to Alan Heeger, Alan MacDiarmid and Hideki Shirawaka for 'the discovery and development of conductive polymers'.[152,153] Some common examples include polyacetylene (**PA**), poly(*p*-phenylene vinylene) (**PPV**) and polythiophene (**PT**), shown in Figure 3.2.



polyacetylene (**PA**) poly(*p*-phenylene vinylene) (**PPV**) polythiophene (**PT**)

Figure 3.2. The structures of three commonly studied conjugated polymers **PA**, **PPV** and **PT**.

It is clear that the conjugation (and consequently structure) of these compounds is intrinsically linked to their photophysical properties, and so any elucidation of the relationship between molecular structure and electronic processes is useful.[154–156] Molecular vibrations are inherent probes of molecular structure as their energies are sensitive to changes in bonding or local environments. Infrared spectroscopy has been a vital tool for exploring the structure-property relationships that define π-conjugated compounds. Of particular interest has been the development of a suite of ultrafast infrared spectroscopies, made possible by the development of lasers and instrumentation with ever shorter instrument response times allowing for the probing of processes down to picosecond time scales.[157–162]

3.3 Ultrafast infrared spectroscopy – A chemist's introduction

The theory and interpretation of TRIR and 2D-IR will be covered first, with illustrative examples drawn from the literature, before summarising the techniques application to the analysis of π-conjugated materials in Section 3.4.

3.3.1 Time-resolved infrared (TRIR)

Time-resolved infrared (TRIR) spectroscopy is a pump-probe transient absorption technique. The fundamental concept is that of delivering two laser pulses to an absorbing

sample with precise control over the time by which the pulses are separated. The first laser pulse (the pump pulse) is used to excite the sample into a given electronic or vibrational state. The second laser pulse (the probe pulse) is used to examine the new state. By altering the time in-between pulses, the decay or relaxation dynamics of spectral features can provide insight into the populated states.

Although the purpose of the pump is to populate an excited state, in any given absorption event only a small subset of molecules is excited, and the subsequent probe light will be largely probing ground state molecules. This is why transient absorption spectra are often presented as difference spectra, where the spectrum of a given molecule *without* pump light (100% ground state, Figure 3.3a solid line) is subtracted from the spectrum of the molecule produced by the probe *with* pump light (x% excited state, [100 – x]% ground state, Figure 3.3a dashed line).

This treatment of the data results in several features common to all spectra. Firstly, the appearance of a negative signal in the location of the pumped mode is indicative of a ground state bleach (GSB) which occurs due to a reduction of signal in the ground state (due to the population of excited state modes). These GSBs are accompanied by transient excited state absorptions (ESAs), which are positive due to their appearance in the pump-on spectra. In the case of IR-pump IR-probe measurements, ESAs always appear at lower energy due to the anharmonicity of the vibrational potential (Figure 3.3d).

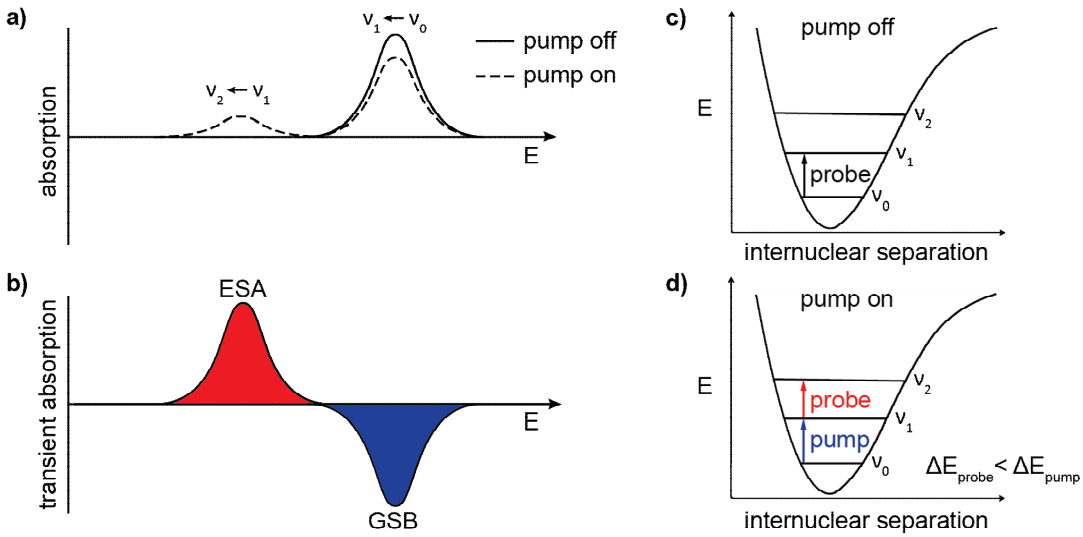


Figure 3.3. (a) Pump on and pump off IR absorption measurements of a simplified vibrational mode. (b) Difference spectra of the pump on and pump off spectra, showing GSB and ESA. (c) The observed transition by the probe in the pump off measurement and (d) the observed transition by the probe in the pump on measurement.

3.3.2 Applications of TRIR

Time-resolved infrared can be used for a host of applications. Often, it finds utility in problems requiring relating molecular and electronic structure. One benefit of TRIR over electronic spectroscopy is the relative narrowness of the infrared absorption bands, which makes them a finer handle with which to explore ultrafast dynamics. Infrared bands are also usually spatially localised (that is, a given infrared vibration can be assigned to a mode within a molecule), and so TRIR can provide more detailed insights into structural dynamics.[163]

Much of the research using TRIR focuses on examining the function of biological domains such as proteins due to the propensity of infrared modes to act as probes for local environment changes.[164–167] For example, seminal work by Hochstrasser and co-workers studied the amide-I band of peptides in detail, finding that the excitons formed upon excitation are delocalised along the length of the peptide, and that the vibrational energy transfer is efficient along the polypeptide chain.[168,169] The resulting models derived from TRIR spectroscopy have been utilised to elucidate the secondary-structure of proteins, which have been difficult and elusive with other techniques such as NMR and crystallography.[170–172]

Another useful development of TRIR spectroscopy has been that of polarisation-sensitive measurements.[163] By changing the relative orientations of the pump and probe laser pulses between parallel and perpendicular, the anisotropy can be recorded. If rotational diffusion is negligible, anisotropy measurements give the angle between the transition dipole moments of the pumped and probed transitions.[165,167,173] This relation has obvious applications to the elucidation of structure if the probed modes are sufficiently localised, such as in CO or CN stretches. For example, anisotropy measurements were used to experimentally determine conformation of the amino acid acetylproline-NH_2 (Figure 3.4a)[169] and the Fe-CO angle in haemoglobin (Figure 3.4b).[174]

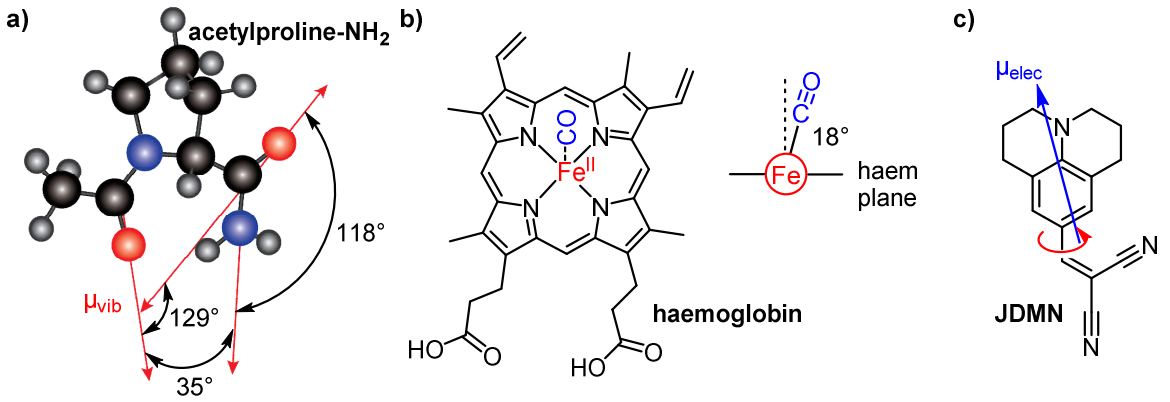


Figure 3.4. Examples of applications of polarisation-sensitive TRIR. (a) The conformation of acetylproline-NH_2, determined by anisotropy measurements between vibrational modes.[169] (b) The binding angle of CO to haemoglobin, determined by interrogating the CO frequency after photolysis with parallel and perpendicular pulses.[174] (c) Observation of a twisted intramolecular charge transfer (TICT) state via rotation (red arrow) upon excitation of the electronic dipole (blue) in juilolidinemalononitrile (**JDMN**) with polarisation-sensitive TRIR.[175] (a) adapted with permission from I. V. Rubtsov and R. M. Hochstrasser, *J. Phys. Chem. B*, 2002, **106**, 9165–9171. Copyright (2002) American Chemical Society. (c) adapted with permission from W. Zhang, Z. Lan, Z. Sun and K. J. Gaffney, *J. Phys. Chem. B*, 2012, **116**, 11527–11536. Copyright (2012) American Chemical Society.

Another illustrative example is the determination of the mechanism of photoisomerisation in juilolidinemalononitrile (**JDMN**).[175] By recording the anisotropy of the CN mode after pumping the photoinduced isomerisation absorption, rotation of the C-C bond of the malonitrile group was observed over time and the mechanism of isomerisation ascribed to proceed via a twisted intramolecular charge transfer (TICT) state.

3.3.3 Two-dimensional infrared spectroscopy (2D-IR)

Like with TRIR spectroscopy, two dimensional infrared spectroscopy (2D-IR) is a cutting-edge technique used to resolve structural and dynamic processes where techniques with slow time-scales (NMR) and with fast timescales (linear absorption spectroscopy) can fail.[176] 2D-IR spectroscopy can be thought of as the infrared analogue of 2D NMR spectroscopy, where a series of radiofrequency pulses are used to interact with nuclear spin transitions. In 2D-IR, however, the infrared pulses correspond to vibrational energy levels of the molecule.

In the simplest description of 2D-IR, it can be thought of as a collection of TRIR slices, where the pump bandwidth is infinitely small and corresponds to the value of the pump axis. In general, there are two methods for acquiring 2D-IR data: frequency domain double resonance 2D-IR[168] and a vibrational photon echo Fourier transform approach.[177] The frequency domain double resonance effectively collects sequential measurements of

pump-probe spectra using a variable 10 cm^{-1} pump pulse. The photon echo technique is an interferometric approach which allows for excitation of the entire pump axis simultaneously, offering faster acquisition times. Generally, the information contained in the resulting spectra is independent of the method chosen, and as such the experimental details of the two approaches are outside the scope of this introduction.*

2D-IR spectra have the general features shown in Figure 3.5a. In some aspects, they can be understood in a similar way to 2D NMR NOESY and COSY spectra, with some key differences. The first thing to note is the appearance of more peaks than are present in the linear FTIR. The negative (blue, 1) and the positive (red, 1') signals that sit on the green dashed line are signals resulting as a standard linear pump-probe experiment, described in Figure 3.3a.

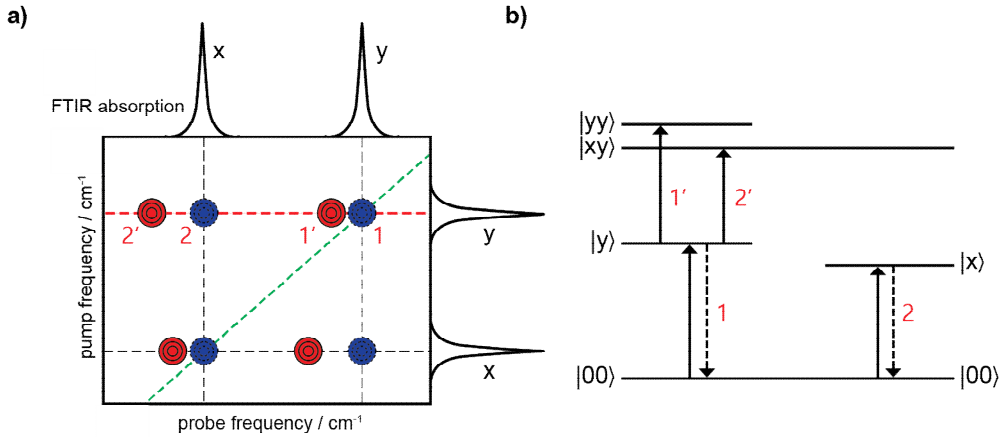


Figure 3.5. (a) Idealised 2D-IR spectrum of two coupled modes, x and y and (b) observed transitions when taking a slice through the 2D spectra (red line in (a)). The green dashed line is the diagonal axis where pump frequency = probe frequency.

The peak pairs away from the diagonal are 'off-diagonal' signals, or cross peaks. It is instructive to perform a thought experiment where a discrete pump (given by the red dashed line, Figure 3.5a) is applied. In the resulting spectra (termed a *slice*) there are four observed peaks. Figure 3.5b describes all of the observed transitions available after initial population of mode y by the pump pulse. The GSB on-diagonal (signal 1) is a negative feature due to the bleaching of the ground state by the pump (i.e. there is less population in the $|00\rangle$ state, so the observed absorption in the pump on experiment is smaller than the pump off). This signal is further amplified by stimulated emission of the $|y\rangle$ state (dashed lines). As some population of the molecules resides in the excited state of y, the

* A number of tutorial reviews[188,226] cover the basics of the experimental methods, and detailed comparisons between them have also been reported.[176,248]

probe light can excite this ensemble to |yy⟩. This transition (1', Figure 3.5b) is lower in energy due to the anharmonic potential of the vibrational mode (Figure 3.3d) and appears as an ESA at lower probe energies.

The off-diagonal GSB, 2, occurs at the pump frequency of the on-diagonal mode. This is because if the modes are coupled, then they share a ground state (|00⟩), and so the occupation of mode y by the pump will also bleach the ground state of mode x. When the probe light corresponding to transition 2 arrives after the pump, a smaller ensemble of molecules are excited resulting in a smaller absorption and negative signals in the difference spectra. The ESA at peak 2' is a transition from the v = 1 state of the y mode (occupied by the pump) to the combination band of y and x. The transition 2' is of different energy to that of 2; population of mode y has changed the energy of mode x so the modes are said to be *coupled*.

3.3.4 Applications of 2D-IR

At the most qualitative level, the appearance of off-diagonal peaks in a 2D-IR spectrum means the pumped modes are coupled – that is, the transition frequency of one oscillator depends on the excitation level of the other oscillator. More insight can be gained from 2D-IR spectra, but this often requires the development of suitable models which can be complex even in the relatively simple case of a dipole-dipole interaction between amide stretches in peptides.[178–180] However, once a model has been devised, such as the dipole-dipole model proposed in Figure 3.6, 2D-IR can offer a unique insight into molecular structure. Illustrative examples include the structural interrogation of DNA[181,182] and proteins.[179,183–186] For example, in Figure 3.6 the observed transition dipole moments of carbonyl stretches retrieved from 2D-IR measurements were combined with a dipole-dipole coupling model (Figure 3.6a/b), which allowed for elucidation of the α-helix peptide structure by finding the relative angles between the transitions Figure 3.6c.[183]

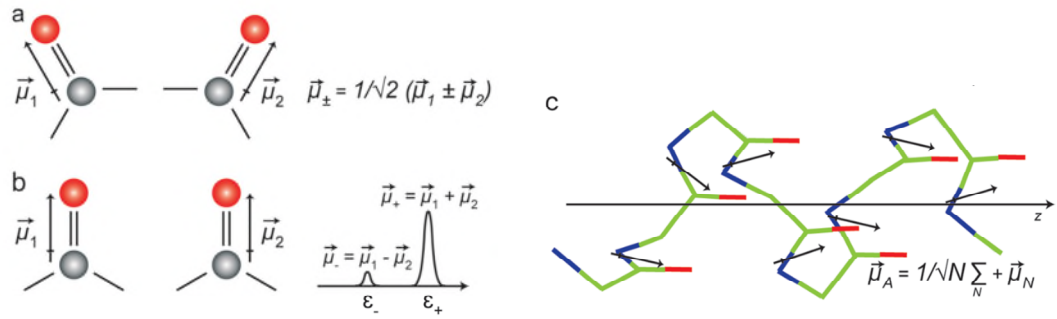


Figure 3.6. An example of a coupling model used in 2D-IR spectroscopy. (a) Two coupled carbonyl stretches are shown with their transition dipole moments and the total observed transition dipole, $\mu_{\pm}$. (b) Parallel vibrational modes in two nearby carbonyl stretches, showing how the coupling and therefore observed $\mu_{\pm}$ of the signals are related to the relative orientations and distance of the two modes. (c) A model α-helix peptide in which the carbonyl groups are shown in red and the transition dipole moments shown as black arrows. Analysis of the 2D-IR spectra allows for the observed transition dipole and therefore the coupling between modes to be determined, allowing 2D-IR to be used as a probe of structure. Adapted with permission from E. B. Dunkelberger, M. Grechko and M. T. Zanni, *J. Phys. Chem. B,* 2015, **119**, 14065–14075. Copyright (2015) American Chemical Society.

Other uses of 2D-IR spectroscopy include the analysis of molecular aggregates.[187] For example in the case of the dye $Re(CO)_3(bypy)CO_2H$ (**ReC**), aggregation results in changes to the observed coupling between vibrational modes, which in turn allows for identification of monomer, dimer and trimer 2D-IR spectra (Figure 3.7). These spectra were then used to determine the structure of deposited dyes on nanoparticles of TiO_2, providing information regarding the most effective methods for deposition to avoid unwanted dimer formation. The 2D-IR studies also allowed for the charge transfer between monomer, dimer and trimer to be studied.

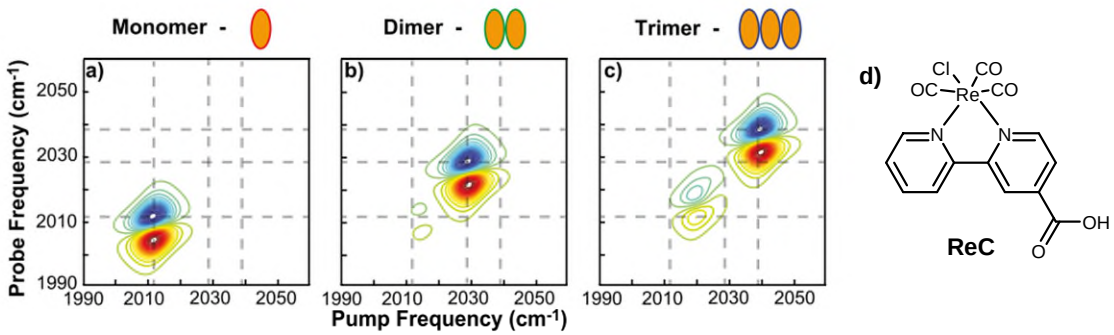


Figure 3.7. The 2D-IR spectra of the (a) monomer, (b) dimer and (c) trimer of dye (d) $Re(CO)_3(bypy)CO_2H$ (**ReC**). Reproduced from T. A. Oudenhoven, Y. Joo, J. E. Laaser, P. Gopalan and M. T. Zanni, *J. Chem. Phys.*, 2015, **142**, 212449 with the permission of AIP Publishing.

Rather than dipole-dipole coupling, sometimes the observed coupling can be the result of mechanical coupling or vibrational energy transfer such as in the work of Rubtsov and co-workers in the establishment of relaxation-assisted 2D-IR (RA-2D-IR). In RA-2D-IR, off-diagonal signals are observed as a result of intramolecular vibrational redistribution (IVR). A schematic description of IVR is shown in Figure 3.8a, where a mode ω_1 is excited by the

pump pulse. This mode transfers energy via IVR, populating a series of other modes in the molecule (purple arrows). Eventually, the mode ω_x is populated (green arrow) which happens to be strongly coupled to mode ω_2. Consequently, when the probe pulse populates ω_2, it finds a mode with different energy to the pump off measurement, and as such appears as an off-diagonal signal. It is worth noting that even though ω_2 is coupled to ω_x (and not directly to ω_1), the off-diagonal still appears at the pump frequency of ω_1 (i.e. the instrument does not know energy has been transferred via IVR, it only knows the wavelength of the initial pump excitation).

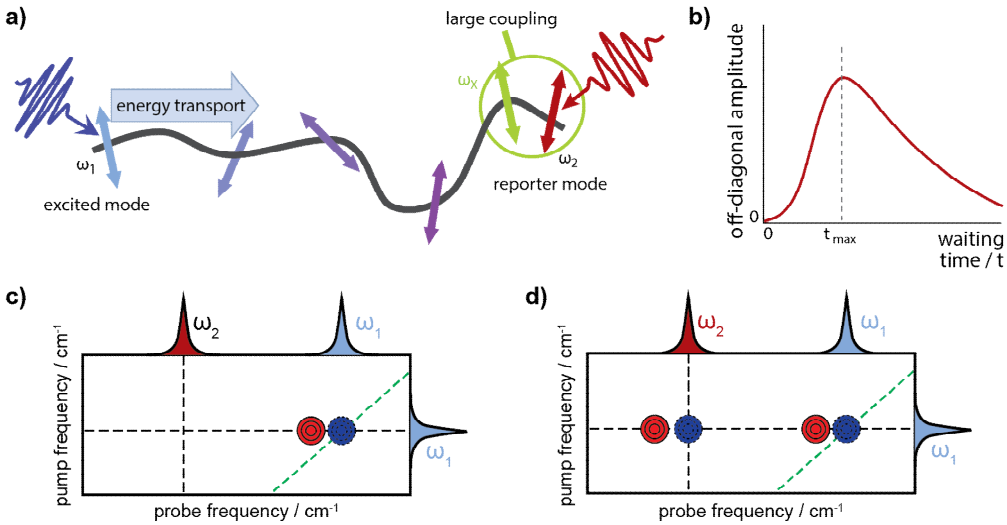


Figure 3.8. (a) Schematic representation of IVR/energy transfer. (b) Time dependant signal strength of the off-diagonal signal if occurring due to IVR. (c) The 2D-IR spectrum of IVR-coupled modes ω_1 and ω_2 at waiting time of t = 0 and (d) t = t_{max}. (a) and (b) adapted with permission of Annual Reviews, from N. I. Rubtsova and I. V. Rubtsov, *Annu. Rev. Phys. Chem.*, 2015, **66**, 717–738.; permission conveyed through Copyright Clearance Center, Inc.

A key hallmark of IVR is the time-dependence of the off-diagonal signals. In IVR, the coupling grows-in over time as the energy is transferred to different modes, whereas in other coupling regimes (such as dipole-dipole) the coupling is instantaneous. Therefore, in the case that ω_1 and ω_2 are not directly coupled, the off-diagonal intensity at t = 0 is negligible (Figure 3.8b) and the 2D-IR spectrum measured will consist of only on-diagonal signal pair (Figure 3.8c). At time t_{max} IVR has populated ω_x, and the resultant coupling to ω_2 causes an off-diagonal signal to appear (Figure 3.8d).

3.3.5 TRIR vs 2D-IR

2D-IR is effectively the two-dimensional analogue to TRIR, in a similar way that a 2D-NOESY NMR experiment relates to a 1D-NOE NMR experiment. The benefits and drawbacks are also comparable to the NMR experiments; in general 2D spectra take

longer to accumulate and require more complex data processing. However, in 2D-IR, the resolution of the pump axis is the major advantage over that of TRIR. In TRIR, if the pump bandwidth is larger than the difference between the probed modes then the observed spectrum will be a combination of on-diagonal and off-diagonal peaks (this can be thought of as all of the pump axis collapsing into one trace).

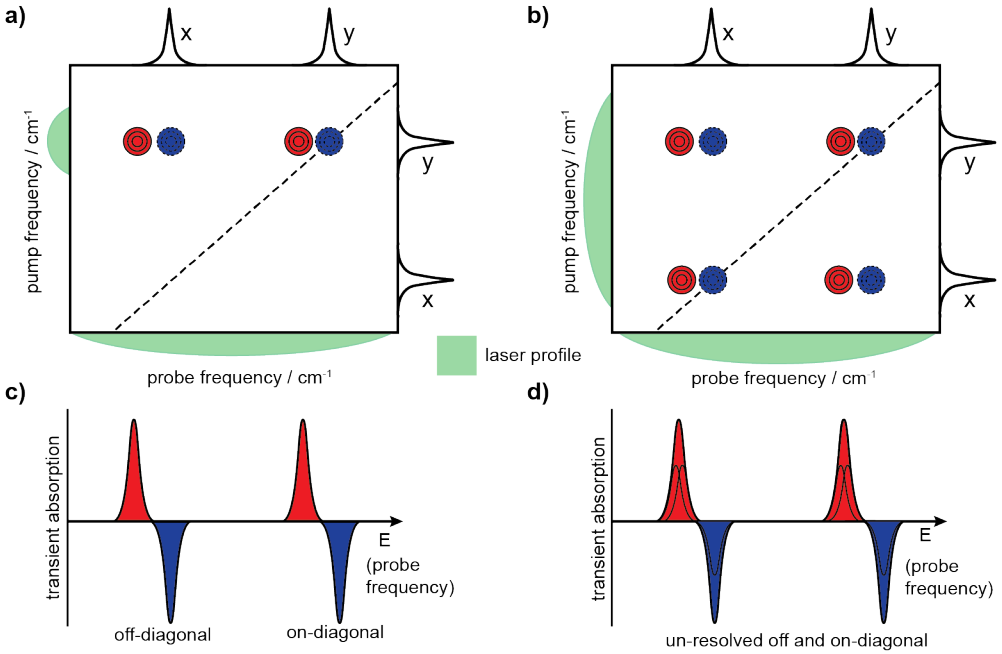


Figure 3.9. (a) 2D-IR spectrum with a narrowband pump pulse centred on mode y. (b) 2D-IR spectrum with a broadband pump exciting both x and y modes. (c) The observed TRIR spectrum using the same laser set up as in (a) showing the clear identification of on and off-diagonal modes. (d) The observed TRIR spectrum using the same laser set up as (b), showing the loss of off-diagonal information.

The utility of 2D-IR therefore arises due to the technical limitations affecting pump bandwidths. If the pump bandwidth is centred on a single mode and is sufficiently narrow to excite that one mode only (such as y in Figure 3.9a), then a TRIR experiment will provide largely the same information as 2D-IR. However, if the pump bandwidth is broad and excites more than one vibrational mode (such as x and y in Figure 3.9b) the TRIR spectrum will lose the coupling information. As the time response of the pump pulse (i.e. its temporal length) is inversely proportional to the band width due to Heisenberg's uncertainty principle,[176] there is a limit to the narrowness of the pump bandwidth achievable without losing early time kinetics.

In general, TRIR is useful when pumped and probed processes are not spectrally close (such as in UV-vis pump, IR probe experiments). 2D-IR is a more useful technique in areas of crowded signals, as the resolved pump axis removes the technical limitations of

the pump bandwidth. The examination of 2D-IR lineshapes can also provide more information about the structure in question, such as homogenous and inhomogenous broadening processes due to changes in local environments.[188–192]

3.4 Ultrafast IR spectroscopy applied to π-conjugated materials

Molecular vibrations are sensitive to their local environment, and provide a handle with which to monitor the mechanisms of electronic processes.[193] For example, TRIR has been extensively used to probe electron transfer reactions between donor and acceptors. Examples include studies between small molecule systems (Figure 3.10a)[194] and between polymer (polythiophene, **PT**) and electron acceptor (phenyl-C61-butyric acid methyl ester, **PCBM**) layers in OPV devices (Figure 3.10b).[193,195,196] In both cases, initial photoexcitation is followed by monitoring of IR modes of interest with TRIR, which allows analysis of the characteristic dynamics and interpretation of charge transport mechanisms.

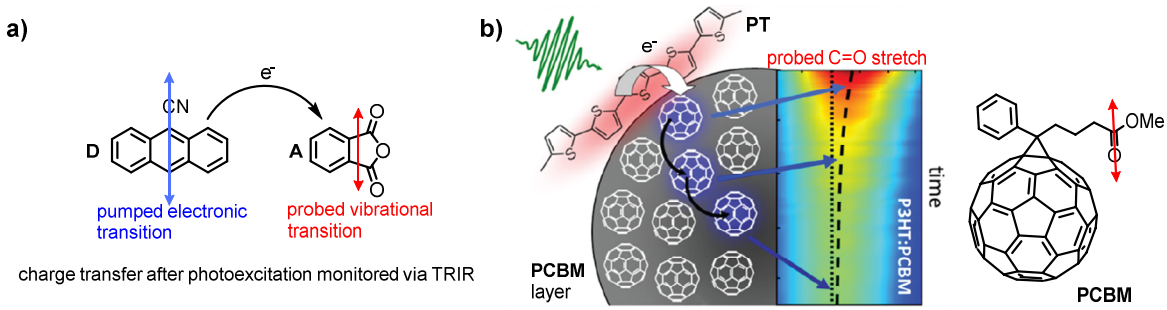


Figure 3.10. Examples of TRIR charge transport studies. (a) The study of electron transfer between donor (**D**) and acceptor (**A**) by probing a vibrational transition (red) after photoexcitation event (blue).[194] (b) The study of charge transport in polythiophene (**PT**) and phenyl-C61-butyric acid methyl ester (**PCBM**) based OPVs.[195] (b) adapted from R. D. Pensack and J. B. Asbury, *Chem. Phys. Lett.*, 2011, **515**, 197–205, Copyright (2011), with permission from Elsevier.

There are some interesting features observed in the TRIR spectra of π-conjugated materials. For example, in a study of poly{[2-methoxy-5-(2-ethylhexyloxy)-1,4-phenylene]vinylene} (**MEH-PPV**) and 1,5-dinitroanthraquinone (**DNAQ**) blends characteristic broad mid-IR absorptions are observed upon charge separation, as well as intensified infrared modes (infrared active vibrations, or IRAVs - Figure 3.11).[197]

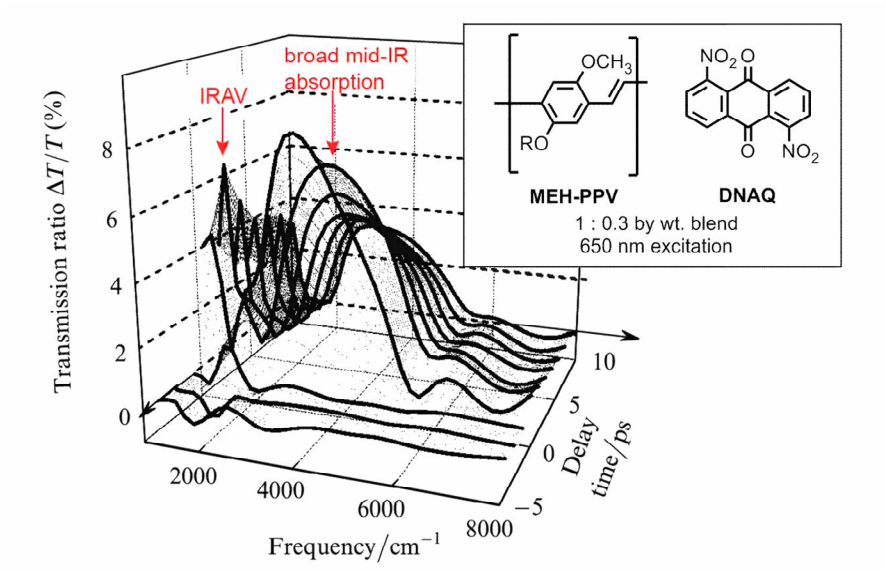


Figure 3.11. TRIR (UV pump, IR probe) spectra of MEH-PPV/DNAQ blend (structures inset) with 650 nm excitation. Photoinduced charge-separated state displays a broad mid-IR absorption and IRAV signals characteristic of polarons. Adapted from A. A. Bakulin, D. Y. Parashchuk, P. van Loosdrecht and M. S. Pshenichnikov, *Quantum Electron.*, 2009, **39**, 643–648, Copyright (2009) 2009 Kvantovaya Elektronika and Turpion Ltd.

These features are as a result of polaron formation. A polaron is a quasiparticle that consists of a localised charge on a conjugated molecule and an associated local lattice distortion, or geometrical redistribution of nuclear co-ordinates.[198] This can be broadly interpreted as a change in structure of the conjugated backbone in response to the formation of a hole or electron. This is understood in the physics literature to be an example of electron-phonon coupling, where localised vibrations localise the charge within the conjugated backbone.[154,199] In conjugated materials, one can often visualise this as a localised change in conjugation along the polymer backbone, for example a polaron in **PT** has been described as shown in Figure 3.12.[198,200,201]

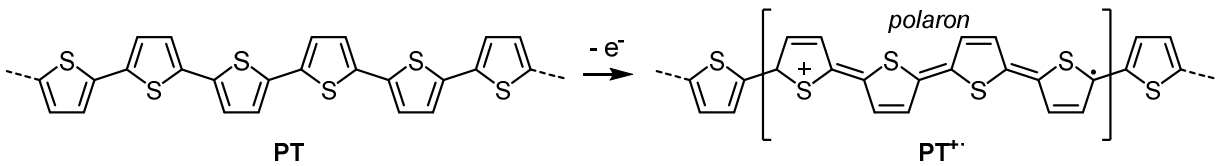


Figure 3.12. Polythiophene (**PT**) and the proposed polaron structure, highlighting the localised charge caused by a redistribution of nuclear co-ordinates (in this case a change in conjugated backbone), localised over four units.[200,201]

The majority of spectra in which these unique polaron features (the phenomenological origins of which will be discussed in Section 4.2.1) have been reported have been photo-excited charge-separated states (i.e. a visible light pump, infrared probe).[173,197,202–208] Little research has been directed at observing the coupling behaviour *between* IRAVs or the dynamics observed after IR-pump, IR-probe experiments. To undertake these

experiments, it is necessary to either add another pump pulse (to form the charge-separated state, then infrared pump, infrared probe) or to chemically generate the charged species first.

In the case of three pump experiments where polarons are generated with a UV pulse, so far only the dynamics of the mid-IR polaron bands have been explored.[209,210] Of the systems where chemically or electrochemically generated charged species are explored, generally only ground state IR spectroscopy have been recorded.[154,209,211–213]

3.5 Prospectus

Ultrafast infrared spectroscopies are cutting-edge techniques useful for the elucidation of structure-property relationships. The ability to probe local IR modes, which are intrinsic probes of molecular structure, allows for insights into ultrafast processes. Some of these processes, such as charge transport or delocalisation in conjugated polymers, are essential for the development of functional π-conjugated materials.

TRIR studies of π-conjugated materials have shown the existence of polarons along the polymer backbone by identification of the hallmark IRAV and mid-IR polaron bands. However, no studies to our knowledge have sought to explore the IR-pump, IR-probe spectroscopy of these features. We have seen that ultrafast IR spectroscopies provide unique information about the structural response to electronic processes, and so it follows that performing TRIR and 2D-IR on these systems will give valuable insights into the structural origins of these polaron features.

4

Ultrafast Spectroscopies as Tools for Exploring Infrared-Active Vibrations (IRAVs) in Porphyrin Molecular Wires

4.1 Abstract 111

4.2 Introduction 111

4.2.1 Charge transport, polarons and IRAVs 111

4.2.2 Porphyrin radical cations 113

4.2.3 Spectroscopic approach 115

4.3 Results 116

4.3.1 Single shot 2D-IR – ULTRA 116

4.3.2 LIFEtime TR-2D-IR 118

4.3.3 Fitting of spectrokinetic data 122

4.3.4 TRIR spectroscopy 125

4.3.5 DFT calculations 127

4.4 Discussion 128

4.5 Experimental Appendices 132

4.5.1 Synthesis 132

4.5.2 Photophysical investigations 132

4.5.3 2D-IR kinetic fitting 136

1.1.1 Grow-in fitting 141

4.5.4 LIFEtime time domain traces 146

4.5.5 Polarisation sensitive TRIR 150

Parts of this chapter were published in: W. J. Kendrick, M. Jirásek, M. D. Peeks, G. M. Greetham, I. V. Sazanovich, P. M. Donaldson, M. Towrie, A. W. Parker and H. L. Anderson, 'Mechanisms of IR Amplification', *Chem. Sci.*, ASAP, DOI: 10.1039/c9sc05717j.

4.1 Abstract

Unusually intense vibrational bands known as *infrared active vibrations* (IRAVs) are found in the radical cations of some conjugated polymers. Here, we investigate the mechanistic origin of this amplification, and show that it provides insights into intramolecular charge migration. Spectroelectrochemical time-resolved infrared (TRIR) and two-dimensional infrared (2D-IR) spectroscopies were used to investigate the radical cations of two butadiyne-linked conjugated porphyrin oligomers, a linear dimer and a cyclic hexamer. The 2D-IR spectra reveal strong coupling between all the IRAVs and the electronic π-π* polaron band. Intramolecular vibrational energy redistribution (IVR) and vibrational relaxation occur within ~0.1–7 ps. TRIR spectra show that the transient ground state bleach (GSB) and excited state absorption (ESA) signals have anisotropies of 0.31 ± 0.07 and 0.08 ± 0.04 for the linear dimer and cyclic hexamer cations, respectively. The small TRIR anisotropy for the cyclic hexamer radical cation indicates that the vibrationally excited polaron migrates round the nanoring on a time scale faster than the measurement, i.e. within 0.5 ps, at 298 K. Density functional theory (DFT) calculations qualitatively reproduce the emergence of the IRAVs. The first singlet (S_1) excited states of the neutral porphyrin oligomers exhibit similar IRAVs to the radical cations, implying that the excitons have similar electronic structures to polarons. Our results show that IRAVs originate from the strong coupling of charge redistribution to nuclear motion, and from the similar energies of electronic and vibrational transitions.

4.2 Introduction

4.2.1 Charge Transport, Polarons and IRAVs

Understanding of charge transport and structure-property relationships in π-conjugated polymers has been essential for the development of organic field-effect transistors (OFETs)[92], organic solar cells[89,91,140] and light-emitting devices such as organic LEDs (OLEDs).[143] The study of charge transport in molecular systems is particularly appealing due to the well characterised nature of the molecular electronic and vibrational structure, which encourages attempts to relate properties to structure.[214]

One theoretical model for charge transport in π-conjugated polymers is that of polaron theory. Here, charges on a conjugated molecule are associated with a lattice distortion, or geometrical redistribution of the nuclear co-ordinates.[198] This can be

broadly understood as a change in structure of the conjugated backbone in response to the presence of a hole or electron. This is understood in the physics literature to be an example of electron-phonon coupling, where vibrations localise the charge within the conjugated backbone.[154,199] Therefore exploring the coupling of electrons and electronic processes to nuclear motions (molecular vibrations) is essential to the understanding of processes occurring in conjugated organic electronic materials.[212]

Polarons are found in π-conjugated polymers or oligomers, for example; in photoexcited charge-separated states of neutral species,[173,197,202–205] in the ground state of the radical cations/anions[211] or in the ground state of doped polymer blends (effectively radical cations or anions due to the charge separated state stabilised by the dopant).[212,215]

There are two common spectroscopic hallmarks of polarons. The first is the observation of broad mid-IR absorptions, referred to here as 'polaron bands'. These are classically electronic transitions arising from newly formed transitions out of and into the singly occupied molecular orbital (SOMO, Figure 4.1b). They are of low energy due to the appearance of these new states within the previous HOMO-LUMO gap (or band gap in polymers).

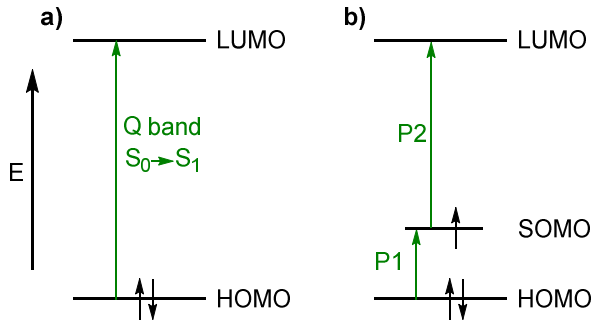


Figure 4.1. (a) The Q band absorption energy level diagram for a porphyrin. (b) Generalised energy level diagram of a polaron, showing the appearance of a singly occupied molecular orbital (SOMO) within the HOMO-LUMO gap. Two polaron bands, P_1 and P_2 bands, are formed upon hole insertion, resulting in two new observed transitions with reduced energies, and hence explaining the appearance of new electronic absorption bands in the mid-IR being a hallmark of polaron formation.[213]

Another hallmark is that of infrared active vibrations, or IRAVs, which are infrared modes with enhanced intensities compared to ground state neutral molecules. IRAVS are reported in conjugated polymer polarons[215,216] and mixed-valence coordination complexes.[217] Their behaviour has been traditionally attributed to infrared activation of Raman modes through loss of symmetry from changes in electric fields.[202,216,218] More recently, however, their phenomenological origin has been attributed to two processes:

polaron (and consequently charge) redistribution coupling to vibrations, increasing the transition dipole moment (Figure 4.2a), or mixing between low-lying electronic and vibrational transitions (Figure 4.2b).[215,217,219,220]

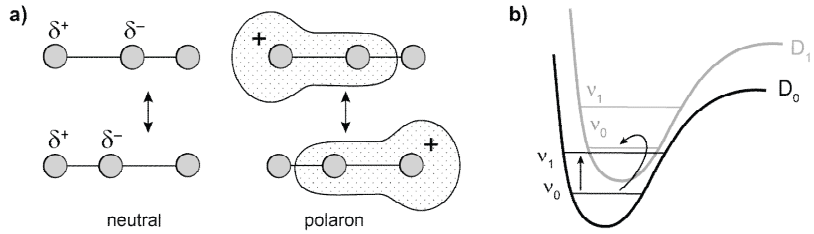


Figure 4.2. Schematic representation of two possible origins of IRAVs. a) The polaron redistributes along the backbone in response a molecular vibration. b) The energies of electronic and vibrational transitions are comparable, leading to strong vibronic coupling.

4.2.2 Porphyrin Radical Cations

Oxidation of a family of π-conjugated porphyrin molecular wires has been shown to form radical cations that exhibit atypical behaviour with respect to the intensity of their electronic and vibrational transitions. The radical cations exhibit a low-energy electronic absorption band in the region 1500–6000 cm^{-1} consistent with the formation of a polaron and the corresponding P_1 transition between the highest occupied molecular orbital (HOMO) and the singly occupied molecular orbital (SOMO).[213,221,222] Another remarkable feature is the intensification of the infrared transitions compared with the neutral compounds (ε ≈ 10–70 mM^{-1} cm^{-1}, for a comparison to the neutrals see Appendix 4.5.2, Figure 4.19 and Figure 4.20) consistent with the previously reported phenomena of IRAVs.[99,221,223] Either of the mechanisms in Figure 4.2 could explain the IRAVs in doped butadiyne-linked porphyrin oligomers, especially as we have shown that the energy of the formally electronic P_1 transition is similar to those of the classically vibrational IRAV transitions (Figure 4.3b).[99]

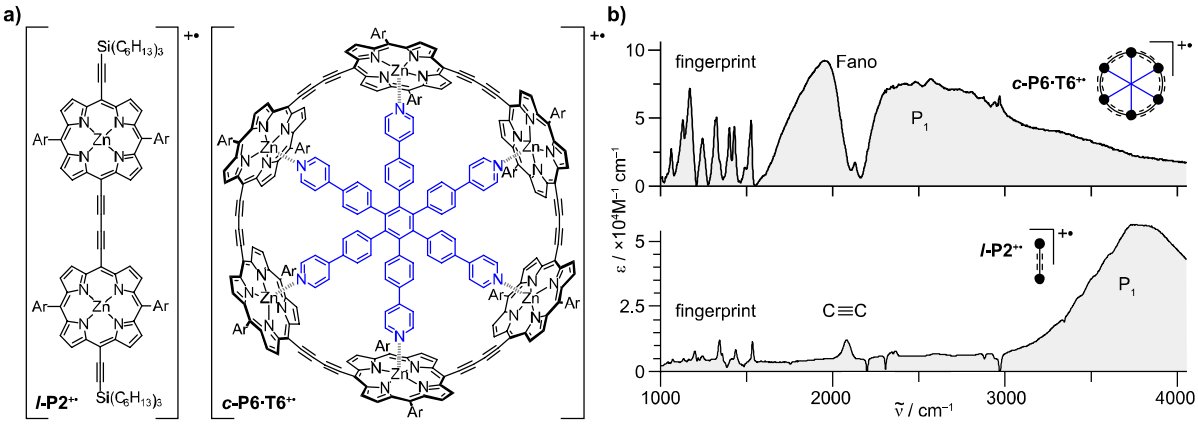


Figure 4.3. (a) Chemical structures of the porphyrin oligomer radical cations ***l*-P2**$^{+\bullet}$ and ***c*-P6·T6**$^{+\bullet}$. Ar = 3,5-bis(trihexylsilyl)phenyl. (b) Their FTIR spectra recorded in CD_2Cl_2 showing the fingerprint region, the C≡C stretch band, the Fano anti-resonance (for ***c*-P6·T6**$^{+\bullet}$) and the P_1 polaron band.

The butadiyne-linked porphyrin oligomer radical cations represent suitable systems to explore the behaviour of IRAVs using advanced ultrafast spectroscopies including two-dimensional infrared spectroscopy (2D-IR) and time-resolved infrared spectroscopy (TRIR). Although polarisation-sensitive ultrafast spectroscopies have been used previously to explore IRAVs[173] and two-dimensional electronic spectroscopy (2D-ES) to explore polarons,[224] both of these studies were undertaken with conjugated polymer blends. This is in contrast to the discrete molecular nature of our systems, which will allow us to elucidate structure-property relationships of polarons on a molecular wire.

Previous work suggests the polaron (i.e. positive charge) in our systems is delocalised over 2–3 porphyrin units, and demonstrates that the charge is fully delocalised in the dimer radical cation (Robin-Day class III).[99] Consequently, we propose the linear dimer ***l*-P2**$^{+\bullet}$ as a model molecular polaron, and contrast its properties with that of the cyclic hexamer ***c*-P6·T6**$^{+\bullet}$ (Figure 4.3a). The dimer radical cation ***l*-P2**$^{+\bullet}$ exhibits a broad P_1 absorption band of electronic origin in the region > 3000 cm^{-1}; a band around 2050 cm^{-1} which is characteristic of the C≡C alkynyl stretch as a discrete intensified vibrational-like absorption; and series of IRAVs in the fingerprint region (1000–1600 cm^{-1}).

The C≡C vibrational stretch must be aligned along the backbone of the porphyrin molecular wire, and this absorption in ***l*-P2**$^{+\bullet}$ is isolated in energy between the formally electronic P_1 band and the other IRAVs in the IR fingerprint region, providing a unique handle to explore the behaviour of the polaron and IRAVs. Conversely, ***c*-P6·T6**$^{+\bullet}$ shows a Fano-type antiresonance at this energy, due to the overlap of the C≡C vibrational alkynyl

stretch with the lower-energy lying P_1 polaron electronic band (Figure 4.3b).[99] This overlap causes a cancellation of oscillator strengths due to quantum interference between the electronic continuum and discrete vibrational transition.[202,222,225]

4.2.3 Spectroscopic approach

The interesting spectral features are found in the IR and mid-IR, and so 2D-IR and TRIR were chosen as the spectroscopies of choice. 2D-IR is a technique used to elucidate equilibrium structural dynamics, vibrational mode coupling and energy transfer in complex molecular structures.[176,188,226,227] It offers simultaneous resolution of the pump and probe axes, as well as ultrafast time resolution (< 1 ps), providing a snapshot of the coupling between vibrational modes at a given pump-probe delay time.[228] Coupling between modes is evidenced by the appearance of off-diagonal signals (c.f. 2D NMR experiments). The interpretation of the coupling is dependent on defining a suitable model, which are often complex even in the case of the relatively simple amide stretch in peptides.[178–180] However, in the most simplified description of coupling the appearance of off-diagonal signals show that the occupation of one vibrational mode leads to a change in energy or character of another.[176] Recording data at varying delay times between pump and probe pulses extends the utility of the technique, enabling analysis of chemical dynamics and kinetic decay processes using a time-resolved 2D-IR experiment (TR-2D-IR).

Time-resolved infrared offers similar insights to 2D-IR, at the expense of a resolved pump axis (c.f. a 1D NOE experiment compared to a 2D NOESY in NMR). For practical reasons TRIR offers faster time response and broader pump and probe pulses, allowing for simultaneous capture of a larger spectral range in a shorter time period. The shorter acquisition times allow for collection of parallel and perpendicular polarised pump-probe orientations without lengthening the time required to perform the experiment by an unsuitable amount (either in terms of sample stability or practicality). The capability to perform polarisation-sensitive TR-IR extends the utility of the technique further, and has been used to probe the angles between molecular vibrations or transition dipoles,[165,167,175] probe molecular dynamics and to study (de)localisation of charged states and excitons.[155,173,197]

With our collaborators at the Central Laser Facility (CLF) we have access to two general laser systems; LIFEtime and ULTRA, described in detail elsewhere.[228] LIFEtime is

an ytterbium laser system with narrower band, longer pulses (100 kHz, > 180 fs, < 200 cm^{-1}). ULTRA is a titanium sapphire amplifier system with broadband, shorter pulse capability (10 kHz, > 50 fs, > 300 cm^{-1}). The ULTRA systems larger bandwidth allows a broader spectral range to be excited by the pump, allowing for the simultaneous capture of more of the pump axis. This is important for simultaneously exciting multiple modes and examining the coupling between them. In practice, ULTRA allows for the recording of larger pump/probe regions but at the expense of longer acquisition times, which makes it more difficult to record TR-2D-IR (that is a sequence of pump-probe delays) when the sample is unstable. ULTRA is still the system of choice for TR-IR (where acquisition times are fast due to not requiring the resolved pump axis) and single-shot 2D-IR due to the beneficial broader spectral windows. TR-2D-IR was undertaken on LIFEtime to take advantage of the faster acquisition times.

4.3 Results

The data collected can be split into three different techniques: single shot broadband 2D-IR, narrowerband TR-2D-IR and polarisation-sensitive TRIR. The three experiments are complementary regarding the information they provide, and as such the results of each experiment are discussed first with the discussion following later.

4.3.1 Single shot 2D-IR – ULTRA

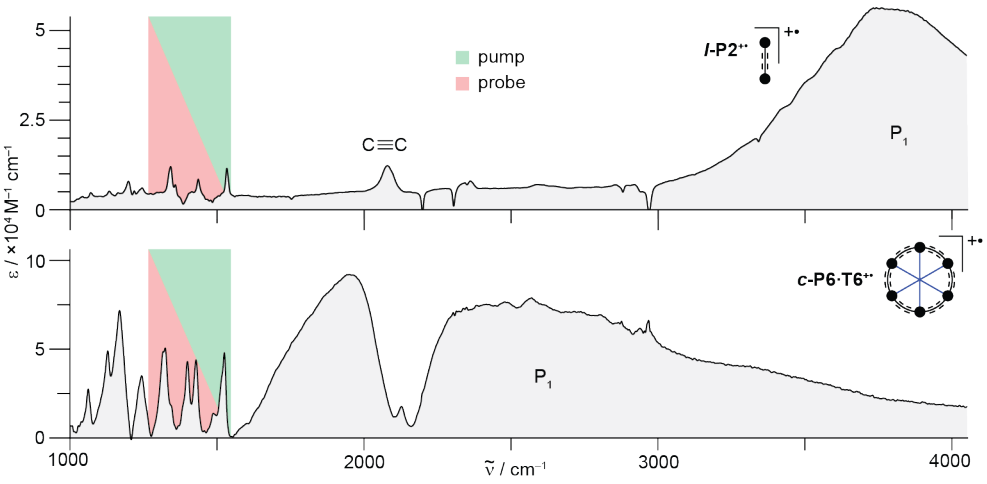


Figure 4.4. Pumped (green) and probed (red) areas of ***l*-P2$^{+\bullet}$** and ***c*-P6·T6$^{+\bullet}$** during ULTRA 2D-IR measurements.

Broadband ULTRA (full-width at half-maximum, FWHM, ~150 cm^{-1}) was used to record 2D-IR spectra of the fingerprint region (1200–1600 cm^{-1}, Figure 4.4). The 2D-IR spectra of the oxidised species ***l*-P2$^{+\bullet}$** and ***c*-P6·T6$^{+\bullet}$** at 500 fs (Figure 4.5 and Figure 4.6) show

significant coupling between the majority of the modes as evidenced by the appearance of off-diagonal features.

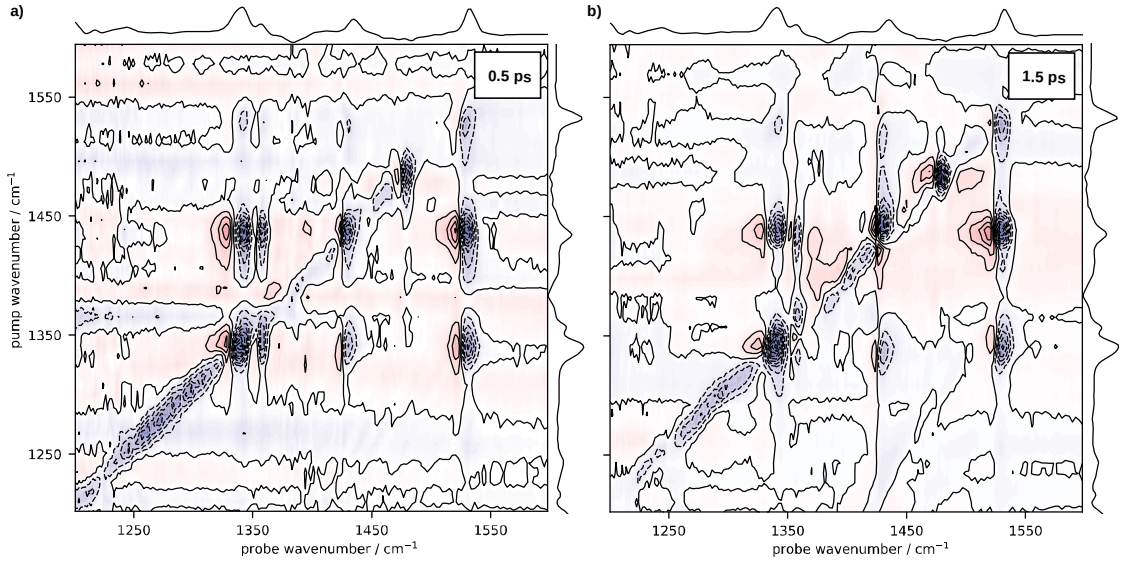


Figure 4.5. 2D-IR spectra of ***l*-P2$^{+\bullet}$** at (a) 0.5 ps delay and (b) 1.5 ps delay in the fingerprint region. Blue and red correspond to positive (ESA) and negative (GSB) signals, respectively. Colour maps are not shared between spectra. Spectra were recorded using a broadband pump centred at ~1325 cm^{-1} (FWHM ~150 cm^{-1}). Optical densities of all samples were ~0.2–0.4 in the fingerprint region.

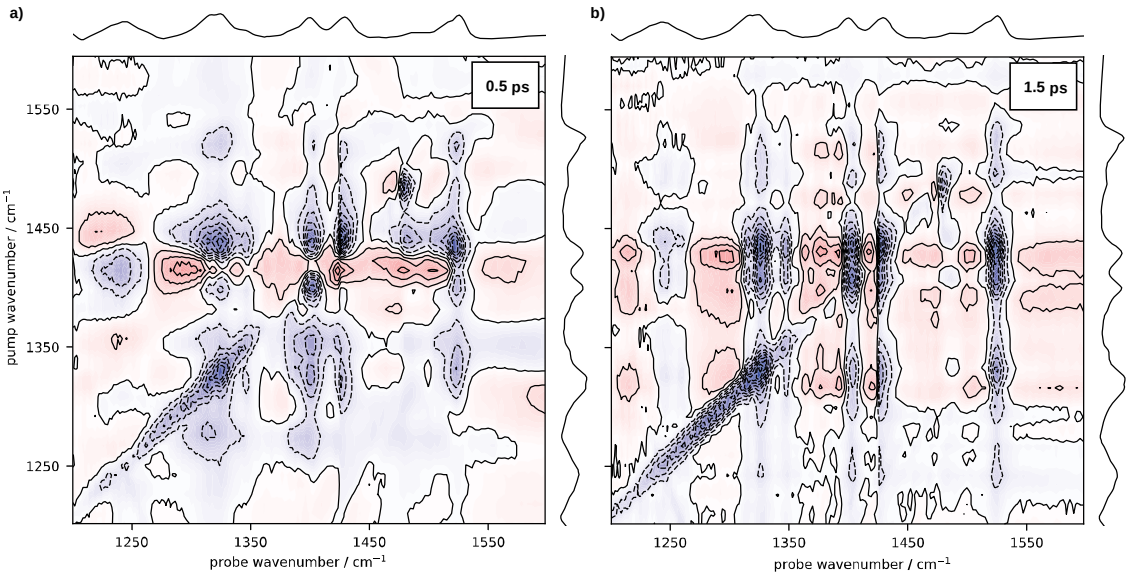


Figure 4.6. 2D-IR spectra of ***c*-P6·T6$^{+\bullet}$** at (a) 0.5 ps delay and (b) 1.5 ps delay in the fingerprint region. Blue and red correspond to positive (ESA) and negative (GSB) signals, respectively. Colour maps are not shared between spectra. Spectra were recorded using a broadband pump centred at ~1325 cm^{-1} (FWHM ~150 cm^{-1}). Optical densities of all samples were ~0.2–0.4 in the fingerprint region.

The ground states bleaches (GSB) in blue are present for every pumped and probed mode as both on-diagonal and off-diagonal signals, indicating coupling. Usually for every GSB there is an associated excited state absorption (ESA) corresponding to the $\nu_2 \leftarrow \nu_1$ transition, which is shifted to lower energy due to the anharmonicity of the vibrational

mode (see Section 3.3.1). At early times though (Figure 4.5a, Figure 4.6a), there is a general feature of the spectra being dominated by the GSB. At later times (Figure 4.5b, Figure 4.6b) the spectra show much more pronounced ESAs with signal strengths of similar magnitudes to the GSB. In general, the GSBs of ***c*-P6·T6$^{+\bullet}$** are expected to be more intense due to the quadratic dependence of signal intensities on the molar absorption coefficient, which is borne out in the spectra.[176] The on-diagonal peak at ~1480 cm^{-1} appearing in both monocation spectra result from residual neutral species, which show a strong on-diagonal peak at this wavelength (Figure 4.7).

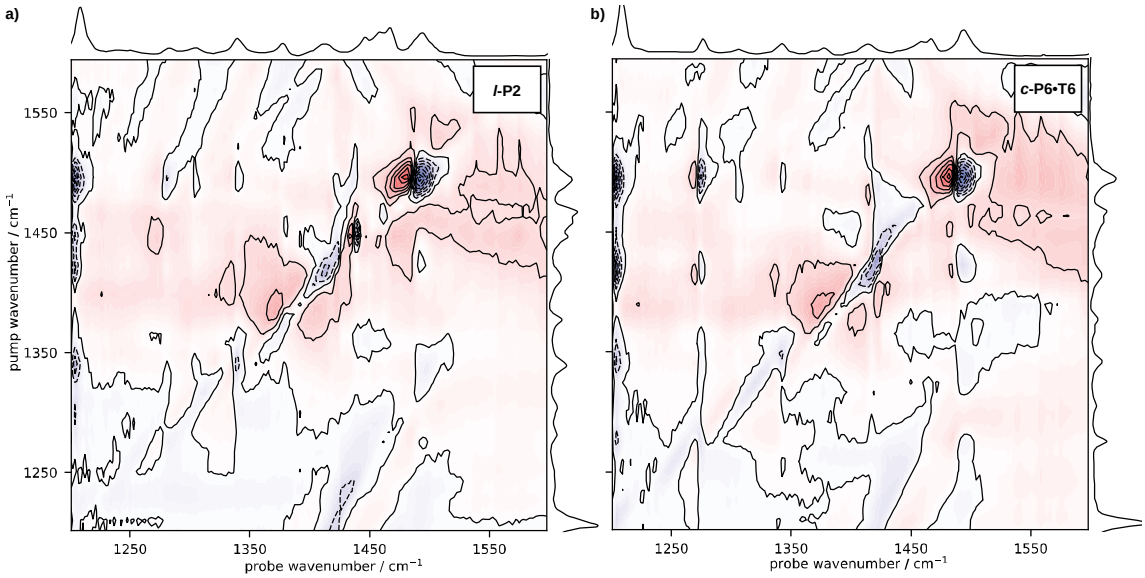


Figure 4.7. 2D-IR spectra of (a) ***l*-P2** and (b) ***c*-P6·T6** at 0.4 ps delay in the fingerprint region. Blue and red correspond to positive (ESA) and negative (GSB) signals, respectively. Colour maps are not shared between spectra. Spectra were recorded using a broadband pump centred at ~1325 cm−1 (FWHM ~150 cm−1). Optical densities of all samples were ~0.2–0.4 in the fingerprint region.

The strong coupling between the IRAVs in ***l*-P2$^{+\bullet}$** and ***c*-P6·T6$^{+\bullet}$** was cause for further investigation. If the couplings between IRAVs are electrostatic in nature, then these modes must share an alignment of their transition dipole moments,[160,176] and if they are mechanically coupled then there must be significant overlap between the coupled modes normal co-ordinates.[229,230] In either case, the spectra show the IRAVs are coupled strongly, and all of the modes are coupled together in the fingerprint region, which suggests a significant degree of shared character and/or origin between them.

4.3.2 LIFEtime TR-2D-IR

Knowing that the IRAVs are coupled, it was decided to try and investigate their spatial relationship to each other. The C≡C stretch in ***l*-P2$^{+\bullet}$** must be along the backbone of the

porphyrin molecular wire and so its direction with respect to the rest of the molecule is well known. It therefore offers a structurally well-defined and spectrally isolated mode, which will aid the interpretation of couplings and of anisotropy measurements and make it an ideal handle with which to explore structure-property relationships of the IRAVs.[165,167,175] As the alkynyl stretch is well isolated from other modes, the broadband pump in ULTRA is not necessary. Instead, the narrower band (FWHM ~80 cm^{-1}) LIFEtime instrument could be used which has the benefit of faster acquisition times, and consequently the ability to record multiple pump – probe delays to perform a time-resolved 2D-IR experiment (TR-2D-IR).[228]

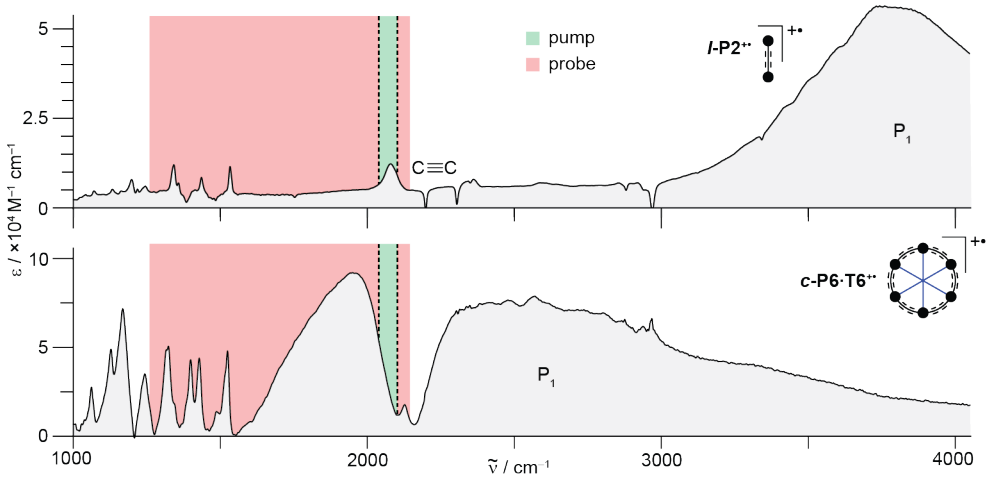


Figure 4.8. Pumped (green) and probed (red) areas of ***l*-P2**$^{+\bullet}$ and ***c*-P6·T6**$^{+\bullet}$ during LIFEtime TR-2D-IR measurements.

A full population-time-delay series was recorded for probe regions 1300 to 2150 cm^{-1} (Figure 4.8, red area). In these experiments a narrowband pump was centred at 2050–2100 cm^{-1} (Figure 4.8, blue area), in direct resonance with the C≡C stretch of ***l*-P2**$^{+\bullet}$ and with the Fano-type anti-resonance in the P_1 band of ***c*-P6·T6**$^{+\bullet}$. The molecular responses were probed by recording two spectral windows simultaneously: probe **a** and probe **b**. Probe **a**, was set to one of four spectral regions centred at ~1370 cm^{-1}, 1520 cm^{-1}, 1650 cm^{-1} or 1800 cm^{-1} for each experiment. Probe **b** was set to the on-diagonal region centred at 2025 cm^{-1}, giving a shared spectral window between each experiment and allowing normalisation.

In the resulting 2D-IR spectra (Figure 4.9, Figure 4.10), off-diagonal signals appear immediately (within 200 fs) for all the IRAVs in the FTIR spectra. Each IRAV probed below 1600 cm^{-1} appears as a GSB with associated ESA as a result of the $\nu_2 \leftarrow \nu_1$ transition occurring at lower energies due to vibrational mode anharmonicity. The GSB signals (blue)

are much stronger at earlier times compared to the anharmonic ESA signals (red), commensurate with the 2D-IR spectra shown in Figure 4.5 and Figure 4.6 recorded with the broadband ULTRA.

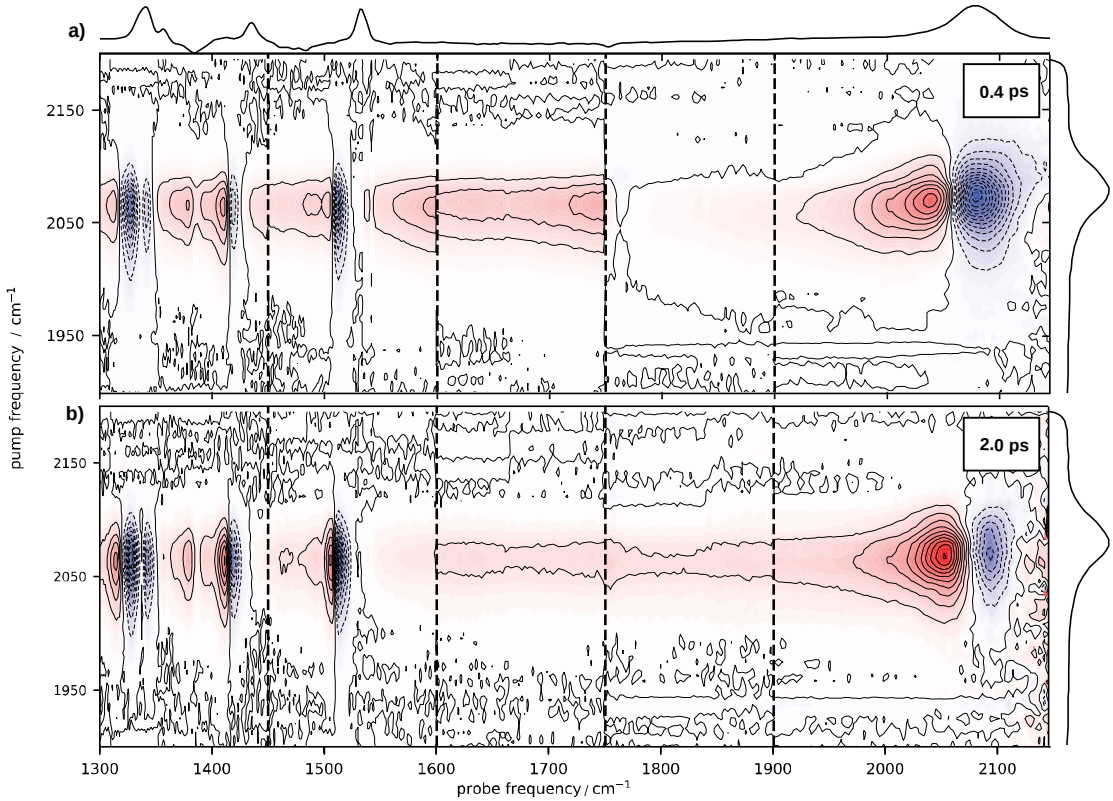


Figure 4.9. 2D-IR spectra of ***l*-P2$^{+\bullet}$** at (a) 0.4 ps delay and (b) 2.0 ps delay, with pump (FWHM ~80 cm^{-1}) centred at 2050 cm^{-1}. Red and blue correspond to positive (ESA) and negative (GSB) signals, respectively. Vertical dashed lines correspond to different experimental spectra, where probe **a** was changed to cover region 1300 cm^{-1} to 1900 cm^{-1} and probe **b** was centreed in the 1900–2150 cm^{-1} region for each experiment (see Appendix 4.5.4.1 for time resolution of each probe window). Probe windows in 1300–1900 cm^{-1} were stitched together by normalising all probe **a** spectra to probe. Colour maps are not shared between (a) and (b) to highlight smaller late-time features.

One major difference between the two species is the absence of a positive ESA signal in the on-diagonal region of the ***c*-P6·T6$^{+\bullet}$** spectra at early times. We observe a broad positive ESA band that extends across the whole spectrum, which appears to be primarily electronic (like the P_1 band). The absence of significant ESA signals for ***c*-P6·T6$^{+\bullet}$** indicates that the IRAV amplification effect is suppressed in the excited polaron. In ***l*-P2$^{+\bullet}$** the GSB and ESA are well-resolved as a result of the discrete vibrational mode being probed, although there is still a broad positive feature extending across the whole fingerprint region. The presence of this feature, even in the absence of direct P_1 pumping, suggests some degree of vibronic coupling in ***l*-P2$^{+\bullet}$** (which is confirmed by observation of the coupling of P_1 to all IRAVs in TRIR, as discussed below).

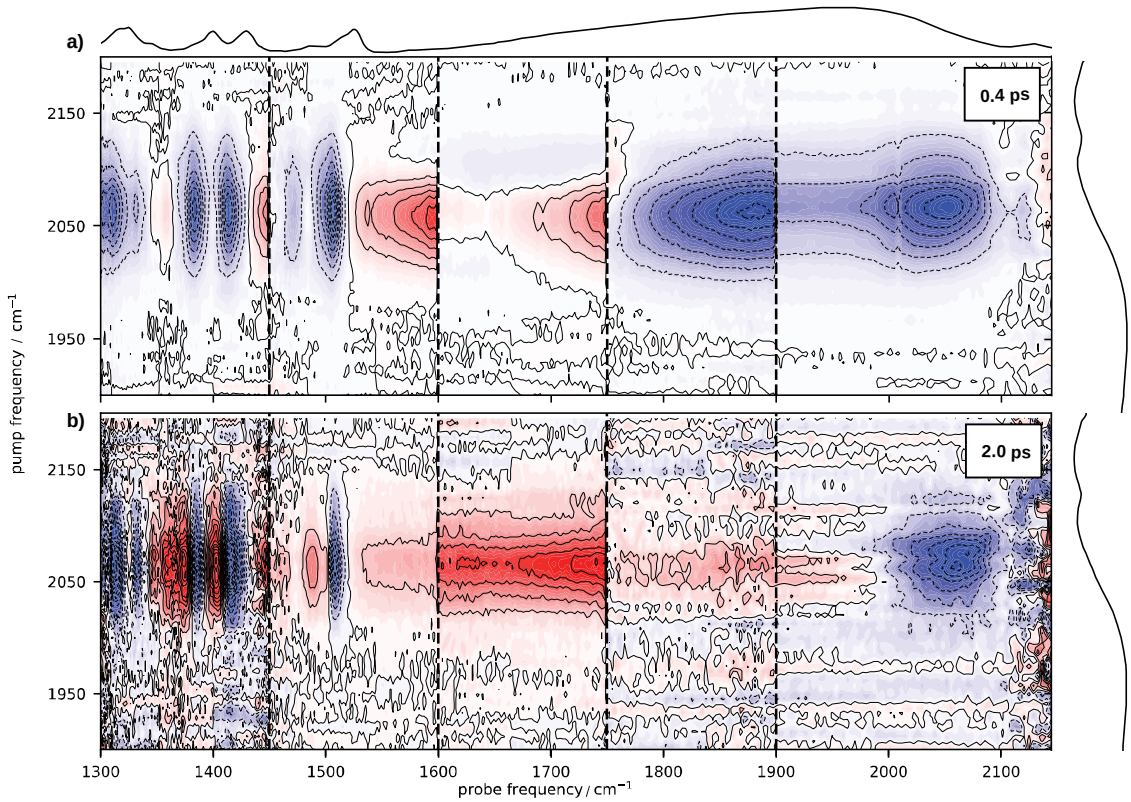


Figure 4.10. 2D-IR spectra of ***c*-P6·T6$^{+\bullet}$** at (a) 0.4 ps delay and (b) 2.0 ps delay, with pump (FWHM ~80 cm^{-1}) centred at 2050 cm^{-1}. Red and blue correspond to positive (ESA) and negative (GSB) signals, respectively. Vertical dashed lines correspond to different experimental spectra, where probe **a** was changed to cover region 1300 cm^{-1} to 1900 cm^{-1} and probe **b** was centreed in the 1900–2150 cm^{-1} region for each experiment (see Appendix 4.5.4.2 for time resolution of each probe window). Probe windows in 1300–1900 cm^{-1} were stitched together by normalising all probe **a** spectra to probe **b**. Colour maps are not shared between (a) and (b) to highlight smaller late-time features.

The evolution of the 2D-IR signals over time showed little change in the peak positions and shapes, with the exception of the ***l*-P2$^{+\bullet}$** on-diagonal ESA/GSB pair (Figure 4.9, ω_{pump} = 2070 cm^{-1} and ω_{probe} = 2045/2078 cm^{-1}) which seem to show a blue shift to higher frequencies at early times. To explore this time dependence of the peak position further, the slice at ω_{pump} = 2070 cm^{-1} for ***l*-P2$^{+\bullet}$** on-diagonal was fitted to a sum of two Voigt profiles (Figure 4.11), which provide more accurate fits to IR data than purely Lorentzian or Gaussian.[231]

Each on-diagonal slice was fitted to the sum of two Voigt profiles, with the GSB Voigt locked to a FWHM of 41.3 cm^{-1} centred at 2084 cm^{-1} (values chosen from initial free fits at later times). The ESA Voigt was allowed to vary in both position and width. The Voigt profile peak positions for the ESA, $\nu_2 \leftarrow \nu_1$, shift to higher frequency over time, resulting in a decrease in the apparent anharmonicity $\Delta\nu$ from 60 cm^{-1} to 20 cm^{-1} (Figure 4.11c). This apparent blue shift of ~ 40 cm^{-1} follows a mono-exponential decay with a lifetime of 0.48 ± 0.01 ps. The FWHM of the ESA stays fairly consistent over time around

50–55 cm^{-1} (Figure 4.11d). It is not clear whether this evolution reflects a true decrease in anharmonicity over time, or the decay of overlapping ESA bands.

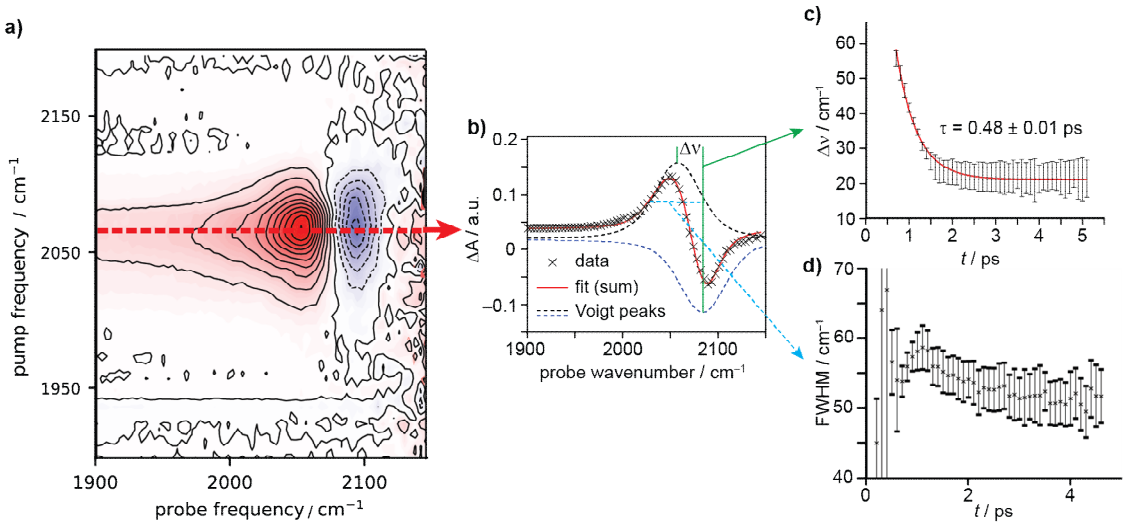


Figure 4.11. (a) Example 2D-IR on-diagonal signal, showing slice through ω_{pump} = 2070 cm^{-1}. (b) Fit of the sum of two voigts, showing individual voigts and fitted date as well as peak separation Δν (green) and FWHM of the ESA voigt (cyan). (c) Plot of the peak separation over time for each fitted time delay. (d) Fitted full-width at half-maximum for the ESA at each time delay.

In any case, this evolution shows the nature, and perhaps origin, of the signals change over the course of < 1 ps, after which they appear as a well-defined ESA/GSB pair with similar FWHM. This suggests there is a shared change in character of the pair occurring over < 1 ps.

The apparent coupling between the C≡C stretch and fingerprint IRAVs in ***l*-P2** is an important insight into the nature of IRAV intensification. The orientation and character of the C≡C stretch is well understood as being along the porphyrin oligomer backbone. Consequently, the IRAV modes are also likely to have a major dipole component along the same axis.

4.3.3 Fitting of spectrokinetic data

The time-resolved nature of the 2D-IR data presented in Figure 4.9 and Figure 4.10 allows the decay traces of the GSB and ESA to be fitted to mono-, bi- or tri-exponential functions, convoluted with the instrument response function (IRF), providing information on the excited-state and vibrational lifetimes.[232] Importantly, fitting the convoluted IRF allows the extraction of early-time features from the instrument response. This allows identification and interpretation of events occurring at short timescales (< 500 fs) that account for much of the spectral evolution in these systems which are complicated by

large initial GSBs, multiple recovery processes and crowded spectra. The functions (described in detail in Appendix 4.5.3) are hereafter referred to as mono-, bi- or tri-exponential, for simplicity.

The decay profiles were categorised into four types based on their appearance and behaviour:

1. On-diagonal GSBs
2. Off-diagonal GSBs
3. ESA peaks (anharmonic bands of the GSBs)
4. The broad ESA stretching across the whole spectrum (most visible around 1550 – 1750 cm^{-1})

In order to describe the salient features of the spectra along with their time dependence as simply as possible, we decided to fit the observed categories to as few shared time constants as possible. The fitting process is described in detail in Appendix 4.3.3 (see Figure 4.21 and Figure 4.22, Table 4.3 and Table 4.4).

We found that the kinetic data for each species (***l*-P2$^{+\bullet}$** or ***c*-P6·T6$^{+\bullet}$**) can be modelled in terms of just three decay lifetimes, τ_1, τ_2 and τ_3. Here we summarise the features of these decay processes and their associated states:

(a) τ_1: Intramolecular energy redistribution

This is a very fast process (***l*-P2$^{+\bullet}$**: τ_1 = 0.15 ± 0.02 ps; ***c*-P6·T6$^{+\bullet}$**: τ_1 = 0.29 ± 0.01 ps) and it is only observed through the decay of the GSB (just on-diagonal for ***l*-P2$^{+\bullet}$**; both on- and off-diagonal for ***c*-P6·T6$^{+\bullet}$**). It sits within the instrument response, but the good fit to the decay profile at early times for every on-diagonal GSB and the agreement with previously reported values of the instrument response for this spectrometer ($\sigma \sim 200$ fs)[228] enables us to confidently detect this fast decay component. τ_1 appears as a rise-time for the ESA signals that decay with time-constants τ_2 and τ_3 (Appendix 4.5.3 Figure 4.23, Figure 4.24, Figure 4.25). This process is consistent with intramolecular vibrational energy redistribution (IVR), as described by Rubtsov and coworkers in their work on acetylproline-NH_2 and relaxation-assisted 2D-IR spectroscopy (RA-2D-IR).[169,229,233]

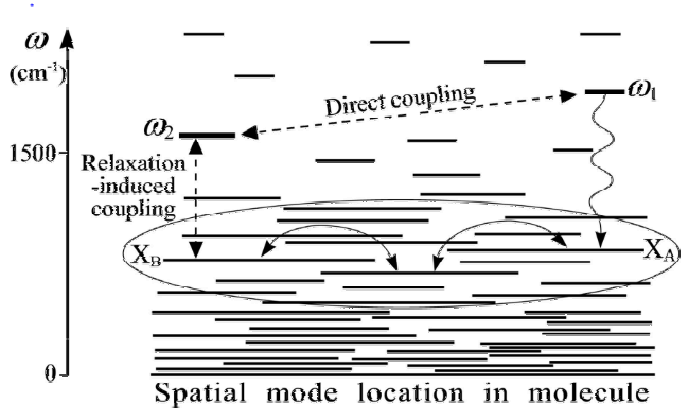


Figure 4.12. IVR process as described by Rubtsov and co-workers. The initial pumped mode ω_1 transfers energy to lower lying modes which then couple back to ω_2. Reproduced from D. V. Kurochkin, S. R. G. Naraharisetty and I. V. Rubtsov, *Proc. Natl. Acad. Sci.*, 2007, **104**, 14209–14214, Copyright (2007) National Academy of Sciences.

This IVR process is understood as the pumped mode (ω_1 in Figure 4.12) transferring energy to lower in energy modes ($X_{a/b}$ in Figure 4.12). These modes are then coupled to ω_2, which manifests as an off-diagonal peak at $\omega_{pump} = \omega_1$. In our case, the low energy modes also couple back to the on-diagonal mode ω_1 as evidenced by the multi-exponential character in the on-diagonal region and grow-in associated with the ESAs. It is worth noting that, due to the electronic and vibrational transitions in our system being so close in energy (and strongly coupled) we cannot say with certainty whether the energy redistribution is vibrational or electronic in nature. What is obvious, though, is that the energy redistribution transfers its energy into two distinct states, τ_1 and τ_2.

(b) τ_2: Relaxation from an "electronic" excited state

(***l*-P2$^{+\bullet}$**: $\tau_2 = 0.92 \pm 0.01$ ps; ***c*-P6·T6$^{+\bullet}$**: $\tau_2 = 0.74 \pm 0.07$ ps). This process is mainly observed through the decay of the extremely broad featureless ESA band extending from 1300 – 2000 cm^{-1}; in ***l*-P2$^{+\bullet}$**, this decay is also detected as a component in the GSBs. The resemblance of this ESA with the P_1 absorption band suggest that this decay originates from a nominally electronic excited state that lacks the IRAVs of the P_1 ground state.

(c) τ_3: Relaxation from a "vibrational" excited state

(***l*-P2$^{+\bullet}$**: $\tau_3 = 5.7 \pm 0.1$ ps; ***c*-P6·T6$^{+\bullet}$**: $\tau_3 = 4.1 \pm 0.3$ ps). This component appears in most of the signals and it is the dominant relaxation process for the sharper ESA signals. It resembles a normal vibrational relaxation process and it originates from a state occupied by the IVR and shows ESA/GSB pairs of similar intensity.

Although the evolution of the spectral features is complex, simplifying it into these three processes does provide more insights into the behaviour and origins of IRAV modes.

In particular, the observed rate of τ_1 correlates nicely with the observed shift in on-diagonal signal presented in Figure 4.11. This supports the assignment of τ_1 to an energy transfer process and the observed shift to the disappearance of the initial state and appearance of the coupling to the state to which energy has been transferred. This makes more sense than the other explanations for the apparent blue shift, which would be either that the anharmonicity changes over time (which is an unphysical phenomena) or that anharmonic hot states ($v_n \leftarrow v_0$, where n > 1) had been occupied (which would require higher laser powers).

4.3.4 TRIR Spectroscopy

The data collected in Section 4.3.2 highlight the coupled nature of the fingerprint IRAVs to the C≡C stretch. To explore this further, we undertook polarisation-sensitive TR IR experiments in an attempt to elucidate the spatial relationship between the coupled modes and their vibrational delocalisation.

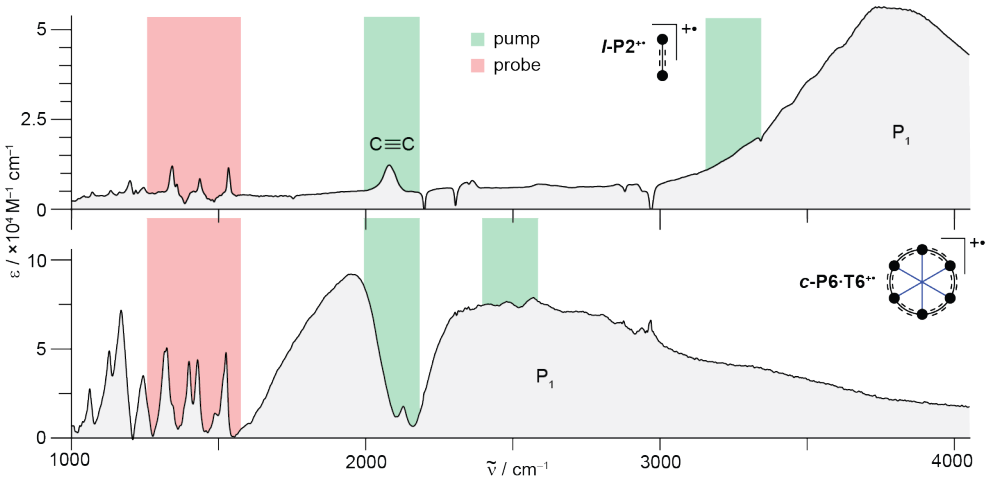


Figure 4.13. Pumped (green) and probed (red) areas of ***l*-P2$^{+\bullet}$** and ***c*-P6·T6$^{+\bullet}$** during ULTRA TR-IR measurements.

A series of TRIR spectra of ***l*-P2$^{+\bullet}$** and ***c*-P6·T6$^{+\bullet}$** were recorded by pumping the regions around 2100 cm^{-1} (***l*-P2$^{+\bullet}$** and ***c*-P6·T6$^{+\bullet}$**), 2500 cm^{-1} (***l*-P2$^{+\bullet}$**) or 3250 cm^{-1} (***c*-P6·T6$^{+\bullet}$**) and probing the fingerprint region (summarised in Figure 4.13). In the fingerprint region, the TRIR spectra of both ***l*-P2$^{+\bullet}$** and ***c*-P6·T6$^{+\bullet}$** are similar for times > 1 ps, irrespective of whether the pump excites the C≡C stretch (in ***l*-P2$^{+\bullet}$**), the Fano-type antiresonance (in ***c*-P6·T6$^{+\bullet}$**) or P_1 polaron band (both). Pumping at higher frequency in general leads to more intense initial bleach features. The presence of such features is less pronounced when the pump is applied at 2100 cm^{-1}.

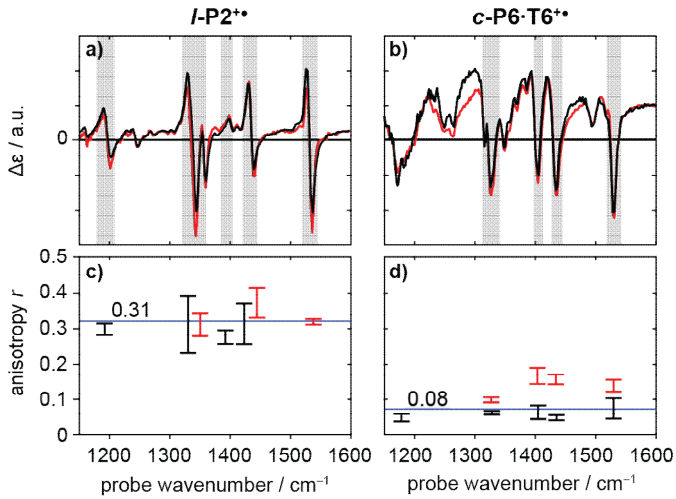


Figure 4.14. TRIR spectra of ***l*-P2**$^{+\bullet}$ (a) and ***c*-P6·T6**$^{+\bullet}$ (b) with pump centred on C≡C stretch mode (2100 cm^{-1}) (black) and on P_1 polaron band (3250 cm^{-1} for ***l*-P2**$^{+\bullet}$, 2500 cm^{-1} for ***c*-P6·T6**$^{+\bullet}$) (red) at 0.8 ps pump-probe time delay. Anisotropy values of the selected TRIR regions (greyed area in the spectra) of ***l*-P2**$^{+\bullet}$ (c) and ***c*-P6·T6**$^{+\bullet}$ (d) are plotted for both pump positions, with error bars indicating standard error.

In order to study the relative orientations of IRAV modes, polarisation-sensitive experiments were performed to calculate the vibrational anisotropy. Experiments of this type are often used to establish the relative orientation between pumped and probed processes.[165,167] The vibrational anisotropy r was calculated using eqn (4.1).[165,173] In isotropic solution, the anisotropy is expected to be in the range $-0.2 < r < 0.4$, corresponding to extremes where the transition dipole moment of the induced absorption is perpendicular or parallel to the excitation, respectively.

$$r = \frac{\Delta A_{\parallel} - \Delta A_{\perp}}{\Delta A_{\parallel} + 2 \cdot \Delta A_{\perp}} \tag{4.1}$$

TRIR spectra were acquired using the magic angle orientation ΔA_{mag} (54.7°), and served as a check for the correct setup. Comparing ΔA_{mag} to $\Delta A_{\parallel}$ and $\Delta A_{\perp}$ showed it obeyed the expected relation described in eqn (4.2), confirming the validity of the experimental setup (Appendix 4.5.5, Figure 4.36).

$$\Delta A_{mag} = \frac{\Delta A_{\parallel} + 2 \cdot \Delta A_{\perp}}{3} \tag{4.2}$$

Since ***l*-P2**$^{+\bullet}$ and ***c*-P6·T6**$^{+\bullet}$ are large molecules with molecular weight of 4.0 kDa and 11 kDa, respectively, no anisotropy decay due to rotational reorientation is expected on the experimental time scale.

As a typical profile, $\Delta A_{\parallel}$ and $\Delta A_{\perp}$ of selected bleaches in the fingerprint region for both ***l*-P2**$^{+\bullet}$ and ***c*-P6·T6**$^{+\bullet}$ are plotted in Figure 4.14a and b, respectively. Due to instrument response effects at early times the anisotropy is analysed at probe delays after 0.5 ps.

Investigation of all probe regions with a signal-to-noise above a selected threshold showed anisotropy values for each signal/bleach pair in the probed window to possess similar values in the range 0.28–0.38 for ***l*-P2$^{+\bullet}$** and 0.03–0.12 for ***c*-P6·T6$^{+\bullet}$** (Figure 4.15).

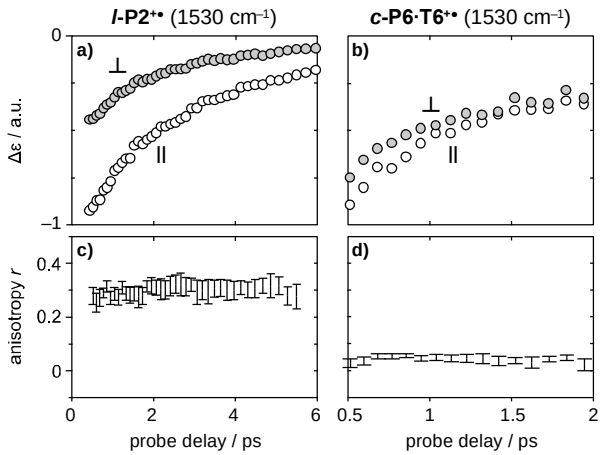


Figure 4.15. Anisotropy of bleach recoveries of (a) ***l*-P2$^{+\bullet}$** and ***c*-P6·T6$^{+\bullet}$** (b) pumped at 2100 cm^{-1} and probed at 1530 cm^{-1}. Bleach intensities over time for parallel and perpendicular pump-probe orientation of ***l*-P2$^{+\bullet}$** (c) and ***c*-P6·T6$^{+\bullet}$** (d).

The consistent anisotropies, independent of pump position, allow averaging of all calculated values for each system, resulting in anisotropies of 0.31 ± 0.07 for ***l*-P2$^{+\bullet}$** and 0.08 ± 0.04 for ***c*-P6·T6$^{+\bullet}$**, both of which are constant over time as seen in Figure 4.15c,d.

4.3.5 DFT Calculations

We sought to elucidate the assignment of the observed IRAVs by carrying out DFT calculations using long range corrected functional LC-ωPBE[234–236] and 6-31G* basis set on the Gaussian09 software.[237] Models of ***l*-P2$^{+\bullet}$** and ***c*-P6·T6$^{+\bullet}$** (without solubilising groups in ***l*-P2$^{+\bullet}$** and without solubilising groups and template in ***c*-P6·T6$^{+\bullet}$**) were built and geometries were minimised assuming charge 1+ and doublet multiplicity. Frequency calculations on neutrals and cations predicted that several IR absorptions are intensified by a factor of 50–100 in the cations, including the C≡C bond stretch and several bands in the fingerprint region (Figure 4.16a,b).

The dipole derivatives of the modes with the most intensified absorptions show 100% directionality along the length of the ***l*-P2$^{+\bullet}$** molecule (Figure 4.16c). The DFT calculated spectra do not match exactly the experimental spectra suggesting a dissimilarity between the modes in neutral and oxidised species as was seen in doped conjugated polymers.[212]

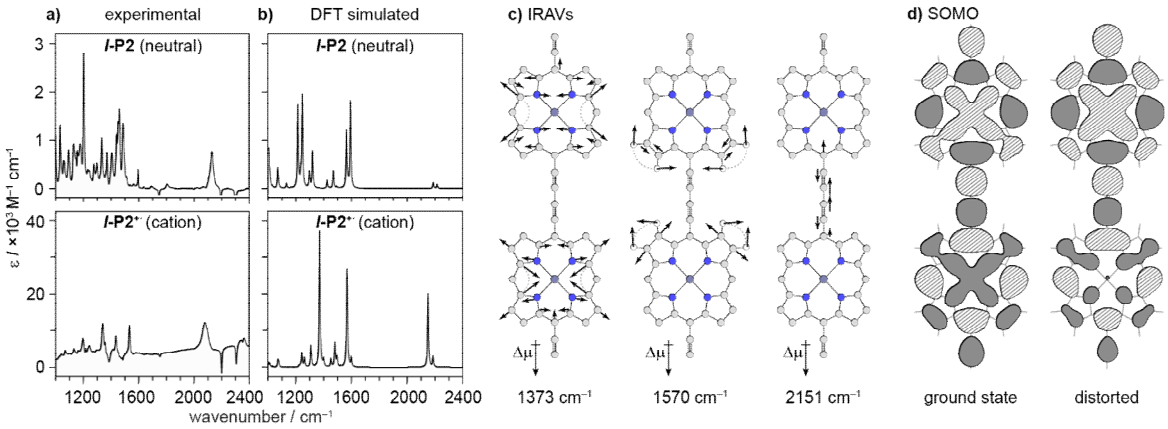


Figure 4.16. a) Experimental and b) DFT simulated IR absorption spectra of ***l*-P2** and ***l*-P2$^{+\bullet}$**. DFT (LC-ωPBE/6-31G*) predicts an increase in relative intensity of some absorptions by a factor of ~50. c) Three most intensified vibrational modes of ***l*-P2$^{+\bullet}$** with displacement vectors and dipole moment change related with the vibrations. d) Calculated HOMO(/SOMO) of vibrationally relaxed and distorted 1570 cm^{-1} mode (~10 of the classical turning point) of ***l*-P2$^{+\bullet}$**, showing SOMO density redistribution away from contracted ring.

4.4 Discussion

The results can be summarised as follows:

1. IRAVs are coupled to the C≡C stretch and polaron absorption band – 2D-IR and TRIR

The 2D-IR spectra reveal coupling between IRAVs in the radical cations ***l*-P2$^{+\bullet}$** and ***c*-P6·T6$^{+\bullet}$**. All of the IRAVs in the fingerprint region are coupled to the C≡C stretch vibration and to the P_1 polaron band, as evidenced by the appearance of 2D-IR off-diagonal signals at early times (Figure 4.5, Figure 4.6, Figure 4.9, Figure 4.10). The TRIR spectra show that pumping the C≡C stretch or the higher energy polaron P_1 bands yields the identical TRIR spectra (Figure 4.14a,b). The spectra do not exhibit significant differences in kinetic response or in anisotropy, suggesting that the species generated by excitation of a classically vibrational mode (C≡C stretch) or a classically electronic transition (the polaron band) are identical, which confirms that the polaron absorption and vibrations must be strongly coupled.

2. The kinetics and evolution of the spectra suggest a fast intramolecular energy redistribution – TR-2D-IR

The kinetic evolutions of the 2D-IR spectra fit a model with just three decay times: τ_1 for IVR, τ_2 for relaxation from an "electronic" excited state and τ_3 for relaxation from a "vibrational" excited state. This "electronic" excited state is unusual: it exhibits a featureless ESA band, extending from 1300 – 2000 cm^{-1}, with no apparent IRAVs in ***c*-P6·T6$^{+\bullet}$**. One explanation for this lack of IRAVs might be that they are suppressed by the

same Fano-type anti-resonance that occurs on overlap of electronic and vibrational transitions in the ground state Figure 4.3b.

3. The IRAVs have a major dipole component aligned with the porphyrin backbone – TR-2D-IR, polarisation-sensitive TRIR

The TRIR anisotropy measurements show similar anisotropies for all of the signals in the fingerprint regions of ***l*-P2$^{+\bullet}$** and ***c*-P6·T6$^{+\bullet}$**, with values of $r \approx 0.4$ and $r \approx 0.1$, respectively (Figure 4.15). This implies that the polaron is located on a straight rod and delocalised around a circle, respectively, just like the excitons studied by fluorescence anisotropy in neutral oligomers.[46] ***l*-P2$^{+\bullet}$** is a linear molecule and its high TRIR anisotropy demonstrates that the intensified vibrations can be assigned to transitions parallel with the length of the molecule, i.e. parallel to the P_1 transition and C≡C stretch vibrations.

At first sight, the low anisotropy measured for ***c*-P6·T6$^{+\bullet}$**, which implies that the polaron is delocalised around the whole nanoring, is surprising because previous results indicated that the polaron is only delocalised over 2–3 porphyrin units. Together, these results imply that, on IR-excitation, the polaron migrates around the circumference of the nanoring faster than the TRIR measurement, i.e. within 0.5 ps, at 298 K. In contrast, in a frozen solvent at 80 K, migration of the ground state polaron is slow on the EPR timescale (~100 ns).[99]

The time-independence of the anisotropies supports the assignment of IRAVs to being within, or a part of, the porphyrin framework, as this assignment fixes the relative orientations of the two transitions. This contrasts with systems that have coupled bonds capable of rotating in relation to each other, which in turn causes a change in anisotropy over time.[175] The apparent observation of IVR effects in ***l*-P2$^{+\bullet}$** is also consistent with the assignment of the IRAV modes to transitions in line, and within, the molecular backbone, as IVR is known to occur efficiently between modes having strong spatial mode overlap (i.e. between modes that share vibrating atoms).[229] The evidence presented above implies that all the IRAV modes in ***l*-P2$^{+\bullet}$** are aligned along the long axis of the butadiyne-containing skeleton, i.e. along the porphyrin-porphyrin axis and the C≡C stretch direction.

Conclusion – the charge redistribution mechanism is most likely for our porphyrin systems.

The presented spectroscopic evidence, together with the assignment of fingerprint vibrations by DFT, is consistent with the polaron redistribution mechanism as proposed

by Zamadar *et al*. (Figure 4.2a). This behaviour has been presented previously as the explanation for infrared 'marker bands' in porphyrin monomers.[220,238] Here, intensified infrared transitions are assigned to contracting and expanding breathing modes with transition dipole moments passing through opposed meso positions (Figure 4.17).

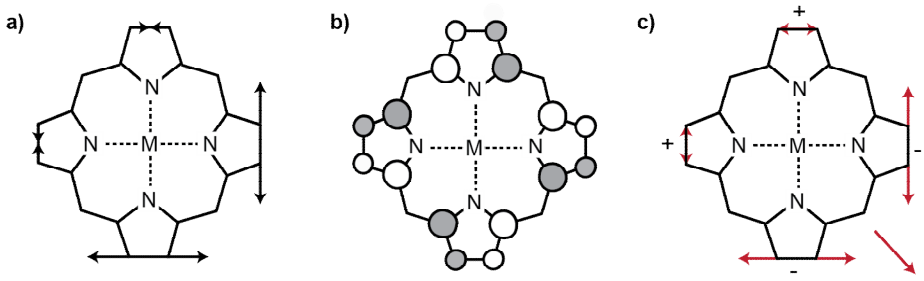


Figure 4.17. (a) Simplified nuclear displacements for one of the infrared marker bands observed by Hu *et al.* (b) a_{1u} HOMO(/SOMO) orbitals showing anti-bonding character of porphyrin β positions. (c) Vibrationally induced charge redistribution as a result of vibrational mode in (a). Overall dipole moment shown passing through *meso* positions. Adapted with permission from S. Hu and T. G. Spiro, *J. Am. Chem. Soc.*, 1993, 115, 12029–12034. Copyright (1993) American Chemical Society.

The intensification in these monomers arises due to the contraction of one side of the porphyrin during vibrational motion (for example the β-β contraction in Figure 4.17a). As the β-β bond has anti-bonding character in the HOMO(/SOMO)[239] (Figure 4.17b) the charge redistributes to minimise the unfavourable interactions (Figure 4.17c). These effects are much larger than in the neutral molecules (as the HOMO in neutral molecules are filled and consequently less polarisable) thus causing an increase in transition dipole moment in the monocations.[238]

DFT calculations of our system, ***l*-P2$^{+\bullet}$**, support the assignment of the intensified vibrations to similar contracting and expanding modes, and the calculated dipole derivatives of the most intensified vibrations are oriented along the long axis of ***l*-P2$^{+\bullet}$** (Figure 4.16c).

The coupling between vibrational modes and charge redistribution can be appreciated by calculating the frontier molecular orbitals (HOMO/SOMO and HOMO–1) at distorted geometries, at which the molecule is mechanically compressed/expanded during a vibration to extend of ~0.12 of the classical turning point (Figure 4.16d). The mechanism of vibronic coupling can thus be explained in the case of ***l*-P2$^{+\bullet}$**: as one porphyrin ring contracts, anti-bonding orbital lobes of the HOMO(/SOMO) are brought closer together. In response to this, the mobile polaron redistributes to the expanded ring, causing a large change in the dipole moment. The IRAVs in our radical cations are activated to a much greater extent than the infrared marker bands, which is consistent

with an increase in transition dipole moment due to the redistribution of an electron across two porphyrin rings compared to one. The electron density in these systems is effectively moving from one porphyrin ring to another, in a way analogous to an electronic transition, providing an explanation for the exceptionally high intensities observed for these vibrations. This mechanism relies on the polaron being mobile along the oligomer backbone and redistributing in response to vibrations. It follows that the polaron must be mobile in ***c*-P6·T6$^{+\bullet}$**, as confirmed by the observed low anisotropy.

The delocalisation length of polarons in conjugated polymers tends to be reduced by strong electron-phonon coupling.[154,199,219] The assignment of the IRAVs (by definition strongly coupled phonon modes) to those of breathing modes across two porphyrin rings is consistent with the previously reported delocalisation length of 2–3 porphyrin units in the radical cations of butadiyne linked porphyrin oligomers.[99]

DFT calculations predict a huge intensification of several vibrational bands, but they fail to reproduce the observed pattern of activated vibrations in the fingerprint region, even for the simpler system of ***l*-P2$^{+\bullet}$**. DFT predicts only two IRAVs in the window 1100–1800 cm^{-1} compared to at least five modes observed in the experimental IR spectrum. This failure to reproduce IRAVs is consistent with previous attempts, and has been cited as evidence for the charge localisation mechanism rather than the activation of Raman modes through symmetry breaking, which would be expected to predict similar modes in both the neutral and radical cation species.[212]

Conclusions

Time-resolved IR spectroscopies have been used to probe the origins of IRAVs in the radical cations of porphyrin oligomers. 2D-IR studies of two compounds, ***l*-P2$^{+\bullet}$** and ***c*-P6·T6$^{+\bullet}$**, show that vibrational coupling occurs at early times between all of the IRAVs and with the P_1 polaron bands. The similarity between spectra arising from pumping in the classically vibrational C≡C stretch and those arising from pumping the electronic P_1 polaron bands demonstrates the presence of strong vibronic coupling between the P_1 band and IRAV modes. This result, in combination with results from DFT calculations and polarisation-dependent TRIR experiments suggest the IRAV modes are in line with the C≡C backbone of ***l*-P2$^{+\bullet}$**. This assignment is consistent with the idea that IRAVs originate from

polaron redistribution in response to, and on the time scale of, the vibration, which amplifies the transition dipole moment of the vibrational mode.

Coupling between vibrational modes and charge transport is frequently an important factor determining the rate of electron transfer through molecular wires in single-molecule electronic devices.[240–242] If we assume that the vibrational modes in ***l*-P2$^{+\bullet}$** are similar to those in ***c*-P6·T6$^{+\bullet}$**, then the anisotropy of ~0.08 recorded for ***c*-P6·T6$^{+\bullet}$** suggests that, in the vibronic excited state, the polaron is mobile along the length of the molecular backbone, consistent with previous discussions of polarons in polymer chains.[219]

4.5 Experimental Appendices

4.5.1 Synthesis

The neutral porphyrin oligomers ***l*-P2** and **c-P6·T6** were gratefully received from Dr Jonathan Cremers, Dr Martin Peeks and Michael Jirasek and were synthesised as reported previously.[19,46] The solubilising groups were chosen to be *meso*-3,5-bis(trihexylsilyl)-phenyl substituents as these improve solubility and prevent aggregation in the absence of pyridine (exclusion of which is essential to avoid unwanted reactions between pyridine and the radical cations).[98,243]

4.5.2 Photophysical investigations

***l*-P2$^{+\bullet}$** and ***c*-P6·T6$^{+\bullet}$** solutions were generated spectroelectrochemically in an optically transparent thin layer electrochemistry (OTTLE) cell comprising platinum gauze working and counter electrodes and a Ag/AgCl quasireference electrode. The cell was fitted with 2 mm CaF_2 windows; path length: ca. 0.2 mm. The OTTLE cell was purchased from Prof. Frantisek Hartl, University of Reading, UK and modified by masking all visible non-electrode containing solution with electrical tape.[244] The electrolyte solution was 0.1 M tetra-*n*-butylammonium hexafluorophosphate (Bu_4NPF_6 or TBAP) in CD_2Cl_2. The cell was filled with neutral solutions of ***l*-P2** and ***c*-P6·T6** with concentrations of ca. 2 mg/mL in CD_2Cl_2/0.1 M TBAP, corresponding to concentrations of ~0.5 and 0.2 mM respectively.

l*-P2$^{+\bullet}$** and ***c*-P6·T6$^{+\bullet}$** concentrations were adjusted to give a maximum optical density of 0.4–0.8 in P_2 bands by NIR spectroscopy (~800–1000 nm), which is equivalent to optical densities of 0.2–0.5 in the fingerprint region, by adjusting the applied voltage with reference to the known oxidation potentials of the porphyrin radical cations (l*-P2$^{+\bullet}$** $E_{ox,1}$ = 0.39 V, ***c*-P6·T6$^{+\bullet}$** $E_{ox,1}$ = 0.20 V, both referenced to Fc/Fc^{+}).[99] This corresponds to a concentration of monocation of ~0.1 mM. [99] In the OTTLE cell, these voltages were in the range 400–900 mV in agreement with the known Ag/AgCl vs Fc/Fc+ value of + 0.49 V in CH_2Cl_2-Bu_4NPF_6 (0.1 M).[245]

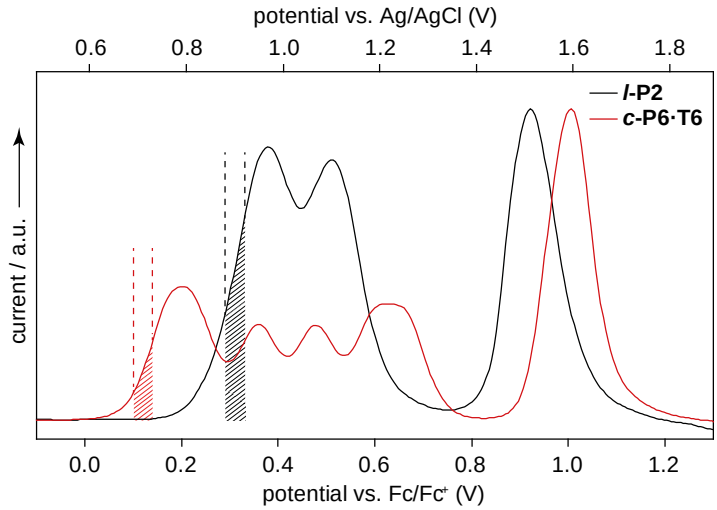


Figure 4.18. Experimental square wave voltammetry (CH_2Cl_2/0.1 M Bu_4NPF_6) of porphyrin oligomers. Setup consisted of glassy carbon working electrode; platinum wire counter electrode and Ag/AgCl reference electrode. Fc/Fc+ was used as an internal reference. 5 mV step potential, 10–50 mV modulation amplitude and 5 Hz frequency was used. Conversion to potential vs Ag/AgCl (+0.49 V)[245] showed for comparison. Shaded areas represent acceptable voltage ranges used for measurement to avoid contamination with dications.

The SWV oxidation profiles in Figure 4.18 show 2+ oxidation states close to the monocation states. To avoid contamination of the desired monocation signal with similarly IR active 2+ states, potentials were adjusted ad hoc for each sample within the regions on the profile shown in Figure 4.18 (dotted lines) to generate mixtures of the neutral (which is relatively silent in the IR) and optically active monocation states. Composition of the oxidised solutions were analysed using UV-Vis spectroscopy, and ratios of the porphyrin Q bands of the neutral and P_2 bands in the monocations (see Figure 4.19 and Figure 4.20) were used to estimate ratio of neutral:monocation.

In general, we found the monocation sample to be stable up to ~45 min–1 hour (while keeping constant applied potential), but often concentrations of monocations

drifted even within this time frame. For LIFEtime measurements, a real-time IR readout allowed for potential adjustment during the measurement to keep the intensity of the IR absorptions (and thus concentrations) constant. For ULTRA TRIR measurements, a UV-vis absorption spectrum of the OTTLE cell was recorded before and after measurements, where possible, to account for potential drifts in the monocation concentrations. Where the concentration of monocation changed significantly (± ~30%), or where there was any evidence of 2+ states, the cell was refilled with fresh solution and the experiment repeated.

The effects of small drifts in concentration on kinetic profiles were minimised by randomising the order in which the various time delays were recorded, where possible. For ULTRA 2D IR measurements, the samples were found to drift back to neutral. However, due to the 40× smaller signals in the neutral species and because only one time delay was recorded, these spectra averaged over the duration of the measurement were deemed to be representative of the monocation species. Due to these sample stability issues, we cannot quantitatively determine monocation concentrations for the experiment.

Chemical oxidations in a Harrick cell were trialled, as these cells were better suited to the laser table set-up. However, the oxidised species were found to be unstable on the timescales of experimental acquisition, an observation also supported by the drift in concentrations at a standard oxidation potential in the OTTLE cell.

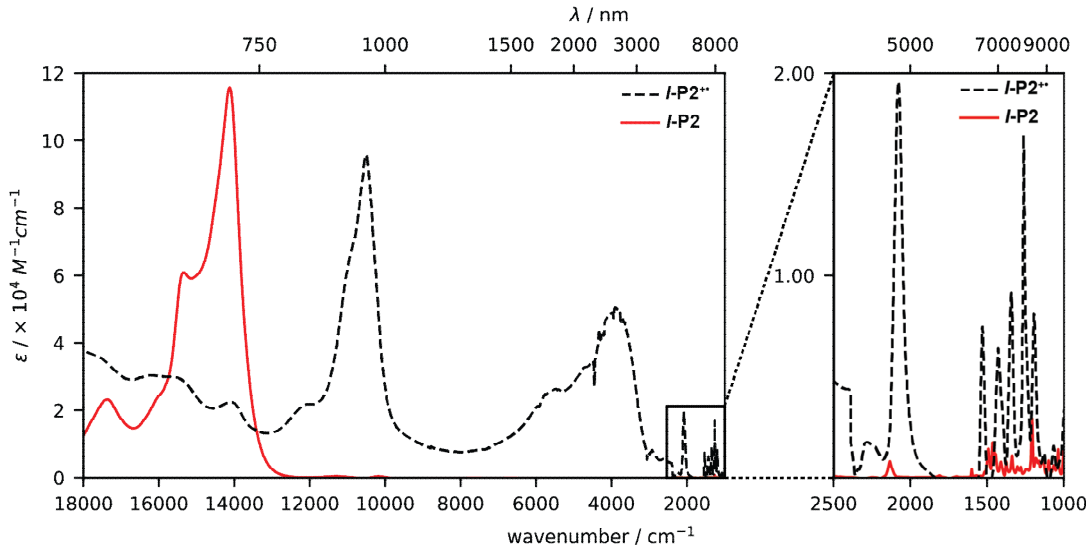


Figure 4.19. UV-vis-NIR-IR absorption spectra of ***l*-P2/*l*-P2$^{+\bullet}$** in CD_2Cl_2 with 0.1 M TBAP as an electrolyte. The distinctive porphyrin Q band at λ = 700 nm and P_2 band (monocation) were used to estimate composition during sample preparation.

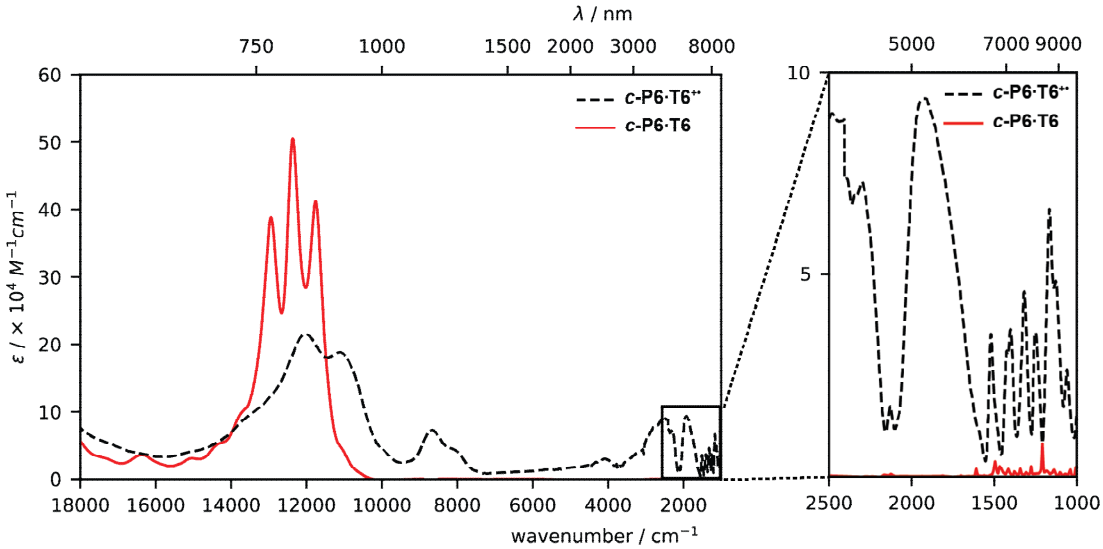


Figure 4.20. UV-vis-NIR-IR absorption spectra of ***c*-P6·T6/*c*-P6·T6$^{+\bullet}$** in CD_2Cl_2 with 0.1 M TBAP as an electrolyte. The distinctive porphyrin Q band at 800 nm and P_2 band (monocation) were used to estimate composition during sample preparation

UV-Vis-NIR-IR spectra of ***l*-P2$^{+\bullet}$** and ***c*-P6·T6$^{+\bullet}$** were recorded previously.[99] FTIR of ***l*-P2$^{+\bullet}$** and ***c*-P6·T6$^{+\bullet}$** with greater resolution were performed by recording a background of the OTTLE cell at 0 V potential. The monocations were then generated as above without moving or adjusting the cell and the FTIR measured. FTIR of ***l*-P2** and ***c*-P6·T6** were recorded using Harrick cells fitted with 2 mm CaF_2 windows; path length: 0.15 mm; solvent: CD_2Cl_2. Typical optical densities were 0.2–0.5 in the fingerprint IR region, which corresponds to a concentration of approximately 5–10 mM.

4.5.3 2D-IR kinetic fitting

Much of the signal evolution happens at very early times for both species (t < 300 fs). As such, we attempted to deconvolute the instrument response from early time decay events using eqn (4.3), derived by Mouton et al,[246] which describes the convolution of the instrument response with the time-dependent concentration profiles of spectrokinetic data.

$$C_i^*(t,\sigma) = \sum_{j=1}^{N} A_j \exp\left(\frac{k_j^2\sigma^2}{2} - k_j t\right)\left(1 - erf\left(\frac{k_j\sigma^2 - t}{\sqrt{2}\sigma}\right)\right) \qquad (4.3)$$

where $C_i^*$is the convoluted kinetic profile, t is the delay time after photoexcitation, σ is the full width half maximum (FWHM) of the Gaussian instrument response function, A_j are the pre-exponential factors and k_j are the decay rates (which can be expressed as lifetimes: $\tau_j = 1/k_j$). σ was fit globally across all the GSBs recovery kinetic profiles.

Time-resolved 2D-IR spectra were visualised in realtime using a home-made Python program that allowed for extraction of decay profiles at given points in the 2D spectra. Decay profiles were chosen at the centre points of the peaks at early times (0.4 ps) and at slightly later times (0.7 ps) for picking out ESAs initially obscured by the GSBs. Visual inspection showed most decay profiles were largely independent of small adjustments in peak positions and as such complicated 2D peak fitting was not undertaken. Some peaks were omitted due to non-trivial decay profiles (e.g. 'dips' or noise due to overlapping features at early times). All GSB profiles were cut to a starting time of − 0.2 ps to avoid negative time interference effects but provide a 'rise' to allow for fitting of the IRF and consequent extraction of early time data. ESA absorptions were cut to ∼ 0.6 ps and 1 ps for ***l*-P2$^{+\bullet}$** and ***c*-P6·T6$^{+\bullet}$** respectively to avoid signal convolution with grow-in, and in the case of ***c*-P6·T6$^{+\bullet}$** allow the ESAs to become resolved from the dominating bleaches at early times.

The selected peaks were separated into 'types', which seemed to show slightly different character. These were: 'On-diagonal GSB', 'Off-diagonal GSB', 'ESA peaks' (i.e. sharper ESA peaks expected in 2D-IR) and 'Broad ESA absorption' (i.e. broad raised baseline observed across the spectrum). Fits were undertaken using the symfit Python package to allow global fitting of shared variables using eqn (4.3).[247]

For ***l*-P2$^{+\bullet}$** mono-exponential fits (N = 1) were poor for all peak types except the Broad ESA transient, so the model was made explicitly bi-exponential for the other 3 groups (N = 2 in eq. S1). Fitting these to the model with unconstrained and unshared time constants showed two useful pieces of information: firstly, that the on-diagonal fit poorly to a bi-exponential fit, and secondly that the rest of the decay profiles seemed to share time constants of a similar value. Consequently, a model was built to fit the ***l*-P2$^{+\bullet}$** data to the minimum amount of decay constants, and can be summarised as follows:

Peak type	Model	Time constant (globally shared)
On-diagonal GSB	Tri-exponential	k_1, k_2, k_3
Off-diagonal GSB	Bi-exponential	k_2, k_3
ESA peaks	Bi-exponential	k_2, k_3
ESA broad transient	Mono-exponential	k_2

Table 4.1. Model for the fitting of ***l*-P2$^{+\bullet}$** kinetic data.

For ***c*-P6·T6$^{+\bullet}$** mono-exponential fits (N = 1) were poor for all peak types including the Broad ESA transient, so the model was made explicitly bi-exponential for all 4 groups (N = 2 in eqn (4.3)). Fitting these to the model with unconstrained and unshared time constants showed the existence of a single shared time constant across all peaks and two others, one shared between the GSBs and one shared for the ESAs. Consequently, a model was built to fit the ***c*-P6·T6$^{+\bullet}$** data to the minimum amount of decay constants, and can be summarised as follows:

Peak type	Model	Time constant (globally shared)
On-diagonal GSB	Bi-exponential	k_1, k_3
Off-diagonal GSB	Bi-exponential	k_1, k_3
ESA peaks	Bi-exponential	k_2, k_3
ESA broad transient	Bi-exponential	k_2, k_3

Table 4.2. Model for the fitting of ***c*-P6·T6$^{+\bullet}$** kinetic data.

The instrument response was shared across all data sets and was fitted as σ = 183 ± 7 and 191 ± 7 for ***l*-P2$^{+\bullet}$** and ***c*-P6·T6$^{+\bullet}$** respectively. This is slightly faster than the reported instrument response in the same spectrometer (250-300 fs)[228] but their similarity suggests a reasonable estimation for our purposes.

4.5.3.1 *l*-P2$^{+\bullet}$

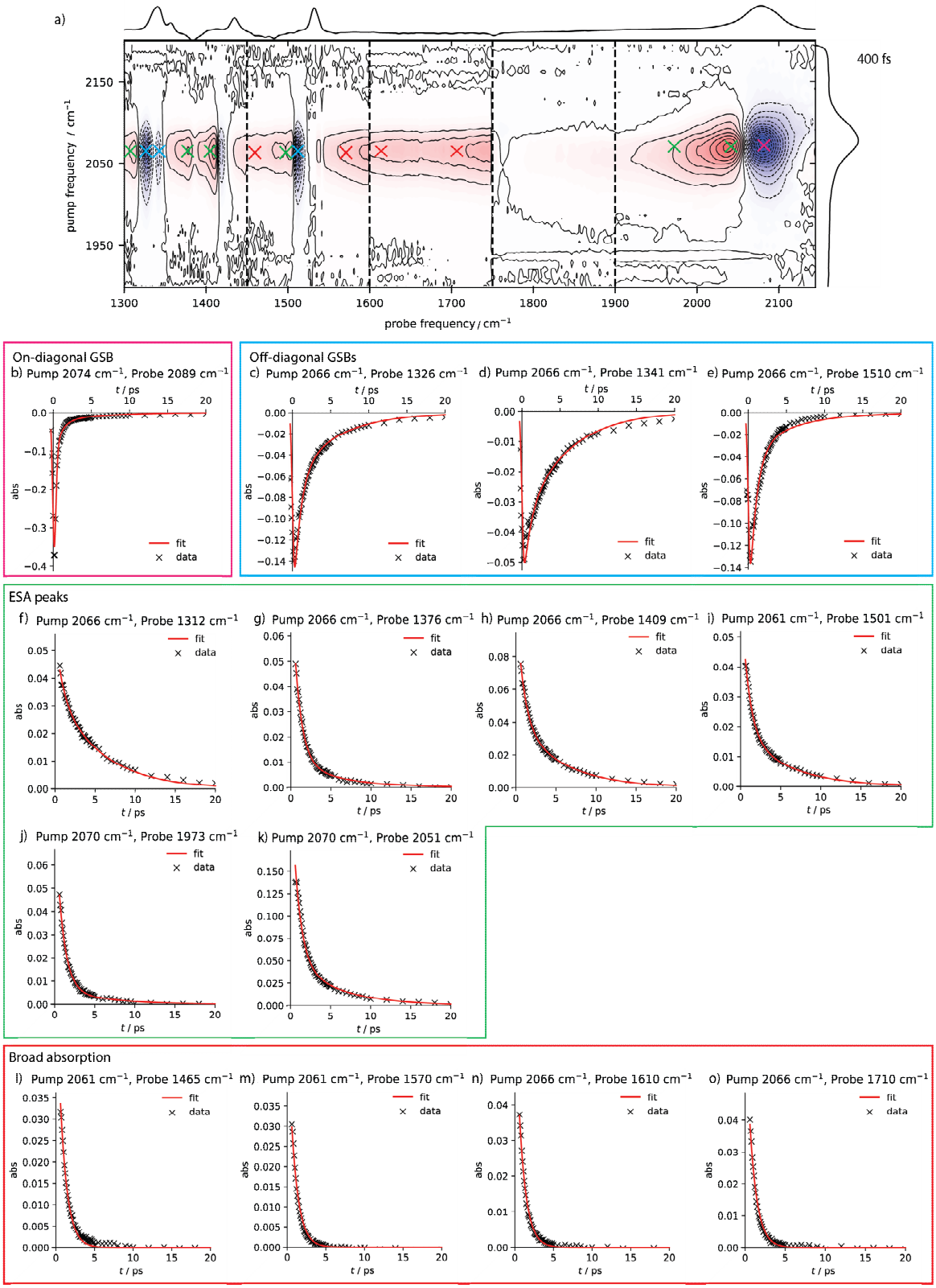


Figure 4.21. (a) 2D-IR spectra of ***l*-P2$^{+\bullet}$** at 0.4 ps showing the selected peaks for peak fitting with coloured crosses. Pump centreed at 2050 cm^{-1} (FWHM ~80 cm^{-1}). Individually recorded windows are stitched together for clarity by normalising to the 2050 cm^{-1} region (see main text). Red/blue correspond to positive(ESA)/negative(GSB) signals. (b-o)

Fitted plots for the selected peaks. GSB at ~ 1520 cm^{-1} omitted due to non-trivial decay shape caused by overlap with broad ESA transient.

	ω / cm^{-1}							
Peak type	**pump**	**probe**	**τ_1 / ps**	**%**	**τ_2 / ps**	**%**	**τ_3 / ps**	**%**
On-diagonal GSB	2074	2089	0.152 ± 0.015	89.8 ± 9.8	0.917 ± 0.010	8.08 ± 2.01	5.70 ± 0.13	2.13 ± 0.43
Off-diagonal GSB	2066	1326	-	-	0.917 ± 0.010	68.2 ± 9.2	5.70 ± 0.13	31.8 ± 4.0
	2066	1341	-	-	0.917 ± 0.010	39.5 ± 7.4	5.70 ± 0.13	60.5 ± 6.1
	2066	1510	-	-	0.917 ± 0.010	80.6 ± 8.6	5.70 ± 0.13	19.4 ± 2.8
ESA peaks	2066	1312	-	-	0.917 ± 0.010	36.9 ± 3.2	5.70 ± 0.13	63.1 ± 2.7
	2066	1376	-	-	0.917 ± 0.010	86.9 ± 1.8	5.70 ± 0.13	13.1 ± 0.5
	2066	1409	-	-	0.917 ± 0.010	64.0 ± 15.2	5.70 ± 0.13	36.0 ± 4.8
	2066	1501	-	-	0.917 ± 0.010	71.4 ± 2.1	5.70 ± 0.13	28.6 ± 0.9
	2070	1973	-	-	0.917 ± 0.010	91.4 ± 1.9	5.70 ± 0.13	8.63 ± 0.41
	2070	2051	-	-	0.917 ± 0.010	79.8 ± 3.4	5.70 ± 0.13	20.2 ± 1.0
ESA broad transient	2061	1465	-	-	0.917 ± 0.010	100	-	-
	2061	1570	-	-	0.917 ± 0.010	100	-	-
	2066	1610	-	-	0.917 ± 0.010	100	-	-
	2066	1710	-	-	0.917 ± 0.010	100	-	-

Table 4.3. Fitted parameters for **l-P2$^{+\bullet}$** from the decay profiles presented in Figure 4.21. % are presented in lieu of normalised intensities and were calculated by the ratio of pre-exponential factors. Errors given as ± 1 S.D.

4.5.3.2 *c*-P6·T6$^{+\bullet}$

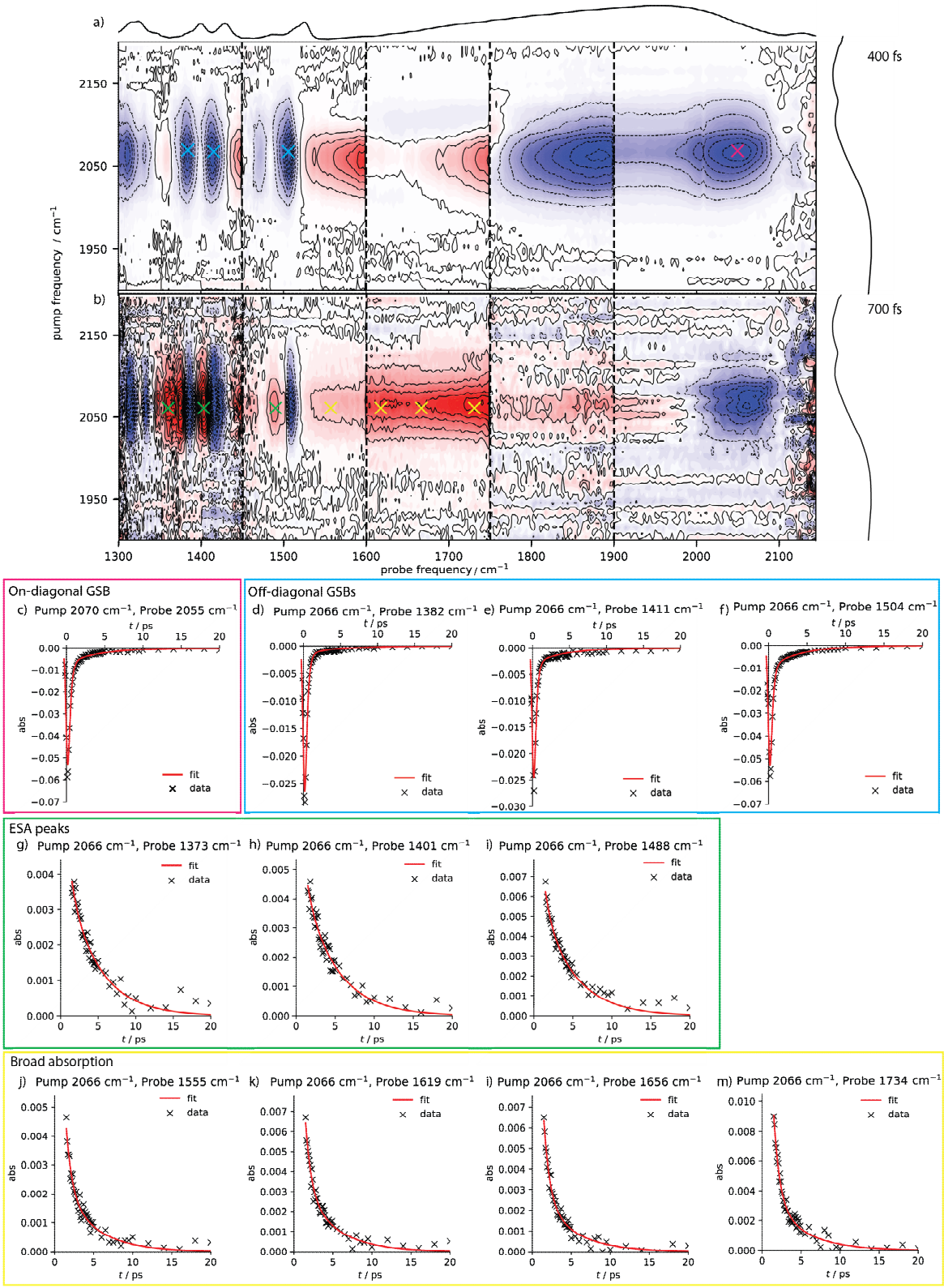


Figure 4.22. 2D-IR spectra of ***c*-P6·T6$^{+\bullet}$** at (a) 0.4 ps and (b) 0.7 ps. Colour maps are *not* shared between the two time delays in order to highlight ESA features that are normally lost due to the intense bleach. Pump centred at 2050

(FWHM ~80 cm^{-1}). Individually recorded windows are stitched together for clarity by normalising to the 2050 cm^{-1} region (see main text). Red/blue correspond to positive(ESA)/negative(GSB) signals. (c-m) show fitted decay traces for the peaks denoted in (a) and (b) by colored crosses. The GSB at 1320 cm^{-1} and 1430 cm^{-1} are omitted due to non-trivial decay profiles caused by their vicinity to the edge of the spectral window.

	ω / cm^{-1}							
Peak type	**pump**	**probe**	**τ_1 / ps**	**%**	**τ_2 / ps**	**%**	**τ_3 / ps**	**%**
On-diagonal GSB	2070	2055	0.287 ± 0.012	94.2 ± 6.5	-	-	4.11 ± 0.26	5.83 ± 0.80
Off-diagonal GSB	2066	1382	0.287 ± 0.012	97.4 ± 5.9	-	-	4.11 ± 0.26	2.60 ± 0.59
	2066	1411	0.287 ± 0.012	94.6 ± 7.4	-	-	4.11 ± 0.26	5.37 ± 0.94
	2066	1504	0.287 ± 0.012	91.7 ±7.3	-	-	4.11 ± 0.26	8.26 ± 1.03
ESA peaks	2066	1373	-	-	0.744 ± 0.072	43.6 ± 27.4	4.11 ± 0.26	56.4 ± 16.7
	2066	1401	-	-	0.744 ± 0.072	38.7 ± 28.5	4.11 ± 0.26	61.3 ± 19.3
	2066	1488	-	-	0.744 ± 0.072	54.3 ± 21.0	4.11 ± 0.26	45.7 ± 10.2
ESA broad transient	2066	1556	-	-	0.744 ± 0.072	85.3 ± 21.8	4.11 ± 0.26	14.7 ± 3.0
	2066	1619	-	-	0.744 ± 0.072	85.7 ± 21.4	4.11 ± 0.26	14.3 ± 2.8
	2066	1656	-	-	0.744 ± 0.072	88.9 ± 22.2	4.11 ± 0.26	11.1 ± 2.3
	2066	1735	-	-	0.744 ± 0.072	90.1 ± 22.7	4.11 ± 0.26	9.93 ± 2.10

Table 4.4. Fitted parameters for **c-P6·T6$^{+\bullet}$** from the decay profiles presented in Figure 4.22. % are presented in lieu of normalised intensities and were calculated by the ratio of pre-exponential factors. Errors given as ± 1 S.D.

1.1.1 Grow-in fitting

To prove the grow-in at early times is consistent to with an energy transfer/IVR process with the same time constants, we attempted to fit the ESA grow-ins to a kinetic model. The mono-exponential data set fit well to the equation

$$abs = \frac{k_1}{k_2 - k_1}(e^{-k_1 t} - e^{-k_2 t})a_0 \qquad (4.4)$$

where a_0 is the arbitrary absorbance and the only variable fit. k_n are the inverse of the values presented in Table 4.3 and Table 4.4. Fits are shown in Figure 4.23.

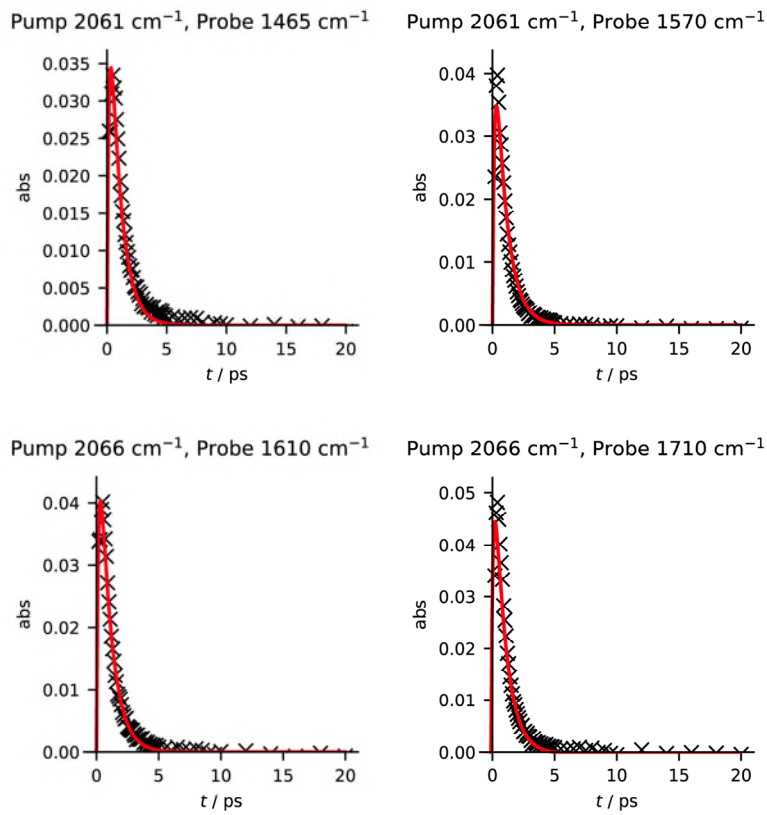


Figure 4.23. Fits of the mono-exponential ***l*-P2$^{+\bullet}$** ESAs to eqn (4.4).

The bi-exponential cases are more complicated. It is clear that not all of the initial IVR population is transferred to the remaining two decaying states, and so an equation of the form of eqn (4.4) with k_2 substituted with $k_2 + k_3$ is a poor model due to the shared a_0 (and does not fit the data). Another potential model would be a special case where the three decay processes transfer energy to each other linearly in an $A \overset{k_1}{\rightarrow} B \overset{k_2}{\rightarrow} C \overset{k_3}{\rightarrow} D$ model, where B and C are the indistinguishable probed processes and D is the ground state. The observed absorbance is given by [B] + [C], which assuming [B] = [C] = 0 at t = 0 gives the following equation:

$$abs = \left(\frac{k_1}{k_2 - k_1}(e^{-k_1 t} - e^{-k_2 t}) + \frac{k_1 * k_2}{k_1 - k_2} e^{-t(k_1+k_2)} * \left(\frac{e^{k_1 t}}{k_2 - k_3} + \frac{e^{k_2 t}}{k_3 - k_1}\right)\right) a_0 \qquad (4.5)$$

This also failed to fit the data. Instead, it seems most likely that the IVR process transfers differing amounts of population to the two consequent states, and thus must satisfy equation:

$$abs = \frac{k_1}{k_2 - k_1}(e^{-k_1 t} - e^{-k_2 t})a_1 + \frac{k_1}{k_3 - k_1}(e^{-k_1 t} - e^{-k_3 t})a_2 \qquad (4.6)$$

The data fit well to this, shown in Figure 4.24 and Figure 4.25. Taking the percentages of a_1 and a_2 presented in Table 4.5 and Table 4.6 and comparing them to the values in Table 4.3 and Table 4.4 shows a strong correlation, agreeing with our previously presented model.

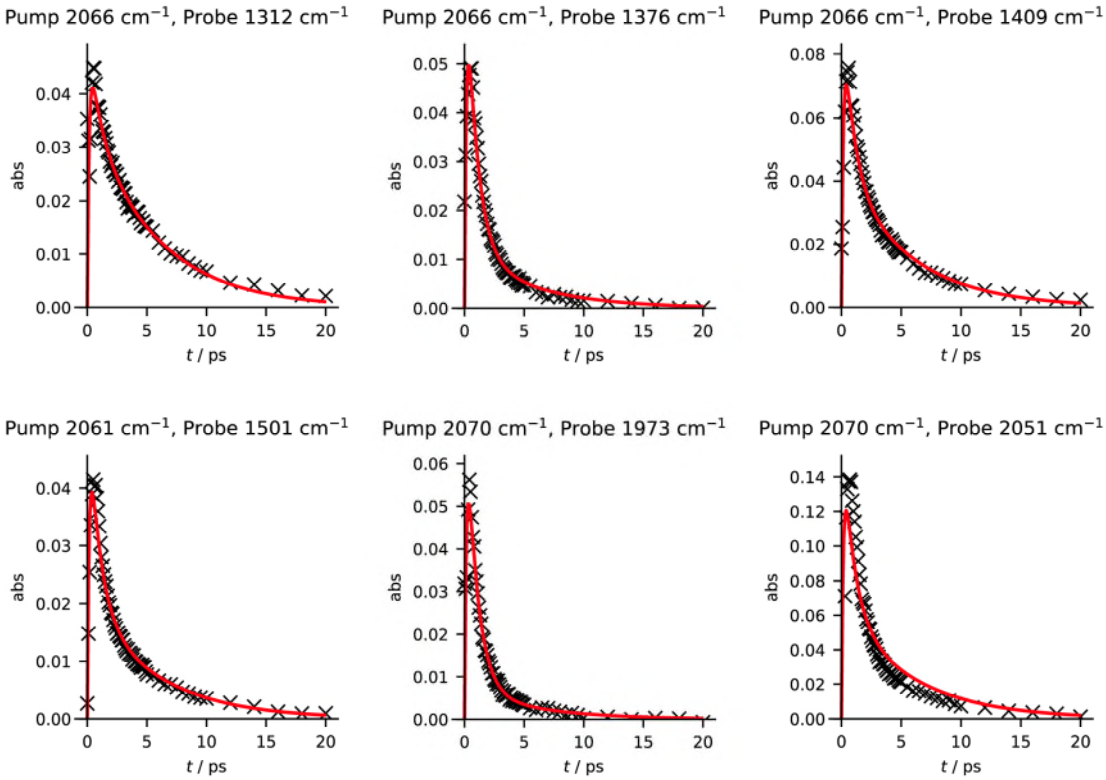


Figure 4.24. Fits of the bi-exponential ***I*-P2$^{+\bullet}$** ESAs to eqn (4.6).

ω / cm^{-1}		% of k_3	% of k_2
pump	**probe**	**component**	**component**
2066	1312	71.3 ± 3.1	28.7 ± 7.6
2066	1376	17.3 ± 1.4	82.7 ± 3.44
2066	1409	47.8 ± 1.6	52.2 ± 3.8
2066	1501	39.6 ± 1.4	60.4 ± 3.3
2070	1973	10.5 ± 2.0	89.5 ± 4.8
2070	2051	32.0 ± 2.0	68.0 ± 5.2

Table 4.5. Percentage composition of the bi-exponential ***I*-P2$^{+\bullet}$** ESA decay traces fit in Figure 4.24.

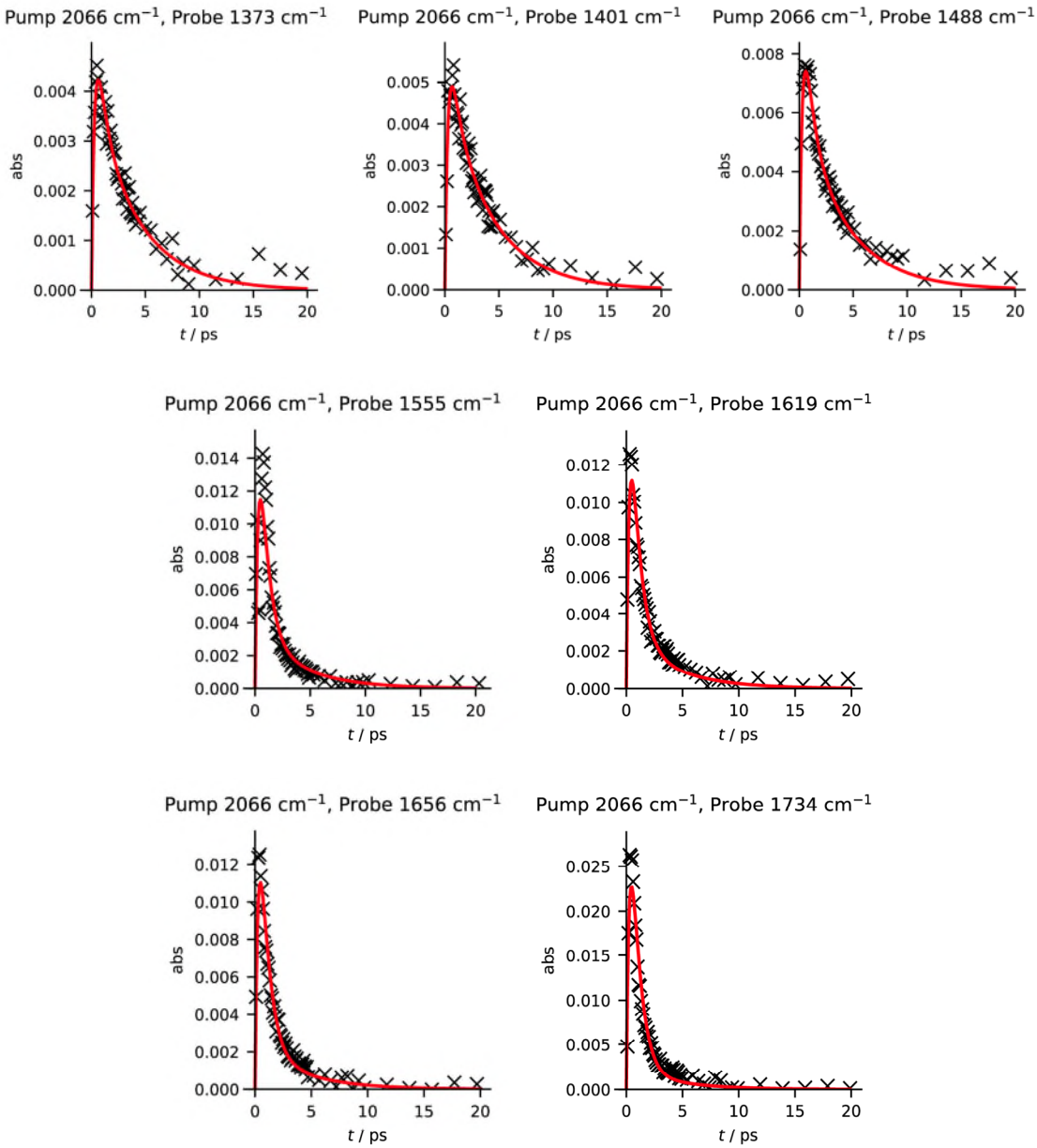


Figure 4.25. Fits of the bi-exponential ***c*-P6·T6$^{+\bullet}$** ESAs to eqn (4.6).

ω / cm^{-1}		% of k_3	% of k_2
pump	probe	component	component
2066	1373	61.7 ± 1.4	38.3 ± 3.6
2066	1401	68.9 ± 1.7	31.1 ± 4.2
2066	1488	54.1 ± 1.3	45.9 ± 3.3
2066	1555	17.3 ± 2.7	82.8 ±6.9
2066	1619	14.6 ± 1.2	85.4 ± 3.0
2066	1656	12.1 ± 1.1	87.9 ± 2.8
2066	1734	5.76 ± 1.36	94.2 ± 3.5

Table 4.6. Percentage composition of the bi-exponential ***c*-P6·T6$^{+\bullet}$** ESA decay traces fit in Figure 4.25.

4.5.4 LIFEtime time domain traces

4.5.4.1 *l*-P2$^{+\bullet}$

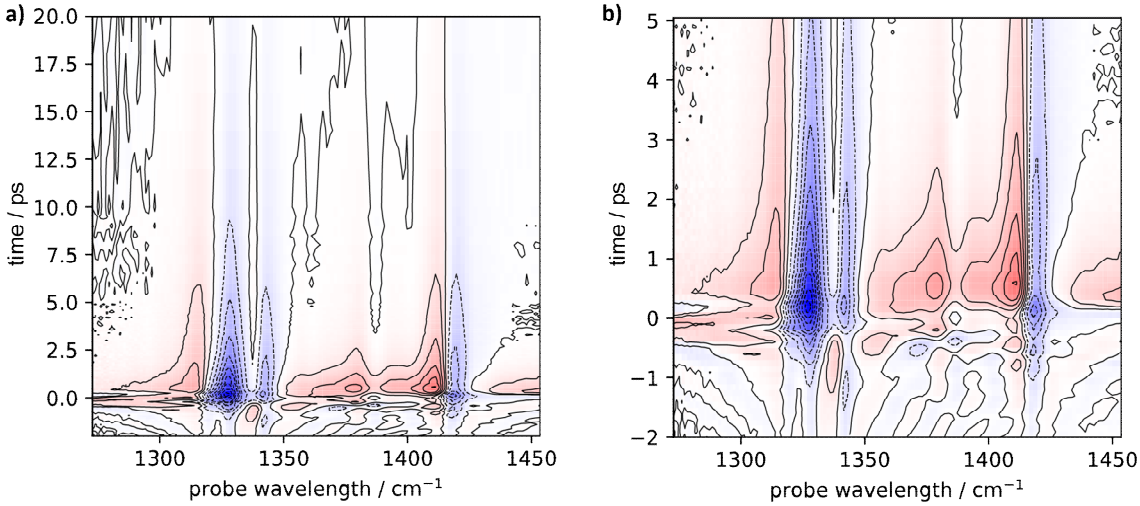


Figure 4.26. A slice (ω_{pump} = 2061 cm^{-1}) of the 2D-IR LIFEtime data recorded for ***l*-P2$^{+\bullet}$** with **probe a** set to the wavenumber region ~1250–1450 cm^{-1} showing (**a**) entire pump-probe delay series and (**b**) early time pump-probe delays. Red/blue correspond to positive(ESA)/negative(GSB) signals.

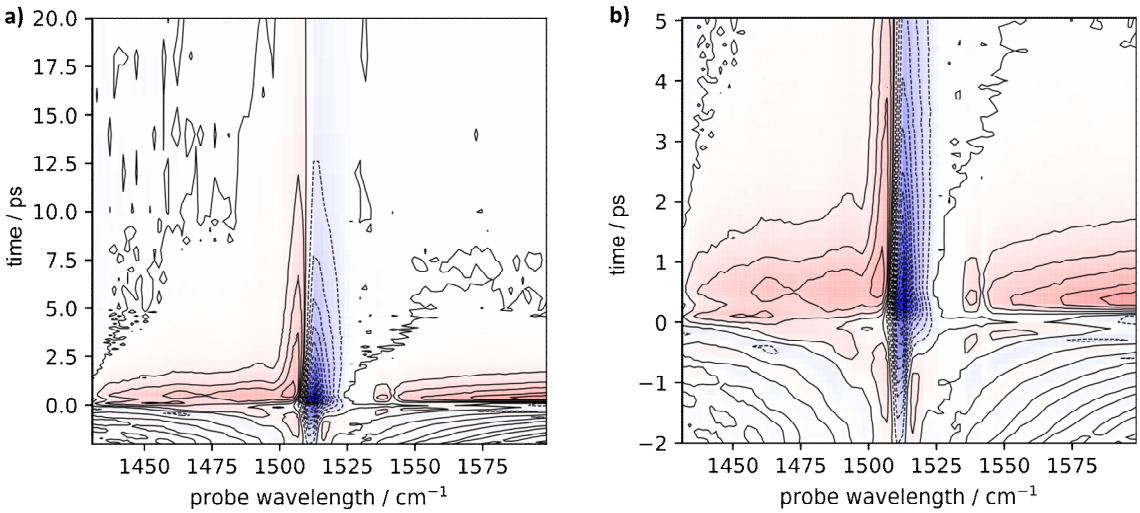


Figure 4.27. A slice (ω_{pump} = 2061 cm^{-1}) of the 2D-IR LIFEtime data recorded for ***l*-P2$^{+\bullet}$** with **probe a** set to the wavenumber region ~1400–1600 cm^{-1} showing (**a**) entire pump-probe delay series and (**b**) early time pump-probe delays. Red/blue correspond to positive(ESA)/negative(GSB) signals.

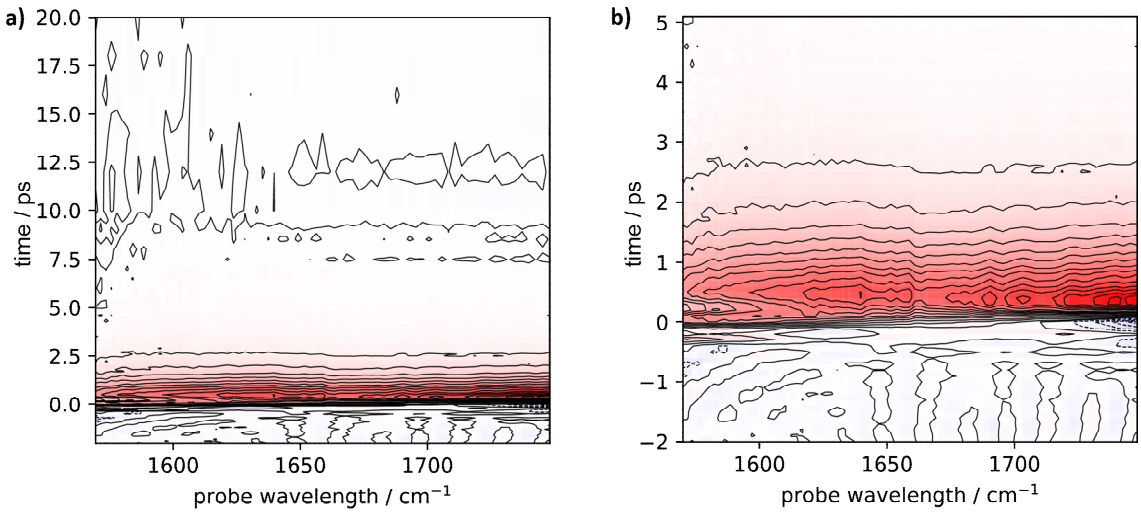


Figure 4.28. A slice (ω_{pump} = 2061 cm^{-1}) of the 2D-IR LIFEtime data recorded for ***l*-P2$^{+\bullet}$** with **probe a** set to the wavenumber region ~1550–1750 cm^{-1} showing (**a**) entire pump-probe delay series and (**b**) early time pump-probe delays. Red/blue correspond to positive(ESA)/negative(GSB) signals.

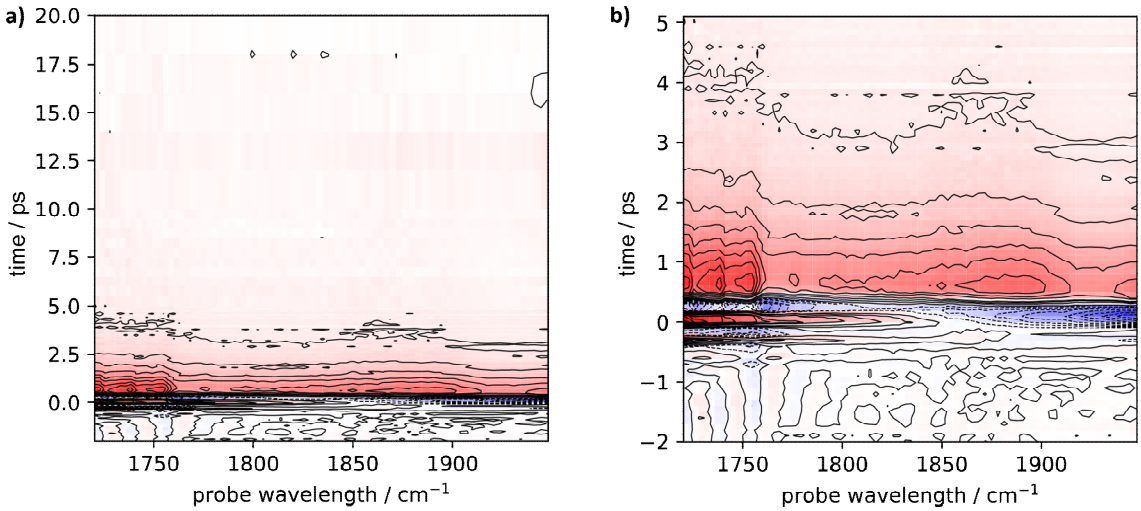


Figure 4.29. A slice (ω_{pump} = 2061 cm^{-1}) of the 2D-IR LIFEtime data recorded for ***l*-P2$^{+\bullet}$** with **probe a** set to the wavenumber region ~1700–1950 cm^{-1} showing (**a**) entire pump-probe delay series and (**b**) early time pump-probe delays. Red/blue correspond to positive(ESA)/negative(GSB) signals.

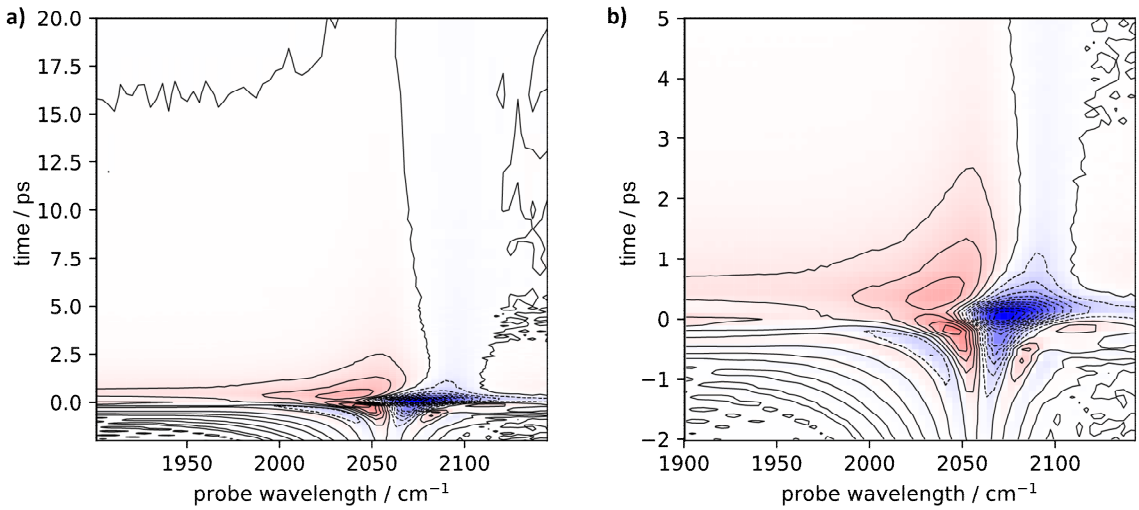


Figure 4.30. A slice (ω_{pump} = 2061 cm^{-1}) of the 2D-IR LIFEtime data recorded for ***l*-P2$^{+\bullet}$** with **probe b** set to the wavenumber region ~1900–2150 cm^{-1} showing (**a**) entire pump-probe delay series and (**b**) early time pump-probe delays. Red/blue correspond to positive(ESA)/negative(GSB) signals.

4.5.4.2 *c*-P6·T6$^{+\bullet}$

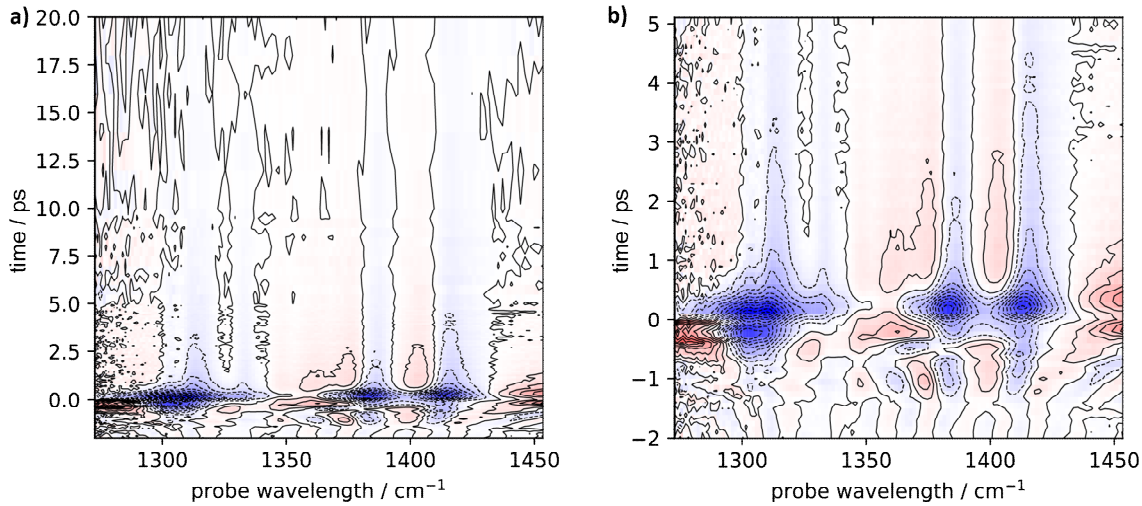


Figure 4.31. A slice (ω_{pump} = 2061 cm^{-1}) of the 2D-IR LIFEtime data recorded for ***c*-P6·T6$^{+\bullet}$** with **probe a** set to the wavenumber region ~1250–1450 cm^{-1} showing (**a**) entire pump-probe delay series and (**b**) early time pump-probe delays. Red/blue correspond to positive(ESA)/negative(GSB) signals.

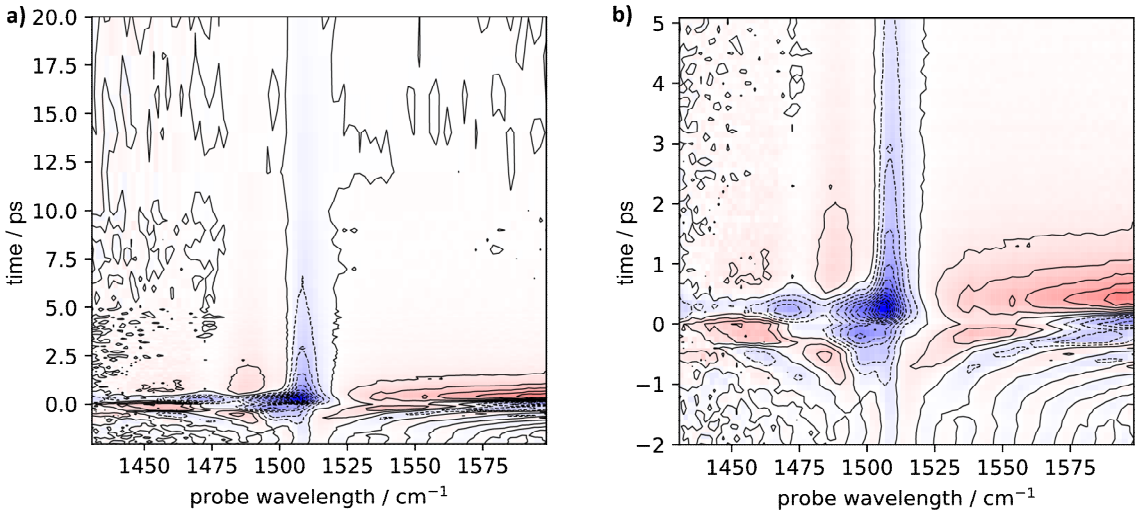


Figure 4.32. A slice (ω_{pump} = 2061 cm^{-1}) of the 2D-IR LIFEtime data recorded for ***c*-P6•T6$^{+\bullet}$** with **probe a** set to the wavenumber region ~1400–1600 cm^{-1} showing (**a**) entire pump-probe delay series and (**b**) early time pump-probe delays. Red/blue correspond to positive(ESA)/negative(GSB) signals.

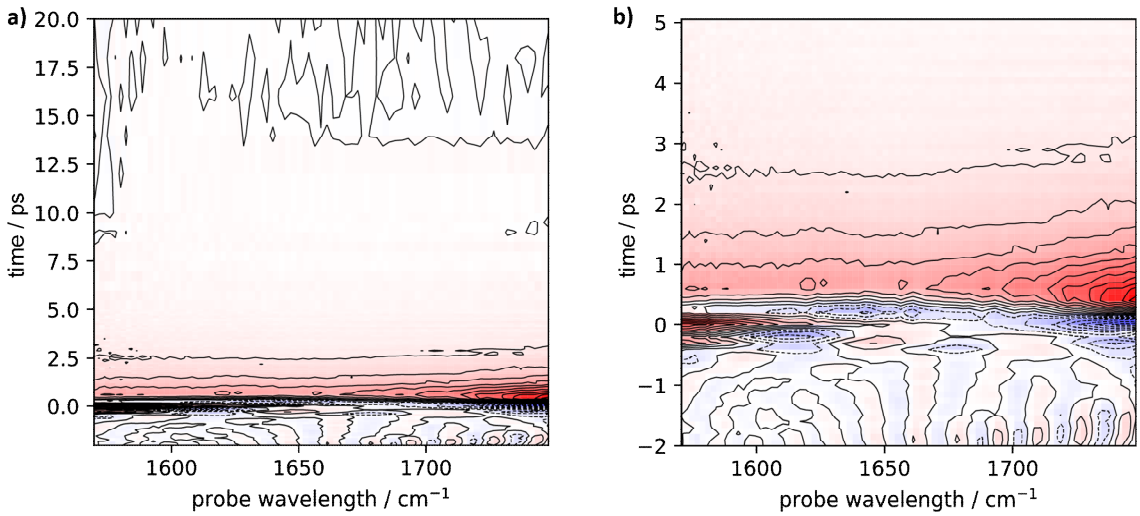


Figure 4.33. A slice (ω_{pump} = 2061 cm^{-1}) of the 2D-IR LIFEtime data recorded for ***c*-P6·T6$^{+\bullet}$** with **probe a** set to the wavenumber region ~1550–1750 cm^{-1} showing (**a**) entire pump-probe delay series and (**b**) early time pump-probe delays. Red/blue correspond to positive(ESA)/negative(GSB) signals.

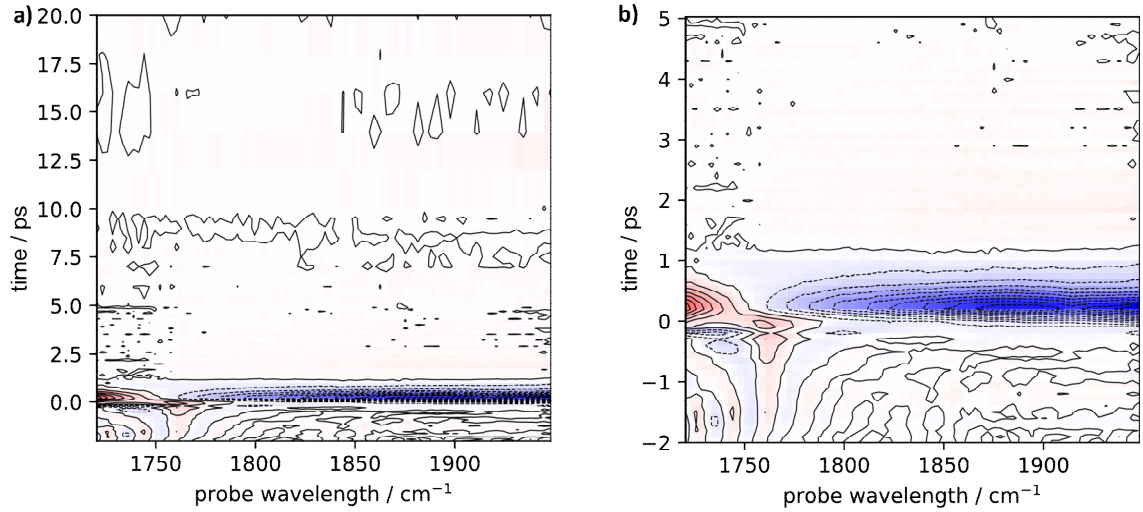


Figure 4.34. A slice (ω_{pump} = 2061 cm^{-1}) of the 2D-IR LIFEtime data recorded for ***c*-P6·T6$^{+\bullet}$** with **probe a** set to the wavenumber region ~1700–1950 cm^{-1} showing (**a**) entire pump-probe delay series and (**b**) early time pump-probe delays. Red/blue correspond to positive(ESA)/negative(GSB) signals.

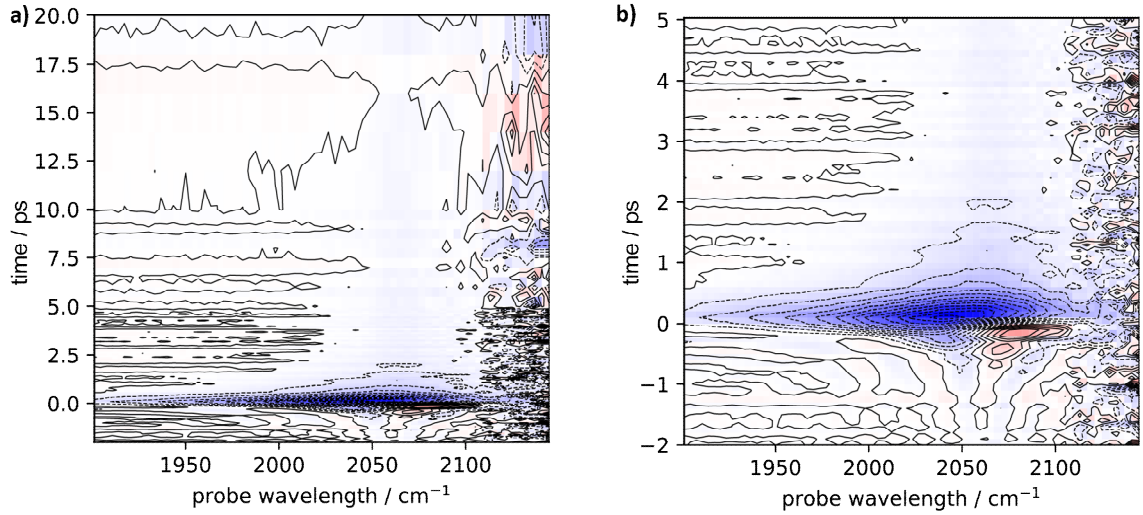


Figure 4.35. A slice (ω_{pump} = 2061 cm^{-1}) of the 2D-IR LIFEtime data recorded for ***c*-P6·T6$^{+\bullet}$** with **probe b** set to the wavenumber region ~1900–2150 cm^{-1} showing (**a**) entire pump-probe delay series and (**b**) early time pump-probe delays. Red/blue correspond to positive(ESA)/negative(GSB) signals.

4.5.5 Polarisation sensitive TRIR

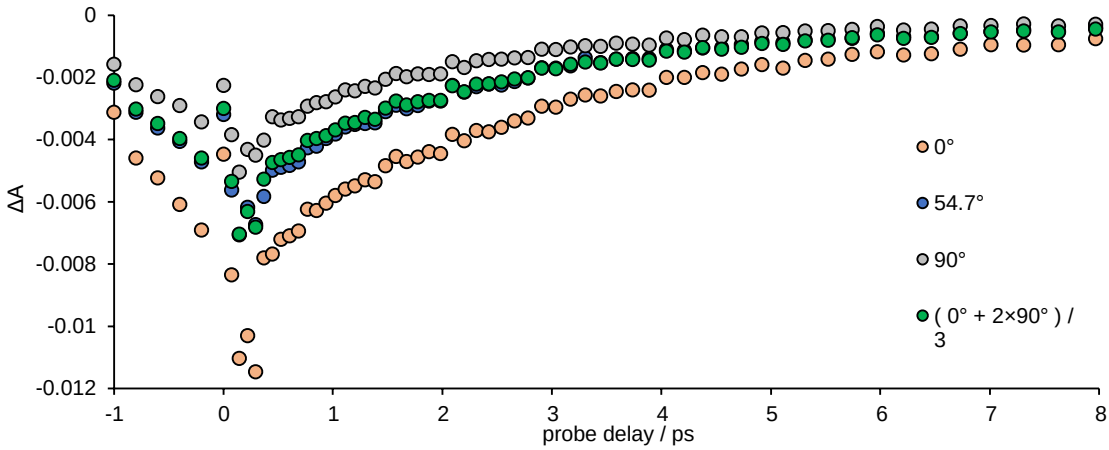


Figure 4.36. GSB intensity of ***l*-P2$^{+\bullet}$** dependence on pump-probe orientation for ω_{pump} = 2050 cm^{-1} and ω_{probe} = 1533 cm^{-1}. Combination of parallel and perpendicular orientations (according to eqn (4.2)) gives values congruent to experimentally observed magic angle data.

5

References

1 G. McDermott, S. M. Prince, A. A. Freer, A. M. Hawthornthwaite-Lawless, M. Z. Papiz, R. J. Cogdell and N. W. Isaacs, 'Crystal structure of an integral membrane light-harvesting complex from photosynthetic bacteria', *Nature*, 1995, **374**, 517–521.

2 J. Koepke, X. Hu, C. Muenke, K. Schulten and H. Michel, 'The crystal structure of the light-harvesting complex II (B800-850) from Rhodospirillum molischianum', *Structure*, 1996, **4**, 581–597.

3 A. W. Roszak, T. D. Howard, J. Southall, A. T. Gardiner, C. J. Law, N. W. Isaacs and R. J. Cogdell, 'Crystal Structure of the RC-LH1 Core Complex from Rhodopseudomonas palustris', *Science*, 2003, **302**, 1969–1972.

4 M. Vicente and K. Smith, 'Syntheses and Functionalizations of Porphyrin Macrocycles', *Curr. Org. Synth.*, 2014, **11**, 3–28.

5 S. Hiroto, Y. Miyake and H. Shinokubo, 'Synthesis and Functionalization of Porphyrins through Organometallic Methodologies', *Chem. Rev.*, 2017, **117**, 2910–3043.

6 J. S. Lindsey, I. C. Schreiman, H. C. Hsu, P. C. Kearney and A. M. Marguerettaz, 'Rothemund and Adler-Longo reactions revisited: synthesis of tetraphenylporphyrins under equilibrium conditions', *J. Org. Chem.*, 1987, **52**, 827–836.

7 E. Baltazzi and L. I. Krimen, 'Recent advances in the chemistry of pyrrole', *Chem. Rev.*, 1963, **63**, 511–556.

8 V. Estévez, M. Villacampa and J. Carlos Menéndez, 'Recent advances in the synthesis of pyrroles by multicomponent reactions', *Chem. Soc. Rev.*, 2014, **43**, 4633–4657.

9 B. J. Littler, M. A. Miller, C. H. Hung, R. W. Wagner, D. F. O'Shea, P. D. Boyle and J. S. Lindsey, 'Refined synthesis of 5-substituted dipyrromethanes', *J. Org. Chem.*, 1999, **64**, 1391–1396.

10 G. P. Arsenault, E. Bullock and S. F. MacDonald, 'Pyrromethanes and Porphyrins Therefrom 1', *J. Am. Chem. Soc.*, 1960, **82**, 4384–4389.

11 A. Osuka, T. Nagata, F. Kobayashi and K. Maruyama, 'An improved synthesis of 5,15-diaryloctaalkylporphyrins', *J. Heterocycl. Chem.*, 1990, **27**, 1657–1659.

12 K. M. Smith, 'Development of porphyrin syntheses', *New J. Chem.*, 2016, **40**, 5644–5649.

13 M. O. Senge, 'Nucleophilic substitution as a tool for the synthesis of unsymmetrical

porphyrins', *Acc. Chem. Res.*, 2005, **38**, 733–743.

14 J. S. Lindsey, 'Synthetic routes to meso-patterned porphyrins', *Acc. Chem. Res.*, 2010, **43**, 300–311.

15 M. O. Senge, 'Stirring the porphyrin alphabet soup - Functionalization reactions for porphyrins', *Chem. Commun.*, 2011, **47**, 1943–1960.

16 D. K. Dogutan, S. H. H. Zaidi, P. Thamyongkit and J. S. Lindsey, 'New route to ABCD-porphyrins via bilanes', *J. Org. Chem.*, 2007, **72**, 7701–7714.

17 X. Feng and M. O. Senge, 'An efficient synthesis of highly functionalized asymmetric porphyrins with organolithium reagents', *J. Chem. Soc. Perkin 1*, 2001, 1030–1038.

18 X. Feng and M. O. Senge, 'One-pot synthesis of functionalized asymmetric 5,10,15,20-substituted porphyrins from 5,15-diaryl-or -dialkyl-porphyrins', *Tetrahedron*, 2000, **56**, 587–590.

19 P. N. Taylor, J. Huuskonen, C. Rumbles, R. T. Aplin, E. Williams and H. L. Anderson, 'Conjugated porphyrin oligomers from monomer to hexamer', *Chem. Commun.*, 1998, 909–910.

20 P. N. Taylor and H. L. Anderson, 'Cooperative self-assembly of double-strand conjugated porphyrin ladders', *J. Am. Chem. Soc.*, 1999, **121**, 11538–11545.

21 R. G. Khoury, L. Jaquinod and K. M. Smith, 'Rational approach to the synthesis of meso-meso (5,5') linked bis-porphyrins', *Chem. Commun.*, 1997, 1057–1058.

22 N. Yoshida, T. Ishizuka, A. Osuka, D. H. Jeong, H. S. Cho, D. Kim, Y. Matsuzaki, A. Nogami and K. Tanaka, 'Fine tuning of photophysical properties of meso-meso-linked Zn II -diporphyrins by dihedral angle control', *Chem. - A Eur. J.*, 2003, **9**, 58–75.

23 V. S. -. Lin and M. J. Therien, 'The Role of Porphyrin-to-Porphyrin Linkage Topology in the Extensive Modulation of the Absorptive and Emissive Properties of a Series of Ethynyl- and Butadiynyl-Bridged Bis- and Tris(porphinato)zinc Chromophores', *Chem. – A Eur. J.*, 1995, **1**, 645–651.

24 L. Rintoul, S. R. Harper and D. P. Arnold, 'A systematic theoretical study of the electronic structures of porphyrin dimers: DFT and TD-DFT calculations on diporphyrins linked by ethane, ethene, ethyne, imine, and azo bridges', *Phys. Chem. Chem. Phys.*, 2013, **15**, 18951–18964.

25 M. D. Peeks, P. Neuhaus and H. L. Anderson, 'Experimental and computational evaluation of the barrier to torsional rotation in a butadiyne-linked porphyrin dimer', *Phys. Chem. Chem. Phys.*, 2016, **18**, 5264–5274.

26 Y. Nakamura, N. Aratani and A. Osuka, 'Cyclic porphyrin arrays as artificial photosynthetic antenna: Synthesis and excitation energy transfer', *Chem. Soc. Rev.*, 2007, **36**, 831–845.

27 S. Anderson, H. L. Anderson and J. K. M. Sanders, 'Expanding Roles for Templates in Synthesis', *Acc. Chem. Res.*, 1993, **26**, 469–475.

28 H. L. Anderson and J. K. M. Sanders, 'Synthesis of a cyclic porphyrin trimer with a semi-rigid cavity', *J. Chem. Soc. Chem. Commun.*, 1989, 1714.

29 S. Anderson, H. L. Anderson and J. K. M. Sanders, 'The roles of templates in the syntheses of porphyrin oligomers', *J. Chem. Soc. Perkin Trans. 1*, 1995, 2255.

30 S. Rucareanu, A. Schuwey and A. Gossauer, 'One-step template-directed synthesis of a macrocyclic tetraarylporphyrin hexamer based on supramolecular interactions with a C3-symmetric tetraarylporphyrin trimer', *J. Am. Chem. Soc.*, 2006, **128**, 3396–3413.

31 J. Song, N. Aratani, H. Shinokubo and A. Osuka, 'A Porphyrin Nanobarrel That Encapsulates C 60', *J. Am. Chem. Soc.*, 2010, **132**, 16356–16357.

32 S. Liu, D. V. Kondratuk, S. A. L. Rousseaux, G. Gil-Ramírez, M. C. O'Sullivan, J. Cremers, T. D. W. Claridge and H. L. Anderson, 'Caterpillar track complexes in template-directed synthesis and correlated molecular motion', *Angew. Chem., Int. Ed.*, 2015, **54**, 5355–5359.

33 D. V. Kondratuk, L. M. A. Perdigaõ, A. M. S. Esmail, J. N. O'Shea, P. H. Beton and H. L. Anderson, 'Supramolecular nesting of cyclic polymers', *Nat. Chem.*, 2015, **7**, 317–322.

34 M. Rickhaus, A. Vargas Jentzsch, L. Tejerina, I. Grübner, M. Jirasek, T. D. W. W. Claridge and H. L. Anderson, 'Single-Acetylene Linked Porphyrin Nanorings', *J. Am. Chem. Soc.*, 2017, **139**, 16502–16505.

35 P. S. Bols and H. L. Anderson, 'Template-Directed Synthesis of Molecular Nanorings and Cages', *Acc. Chem. Res.*, 2018, **51**, 2083–2092.

36 P. Liu, P. Neuhaus, D. V. Kondratuk, T. S. Balaban and H. L. Anderson, 'Cyclodextrin-templated porphyrin nanorings', *Angew. Chem., Int. Ed.*, 2014, **53**, 7770–7773.

37 J. Cremers, S. Richert, D. V. Kondratuk, T. D. W. Claridge, C. R. Timmel and H. L. Anderson, 'Nanorings with copper(ii) and zinc(ii) centers: forcing copper porphyrins to bind axial ligands in heterometallated oligomers', *Chem. Sci.*, 2016, **7**, 6961–6968.

38 P. S. Bols and H. L. Anderson, 'Shadow Mask Templates for Site-Selective Metal Exchange in Magnesium Porphyrin Nanorings', *Angew. Chem., Int. Ed.*, 2018, **57**, 7874–7877.

39 P. Parkinson, N. Kamonsutthipaijit, H. L. Anderson and L. M. Herz, 'Size-Independent Energy Transfer in Biomimetic Nanoring Complexes', *ACS Nano*, 2016, **10**, 5933–5940.

40 C. Roche, Q. Luo, G. Gil-Ramírez, H. W. Jiang, D. R. Kohn, Y. Xiong, A. L. Thompson and H. L. Anderson, 'Unexpected Interactions between Alkyl Straps and Pyridine Ligands in Sulfur-Strapped Porphyrin Nanorings', *J. Org. Chem.*, 2017, **82**, 7446–7462.

41 M. Hoffmann, C. J. Wilson, B. Odell and H. L. Anderson, 'Template-directed synthesis of a π;-conjugated porphyrin nanoring', *Angew. Chem., Int. Ed.*, 2007, **46**, 3122–3125.

42 P. Liu, Y. Hisamune, M. D. Peeks, B. Odell, J. Q. Gong, L. M. Herz and H. L. Anderson, 'Synthesis of Five-Porphyrin Nanorings by Using Ferrocene and Corannulene Templates', *Angew. Chem., Int. Ed.*, 2016, **55**, 8358–8362.

43 D. V. Kondratuk, L. M. A. Perdigao, M. C. O'Sullivan, S. Svatek, G. Smith, J. N. O'Shea, P. H. Beton and H. L. Anderson, 'Two vernier-templated routes to a 24-porphyrin nanoring', *Angew. Chem., Int. Ed.*, 2012, **51**, 6696–6699.

44 S. A. L. Rousseaux, J. Q. Gong, R. Haver, B. Odell, T. D. W. Claridge, L. M. Herz and H. L. Anderson, 'Self-Assembly of Russian Doll Concentric Porphyrin Nanorings', *J. Am. Chem. Soc.*, 2015, **137**, 12713–12718.

45 P. Parkinson, D. V. Kondratuk, C. Menelaou, J. Q. Gong, H. L. Anderson and L. M. Herz, 'Chromophores in molecular nanorings: When is a ring a ring?', *J. Phys. Chem. Lett.*, 2014, **5**, 4356–4361.

46 J. K. Sprafke, D. V. Kondratuk, M. Wykes, A. L. Thompson, M. Hoffmann, R. Drevinskas, W. H. Chen, C. K. Yong, J. Kärnbratt, J. E. Bullock, M. Malfois, M. R. Wasielewski, B. Albinsson, L. M. Herz, D. Zigmantas, D. Beljonne and H. L. Anderson, 'Belt-shaped π-systems: Relating geometry to electronic structure in a six-porphyrin nanoring', *J. Am. Chem. Soc.*, 2011, **133**, 17262–17273.

47 C. K. Yong, P. Parkinson, D. V. Kondratuk, W. H. Chen, A. Stannard, A. Summerfield, J. K. Sprafke, M. C. O'Sullivan, P. H. Beton, H. L. Anderson and L. M. Herz, 'Ultrafast delocalization of excitation in synthetic light-harvesting nanorings', *Chem. Sci.*, 2015, **6**, 181–189.

48 P. Parkinson, C. E. I. Knappke, N. Kamonsutthipaijit, K. Sirithip, J. D. Matichak, H. L. Anderson and L. M. Herz, 'Ultrafast energy transfer in biomimetic multistrand nanorings', *J. Am. Chem. Soc.*, 2014, **136**, 8217–8220.

49 M. Hoffmann, J. Kärnbratt, M. H. Chang, L. M. Herz, B. Albinsson and H. L. Anderson, 'Enhanced π conjugation around a porphyrin[6] nanoring', *Angew. Chem., Int. Ed.*, 2008, **47**, 4993–4996.

50 R. Haver, L. Tejerina, H.-W. Jiang, M. Rickhaus, M. Jirasek, I. Grübner, H. J. Eggimann, L. M. Herz and H. L. Anderson, 'Tuning the Circumference of Six-Porphyrin Nanorings', *J. Am. Chem. Soc.*, 2019, **141**, 7965–7971.

51 S. Richert, J. Cremers, I. Kuprov, M. D. Peeks, H. L. Anderson and C. R. Timmel, 'Constructive quantum interference in a bis-copper six-porphyrin nanoring', *Nat. Commun.*, 2017, **8**, 14842.

52 C. J. Lambert, 'Basic concepts of quantum interference and electron transport in single-molecule electronics', *Chem. Soc. Rev.*, 2015, **44**, 875–888.

53 T. M. Krygowski, M. K. Cyrañski, Z. Czarnocki, G. Häfelinger and A. R. Katritzky, 'Aromaticity: a Theoretical Concept of Immense Practical Importance', *Tetrahedron*, 2000, **56**, 1783–1796.

54 J. A. N. F. Gomes and R. B. Mallion, 'Aromaticity and Ring Currents', *Chem. Rev.*, 2001, **101**, 1349–1384.

55 M. D. Peeks, T. D. W. Claridge and H. L. Anderson, 'Aromatic and antiaromatic ring currents in a molecular nanoring', *Nature*, 2017, **541**, 200–203.

56 M. Rickhaus, M. Jirasek, L. Tejerina, H. Gotfredsen, M. D. Peeks, R. Haver, H.-W. Jiang and T. D. W. Claridge, 'Global Aromaticity at the Nanoscale', *Nat. Chem.*, 2020, preprint, DOI: 10.1038/s41557-019-0398-3.

57 T. Soya, W. Kim, D. Kim and A. Osuka, 'Stable [48]-, [50]-, and [52]Dodecaphyrins(1.1.0.1.1.0.1.1.0.1.1.0): The Largest Hückel Aromatic Molecules', *Chem. - A Eur. J.*, 2015, **21**, 8341–8346.

58 M. D. Peeks, M. Jirasek, T. D. W. Claridge and H. L. Anderson, 'Global Aromaticity and Antiaromaticity in Porphyrin Nanoring Anions', *Angew. Chem., Int. Ed.*, 2019, **58**, 15717–15720.

59 R. D. Mukhopadhyay, Y. Kim, J. Koo and K. Kim, 'Porphyrin Boxes', *Acc. Chem. Res.*, 2018, **51**, 2730–2738.

60 T. Tanaka and A. Osuka, 'Conjugated porphyrin arrays: Synthesis, properties and applications for functional materials', *Chem. Soc. Rev.*, 2015, **44**, 943–969.

61 S. Durot, J. Taesch and V. Heitz, 'Multiporphyrinic Cages: Architectures and Functions', *Chem. Rev.*, 2014, **114**, 8542–8578.

62 J. Aimi, Y. Nagamine, A. Tsuda, A. Muranaka, M. Uchiyama and T. Aida, ''Conformational' solvatochromism: Spatial discrimination of nonpolar solvents by using a supramolecular box of a π-conjugated zinc bisporphyrin rotamer', *Angew. Chem., Int. Ed.*, 2008, **47**, 5153–5156.

63 A. Tsuda, Y. Nagamine, R. Watanabe, Y. Nagatani, N. Ishii and T. Aida, 'Spectroscopic visualization of sound-induced liquid vibrations using a supramolecular nanofibre', *Nat. Chem.*, 2010, **2**, 977–983.

64 J. Aimi, K. Oya, A. Tsuda and T. Aida, 'Chiroptical sensing of asymmetric hydrocarbons using a homochiral supramolecular box from a bismetalloporphyrin rotamer', *Angew. Chem., Int. Ed.*, 2007, **46**, 2031–2035.

65 A. Tsuda, H. Hu, R. Tanaka and T. Aida, 'Planar or perpendicular? Conformational preferences of π-conjugated metalloporphyrin dimers and trimers in supramolecular tubular arrays', *Angew. Chem., Int. Ed.*, 2005, **44**, 4884–4888.

66 A. Tsuda, H. Hu, R. Watanabe and T. Aida, in *Journal of Porphyrins and Phthalocyanines*, Society of Porphyrins and Phthalocyanines (SPP), 2003, vol. 7, pp. 388–393.

67 R. V. Slone and J. T. Hupp, 'Synthesis, Characterization, and Preliminary Host−Guest Binding Studies of Porphyrinic Molecular Squares Featuring fac -Tricarbonylrhenium(I) Chloro Corners', *Inorg. Chem.*, 1997, **36**, 5422–5423.

68 J. L. Suk, K. L. Mulfort, X. Zuo, A. J. Goshe, P. J. Wesson, S. B. T. Nguyen, J. T. Hupp and D. M. Tiede, 'Coordinative self-assembly and solution-phase X-ray structural characterization of cavity-tailored porphyrin boxes', *J. Am. Chem. Soc.*, 2008, **130**, 836–838.

69 M. Yoshizawa, J. K. Klosterman and M. Fujita, 'Functional Molecular Flasks: New Properties and Reactions within Discrete, Self-Assembled Hosts', *Angew. Chem., Int. Ed.*, 2009, **48**, 3418–3438.

70 S. J. Lee, S.-H. Cho, K. L. Mulfort, D. M. Tiede, J. T. Hupp and S. T. Nguyen, 'Cavity-Tailored, Self-Sorting Supramolecular Catalytic Boxes for Selective Oxidation', *J. Am. Chem. Soc.*, 2008, **130**, 16828–16829.

71 W. Meng, B. Breiner, K. Rissanen, J. D. Thoburn, J. K. Clegg and J. R. Nitschke, 'A Self-Assembled M8L6 Cubic Cage that Selectively Encapsulates Large Aromatic Guests', *Angew. Chem., Int. Ed.*, 2011, **50**, 3479–3483.

72 W. Brenner, T. K. Ronson and J. R. Nitschke, 'Separation and Selective Formation of Fullerene Adducts within an M II 8 L 6 Cage', *J. Am. Chem. Soc.*, 2017, **139**, 75–78.

73 F. J. Rizzuto and J. R. Nitschke, 'Stereochemical plasticity modulates cooperative binding in a CoII12L6 cuboctahedron', *Nat. Chem.*, 2017, **9**, 903–908.

74 J. Mosquera, B. Szyszko, S. K. Y. Ho and J. R. Nitschke, 'Sequence-selective encapsulation and protection of long peptides by a self-assembled FeII8L6 cubic cage', *Nat. Commun.*, 2017, **8**, 14882.

75 F. J. Rizzuto, D. M. Wood, T. K. Ronson and J. R. Nitschke, 'Tuning the Redox Properties of Fullerene Clusters within a Metal–Organic Capsule', *J. Am. Chem. Soc.*, 2017, **139**, 11008–11011.

76 F. J. Rizzuto, W. J. Ramsay and J. R. Nitschke, 'Otherwise Unstable Structures Self-Assemble in the Cavities of Cuboctahedral Coordination Cages', *J. Am. Chem. Soc.*, 2018, **140**, 11502–11509.

77 A. Satake and Y. Kobuke, 'Dynamic supramolecular porphyrin systems', *Tetrahedron*, 2005, **61**, 13–41.

78 M. Kawaguchi, A. Ikeda and S. Shinkai, 'A novel porphyrin-homooxacalix[3]arene conjugate which creates a C3-symmetrical capsular space', *Tetrahedron Lett.*, 2001, **42**, 3725–3728.

79 P. Neuhaus, A. Cnossen, J. Q. Gong, L. M. Herz and H. L. Anderson, 'A Molecular Nanotube with Three-Dimensional π-Conjugation', *Angew. Chem., Int. Ed.*, 2015, **54**, 7344–7348.

80 R. Haver and H. L. Anderson, 'Synthesis and Properties of Porphyrin Nanotubes', *Helv. Chim. Acta*, 2019, **102**, e1800211.

81 R. Haver, 'Synthesis and Properties of Porphyrin Nanotubes', DPhil Thesis, University of Oxford, 2018.

82 J. Cremers, R. Haver, M. Rickhaus, J. Q. Gong, L. Favereau, M. D. Peeks, T. D. W. Claridge, L. M. Herz and H. L. Anderson, 'Template-Directed synthesis of a conjugated zinc porphyrin nanoball', *J. Am. Chem. Soc.*, 2018, **140**, 5352–5355.

83 J. Cremers, 'Electronic communication in heterometallated porphyrin oligomers', DPhil Thesis, University of Oxford, 2017.

84 R. P. Xu, Y. Q. Li and J. X. Tang, *J. Mater. Chem. C*, 2016, 4, 9116–9142.

85 E. Zysman-Colman, 'Recent advances in materials for organic light emitting diodes', *Beilstein J. Org. Chem.*, 2018, **14**, 1944–1945.

86 B. Geffroy, P. le Roy and C. Prat, 'Organic light-emitting diode (OLED) technology: Materials, devices and display technologies', *Polym. Int.*, 2006, **55**, 572–582.

87 L. Duan, L. Hou, T.-W. Lee, J. Qiao, D. Zhang, G. Dong, L. Wang and Y. Qiu, 'Solution processable small molecules for organic light-emitting diodes', *J. Mater. Chem.*, 2010, **20**, 6392.

88 A. Facchetti, 'π-Conjugated polymers for organic electronics and photovoltaic cell applications', *Chem. Mater.*, 2011, **23**, 733–758.

89 M. C. Scharber and N. S. Sariciftci, 'Efficiency of bulk-heterojunction organic solar cells', *Prog. Polym. Sci.*, 2013, **38**, 1929–1940.

90 S. Holliday, Y. Li and C. K. Luscombe, 'Recent advances in high performance donor-acceptor polymers for organic photovoltaics', *Prog. Polym. Sci.*, 2017, **70**, 34–51.

91 A. Facchetti, 'Polymer donor-polymer acceptor (all-polymer) solar cells', *Mater. Today*, 2013, **16**, 123–132.

92 H. Sirringhaus, '25th anniversary article: Organic field-effect transistors: The path beyond amorphous silicon', *Adv. Mater.*, 2014, **26**, 1319–1335.

93 W. Tang, Y. Huang, L. Han, R. Liu, Y. Su, X. Guo and F. Yan, *J. Mater. Chem. C*, 2019, 7, 790–808.

94 H. Li, W. Shi, J. Song, H. J. Jang, J. Dailey, J. Yu and H. E. Katz, *Chem. Rev.*, 2019, 119, 3–35.

95 L. Torsi, M. Magliulo, K. Manoli and G. Palazzo, 'Organic field-effect transistor sensors: A tutorial review', *Chem. Soc. Rev.*, 2013, **42**, 8612–8628.

96 H. L. Anderson, 'Conjugated Porphyrin Ladders', *Inorg. Chem.*, 1994, **33**, 972–981.

97 H. L. Anderson, 'Building molecular wires from the colours of life: Conjugated porphyrin oligomers', *Chem. Commun.*, 1999, 2323–2330.

98 F. C. Grozema, C. Houarner-Rassin, P. Prins, L. D. A. Siebbeles and H. L. Anderson, 'Supramolecular control of charge transport in molecular wires', *J. Am. Chem. Soc.*, 2007, **129**, 13370–13371.

99 M. D. Peeks, C. E. Tait, P. Neuhaus, G. M. Fischer, M. Hoffmann, R. Haver, A. Cnossen, J. R. Harmer, C. R. Timmel and H. L. Anderson, 'Electronic Delocalization in the Radical Cations of Porphyrin Oligomer Molecular Wires', *J. Am. Chem. Soc.*, 2017, **139**, 10461–10471.

100 M. Gilbert Gatty, A. Kahnt, L. J. Esdaile, M. Hutin, H. L. Anderson and B. Albinsson, 'Hopping versus Tunneling Mechanism for Long-Range Electron Transfer in Porphyrin Oligomer Bridged Donor-Acceptor Systems', *J. Phys. Chem. B*, 2015, **119**, 7598–7611.

101 G. Sedghi, V. M. García-Suárez, L. J. Esdaile, H. L. Anderson, C. J. Lambert, S. Martín, D. Bethell, S. J. Higgins, M. Elliott, N. Bennett, J. E. MacDonald and R. J. Nichols, 'Long-range electron tunnelling in oligo-porphyrin molecular wires', *Nat. Nanotechnol.*, 2011, **6**, 517–523.

102 G. Sedghi, L. J. Esdaile, H. L. Anderson, S. Martin, D. Bethell, S. J. Higgins and R. J. Nichols, 'Comparison of the conductance of three types of porphyrin-based molecular wires: β,Meso,β-fused tapes, meso-butadiyne-linked and twisted meso-meso linked oligomers', *Adv. Mater.*, 2012, **24**, 653–657.

103 B. Limburg, J. O. Thomas, G. Holloway, H. Sadeghi, S. Sangtarash, I. C. Y. Hou, J. Cremers, A. Narita, K. Müllen, C. J. Lambert, G. A. D. Briggs, J. A. Mol and H. L. Anderson, 'Anchor Groups for Graphene-Porphyrin Single-Molecule Transistors',

Adv. Funct. Mater., 2018, **28**, 1–11.

104 O. Fenwick, J. K. Sprafke, J. Binas, D. V. Kondratuk, F. Di Stasio, H. L. Anderson and F. Cacialli, 'Linear and cyclic porphyrin hexamers as near-infrared emitters in organic light-emitting diodes', *Nano Lett.*, 2011, **11**, 2451–2456.

105 M. C. O'Sullivan, J. K. Sprafke, D. V. Kondratuk, C. Rinfray, T. D. W. Claridge, A. Saywell, M. O. Blunt, J. N. O'Shea, P. H. Beton, M. Malfois and H. L. Anderson, 'Vernier templating and synthesis of a 12-porphyrin nano-ring', *Nature*, 2011, **469**, 72–75.

106 D. V. Kondratuk, J. K. Sprafke, M. C. O'Sullivan, L. M. A. Perdigao, A. Saywell, M. Malfois, J. N. O'Shea, P. H. Beton, A. L. Thompson and H. L. Anderson, 'Vernier-templated synthesis, crystal structure, and supramolecular chemistry of a 12-porphyrin nanoring', *Chem. - A Eur. J.*, 2014, **20**, 12826–12834.

107 E. Leary, C. Roche, H.-W. W. Jiang, I. Grace, M. T. González, G. Rubio-Bollinger, C. Romero-Muñiz, Y. Xiong, Q. Al-Galiby, M. Noori, M. A. Lebedeva, K. Porfyrakis, N. Agräit, A. Hodgson, S. J. Higgins, C. J. Lambert, H. L. Anderson and R. J. Nichols, 'Detecting Mechanochemical Atropisomerization within an STM Break Junction', *J. Am. Chem. Soc.*, 2018, **140**, 710–718.

108 M. D. Peeks, J. Q. Gong, K. McLoughlin, T. Kobatake, R. Haver, L. M. Herz and H. L. Anderson, 'Aromaticity and Antiaromaticity in the Excited States of Porphyrin Nanorings', *J. Phys. Chem. Lett.*, 2019, **10**, 2017–2022.

109 J. Q. Gong, L. Favereau, H. L. Anderson and L. M. Herz, 'Breaking the Symmetry in Molecular Nanorings', *J. Phys. Chem. Lett.*, 2016, **7**, 332–338.

110 L. Favereau, A. Cnossen, J. B. Kelber, J. Q. Gong, R. M. Oetterli, J. Cremers, L. M. Herz and H. L. Anderson, 'Six-Coordinate Zinc Porphyrins for Template-Directed Synthesis of Spiro-Fused Nanorings', *J. Am. Chem. Soc.*, 2015, **137**, 14256–14259.

111 N. Basarić, S. S. Thomas, V. B. Bregović, N. Cindro and C. Bohne, 'Phototautomerization in Pyrrolylphenylpyridine Terphenyl Systems', *J. Org. Chem.*, 2015, **80**, 4430–4442.

112 T. Y. Kim, L. Digal, M. G. Gardiner, N. T. Lucas and J. D. Crowley, 'Octahedral [Pd6L8]12+ Metallosupramolecular Cages: Synthesis, Structures and Guest-Encapsulation Studies', *Chem. - A Eur. J.*, 2017, **23**, 15089–15097.

113 T. Ishiyama, M. Murata and N. Miyaura, 'Palladium(0)-Catalyzed Cross-Coupling Reaction of Alkoxydiboron with Haloarenes: A Direct Procedure for Arylboronic Esters', *J. Org. Chem.*, 1995, **60**, 7508–7510.

114 S. Hitosugi, D. Tanimoto, W. Nakanishi and H. Isobe, 'A facile chromatographic method for purification of pinacol boronic esters', *Chem. Lett.*, 2012, **41**, 972–973.

115 M. R. Talipov, A. Boddeda, Q. K. Timerghazin and R. Rathore, 'Key Role of End-Capping Groups in Optoelectronic Properties of Poly- p -phenylene Cation Radicals', *J. Phys. Chem. C*, 2014, **118**, 21400–21408.

116 J.-R. Wang and K. Manabe, 'Transition-Metal-Catalyzed Site-Selective Cross-Coupling of Di- and Polyhalogenated Compounds', *Synthesis*, 2009, **2009**, 1405–1427.

117 G. Gaefke and S. Höger, '[(3-Cyanopropyl)diisopropylsilyl]acetylene, a More Stable Analogue of [(3-Cyanopropyl)dimethylsilyl]acetylene', *Synthesis*, 2008, **2008**, 2155–2157.

118 S. Höger and K. Bonrad, '[(3-Cyanopropyl)dimethylsilyl]acetylene, a polar analogue of (trimethylsilyl)acetylene: Synthesis and applications in the preparation of monoprotected bisacetylenes', *J. Org. Chem.*, 2000, **65**, 2243–2245.

119 H. Jia, Z. Sun, D. Jiang and P. Du, 'Covalent Cobalt Porphyrin Framework on Multiwalled Carbon Nanotubes for Efficient Water Oxidation at Low Overpotential', *Chem. Mater.*, 2015, **27**, 4586–4593.

120 M. John Plater, S. Aiken and G. Bourhill, 'Metallated porphyrins containing lead(II), copper(II) or zinc(II)', *Tetrahedron*, 2002, **58**, 2415–2422.

121 A. S. Batsanov, J. C. Collings, I. J. S. Fairlamb, J. P. Holland, J. A. K. Howard, Z. Lin, T. B. Marder, A. C. Parsons, R. M. Ward and J. Zhu, 'Requirement for an oxidant in Pd/Cu co-catalyzed terminal alkyne homocoupling to give symmetrical 1,4-disubstituted 1,3-diynes', *J. Org. Chem.*, 2005, **70**, 703–706.

122 T. E. O. Screen, K. B. Lawton, G. S. Wilson, N. Dolney, R. Ispasoiu, T. Goodson, S. J. Martin, D. D. C. Bradley and H. L. Anderson, 'Synthesis and third order nonlinear optics of a new soluble conjugated porphyrin polymer', *J. Mater. Chem.*, 2001, **11**, 312–320.

123 G. Scott Wilson and H. L. Anderson, 'A conjugated triple strand porphyrin array', *Chem. Commun.*, 1999, 1539–1540.

124 F. V. A. Camargo, H. L. Anderson, S. R. Meech and I. A. Heisler, 'Time-Resolved Twisting Dynamics in a Porphyrin Dimer Characterized by Two-Dimensional Electronic Spectroscopy', *J. Phys. Chem. B*, 2015, **119**, 14660–14667.

125 I. Grübner, 'Understanding the Origins of Strong Multivalent Cooperativity', DPhil Thesis, University of Oxford, 2019.

126 Y. Yan, J. Huang and B. Z. Tang, 'Kinetic trapping-a strategy for directing the self-assembly of unique functional nanostructures', *Chem. Commun.*, 2016, **52**, 11870–11884.

127 Y. Jin, C. Yu, R. J. Denman and W. Zhang, 'Recent advances in dynamic covalent chemistry', *Chem. Soc. Rev.*, 2013, **42**, 6634–6654.

128 H. J. Hogben, J. K. Sprafke, M. Hoffmann, M. Pawlicki and H. L. Anderson, 'Stepwise effective molarities in porphyrin oligomer complexes: Preorganization results in exceptionally strong chelate cooperativity', *J. Am. Chem. Soc.*, 2011, **133**, 20962–20969.

129 S. J. Su, D. Tanaka, Y. J. Li, H. Sasabe, T. Takeda and J. Kido, 'Novel four-pyridylbenzene-armed biphenyls as electron-transport materials for phosphorescent OLEDs', *Org. Lett.*, 2008, **10**, 941–944.

130 Y. Liang, M. G. Schwab, L. Zhi, E. Mugnaioli, U. Kolb, X. Feng and K. Müllen, 'Direct access to metal or metal oxide nanocrystals integrated with one-dimensional nanoporous carbons for electrochemical energy storage', *J. Am. Chem. Soc.*, 2010, **132**, 15030–15037.

131 R. Rathore, C. L. Burns and M. I. Deselnicu, 'Multiple-electron transfer in a single step. Design and synthesis of highly charged cation-radical salts', *Org. Lett.*, 2001, **3**, 2887–2890.

132 T. Lange, J. D. Van Loon, R. R. Tykwinski, M. Schreiber and F. Diederich, 'Towards the synthesis of tetraethynylallene', *Synthesis*, 1996, **1996**, 537–550.

133 H. L. Anderson, 'Meso-alkynyl porphyrins', *Tetrahedron Lett.*, 1992, **33**, 1101–1104.

134 J. Clayden, N. Greeves and S. G. Warren, *Organic Chemistry*, Oxford University Press, Oxford, 2nd edn., 2012.

135 P. Karrer, A. Helfenstein, H. Wehrli and A. Wettstein, 'Pflanzenfarbstoffe XXV. Über die Konstitution des Lycopins und Carotins', *Helv. Chim. Acta*, 1930, **13**, 1084–1099.

136 D. L. Fox, 'Feather carotenoids of an interspecific hybrid flamingo', *Comp. Biochem. Physiol. -- Part B Biochem.*, 1974, **48**, 295–298.

137 I. Fleming, 'Absolute configuration and the structure of chlorophyll', *Nature*, 1967, **216**, 151–152.

138 S. R. Forrest, 'The path to ubiquitous and low-cost organic electronic appliances on plastic', *Nature*, 2004, **428**, 911–918.

139 Y. Zhao, Y. Guo and Y. Liu, '25th Anniversary Article: Recent advances in n-type and ambipolar organic field-effect transistors', *Adv. Mater.*, 2013, **25**, 5372–5391.

140 H. Bässler and A. Köhler, 'Charge transport in organic semiconductors', *Top. Curr. Chem.*, 2012, **312**, 1–65.

141 G. Li, R. Zhu and Y. Yang, 'Polymer solar cells', *Nat. Photonics*, 2012, **6**, 153–161.

142 R. A. J. Janssen and J. Nelson, 'Factors limiting device efficiency in organic photovoltaics', *Adv. Mater.*, 2013, **25**, 1847–1858.

143 S. Shahnawaz, S. Sudheendran Swayamprabha, M. R. Nagar, R. A. K. Yadav, S. Gull, D. K. Dubey and J. H. Jou, 'Hole-transporting materials for organic light-emitting diodes: An overview', *J. Mater. Chem. C*, 2019, **7**, 7144–7158.

144 J. J. Urban, A. K. Menon, Z. Tian, A. Jain and K. Hippalgaonkar, 'New horizons in thermoelectric materials: Correlated electrons, organic transport, machine learning, and more', *J. Appl. Phys.*, 2019, **125**, 180902.

145 B. Russ, A. Glaudell, J. J. Urban, M. L. Chabinyc and R. A. Segalman, 'Organic thermoelectric materials for energy harvesting and temperature control', *Nat. Rev. Mater.*, 2016, **1**, 16050.

146 F. Li, T. Li, F. Chen and F. Zhang, 'Excellent spin transport in spin valves based on the conjugated polymer with high carrier mobility', *Sci. Rep.*, 2015, **5**, 9355.

147 J. Devkota, R. Geng, R. C. Subedi and T. D. Nguyen, 'Organic Spin Valves: A Review', *Adv. Funct. Mater.*, 2016, **26**, 3881–3898.

148 X. Sun, S. Vélez, A. Atxabal, A. Bedoya-Pinto, S. Parui, X. Zhu, R. Llopis, F. Casanova and L. E. Hueso, 'A molecular spin-photovoltaic device', *Science*, 2017, **357**, 677–680.

149 S. Muench, A. Wild, C. Friebe, B. Häupler, T. Janoschka and U. S. Schubert, 'Polymer-

Based Organic Batteries', *Chem. Rev.*, 2016, **116**, 9438–9484.

150 J. Xie, P. Gu and Q. Zhang, 'Nanostructured Conjugated Polymers: Toward High-Performance Organic Electrodes for Rechargeable Batteries', *ACS Energy Lett.*, 2017, **2**, 1985–1996.

151 H. Jia and T. Lei, 'Emerging research directions for n-type conjugated polymers', *J. Mater. Chem. C*, 2019, **7**, 12809–12821.

152 The Nobel Foundation, Press Release - 2000 Nobel Prize in Chemistry, www.nobelprize.org/prizes/chemistry/2000/press-release, (accessed 9 December 2019).

153 H. Shirakawa, 'The Discovery of Polyacetylene Film: The Dawning of an Era of Conducting Polymers (Nobel Lecture)', *Angew. Chem., Int. Ed.*, 2001, **40**, 2574–2580.

154 C. Cobet, J. Gasiorowski, R. Menon, K. Hingerl, S. Schlager, M. S. White, H. Neugebauer, N. S. Sariciftci and P. Stadler, 'Influence of molecular designs on polaronic and vibrational transitions in a conjugated push-pull copolymer', *Sci. Rep.*, 2016, **6**, 35096.

155 J. G. Müller, J. M. Lupton, J. Feldmann, U. Lemmer, M. C. Scharber, N. S. Sariciftci, C. J. Brabec and U. Scherf, 'Ultrafast dynamics of charge carrier photogeneration and geminate recombination in conjugated polymer:fullerene solar cells', *Phys. Rev. B - Condens. Matter Mater. Phys.*, 2005, **72**, 195208.

156 C. S. Ponseca, P. Chábera, J. Uhlig, P. Persson and V. Sundström, 'Ultrafast Electron Dynamics in Solar Energy Conversion', *Chem. Rev.*, 2017, **117**, 10940–11024.

157 G. M. Greetham, P. M. Donaldson, C. Nation, I. V. Sazanovich, I. P. Clark, D. J. Shaw, A. W. Parker and M. Towrie, 'A 100 kHz time-resolved multiple-probe femtosecond to second infrared absorption spectrometer', *Appl. Spectrosc.*, 2016, **70**, 645–653.

158 G. M. Greetham, D. Sole, I. P. Clark, A. W. Parker, M. R. Pollard and M. Towrie, 'Time-resolved multiple probe spectroscopy', *Rev. Sci. Instrum.*, 2012, **83**, 103107.

159 T. A. A. Oliver, 'Recent advances in multidimensional ultrafast spectroscopy', *R. Soc. Open Sci.*, 2018, **5**, 171425.

160 C. T. Kuhs, B. M. Luther and A. T. Krummel, 'Recent Advances in 2D IR Spectroscopy Driven by Advances in Ultrafast Technology', *IEEE J. Sel. Top. Quantum Electron.*, 2019, **25**, 1–1.

161 T. A. A. Oliver, N. H. C. Lewis and G. R. Fleming, 'Correlating the motion of electrons and nuclei with two-dimensional electronic-vibrational spectroscopy', *Proc. Natl. Acad. Sci. U. S. A.*, 2014, **111**, 10061–10066.

162 M. Liebel, C. Schnedermann, T. Wende and P. Kukura, 'Principles and Applications of Broadband Impulsive Vibrational Spectroscopy', *J. Phys. Chem. A*, 2015, **119**, 9506–9517.

163 W. K. Zhang, 'Polarization Dependent Time-Resolved Infrared Spectroscopy and Its Applications', *Chinese J. Chem. Phys.*, 2016, **29**, 1–9.

164 M. Di Donato and M. L. Groot, 'Ultrafast infrared spectroscopy in photosynthesis',

Biochim. Biophys. Acta - Bioenerg., 2015, **1847**, 2–11.

165 M. Kondo, J. Nappa, K. L. Ronayne, A. L. Stelling, P. J. Tonge and S. R. Meech, 'Ultrafast Vibrational Spectroscopy of the Flavin Chromophore', *J. Phys. Chem. B*, 2006, **110**, 20107–20110.

166 M. D. Fayer, *Ultrafast Infrared Vibrational Spectroscopy*, CRC Press, Boca Raton, Fla., 2013.

167 A. L. Stelling, K. L. Ronayne, J. Nappa, P. J. Tonge and S. R. Meech, 'Ultrafast structural dynamics in BLUF domains: Transient infrared spectroscopy of AppA and its mutants', *J. Am. Chem. Soc.*, 2007, **129**, 15556–15564.

168 P. Hamm, M. Lim and R. M. Hochstrasser, 'Structure of the Amide I Band of Peptides Measured by Femtosecond Nonlinear-Infrared Spectroscopy', *J. Phys. Chem. B*, 1998, **102**, 6123–6138.

169 I. V. Rubtsov and R. M. Hochstrasser, 'Vibrational dynamics, mode coupling, and structural constraints for acetylproline-NH2', *J. Phys. Chem. B*, 2002, **106**, 9165–9171.

170 A. Barth and C. Zscherp, 'What vibrations tell us about proteins', *Q. Rev. Biophys.*, 2002, **35**, 369–430.

171 A. Barth, 'Infrared spectroscopy of proteins', *Biochim. Biophys. Acta - Bioenerg.*, 2007, **1767**, 1073–1101.

172 A. Ghosh, J. S. Ostrander and M. T. Zanni, 'Watching Proteins Wiggle: Mapping Structures with Two-Dimensional Infrared Spectroscopy', *Chem. Rev.*, 2017, **117**, 10726–10759.

173 A. A. Bakulin, D. Y. Parashchuk, P. van Loosdrecht and M. S. Pshenichnikov, 'Ultrafast polarisation spectroscopy of photoinduced charges in a conjugated polymer', *Quantum Electron.*, 2009, **39**, 643–648.

174 J. N. Moore, P. A. Hansen and R. M. Hochstrasser, 'Iron-carbonyl bond geometries of carboxymyoglobin and carboxyhemoglobin in solution determined by picosecond time-resolved infrared spectroscopy.', *Proc. Natl. Acad. Sci.*, 1988, **85**, 5062–5066.

175 W. Zhang, Z. Lan, Z. Sun and K. J. Gaffney, 'Resolving Photo-Induced Twisted Intramolecular Charge Transfer with Vibrational Anisotropy and TDDFT', *J. Phys. Chem. B*, 2012, **116**, 11527–11536.

176 P. Hamm and M. Zanni, *Concepts and methods of 2D infrared spectroscopy*, Cambridge University Press, Cambridge, 2011.

177 M. C. Asplund, M. T. Zanni and R. M. Hochstrasser, 'Two-dimensional infrared spectroscopy of peptides by phase-controlled femtosecond vibrational photon echoes', *Proc. Natl. Acad. Sci.*, 2000, **97**, 8219–8224.

178 P. Hamm, M. Lim, W. F. Degrado and R. M. Hochstrasser, 'The two-dimensional IR nonlinear spectroscopy of a cyclic penta-peptide in relation to its three-dimensional structure', *Proc. Natl. Acad. Sci. U. S. A.*, 1999, **96**, 2036–2041.

179 C. Fang, J. Wang, Y. S. Kim, A. K. Charnley, W. Barber-Armstrong, A. B. Smith, S. M.

Decatur and R. M. Hochstrasser, 'Two-dimensional infrared spectroscopy of isotopomers of an alanine rich α-helix', *J. Phys. Chem. B*, 2004, **108**, 10415–10427.

180 C. Fang and R. M. Hochstrasser, 'Two-dimensional infrared spectra of the 13C= 18O isotopomers of alanine residues in an α-helix', *J. Phys. Chem. B*, 2005, **109**, 18652–18663.

181 G. Hithell, D. J. Shaw, P. M. Donaldson, G. M. Greetham, M. Towrie, G. A. Burley, A. W. Parker and N. T. Hunt, 'Long-range vibrational dynamics are directed by Watson-Crick base pairing in duplex DNA', *J. Phys. Chem. B*, 2016, **120**, 4009–4018.

182 L. A. I. Ramakers, G. Hithell, J. J. May, G. M. Greetham, P. M. Donaldson, M. Towrie, A. W. Parker, G. A. Burley and N. T. Hunt, '2D-IR spectroscopy shows that optimized DNA minor groove binding of Hoechst33258 follows an induced fit model', *J. Phys. Chem. B*, 2017, **121**, 1295–1303.

183 E. B. Dunkelberger, M. Grechko and M. T. Zanni, 'Transition Dipoles from 1D and 2D Infrared Spectroscopy Help Reveal the Secondary Structures of Proteins: Application to Amyloids', *J. Phys. Chem. B*, 2015, **119**, 14065–14075.

184 L. Minnes, D. J. Shaw, B. P. Cossins, P. M. Donaldson, G. M. Greetham, M. Towrie, A. W. Parker, M. J. Baker, A. J. Henry, R. J. Taylor and N. T. Hunt, 'Quantifying Secondary Structure Changes in Calmodulin Using 2D-IR Spectroscopy', *Anal. Chem.*, 2017, **89**, 10898–10906.

185 M. Maj, J. P. Lomont, K. L. Rich, A. M. Alperstein and M. T. Zanni, 'Site-specific detection of protein secondary structure using 2D IR dihedral indexing: A proposed assembly mechanism of oligomeric hIAPP', *Chem. Sci.*, 2018, **9**, 463–474.

186 M. Grechko and M. T. Zanni, 'Quantification of transition dipole strengths using 1D and 2D spectroscopy for the identification of molecular structures via exciton delocalization: Application to α-helices', *J. Chem. Phys.*, 2012, **137**, 184202.

187 T. A. Oudenhoven, Y. Joo, J. E. Laaser, P. Gopalan and M. T. Zanni, 'Dye aggregation identified by vibrational coupling using 2D IR spectroscopy', *J. Chem. Phys.*, 2015, **142**, 212449.

188 N. T. Hunt, '2D-IR spectroscopy: Ultrafast insights into biomolecule structure and function', *Chem. Soc. Rev.*, 2009, **38**, 1837–1848.

189 M. Khalil, N. Demirdöven and A. Tokmakoff, 'Coherent 2D IR spectroscopy: Molecular structure and dynamics in solution', *J. Phys. Chem. A*, 2003, **107**, 5258–5279.

190 S. T. Roberts, J. J. Loparo and A. Tokmakoff, 'Characterization of spectral diffusion from two-dimensional line shapes', *J. Chem. Phys.*, 2006, **125**, 212427.

191 S. Park, K. Kwak and M. D. Fayer, 'Ultrafast 2D-IR vibrational echo spectroscopy: A probe of molecular dynamics', *Laser Phys. Lett.*, 2007, **4**, 704–718.

192 J. Zheng, K. Kwak and M. D. Fayer, 'Ultrafast 2D IR Vibrational Echo Spectroscopy', *Acc. Chem. Res.*, 2007, **40**, 75–83.

193 K. T. Munson, E. R. Kennehan and J. B. Asbury, 'Structural origins of the electronic properties of materials: Via time-resolved infrared spectroscopy', *J. Mater. Chem.*

C, 2019, **7**, 5889–5909.

194 B. Dereka, M. Koch and E. Vauthey, 'Looking at Photoinduced Charge Transfer Processes in the IR: Answers to Several Long-Standing Questions', *Acc. Chem. Res*, 2017, **50**, 58.

195 R. D. Pensack and J. B. Asbury, 'Ultrafast probes of charge transfer states in organic photovoltaic materials', *Chem. Phys. Lett.*, 2011, **515**, 197–205.

196 K. S. Jeong, R. D. Pensack and J. B. Asbury, 'Vibrational spectroscopy of electronic processes in emerging photovoltaic materials', *Acc. Chem. Res.*, 2013, **46**, 1538–1547.

197 A. A. Bakulin, D. S. Martyanov, D. Y. Paraschuk, M. S. Pshenichnikov and P. H. M. van Loosdrecht, 'Ultrafast Charge Photogeneration Dynamics in Ground-State Charge-Transfer Complexes Based on Conjugated Polymers', *J. Phys. Chem. B*, 2008, **112**, 13730–13737.

198 J. L. Bredas and G. B. Street, 'Polarons, bipolarons, and solitons in conducting polymers', *Acc. Chem. Res.*, 1985, **18**, 309–315.

199 W. Barford, M. Marcus and O. R. Tozer, 'Polarons in π-Conjugated Polymers: Anderson or Landau?', *J. Phys. Chem. A*, 2016, **120**, 615–620.

200 G. Harbeke, D. Baeriswyl, H. Kiess and W. Kobel, 'Polarons and bipolarons in doped polythiophenes', *Phys. Scr.*, 1986, **1986**, 302–305.

201 J. L. Brédas, F. Wudl and A. J. Heeger, 'Polarons and bipolarons in doped polythiophene: A theoretical investigation', *Solid State Commun.*, 1987, **63**, 577–580.

202 R. Österbacka, C. P. An, X. M. Jiang and Z. V. Vardeny, 'Two-dimensional electronic excitations in self-assembled conjugated polymer nanocrystals', *Science*, 2000, **287**, 839–842.

203 P. A. Lane, X. Wei and Z. A. Vardeny, 'Studies of charged excitations in Π-conjugated oligomers and polymers by optical modulation', *Phys. Rev. Lett.*, 1996, **77**, 1544–1547.

204 J. Guo, H. Ohkita, H. Benten and S. Ito, 'Near-IR femtosecond transient absorption spectroscopy of ultrafast polaron and triplet exciton formation in polythiophene films with different regioregularities', *J. Am. Chem. Soc.*, 2009, **131**, 16869–16880.

205 C. X. Sheng, M. Tong, S. Singh and Z. V. Vardeny, 'Experimental determination of the charge/neutral branching ratio η in the photoexcitation of π -conjugated polymers by broadband ultrafast spectroscopy', *Phys. Rev. B - Condens. Matter Mater. Phys.*, 2007, **75**, 085206.

206 S. Das, P. P. Khlyabich, B. Burkhart, S. T. Roberts, E. Couderc, B. C. Thompson and S. E. Bradforth, 'Quantifying charge recombination in solar cells based on donor-acceptor p3ht analogues', *J. Phys. Chem. C*, 2014, **118**, 6650–6660.

207 O. G. Reid, R. D. Pensack, Y. Song, G. D. Scholes and G. Rumbles, 'Charge photogeneration in neat conjugated polymers', *Chem. Mater.*, 2014, **26**, 561–575.

208 E. Lioudakis, I. Alexandrou and A. Othonos, 'Ultrafast dynamics of localized and

delocalized polaron transitions in P3HT/PCBM blend materials: The effects of PCBM concentration', *Nanoscale Res. Lett.*, 2009, **4**, 1475–1480.

209 F. Provencher, N. Bérubé, A. W. Parker, G. M. Greetham, M. Towrie, C. Hellmann, M. Côté, N. Stingelin, C. Silva and S. C. Hayes, 'Direct observation of ultrafast long-range charge separation at polymer-fullerene heterojunctions', *Nat. Commun.*, 2014, **5**, 4288.

210 M. G. Voss, D. T. Scholes, J. R. Challa and B. J. Schwartz, 'Ultrafast transient absorption spectroscopy of doped P3HT films: distinguishing free and trapped polarons', *Faraday Discuss.*, 2019, **216**, 339–362.

211 C. Wiebeler, R. Tautz, J. Feldmann, E. Von Hauff, E. Da Como and S. Schumacher, 'Spectral signatures of polarons in conjugated co-polymers', *J. Phys. Chem. B*, 2013, **117**, 4454–4460.

212 M. Anderson, C. Ramanan, C. Fontanesi, A. Frick, S. Surana, D. Cheyns, M. Furno, T. Keller, S. Allard, U. Scherf, D. Beljonne, G. D'Avino, E. Von Hauff and E. Da Como, 'Displacement of polarons by vibrational modes in doped conjugated polymers', *Phys. Rev. Mater.*, 2017, **1**, 055604.

213 N. Takeda and J. R. Miller, 'Poly(3-decylthiophene) radical anions and cations in solution: Single and multiple polarons and their delocalization lengths in conjugated polymers', *J. Phys. Chem. B*, 2012, **116**, 14715–14723.

214 A. Troisi, 'Charge transport in high mobility molecular semiconductors: classical models and new theories', *Chem. Soc. Rev.*, 2011, **40**, 2347.

215 J. Yin, Z. Wang, D. Fazzi, Z. Shen and C. Soci, 'First-Principles Study of the Nuclear Dynamics of Doped Conjugated Polymers', *J. Phys. Chem. C*, 2016, **120**, 1994–2001.

216 S. Kahmann, M. A. Loi and C. J. Brabec, 'Delocalisation softens polaron electronic transitions and vibrational modes in conjugated polymers', *J. Mater. Chem. C*, 2018, **6**, 6008–6013.

217 C. H. Londergan, J. C. Salsman, S. Ronco and C. P. Kubiak, 'Infrared activity of symmetric bridging ligand modes in pyrazine-bridged hexaruthenium mixed-valence clusters', *Inorg. Chem.*, 2003, **42**, 926–928.

218 S. Hotta, W. Shimotsuma and M. Taketani, 'Fourier transform infrared study of electrochemically prepared polythienylene films with varying doping levels', *Synth. Met.*, 1984, **10**, 85–94.

219 M. Zamadar, S. Asaoka, D. C. Grills and J. R. Miller, 'Giant infrared absorption bands of electrons and holes in conjugated molecules', *Nat. Commun.*, 2013, **4**, 2818.

220 E. T. Shimomura, M. A. Phillippi, H. M. Goff, W. F. Scholz and C. A. Reed, 'Infrared Spectroscopy of Oxidized Metalloporphyrins: Detection of a Band Diagnostic of Porphyrin-Centered Oxidation', *J. Am. Chem. Soc.*, 1981, **103**, 6778–6780.

221 D. P. Arnold, R. D. Hartnell, G. A. Heath, L. Newby and R. D. Webster, 'Remarkable homology in the electronic spectra of the mixed-valence cation and anion radicals of a conjugated bis(porphyrinyl)butadiyne', *Chem. Commun.*, 2002, **2**, 754–755.

222 R. Österbacka, X. M. Jiang, C. P. An, B. Horovitz and Z. V. Vardeny, 'Photoinduced

Quantum Interference Antiresonances in Pi-Conjugated Polymers', *Phys. Rev. Lett.*, 2002, **88**, 4.

223 J. Rawson, P. J. Angiolillo and M. J. Therien, 'Extreme electron polaron spatial delocalization in ϕ-conjugated materials', *Proc. Natl. Acad. Sci. U. S. A.*, 2015, **112**, 13779–13783.

224 A. De Sio, F. Troiani, M. Maiuri, J. Réhault, E. Sommer, J. Lim, S. F. Huelga, M. B. Plenio, C. A. Rozzi, G. Cerullo, E. Molinari and C. Lienau, 'Tracking the coherent generation of polaron pairs in conjugated polymers', *Nat. Commun.*, 2016, **7**, 13742.

225 C. Minot and C. Flytzanis, 'Fano interference effects in the vibronic coupling of one-dimensional conjugated semiconductors', *Chem. Phys. Lett.*, 1979, **68**, 501–506.

226 N. T. Hunt, 'Transient 2D-IR spectroscopy of inorganic excited states', *Dalton Trans.*, 2014, **43**, 17578–17589.

227 A. L. Le Sueur, R. E. Horness and M. C. Thielges, 'Applications of two-dimensional infrared spectroscopy', *Analyst*, 2015, **140**, 4336–4349.

228 P. M. Donaldson, G. M. Greetham, D. J. Shaw, A. W. Parker and M. Towrie, 'A 100 kHz Pulse Shaping 2D-IR Spectrometer Based on Dual Yb:KGW Amplifiers', *J. Phys. Chem. A*, 2018, **122**, 780–787.

229 N. I. Rubtsova and I. V. Rubtsov, 'Vibrational Energy Transport in Molecules Studied by Relaxation-Assisted Two-Dimensional Infrared Spectroscopy', *Annu. Rev. Phys. Chem.*, 2015, **66**, 717–738.

230 V. M. Kasyanenko, Z. Lin, G. I. Rubtsov, J. P. Donahue and I. V. Rubtsov, 'Energy transport via coordination bonds', *J. Chem. Phys.*, 2009, **131**, 154508.

231 J. T. Reilly, J. M. Walsh, M. L. Greenfield and M. D. Donohue, 'Analysis of FT-IR spectroscopic data: The Voigt profile', *Spectrochim. Acta Part A Mol. Spectrosc.*, 1992, **48**, 1459–1479.

232 C. Ruckebusch, M. Sliwa, P. Pernot, A. de Juan and R. Tauler, 'Comprehensive data analysis of femtosecond transient absorption spectra: A review', *J. Photochem. Photobiol. C Photochem. Rev.*, 2012, **13**, 1–27.

233 D. V. Kurochkin, S. R. G. Naraharisetty and I. V. Rubtsov, 'A relaxation-assisted 2D IR spectroscopy method', *Proc. Natl. Acad. Sci.*, 2007, **104**, 14209–14214.

234 O. A. Vydrov and G. E. Scuseria, 'Assessment of a long-range corrected hybrid functional', *J. Chem. Phys.*, 2006, **125**, 234109.

235 O. A. Vydrov, J. Heyd, A. V. Krukau and G. E. Scuseria, 'Importance of short-range versus long-range Hartree-Fock exchange for the performance of hybrid density functionals', *J. Chem. Phys.*, 2006, **125**, 74106.

236 O. A. Vydrov, G. E. Scuseria and J. P. Perdew, 'Tests of functionals for systems with fractional electron number', *J. Chem. Phys.*, 2007, **126**, 154109.

237 M. J. Frisch, G. W. Trucks, H. B. Schlegel, G. E. Scuseria, M. A. Robb, J. R. Cheeseman, G. Scalmani, V. Barone, B. Mennucci, G. A. Petersson, H. Nakatsuji, M. Caricato, X. Li, H. P. Hratchian, A. F. Izmaylov, J. Bloino, G. Zheng, J. L. Sonnenberg, M. Hada, M.

Ehara, K. Toyota, R. Fukuda, J. Hasegawa, M. Ishida, T. Nakajima, Y. Honda, O. Kitao, H. Nakai, T. Vreven, J. A. Montgomery, J. E. Peralta, F. Ogliaro, M. Bearpark, J. J. Heyd, E. Brothers, K. N. Kudin, V. N. Staroverov, R. Kobayashi, J. Normand, K. Raghavachari, A. Rendell, J. C. Burant, S. S. Iyengar, J. Tomasi, M. Cossi, N. Rega, J. M. Millam, M. Klene, J. E. Knox, J. B. Cross, V. Bakken, C. Adamo, J. Jaramillo, R. Gomperts, R. E. Stratmann, O. Yazyev, A. J. Austin, R. Cammi, C. Pomelli, J. W. Ochterski, R. L. Martin, K. Morokuma, V. G. Zakrzewski, G. A. Voth, P. Salvador, J. J. Dannenberg, S. Dapprich, A. D. Daniels, Farkas, J. B. Foresman, J. V Ortiz, J. Cioslowski and D. J. Fox, 'Gaussian 09, Revision D.01, Gaussian, Inc., Wallingford CT', Gaussian 09, Revision D.01, Gaussian, Inc., Wallin.

238 S. Hu and T. G. Spiro, 'The Origin of Infrared Marker Bands of Porphyrin π-Cation Radicals: Infrared Assignments for Cations of Copper(II) Complexes of Octaethylporphine and Tetraphenylporphine', *J. Am. Chem. Soc.*, 1993, **115**, 12029–12034.

239 S. A. Sibilia, R. S. Czernuszewicz, M. J. Crossley and T. G. Spiro, 'Orbital Ordering in β-Substituted Porphyrins: Resonance Raman Spectra of the Radical Cations', *Inorg. Chem.*, 1997, **36**, 6450–6453.

240 M. Galperin, M. A. Ratner and A. Nitzan, 'Molecular transport junctions: Vibrational effects', *J. Phys. Condens. Matter*, 2007, **19**, 103201.

241 J. Koch and F. Von Oppen, 'Franck-Condon blockade and giant Fano factors in transport through single molecules', *Phys. Rev. Lett.*, 2005, **94**, 206804.

242 E. Burzurí, Y. Yamamoto, M. Warnock, X. Zhong, K. Park, A. Cornia and H. S. J. Van Der Zant, 'Franck-condon blockade in a single-molecule transistor', *Nano Lett.*, 2014, **14**, 3191–3196.

243 C. E. Tait, P. Neuhaus, M. D. Peeks, H. L. Anderson and C. R. Timmel, 'Excitation wavelength-dependent EPR study on the influence of the conformation of multiporphyrin arrays on triplet state delocalization', *Phys. Chem. Chem. Phys.*, 2016, **18**, 5275–5280.

244 M. Krejčik, M. Daněk and F. Hartl, 'Simple construction of an infrared optically transparent thin-layer electrochemical cell. Applications to the redox reactions of ferrocene, Mn2(CO)10 and Mn(CO)3(3,5-di-t-butyl-catecholate)-', *J. Electroanal. Chem.*, 1991, **317**, 179–187.

245 W. Wang, N. Zhao, Y. Geng, S. Bin Cui, J. Hauser, S. Decurtins and S. X. Liu, 'A highly sensitive TTF-functionalised probe for the determination of physiological thiols and its application in tumor cells', *RSC Adv.*, 2014, **4**, 32639–32642.

246 N. Mouton, M. Sliwa, G. Buntinx and C. Ruckebusch, 'Deconvolution of femtosecond time-resolved spectroscopy data in multivariate curve resolution. Application to the characterization of ultrafast photo-induced intramolecular proton transfer', *J. Chemom.*, 2010, **24**, 424–433.

247 M. Roelfs and P. C. Kroon, *Zenodo*, 2019, June 21.

248 W. Rock, Y. L. Li, P. Pagano and C. M. Cheatum, '2D IR spectroscopy using four-wave mixing, pulse shaping, and IR upconversion: A quantitative comparison', *J. Phys. Chem. A*, 2013, **117**, 6073–6083.